Magnetic properties and magnetic resonances of single crystals based on iron borate : Experimental studies and modelling

Kira Seleznyova

THÈSE EN COTUTELLE

PRÉSENTÉE POUR OBTENIR LE GRADE DE DOCTEUR

DE L'UNIVERSITÉ DE BORDEAUX

ET DE L'UNIVERSITÉ FÉDÉRALE V.I. VERNADSKI DE CRIMÉE

ÉCOLE DOCTORALE DES SCIENCES PHYSIQUES ET DE L'INGENIEUR DE L'UNIVERSITÉ DE BORDEAUX

ET ÉCOLE DOCTORALE DE L'UNIVERSITÉ FÉDÉRALE DE CRIMÉE

SPÉCIALITÉS : LASERS, MATIÈRE ET NANOSCIENCES

ET PHYSIQUE DE L'ÉTAT CONDENSÉ ET PHYSIQUE DES PHÉNOMÈNES MAGNÉTIQUES

Par **Kira SELEZNYOVA**

MAGNETIC PROPERTIES AND MAGNETIC RESONANCES OF SINGLE CRYSTALS BASED ON IRON BORATE: EXPERIMENTAL STUDIES AND MODELLING

Sous la direction de Janis KLIAVA et de Mark STRUGATSKY

Soutenue le 16 décembre 2016

Membres du Jury :

M. BARBARA Bernard, Institut Néel : président

M. KIMEL Alexey, Université Radboud de Nimègue : rapporteur

Mme SHALYGUINA Elena, Université d'État de Moscou : rapporteuse

M. CURÉLY Jacques, Université de Bordeaux : examinateur

M. KLIAVA Janis, Université de Bordeaux : co-directeur

M. STRUGATSKY Mark, Université Fédérale de Crimée : co-directeur

To the memory of Professor V.N. Seleznev,
my grandfather

Acknowledgements

First of all, I express my cordial appreciation to both my scientific supervisors, Professors Janis Kliava and Mark Strugatsky. You have directed my research with a great efficiency, kindness and competence. You have given me more than knowledge, more than skills and experience — you have taught me to think. Owing to you, I fell in love with science, and all years of my PhD studies were interesting, enjoyable, exciting, sometimes intriguing and very fruitful. Thank you for improving my scientific English, French, as well as Russian, initiating in Latin, Greek, *etc.* I am sincerely grateful to you for support, 24 hours a day and 7 days a week, even in solving not wholly scientific problems. You have become "godparents" for me during these years. Moreover, I really hope that my thesis is only a start for our future joint work.

Next, I would like to thank both Universities that hosted me, in particular the Laboratoire Ondes et Matière d'Aquitaine of the University of Bordeaux and Physics and Technology Institute of the Crimean Federal University.

Certainly, I would like to thank the other members of the jury: M. Bernard Barbara, M. Alexey Kimel, Mme Elena Shalyguina and M. Jacques Curély for accepting to evaluate my work and interesting discussion during the defence.

I had been involved in crystal synthesis during my bachelor's studies. For this fact, as well as for continuous support, I express a particular gratitude to M. Sergey Yagupov, the head of the Crystal Growth Laboratory at the Crimean University. Thank you for directing my research work aimed at preparing the samples that have become the basis for this work.

I'm deeply indebted to all members of the Department of Theoretical and Solid State Physics of Physics and Technology Institute of the Crimean University. Special thanks are due to Mme Natalia Postivey and Mme Yuliya Mogilenec – for collaboration in crystal synthesis, Mme Elena Maksimova and M. Igor Nauhatsky – in X-ray diffraction studies.

I have much owned from collaboration with Mme Natalia Kreines and M. Alexey Drovosekov of the Kapitsa Institute for Physical Problems (Moscow), Mme Alla Artemenko of the Institut de Chimie de la Matière Condensée de Bordeaux CNRS (ICMCB) – Electron magnetic resonance studies, M. Patrick Rosa of the ICMCB – SQUID measurements, M. Nikolaj Sergeev and his group of the Uniwersytet Szczeciński (Poland) – Nuclear magnetic resonance studies, as well as M. Victor Zubov of the the Lomonosov Moscow State University – interesting discussions on the theory of surface magnetism.

Dear Irina Samsonovna Edelman, you have become my "guardian angel" for my research work; you have shown me the way to follow and continuously supported me till the very moment of the thesis defense.

Undoubtly, I am infinitely grateful to my parents and grandparents, to all my family and M. Alexander Matveenko. Thank you not only for your support, attention and patience in the recent years, thank you for the fact that I became who I became.

This work is devoted to the memory of Professor Seleznev, my grandfather. Many years ago he had created a scientific school in solid state physics in Crimea. I am so proud to belong to this school and pursue his work and his ideas.

Propriétés magnétiques et résonances magnétiques de monocristaux à base de borate de fer: Études expérimentales et modélisation

La thèse porte sur la synthèse et l'étude des propriétés magnétiques de borates de fer-gallium, $Fe_xGa_{1-x}BO_3$ avec $0 \leqslant x \leqslant 1$. Ces matériaux sont prometteurs pour les applications; en plus, grâce à la présence, en fonction de *x*, de différents types d'ordre magnétique, ils sont bien adaptés au traitement de nombreux problèmes du magnétisme des solides.

Le borate de fer, $FeBO_3$ est un antiferromagnétique possédant un plan de facile aimantation et un faible ferromagnétisme. Les caractéristiques du borate de fer sont radicalement modifiées par substitution isomorphe fer – gallium diamagnétique.

Nous avons mis au point une route de synthèse de monocristaux $Fe_xGa_{1-x}BO_3$ de haute qualité. Comme principales techniques expérimentales, nous avons choisi les résonances magnétiques électronique (RME) et nucléaire (RMN). Selon le contenu du fer, nous avons observé:(i) la résonance antiferromagnétique, (ii) la résonance de clusters magnétiques et (iii) la résonance paramagnétique électronique (RPE).

Les différents états magnétiques ont été identifiés et leurs caractéristiques – la température de Néel, le champ de Dzyaloshinskii-Moriya; les paramètres de l'hamiltonien de spin de Fe^{3+}, *etc.* – ont été déterminées. La coordinence et la symétrie de sites de ^{11}B et ^{71}Ga ont été précisées par RMN à rotation sous l'angle « magique » (MAS). Moyennant la simulation des spectres de RPE et de MAS RMN, à l'aide de codes mis au point *ad hoc*, les distributions de paramètres dues au désordre local ont été déterminées. L'analyse théorique, tenant compte de contributions du champ cristallin et de l'interaction dipôle-dipôle, permet d'expliquer l'anisotropie magnétocristalline de volume et de surface.

Mots clés : borate de fer-gallium, synthèse de cristaux, résonance magnétique électronique, résonance magnétique nucléaire, anisotropie magnétocristalline, magnétisme de surface.

Magnetic properties and magnetic resonances of single crystals based on iron borate: Experimental studies and modelling

The thesis is concerned with synthesis and studying magnetic properties of iron-gallium borates, $Fe_xGa_{1-x}BO_3$ with $0 \leqslant x \leqslant 1$. These materials are promising candidates for applications; besides, occurrence of different types of magnetic ordering, depending on x, makes them suitable for treating a number of fundamental problems in solid state magnetism.

Iron borate, $FeBO_3$ is a two-sublattice easy-plane antiferromagnet with weak ferromagnetism. Physical characteristics of iron borate are radically modified by isomorphous substitution of a part of iron by diamagnetic gallium.

We have started with developing a synthesis route for growing high-quality $Fe_xGa_{1-x}BO_3$ single crystals. As main experimental techniques, we have chosen Electron and Nuclear Magnetic Resonances (EMR, NMR). Depending on iron contents and temperature, we have observed: (i) Antiferromagnetic, (ii) Cluster Magnetic and (iii) Electron Paramagnetic Resonance (EPR).

Different magnetic states have been identified and their characteristics: Néel temperature, Dzyaloshinskii-Moriya field; spin Hamiltonian parameters of isolated Fe^{3+} ion, *etc.*, have been determined. Coordination and site symmetry of ^{11}B and ^{71}Ga nuclei have been specified by means of Magic Angle Spininng (MAS) NMR. Carrying out computer simulations of EPR and MAS NMR spectra with laboratory-developed codes, the parameter distributions caused by local disorder have been determined. Theoretical analysis taking into account crystal field and dipole-dipole contributions allow interpreting volume and surface magnetocrystalline anisotropy of the crystals.

Keywords : iron-gallium borate, crystal synthesis, electron magnetic resonance, nuclear magnetic resonance, magnetocrystalline anisotropy, surface magnetism.

Unité de recherche :

Laboratoire Ondes et Matière d'Aquitaine (LOMA)

UMR 5798 - Université de Bordeaux - CNRS

et Department of Theoretical and Solid State Physics, Physics and Technology Institute, V.I. Vernadsky Crimean Federal University, 295-007 Simferopol, Republic of Crimea

Sommaire

L'intérêt de la recherche du borate de fer, $FeBO_3$ est principalement lié à ses remarquables caractéristiques magnétiques, magnéto-acoustiques, optiques, magnéto-optiques, *etc.* Ce matériau est prometteur pour les applications dans des diverses branches des sciences expérimentales et de l'ingénierie. En particulier, éléments de mémoire magnétique à haute densité d'enregistrement, transducteurs magnéto-acoustiques et magnéto-optiques, instruments de mesure des champs magnétiques ultra-faibles, de la température et de la pression peuvent être fabriqués sur la base du borate de fer. $FeBO_3$ peut être appliqué dans les batteries lithium-ion afin d'augmenter leur capacité. Par ailleurs, le borate de fer peut être utilisé comme un monochromateur du rayonnement synchrotron pour la spectroscopie Mössbauer.

Le premier chapitre « Crystal and magnetic structure of iron borate » présente la structure cristalline et magnétique de $FeBO_3$. Ce cristal a une structure de calcite rhomboédrique de groupe d'espace D_{3d}^6, possédant un axe C_3 orthogonal au plan de base. Du point de vue de la structure magnétique, en dessous de la température de Néel T_N =348 K, $FeBO_3$ est antiferromagnétique à deux sous-réseaux, possédant un plan de facile aimantation qui est le plan de base ; cependant, les aimantations des sous-réseaux ne sont pas tout à fait antiparallèles, ce qui engendre un faible ferromagnétisme dû à l'interaction Dzyaloshinskii-Moriya.

Par ailleurs, les caractéristiques physiques du borate de fer sont radicalement modifiées par substitution isomorphe d'une partie du fer paramagnétique par le gallium diamagnétique. Nous avons mis au point la route de synthèse de monocristaux de borates de fer-gallium $Fe_xGa_{1-x}BO_3$, par solution en fonte, décrite dans le deuxième chapitre « Synthesis of iron-gallium borate single crystals ». Des monocristaux de haute qualité ont été synthétisés dans toute la gamme des compositions $0 \leqslant x \leqslant 1$. À l'aide de l'analyse thermodifférentielle et de la technique de sonde, nous avons déterminé les rapports de composants dans la charge et les modes de température correspondants, optimaux pour la synthèse de monocristaux avec différents x. Après la synthèse, la composition des cristaux et les paramètres du réseau cristallin ont été déterminés par la spectrométrie de fluorescence et diffraction des rayons X (SFX et DRX, respectivement). La SFX a révélé une certaine distribution de concentrations d'ions Fe^{3+} et Ga^{3+} dans les cristaux extraits du même creuset. L'analyse par DRX a montré que dans les borates mixtes de fer-gallium la modification des paramètres du réseau cristallin suit de près la loi de Vegard.

Les cristaux $Fe_xGa_{1-x}BO_3$ présentent d'un grand intérêt, tant pour la physique du solide que pour la science des matériaux, dans la mesure où ils permettent :

- ✓ de suivre la transformation des propriétés magnétiques sous la transition entre l'état magnétiquement ordonné et l'état paramagnétique ;
- ✓ d'interpréter les propriétés magnétiques des cristaux dilués, en particulier, l'anisotropie magnétocristalline, pour mieux comprendre la nature de ces propriétés dans le borate de fer pur. En effet, les différents mécanismes responsables des propriétés magnétiques de $FeBO_3$ possèdent différentes dépendances en température et en concentration en fer ;

- ✓ la solution en fonte permet de synthétiser les cristaux de haute qualité avec les propriétés magnétiques prédéterminées, adaptées aux applications pratiques.

Les chapitres suivants traitent les études expérimentales et théoriques de borates de fer-gallium. Pour autant que nous soyons intéressés par les propriétés magnétiques des cristaux, nous avons choisi comme principales techniques expérimentales les résonances magnétiques électronique (RME) et nucléaire (RMN).

Le troisième chapitre « Electron magnetic resonance of iron-gallium borate single crystals with $0.2 \leq x \leq 1$ » présente les études de $Fe_xGa_{1-x}BO_3$ avec $0 < x \leqslant 1$ par RME. Cette technique permet d'identifier les états magnétiques des cristaux à différentes teneurs en fer et à différentes températures. En fonction de x, les spectres de RME montrent un passage graduel de la résonance antiferromagnétique (RAFM) à $x = 1$ vers la résonance paramagnétique électronique (RPE) d'ions de fer dilués à $x \ll 1$, en passant pour $0.34 \leqslant x \leqslant 0.85$ par une coexistence de RAFM et de la résonance de clusters magnétiques (RCM), provenant, respectivement, des régions du cristal magnétiquement ordonnées et partiellement désordonnées ; pour $x < 0.34$ seule la RCM est présente.

Les températures de Néel pour les cristaux avec $0.34 \leqslant x \leqslant 0.85$ ont été déterminées par des RME et SQUID (Superconducting Quantum Interference Device) techniques. Avec la diminution de x, T_N sensiblement diminue. Les dépendances en température du champ de RAFM suggèrent une présence de transitions magnétiques aux environs de 80 et 20 K pour $x = 0.65$ and 0.34, respectivement, les températures de Néel correspondantes proches de 244 et 77 K. Nous supposons qu'à basses températures ces cristaux subissent la transition de Morin à la température T_M. Au-dessus de T_M, la structure magnétique de ces cristaux est la même que celle de borate de fer pur, c'à-d. antiferromagnétique avec un plan de facile aimantation. En dessous de T_M, les cristaux sont antiferromagnétiques avec C_3 pour l'axe de facile aimantation ; par conséquent, le faible ferromagnétisme disparaît. Avec la diminution de x, à la fois le champ de Dzyaloshinskii-Moriya, H_D et l'écart d'énergie isotrope, H_Δ^2 diminuent. Pour les cristaux avec $x < 1$, en abaissant la température en dessous de T_N, H_D d'abord augmente, puis passe par un maximum et enfin décroît. Pour les cristaux avec $x = 0.65$ et 0.34, ce maximum se produit aux alentours de. 80 et 20 K, respectivement, ce qui corrobore l'hypothèse de la transition du Morin dans ces cristaux.

L'intensité de la raie de RMC, observée dans tous les cristaux avec $x < 1$ sauf à des valeurs de x très faibles, ne suit pas la loi de Curie en T^{-1}, ce qui suggère que cette raie est due aux clusters magnétiques. L'écart d'énergie anisotrope, déterminé pour le cristal avec $x = 1$ à 77 K, a permis de calculer la constante effective de l'anisotropie hexagonale; ce dernier a été utilisé dans l'analyse de l'anisotropie magnétocristalline de base.

La RPE d'ions Fe^{3+} isolés dans les cristaux avec $x \ll 1$ a été utilisée pour déterminer la symétrie des sites de fer et les paramètres de l'hamiltonien de spin dans les borates de fer-gallium. Ces données sont nécessaires pour obtenir une description complète de l'anisotropie magnétocristalline dans ces cristaux. Une facette essentielle des études de RPE est l'analyse

numérique – modélisation par ordinateur – des spectres expérimentaux. Le quatrième chapitre « EPR of iron-gallium borate single crystals with low x » décrit la paramétrisation des spectres de RPE d'ions Fe^{3+} à l'aide de codes informatique mis au point *ad hoc*. Dans un premier temps, nous avons développé un code basé sur l'hamiltonien de spin conventionnel, ce qui a permis de bonnes simulations des spectres expérimentaux, au moins, en ce qui concerne les champs de résonance. Cependant, nous avons constaté que dans cette approche deux jeux de paramètres différents sont possibles, dans la mesure où ils aboutissent à la même matrice de l'hamiltonien de spin. Cette dichotomie a pu être résolue en testant la compatibilité de ces deux jeux de paramètres avec les prédictions du modèle de superposition de Newman. A cet effet, nous avons utilisé l'hamiltonien de spin général pour les sites de symétrie trigonale. Les tests ont montré sans ambiguïté que seul l'un de ces jeux de paramètres est compatible avec le modèle de Newman.

À l'aide des simulations utilisant les deux hamiltoniens de spin – conventionnel et général – on obtient un bon ajustement des positions des raies de résonance ; en revanche, d'importantes divergences subsistent entre les amplitudes et largeurs des raies correspondantes dans les spectres expérimentaux et théoriques. Nous avons attribué ces divergences, à l'existence d'un certain degré de désordre local dans les cristaux. Dans le but de prendre en compte ce désordre dans l'hamiltonien de spin, nous avons exprimé celui-ci au moyen des opérateurs équivalents tesséraux à deux vecteurs, le spin effectif et le champ magnétisant. Cette approche nous a permis d'établir des relations entre d'une part, les distributions dues au désordre, des coordonnées d'oxygènes dans l'entourage de fer, et d'autre par les distributions des paramètres de l'hamiltonien de spin. Les simulations par ordinateur effectuées en utilisant un code basé sur ce modèle ont permis d'obtenir un très bon accord entre les spectres théoriques et expérimentaux en ce qui concerne à la fois les positions des raies et leurs amplitudes et largeurs. Ainsi, l'hypothèse de la présence du désordre local dans les cristaux fut confirmée.

Les études par RMN à rotation sous l'angle « magique » (MAS) des cristaux $Fe_xGa_{1-x}BO_3$ avec $0 \leqslant x \leqslant 0.02$, sont présentées dans le cinquième chapitre « NMR studies of iron-gallium borates ». Le double objectif de ces études a été de préciser la coordination et la symétrie de sites de bore et de gallium ainsi que corroborer, de façon indépendante, la présence d'un certain degré de désordre local dans ces cristaux. Les simulations par ordinateur des spectres de MAS RMN de noyaux ^{11}B et ^{71}Ga confirment la triple coordinence et la symétrie intrinsèque C_3 pour le bore, et la sextuple coordinance et une symétrie plus faible que la symétrie cubique pour le gallium. Pour les deux noyaux, l'élargissement des spectres de MAS RMN avec l'augmentation de teneur en fer a été attribué aux distributions des paramètres quadripolaires et du déplacement chimique, dans le cas de ^{71}Ga, causés par le désordre local, comme attendu. Comme dans le cas de RPE, les spectres ont été simulés par ordinateur ; dans le cas de RMN nous avons utilisé deux différents modèles de la fonction de distribution des paramètres, celles de Czjzek et de Maurer. Une analyse comparative des ces modèles a été réalisée en vue de leur application pour tenir compte de l'élargissement des spectres de MAS RMN induite par le désordre local dans les cristaux. Le modèle de Czjzek est bien adapté au cas des solides fortement désordonnés ; cependant, il ne tient pas compte d'ordre local partiellement conservé dans les cristaux présentant un certain désordre. En effet, il ne prend pas en considération les valeurs moyennes non nulles des

paramètres quadripolaires et il ne contient qu'un seul paramètre de largeur de distribution. Au contraire, le modèle de Maurer n'a pas ces limitations, il est donc mieux adapté aux simulations des spectres de RMN expérimentaux dans les cristaux à faible désordre local.

Les résultats des études de résonance magnétique ont permis de donner une nouvelle description théorique de l'anisotropie magnétocristalline dans le borate de fer et les borates mixtes de fer-gallium. Cette anisotropie comprend deux contributions : (i) du champ cristallin et (ii) de l'interaction dipôle-dipôle.

Dans la mesure où les ions Fe^{3+} dans $FeBO_3$ se trouvent dans un fort champ d'échange, la première contribution peut être calculée dans la théorie des perturbations, en exprimant les constantes d'anisotropie par l'intermédiaire des paramètres de l'hamiltonien de spin déterminés par RPE.

D'autre part, auparavant la contribution dipôle-dipôle a été considérée en négligeant la taille les dipôles (dipôles « ponctuels ») auquel cas elle contribuerait uniquement à l'anisotropie uniaxe (suivant l'axe C_3), mais pour des raisons de symétrie ne donnerait pas de contribution dans l'anisotropie de base. En effet, dans le borate de fer cette dernière est hexagonale, alors que l'énergie d'interaction de dipôles ponctuels dans le plan de base du borate de fer reste isotrope. Nous avons réexaminé ce problème en tenant compte des dimensions des dipôles (dipôles « étendus »). En supposant un rapport non négligeable entre la taille du dipôle et la distance dipôle-dipôle et en développant l'énergie d'interaction dipôle-dipôle en série de Taylor, les différents termes de ce développement permettent de rendre compte d'interactions de différentes symétries. Toutefois, pour explicitement calculer ces termes, on a besoin d'un modèle du dipôle étendu.

À cet effet, nous avons présenté une description théorique de trois modèles : (i) une sphère uniformément aimantée, (ii) une boucle de courant circulaire (un courant ampérien) et (iii) une paire de deux « charges magnétiques » fictifs. Nous avons démontré que les trois modèles donnent des résultats identiques à grandes distances. En effet, le premier terme du développement de Taylor de l'énergie dipôle-dipôle dans les modèles d'une boucle de courant circulaire et d'une paire de charges magnétiques coïncident avec l'expression de cette énergie pour les dipôles ponctuels (ou pour deux sphères uniformément aimantées non pénétrantes mutuellement).

Pour le calcul de la contribution dipôle-dipôle à l'anisotropie magnétocristalline du $FeBO_3$, nous avons utilisé la sommation sur le réseau cristallin pour deux modèles de dipôles étendus, à savoir une paire de charges magnétiques et une boucle de courant circulaire. La comparaison avec les données expérimentales élimine le modèle d'une paire de charges magnétiques ; en revanche, le modèle d'une boucle de courant circulaire paraît tout à fait adapté dans la mesure où il permet de rendre compte de la symétrie hexagonale de base et, accessoirement, fournit deux estimations plus ou moins réalistes de la taille des dipôles associés à ion Fe^{3+}.

L'énergie d'interaction dipôle-dipôle pour les borates mixtes $Fe_xGa_{1-x}BO_3$ a été calculée par la même technique que pour $FeBO_3$. Afin de modéliser le un réseau cristallin diamagnétiquement dilué, nous avons utilisé la technique de Monte Carlo. Ainsi nous avons obtenu les contributions dipôle-dipôle aux constantes d'anisotropie magnétocristalline uniaxe et de base pour des cristaux

avec différents *x*. Les résultats de cette analyse sont décrites dans le sixième chapitre « Magnetocrystalline anisotropy of iron borate and iron-gallium borates ».

Les propriétés surfaciques constituent un véritable défi compte tenu de leur importance primordiale pour la miniaturisation des éléments de micro-électronique. Auparavant, l'anisotropie magnétocristalline de surface dans le borate de fer volumique avait été décrite en ne tenant compte que de la contribution dipôle-dipôle. Dans le septième chapitre « Surface magnetocrystalline anisotropy of iron borate single crystals » nous avons étendu la théorie du magnétisme de surface de borate de fer, en tenant compte de la contribution du champ cristallin.

Nous avons développé un modèle de distorsions structurales dans la couche surfacique pour la face $(10\bar{1}4)$ de borate de fer, dans l'hypothèse que les positions de tous les ions dans cette couche soient décalées proportionnellement à leur distance d'un plan de référence, supposé rester immobile, parallèle à la face du cristal. Afin de calculer les paramètres de l'hamiltonien de spin pour les ions Fe^{3+} dans la couche surfacique en tenant compte de la baisse de symétrie, nous avons utilisé l'hamiltonien de spin généralisé exprimé au moyen des opérateurs équivalents tesséraux à deux vecteurs (voir chapitre 4) et le modèle de superposition. Pour les ions fer dans la couche surfacique, nous avons utilisé les mêmes paramètres du modèle de superposition que dans le volume, v. chapitre 4, dans la mesure où ces paramètres devraient rester inchangés tant que les distorsions structurales restent faibles. La contribution du champ cristallin à l'énergie d'anisotropie surfacique a été calculée dans la théorie des perturbations. Les résultats de ce calcul montrent que la prise en compte des modifications du champ cristallin dues aux distorsions structurales produit une contribution significative à l'anisotropie surfacique. La comparaison avec la détermination expérimentale de l'anisotropie magnétocristalline surfacique du borate de fer permet de conclure que les distorsions (contractions) relatives dans la couche surfacique sont proches de 1%.

Les résultats de ma thèse ont été présentés dans un certain nombre de conférences internationales et donné lieu à plusieurs publications, voir la liste à la fin de la thèse.

Contents

Introduction

The research interest in iron borate $FeBO_3$ is mainly due to its remarkable magnetic, magneto-acoustical, optical, magneto-optical, resonance, *etc.* characteristics [1-16]. This material is a first-rate candidate for practical applications in various branches of experimental science and engineering. In particular, magnetic memory elements possessing high density of recording, magneto-acoustic and magneto-optical transducers, instruments for measuring ultra-weak magnetic fields, temperature and pressure can be created on the basis of iron borate. $FeBO_3$ can be applied in modern lithium-ion batteries in order to substantially increase their capacity [17-19]. Besides, iron borate can be used as an excellent monochromator for synchrotron Mössbauer spectroscopy [20, 21].

Chapter 1, "Crystal and magnetic structure of iron borate" describes in detail crystal and magnetic structure of $FeBO_3$. This crystal has a rhombohedral calcite structure of D^6_{3d} space group [22]. From the viewpoint of magnetic structure, iron borate is a two-sublattice easy-plane antiferromagnet with the Néel temperature T_N = 348 K, showing a weak ferromagnetism caused by the Dzyaloshinskii-Moriya interaction [22].

A route for obtaining $FeBO_3$ single crystals of high structural perfection has been developed in the Crystal Growth Laboratory at the Simferopol University [23, 24], one of world-known leaders in the field of synthesis of iron borate-based single crystals. The crystals grown in this laboratory have been studied in a number of institutes of the Russian Academy of Sciences, *viz.*, the Kurchatov Institute, the Kapitsa Institute for Physical Problems, the Prokhorov General Physics Institute, the Kirensky Institute of Physics, the Institute of Crystallography and the Chair of Magnetism at the Lomonosov Moscow State University, as well as in many European institutions, *viz.*, in the Institut d'électronique, de microélectronique et de nanotechnologie (Lille), at the Radboud Universiteit (Nijmegen, Netherlands), the Uniwersytet Szczeciński (Poland), *etc.*

Magnetic characteristics of iron borate can be fine-tuned by isomorphous substitution of paramagnetic iron by diamagnetic gallium. I have actively collaborated with the Crystal Growth Laboratory in working out the solution-in-the-melt synthesis route for mixed iron-gallium borates $Fe_xGa_{1-x}BO_3$, as described in Chapter 2, "Synthesis of iron-gallium borate single crystals" concerned with preparing high-quality single crystals in the whole range of compositions. After successful synthesis, exact crystal composition and parameters of the crystal lattice have been determined by X-ray fluorescence analysis (XRF) and X-ray diffraction (XRD), respectively.

$Fe_xGa_{1-x}BO_3$ crystals are of a great interest because of the following reasons:

(i) They allow monitoring transformation of magnetic properties under the transition from magnetically ordered to paramagnetic state.

(ii) Understanding magnetic properties of diluted crystals, in particular, the magnetocrystalline anisotropy, allows specifying the nature of such properties in pure iron borate. Indeed, various mechanisms responsible for magnetic properties of $FeBO_3$

have different concentration and temperature dependences; consequently, the series of $Fe_xGa_{1-x}BO_3$ crystals offers a possibility to get a better insight in their nature.

(iii) The solution in the melt technique allows synthesizing high quality crystals with predetermined magnetic properties, suitable for practical applications.

Thus, mixed iron-gallium borates are of a major importance both in solid state physics and in materials science.

The following chapters deal with experimental and theoretical studies of iron-gallium borates. As far as we are mainly interested in magnetic properties of the crystals, as key experimental techniques we have chosen magnetic resonances, namely Electron Magnetic Resonance (EMR) and Nuclear Magnetic Resonance (NMR).

Chapter 3, "Electron magnetic resonance of iron-gallium borate single crystals with $0.2 \leq x \leq 1$" describes EMR studies of $Fe_xGa_{1-x}BO_3$ crystals with $0 < x \leqslant 1$. This technique allows identifying magnetic states occurring for different iron contents and at different temperatures. In particular, the Antiferromagnetic Resonance (AFMR) in crystals possessing magnetic ordering allows specifying the Néel temperature, the Dzyaloshinskii-Moriya field; studying the magnetocrystalline anisotropy of the samples. The Electron Paramagnetic Resonance of isolated Fe^{3+} ions in crystals with $x \ll 1$ serves as a powerful technique for specifying the symmetry of iron sites and determining spin Hamiltonian parameters of isolated Fe^{3+} ions. These data are necessary for a consistent description of the magnetocrystalline anisotropy in the crystals. An essential facet of the EPR spectroscopic studies is the numerical analysis – computer modelling – of the experimental spectra. Chapter 4, "EPR of iron-gallium borate single crystals with low x" describes the full parametrization of the EPR spectra of diluted Fe^{3+} ions by means of detailed computer simulations with the help of laboratory-developed codes, explicitly taking into account parameter distributions and thus allowing to estimate the degree of local disorder in the crystals. We have used different spin Hamiltonians in order to resolve the ambiguity in the choice of different sets of parameters.

The Magic Angle Spinning (MAS) NMR studies of $Fe_xGa_{1-x}BO_3$ crystals with $0 \leqslant x \leqslant 0.02$, described in Chapter 5, "NMR studies of iron-gallium borates", have been made in order to specify coordination and site symmetry of ^{11}B and ^{71}Ga nuclei. As in the case of EPR, we have followed the approach of computer simulations, applying different distribution functions of quadrupole parameters and chemical shift. A comparative analysis of the Czjzek's and Maurer's models of the joint distribution density of NMR quadrupole parameters has been carried out in view of their application to account for MAS NMR spectra broadening induced by local disorder in the crystals.

The results of the magnetic resonance studies have allowed to give a new theoretical description of magnetocrystalline anisotropy in iron borate and mixed iron-gallium borates. This anisotropy includes (i) crystal field and (ii) dipole-dipole contributions. The first contribution has been calculated in perturbation theory, expressing the anisotropy constants through the spin Hamiltonian parameters determined by EPR. The second contribution is usually considered for "point dipoles" having a negligible size. In this case only uniaxial anisotropy is accounted for,

basal anisotropy being ruled out on the grounds of symmetry. Indeed, the basal anisotropy in iron borate has hexagonal symmetry, whereas the interaction energy of point dipoles in the basal plane is isotropic. We have reexamined the dipole-dipole contribution using the concept of "extended dipoles" having non-negligible size. Taking into account higher-order terms in the expansion of the dipole-dipole interaction energy in a Taylor series in the small parameter dipole size/interdipole distance opens the possibility of describing more sophisticated issues, in particular, the hexagonal magnetocrystalline anisotropy. However, in order to explicitly calculate these terms we need a physical model of the extended dipole. For this purpose we have put forward a theoretical description of three models of the extended dipoles: (i) a uniformly magnetized sphere, (ii) an Ampérian current and (iii) an assembly of two fictitious "magnetic charges". For calculating the dipole-dipole contribution to the magnetocrystalline anisotropy we have used the lattice-sum method; for the mixed borates, a diamagnetically diluted crystal lattice has been generated by Monte Carlo technique [25]. A comparison between the calculation and the experimental data provides a consistent description of the basal magnetocrystalline anisotropy; moreover, it allows estimating the size of the extended dipoles. The results of this analysis are described in Chapter 6, "Magnetocrystalline anisotropy of iron borate and iron-gallium borates".

Surface properties represent a true challenge, as far as these properties are important for miniaturization of elements of microelectronics. Previously, the surface magnetocrystalline anisotropy in bulk iron borate had been described taking into account only the dipole-dipole contribution [6]. In Chapter 7, "Surface magnetocrystalline anisotropy of iron borate single crystals", we extend the theory of surface magnetism, taking into account the crystal field contribution. With this aim in view, we have put forward a model of structural distortions in the near-surface layer, allowing a complete description of the surface magnetocrystalline anisotropy of iron borate.

The results of my thesis have been presented in a number of international conferences and given rise to several publications, see the list at the end of the thesis.

References

1. M. Eibshütz and M.E. Lines, *Sublattice magnetization of single crystals by Mössbauer effect*, Phys. Rev. B **7** (1973) 4907-4915
2. M. Kalashnikova, A.V. Kimel, R.V. Pisarev, V.N. Gridnev, P.A. Usachev, A. Kirilyuk and Th. Rasing, *Laser excitation of lattice-driven anharmonic magnetization dynamics in dielectric* $FeBO_3$, Phys. Rev. B **78** (2008) 104301, 1-21
3. D. Afanasiev, I. Razdolski, K.M. Skibinsky, D. Bolotin, S.V. Yagupov, M.B. Strugatsky, A. Kirilyuk, Th. Rasing and A.V. Kimel, *Laser excitation of lattice-driven anharmonic magnetization dynamics in dielectric* $FeBO_3$, Phys. Rev. Lett. **112** (2014) 147403, 1-5
4. V.P. Glazkov, S.E. Kichanov, D.P. Kozlenko, B.N. Savenko and V.A. Somenkov, *Pressure-induced changes in magnetic structure of* $FeBO_3$, J. Magn. Magn. Mater. **258** (2003) 543-544
5. K. Parlinski, J. Łażewski, P.T. Jochym, A. Chumakov, R. Rüffer and G. Kresse, *Influence of magnetic interaction on lattice dynamics of* $FeBO_3$, Europhys. Lett. **56** (2001) 275-281
6. E.M. Maksimova, I.A. Nauhatsky, M.B. Strugatsky and V.E. Zubov, *Surface magnetism of real iron borate monocrystals*, J. Magn. Magn. Mater. **322** (2010) 477-480
7. I.A. Troyan, M.I. Eremets, A.G. Gavrilyuk, I.S. Lyubutin and V.A. Sarkisyan, *Transport and optical properties of iron borate* $FeBO_3$ *under high pressures*, JETP Letters **78** (2003) 13-16
8. M. Kalashnikova, A.V. Kimel, R.V. Pisarev, V.N. Gridnev, P.A. Usachev, A. Kirilyuk and Th. Rasing, *Impulsive generation of coherent magnons by linearly polarized light in the easy-plane antiferromagnet* $FeBO_3$, Phys. Rev. Lett. **99** (2007) 167205, 1-4
9. A.V. Malakhovskii and I.S. Edelman, *Optical and magneto-optical spectra of* $FeBO_3$ *in the region of strong absorption*, Phys. Stat. Sol. (b) **74** (1976) K145-149
10. W. Jantz, J.R. Sandercock and W. Wettling, *Determination of magnetic and elastic properties of* $FeBO_3$ *by light scattering*, J. Phys. C **9** (1976) 2229-2240
11. E.A. Turov, *Acoustics and acoustooptics of easy plane antiferromagnets*, Solid St. Communs. **87** (1993) 1137-1140
12. M.B. Strugatsky, K.M. Skibinsky, V.V. Tarakanov and V.I. Khizhnyi, *Fine structure of Gakel'-Turov oscillations in iron borate*, J. Magn. Magn. Mater. **241** (2002) 330-334
13. M.B. Strugatsky and K.M. Skibinsky, *Acoustic resonances in antiferromagnet* $FeBO_3$, J. Magn. Magn. Mater. **309** (2007) 64-70
14. M. Eibschutz, L. Pfeiffer and J.W. Nielsen, *Critical-point behavior of* $FeBO_3$ *single crystals by Mössbauer effect*, J. Appl. Phys. **41** (1970) 1276-1277
15. V.V. Tarakanov, V.I. Khizhnyi, A.P. Korolyuk and M.B. Strugatsky, *Excitation of magnetic polaritons in plates of* $FeBO_3$, Physica B **284** (2000) 1452-1453
16. L.V. Velikov, A.S. Prokhorov, E.G. Rudashevskii and V.N. Seleznev, *Antiferromagnetic resonance in* $FeBO_3$, Soviet Physics JETP **39** (1974) 909-915
17. J.L.C. Rowsell, J. Gaubicher and L.F. Nazar, *A new class of materials for lithium-iron battaries: iron* (III) *borates*, J. Power Sources **97-98** (2001) 254-257

18. Shigeto Okada, Toshiyuki Tonuma, Yasushi Uebo and Jun-ichi Yamaki, *Anode properties of calcite-type* MBO_3 (*M*: V, Fe), J. Power Sources **119-121** (2003) 621-625
19. A. Ibarra-Palos, C. Darie, O. Proux, J.L. Hazemann, L. Aldon, J.C. Jumas, M. Morcrette and P. Strobel, *Electrochemical reactions of iron borates with lithium: Electrochemical and in situ Mössbauer and X-ray absorption studies*, Chem. Mater. **14** (2002) 1166-1173
20. V. Potapkin, A.I. Chumakov, G.V. Smirnov, J.-Ph. Celse, R. Rüffer, C. McCammon and L. Dubrovinsky, *The* ^{57}Fe *synchrotron Mössbauer source at the ESRF*, J. Synchrotron Radiation **19** (2012) 559-569
21. V. Potapkin, A.I. Chumakov, G.V. Smirnov, R. Rüffer, C. McCammon and L. Dubrovinsky, *Angular, spectral, and temporal properties of nuclear radiation from a* ^{57}Fe *synchrotron Mössbauer source*, Phys. Rev. A **86** (2012) 053808, 1-5
22. R. Diehl, W. Jantz, B.I. Nolang and W. Wettling, *Growth and properties of iron borate,* $FeBO_3$, in*: Current Topics in Materials Science*, E. Kaldis ed., Elsevier, New-York, v. **11** (1984) pp. 241-387
23. А.К. Панкратов, М.Б. Стругацкий и С.В. Ягупов, *Газотранспортный синтез и морфология изометричных монокристаллов бората железа*, Уч. записки Таврического национального университета им. В. И. Вернадского, Сер. Физ. **20(59)** (2007) 64-73
24. М.Б. Стругацкий и С.В. Ягупов, *Растворр-расплавный синтез монокристаллов бората железа*, Уч. записки Таврического национального университета им. В. И. Вернадского, Сер. Физ. **19(58)** (2006) 76-78
25. L. Devroye, *Non-Uniform Random Variate Generation*, Springer, New York, Berlin, Heidelberg, Tokyo (1986) 843 pp.

1. Crystal and magnetic structure of iron borate

1.1 Crystal structure

Synthesis of $FeBO_3$ single crystals and determination of their crystal structure were first reported by Bernal *et al.* [1.1]. Iron borate has rhombohedral calcite-type structure with point group symmetry D_{3d} and the space group D_{3d}^6 in Schönflies notation. The stereographic projection of its structure is shown in Figure 1.1. Two-fold axes, perpendicular to three-fold axis C_3, and planes of symmetry are denoted as C_2 and m, respectively. Structural parameters have been later refined by Diehl *et al.* [1.2, 1.3]. This space group has the R-type Bravais lattice; thus, lattice parameters can be specified in both hexagonal and rhombohedral settings, see Table 1.1. The relations between hexagonal and rhombohedral lattice parameters are:

$$\begin{aligned} a_h &= 2a_r \sin\tfrac{1}{2}\alpha_r \\ c_h &= \sqrt{3}a_r \left(1+2\cos\alpha_r\right)^{1/2}. \end{aligned} \tag{1.1}$$

The rhombohedral, see Figure 1.2, and hexagonal unit cells of $FeBO_3$ contain two and six formula units, respectively.

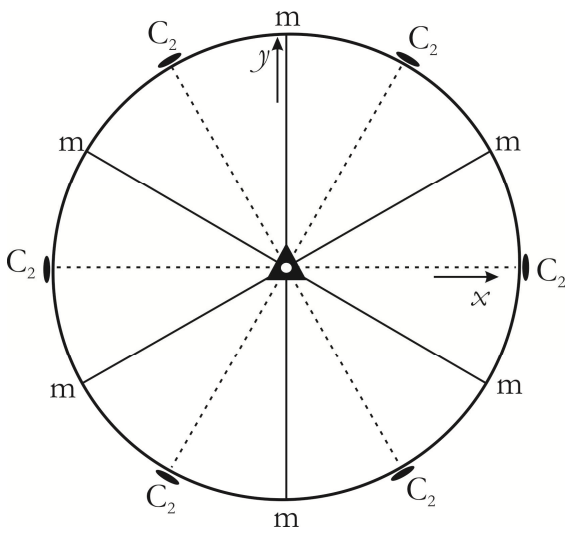

Figure 1.1 Stereographic projection of iron borate structure. The Cartesian coordinate axes are directed as follows: $x \parallel C_2$, $y \parallel m$ and $z \parallel C_3$. The z-axis is perpendicular to the plane of the figure and points towards the reader.

Table 1.1 Lattice parameters of $FeBO_3$ [1.3].

Hexagonal set	Rhombohedral set
$a_h = 4.626(1)$ Å	$a_r = 5.52$ Å
$c_h = 14.493(6)$ Å	$\alpha_r = 49.54^\circ$
$V_h = 268.596$ Å^{3} *	$V_r = 89.532$ Å^{3} *

* V_h and V_r are unit cell volumes.

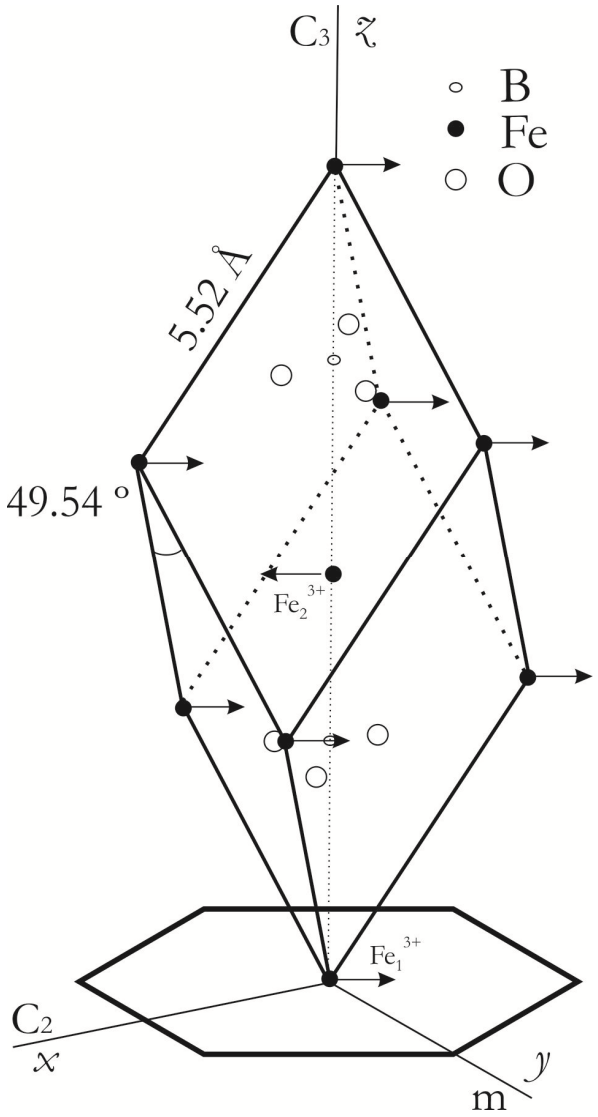

Figure 1.2 Rhombohedral unit cell of $FeBO_3$. The Cartesian coordinate axes are directed as in Figure 1.1: $x \parallel C_2$, $y \parallel m$ and $z \parallel C_3$.

In order to specify the atomic arrangement in iron borate, the so-called oxygen parameter x_h should be determined. Bernal *et al.* [1.1] and Diehl *et al.* [1.3] quote $x_h = 0.2900$ while Diehl [1.2] gives $x_h = 0.2981$. Atomic coordinations and allocations of different atoms to different sites in the unit cell of $FeBO_3$ have been obtained by X-ray analysis [1.2] taking into account transformations of D_{3d}^6 symmetry group [1.3], see Table 1.2. Interatomic distances and bond angles are given in Table 1.3. Each iron is surrounded by six oxygens forming a nearly perfect octahedron. In turn, borons are located at the centres of equilateral oxygen triangles, so that Fe^{3+} cations can *alternatively* be considered as sixfold-coordinated by flat BO_3^{3-} groups playing the role of anions, see Figure 1.3.

Table 1.2 Fractional coordinates of atoms in the unit cell of $FeBO_3$ [1.3].

Atoms	Hexagonal setting	Rhombohedral setting
Fe	$0,0,0;\ 0,0,\frac{1}{2}$	$0,0,0;\ \frac{1}{2},\frac{1}{2},\frac{1}{2}$
B	$0,0,\frac{1}{4};\ 0,0,\frac{3}{4}$	$\frac{1}{4},\frac{1}{4},\frac{1}{4};\ \frac{3}{4},\frac{3}{4},\frac{3}{4}$
O	$\pm\left(x_h,0,\frac{1}{4};0,x_h,\frac{1}{4};\bar{x}_h,\bar{x}_h,\frac{1}{4}\right)$	$\pm\left(x_r,\frac{1}{2}-x_r,\frac{1}{4};\frac{1}{2}-x_r,\frac{1}{4},x_r;\frac{1}{4},x_r,\frac{1}{2}-x_r\right)^*$

$^*x_r = x_h + \frac{1}{4}$

Table 1.3 Interatomic distances and bond angles in $FeBO_3$ [1.3].

Fe—O	2.028(1) Å
B—O	1.379(2) Å
Fe—Fe	3.601(0) Å
O—Fe—O	91.82(5) and 88.18(5)°

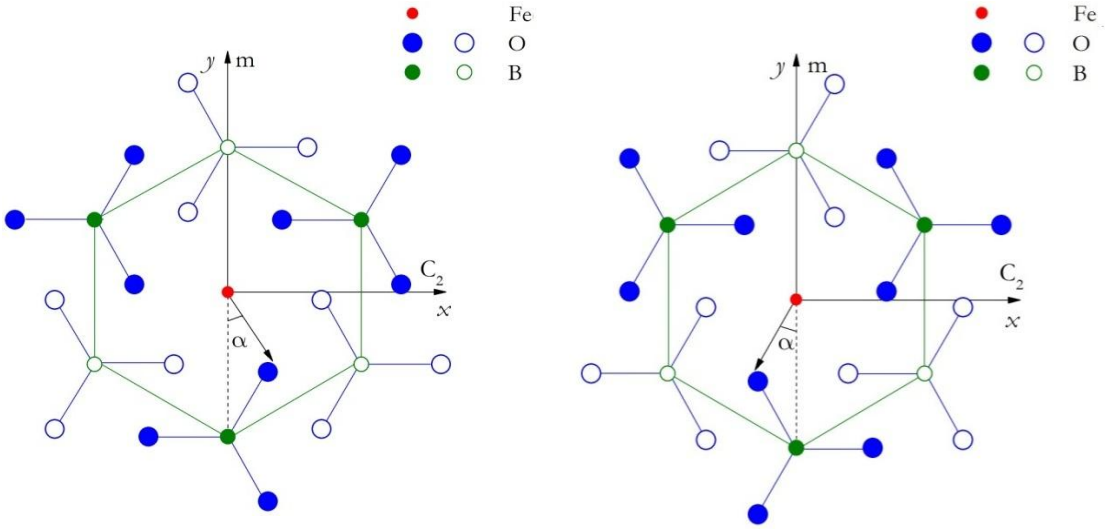

Figure 1.3 Two non-equivalent sites of Fe^{3+}. The Cartesian coordinate axes are directed as in Figure 1.1. The z-axis is perpendicular to the plane of the figure and points towards the reader. Full and empty circles represent ions located above and below this plane, respectively.

1.2 Magnetic structure

Neutron diffraction studies have shown that iron borate is an antiferromagnet with weak ferromagnetism [1.4]. Indeed, $FeBO_3$ crystals possess two magnetic sublattices. The magnetic moments $\boldsymbol{m}_1$ and $\boldsymbol{m}_2$ of Fe_1^{3+} and Fe_2^{3+} ions have equal norms, $m_1 = m_2$. Within the accuracy of measurements [1.4], these vectors lie in the basal plane and are almost antiparallel. However, because of a slight tilt of $\boldsymbol{m}_1$ and $\boldsymbol{m}_2$, apart from a strong antiferromagnetic moment $\boldsymbol{a} = \boldsymbol{m}_1 - \boldsymbol{m}_2$, a weak ferromagnetic moment $\boldsymbol{f} = \boldsymbol{m}_1 + \boldsymbol{m}_2$ occurs, as shown in Figure 1.4. Obviously, $\boldsymbol{f} \perp \boldsymbol{a}$ and $f \ll a$.

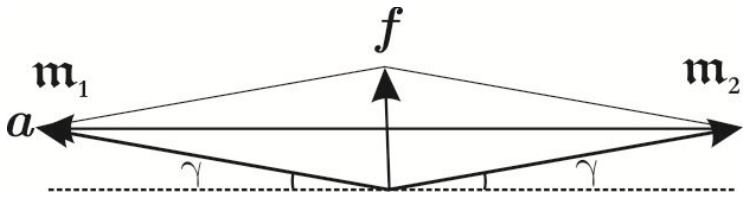

Figure 1.4 Scheme of orientation of magnetic moments of two non-equivalent iron ions, illustrating the emergence of antiferromagnetism and weak ferromagnetism.

Since the neutron diffraction measurements by Pernet *et al.* [1.4] have been carried out on a polycrystalline iron borate, they could not determine the orientation of $\boldsymbol{a}$ in the basal plane.

Various vectors used in describing the magnetic structure of $FeBO_3$ are defined in Table 1.4.

Table 1.4 Definition of various magnetic vectors.

Vector	Definition
Sublattice magnetizations	$\mathscr{M}_{1,2} = \frac{1}{2} N \boldsymbol{m}_{1,2}$ *
Ferromagnetic vector or spontaneous magnetization	$\boldsymbol{M} = \mathscr{M}_1 + \mathscr{M}_2 = \frac{1}{2} N \boldsymbol{f}$
Antiferromagnetic vector	$\boldsymbol{L} = \mathscr{M}_1 - \mathscr{M}_2 = \frac{1}{2} N \boldsymbol{a}$
Reduced ferromagnetic vector	$\boldsymbol{m} = \frac{1}{2} \boldsymbol{M} / \mathscr{M}$ **
Reduced antiferromagnetic vector	$\boldsymbol{l} = \frac{1}{2} \boldsymbol{L} / \mathscr{M}$

* N is the iron concentration

** $\mathscr{M}$ is the norm of the sublattice magnetization. For $FeBO_3$ at 0 K $\mathscr{M}_0 = 520\,\mathrm{G}$ [1.3].

Note that

$$l^2 + m^2 = 1 \tag{1.2}$$

Taking into account the value of the tilt angle, $\gamma \sim 55'$ [1.5], *cf.* Figure 1.4, allows estimating the norms of $\boldsymbol{l}$ and $\boldsymbol{m}$:

$$l \approx 0.999 \quad ; \quad m \approx 0.016. \tag{1.3}$$

The magnetic energy of $FeBO_3$ includes exchange energy $\mathcal{E}_E$ and magnetocrystalline anisotropy energy $\mathcal{E}_A$:

$$\mathcal{E} = \mathcal{E}_E + \mathcal{E}_A . \tag{1.4}$$

As far as for Fe^{3+} ($3d^5$ electron configuration) the orbital moment equals zero, $\mathcal{E}_E$ in a good approximation is isotropic. Thus, $\mathcal{E}_A$ includes only contributions of dipole-dipole and crystal field terms [1.6].

$\mathcal{E}_E$ is related to $\mathscr{M}_1$ and $\mathscr{M}_2$ as follows:

$$\mathcal{E}_E = -\frac{1}{2}\left(E_1 \mathscr{M}_1^{\,2} + E_2 \mathscr{M}_2^{\,2}\right) - E_{12} \mathscr{M}_1 \cdot \mathscr{M}_2 \tag{1.5}$$

where E_1 and E_2 are intra-sublattice exchange constants, and E_{12} is an inter-sublattice exchange constant. Using the definition of $\boldsymbol{l}$ and $\boldsymbol{m}$, see Table 1.4, we can rewrite this equation in the following manner:

$$\mathcal{E}_{\mathrm{E}} = \mathscr{M}^2\left[-E_1\left(l^2+m^2\right)-E_{12}\left(m^2-l^2\right)\right], \tag{1.6}$$

and taking into account eq. (1.2), we get:

$$\mathcal{E}_{\mathrm{E}} = E_0 + \tfrac{1}{2}Em^2 \tag{1.7}$$

where $E_0 = \mathscr{M}^2\left(-E_1+E_{12}\right)$ and $E=-4\mathscr{M}^2E_{12}$.

We expand $\mathcal{E}$ in a series of products of tesseral harmonics of the components of unit vectors $\boldsymbol{\lambda} = \boldsymbol{l}/l$ and $\boldsymbol{\mu} = \boldsymbol{m}/m$:

$$\mathcal{E} = \sum_{i_l}\sum_{j_l}\sum_{i_m}\sum_{j_m} K_{i_l j_l i_m j_m} l^{i_l} m^{i_m} Z_{i_l}^{j_l}(\boldsymbol{\lambda}) Z_{i_m}^{j_m}(\boldsymbol{\mu}). \tag{1.8}$$

Here i_l, i_l, i_m, j_m are integers numbering the harmonics, $i_l \geqslant 0$, $i_m \geqslant 0$, $i_l + i_m = 2p$ $\left(p=0,1,2,\ldots\right)$ is the rank of the corresponding expansion term; $j_{l,m} = -i_{l,m}, -i_{l,m}+1, \cdots, i_{l,m}$, and $K_{i_l j_l i_m j_m}$ are the corresponding constants.

As far as experiments have attested the existence of hexagonal anisotropy in the basal plane of $FeBO_3$ [1.7], the expansion of $\mathcal{E}$ should be extended up to the sixth rank in tesseral harmonics. Obviously, its expression can include only terms invariant under all transformations of the relevant point group. Besides, as in the case of $FeBO_3$ $m \ll l$, *cf.* eq. (1.3), for $p>1$ we can neglect terms with $i_m > 1$.

Taking into account all above considerations, eq. (1.8) reduces to

$$\begin{aligned}
\mathcal{E} &= K_{0000} Z_0^0(\boldsymbol{\lambda}) Z_0^0(\boldsymbol{\mu}) \\
&+ lm\left[K_{1\bar{1}11} Z_1^{-1}(\boldsymbol{\lambda}) Z_1^1(\boldsymbol{\mu}) + K_{111\bar{1}} Z_1^1(\boldsymbol{\lambda}) Z_1^{-1}(\boldsymbol{\mu})\right] \\
&+ K_{2000} l^2 Z_2^0(\boldsymbol{\lambda}) Z_0^0(\boldsymbol{\mu}) + K_{0020} m^2 Z_0^0(\boldsymbol{\lambda}) Z_2^0(\boldsymbol{\mu}) \\
&+ K_{3310} l^3 m Z_3^3(\boldsymbol{\lambda}) Z_1^0(\boldsymbol{\mu}) + K_{4\bar{3}00} l^4 Z_4^{-3}(\boldsymbol{\lambda}) Z_0^0(\boldsymbol{\mu}) \\
&+ K_{5310} l^5 m Z_5^3(\boldsymbol{\lambda}) Z_1^0(\boldsymbol{\mu}) + K_{6600} l^6 Z_6^6(\boldsymbol{\lambda}) Z_0^0(\boldsymbol{\mu}).
\end{aligned} \tag{1.9}$$

Note that in order to possess the required symmetry, the relation $K_{1\bar{1}11} = -K_{111\bar{1}}$ should hold. Explicit expressions of the tesseral harmonics featuring in this expression are [1.8]:

$$\begin{gathered}
Z_0^0 = \tfrac{1}{2\sqrt{\pi}} \quad ; \quad Z_1^{-1} = \tfrac{1}{2}\sqrt{\tfrac{3}{\pi}}\kappa_y \quad ; \quad Z_1^0 = \tfrac{1}{2}\sqrt{\tfrac{3}{\pi}}\kappa_z \quad ; \quad Z_1^1 = \tfrac{1}{2}\sqrt{\tfrac{3}{\pi}}\kappa_x \\
Z_2^0 = \tfrac{1}{4}\sqrt{\tfrac{5}{\pi}}\left(3\kappa_z^{\,2}-1\right) \quad ; \quad Z_3^3 = \sqrt{\tfrac{35}{32\pi}}\left(\kappa_x^{\,3}-3\kappa_x\kappa_y^{\,2}\right) \\
Z_4^{-3} = \tfrac{3}{8}\sqrt{\tfrac{70}{\pi}}\left(3\kappa_x^{\,2}\kappa_y-\kappa_y^{\,3}\right)\kappa_z \quad ; \quad Z_5^3 = \tfrac{1}{16}\sqrt{\tfrac{385}{2\pi}}\left(\kappa_x^{\,3}-3\kappa_x\kappa_y^{\,2}\right)\left(9\kappa_z^{\,2}-1\right) \\
Z_6^6 = \tfrac{1}{64}\sqrt{\tfrac{6006}{\pi}}\left(\kappa_x^{\,4}-14\kappa_x^{\,2}\kappa_y^{\,2}+\kappa_y^{\,4}\right)\left(\kappa_x^{\,2}-\kappa_y^{\,2}\right)
\end{gathered} \tag{1.10}$$

where $\kappa = \lambda, \mu$. Substituting these expressions in eq. (1.9), we get:

$$\begin{aligned}\mathcal{E} &= \tfrac{1}{4\pi}K_{0000} + \tfrac{3}{4\pi}K_{111\bar{1}}lm\left(\lambda_x\mu_y - \lambda_y\mu_x\right)\\ &+ \tfrac{\sqrt{5}}{8\pi}\left[K_{2000}l^2\left(3\lambda_z^{\,2}-1\right) + K_{0020}m^2\left(3\mu_z^{\,2}-1\right)\right]\\ &+ \tfrac{\sqrt{210}}{16\pi}K_{3310}l^3m\left(\lambda_x^{\,3} - 3\lambda_x\lambda_y^{\,2}\right)\mu_z + \tfrac{3\sqrt{70}}{16\pi}K_{4\bar{3}00}l^4\left(3\lambda_x^{\,2}\lambda_y - \lambda_y^{\,3}\right)\lambda_z\\ &+ \tfrac{\sqrt{2310}}{64\pi}K_{5310}l^5m\left(\lambda_x^{\,3} - 3\lambda_x\lambda_y^{\,2}\right)\left(9\lambda_z^{\,2}-1\right)\mu_z\\ &+ \tfrac{\sqrt{6006}}{128\pi}K_{6600}l^6\left(\lambda_x^{\,4} - 14\lambda_x^{\,2}\lambda_y^{\,2} + \lambda_y^{\,4}\right)\left(\lambda_x^{\,2} - \lambda_y^{\,2}\right).\end{aligned} \tag{1.11}$$

This expression can also be written in terms of components of $\boldsymbol{l}$ and $\boldsymbol{m}$:

$$\begin{aligned}\mathcal{E} &= \tfrac{1}{4\pi}K_{0000} + \tfrac{3}{4\pi}K_{111\bar{1}}\left(l_x m_y - l_y m_x\right) + \tfrac{\sqrt{5}}{8\pi}\left[K_{2000}\left(3l_z^{\,2}-l^2\right) + K_{0020}\left(3m_z^{\,2}-m^2\right)\right]\\ &+ \tfrac{\sqrt{210}}{16\pi}K_{3310}\left(l_x^{\,2} - 3l_y^{\,2}\right)l_x m_z + \tfrac{3\sqrt{70}}{16\pi}K_{4\bar{3}00}\left(3l_x^{\,2} - l_y^{\,2}\right)l_y l_z\\ &+ \tfrac{\sqrt{2310}}{64\pi}K_{5310}\left(l_x^{\,2} - 3l_y^{\,2}\right)\left(9l_z^{\,2}-l^2\right)l_x m_z\\ &+ \tfrac{\sqrt{6006}}{128\pi}K_{6600}\left(l_x^{\,4} - 14l_x^{\,2}l_y^{\,2} + l_y^{\,4}\right)\left(l_x^{\,2} - l_y^{\,2}\right).\end{aligned} \tag{1.12}$$

Simplifying the notation of the constants, up to a constant term we get:

$$\begin{aligned}\mathcal{E} &= \tfrac{1}{2}Em^2 + D\left(l_x m_y - l_y m_x\right) + \tfrac{1}{6}a\left(3l_z^{\,2}-l^2\right) + \tfrac{1}{6}b\left(3m_z^{\,2}-m^2\right)\\ &+ c\left(l_x^{\,2} - 3l_y^{\,2}\right)l_x m_z + d\left(3l_x^{\,2} - l_y^{\,2}\right)l_y l_z\\ &+ f\left(l_x^{\,2} - 3l_y^{\,2}\right)\left(9l_z^{\,2}-1\right)l_x m_z + e\left(l_x^{\,4} - 14l_x^{\,2}l_y^{\,2} + l_y^{\,4}\right)\left(l_x^{\,2} - l_y^{\,2}\right).\end{aligned} \tag{1.13}$$

Here the first term on the right-hand side describes isotropic exchange, *cf.* eq. (1.7); the second term accounts for antisymmetric exchange – the Dzyaloshinskii-Moriya interaction, responsible for weak ferromagnetism; the third and fourth terms represent uniaxial magnetocrystalline anisotropy; the remaining terms describe higher-order magnetocrystalline anisotropy. Relations between the constants featuring in eqs. (1.12) and (1.13) are straightforward.

Data available for certain constants in $FeBO_3$ are summarized in Table 1.5.

Table 1.5 Values of some constants for $FeBO_3$ at 0 K, taken or calculated from the corresponding references.

Constant	**Value**, Jm^{-3}
E	$6.26\cdot10^8$ [1.9, 1.10]
D	$1.05\cdot10^7$ [1.11]
a	$3.29\cdot10^5$ [1.11, 1.12]

The parameters d and e have not been experimentally determined. In Chapter 6, "Magnetocrystalline anisotropy of iron borate and iron-gallium borates", we provide a theoretical analysis of these quantities, resulting in the following order-of-magnitude estimates $d \sim 10^3 - 10^4$ and $e \sim 10^0 - 10^1$ Jm^{-3}. We can reasonably assume that constants describing the same-order magnetocrystalline anisotropy are of the same order, $b \sim a, c \sim d, f \sim e$. It should be noted that Curély *et al.* have shown that negative sign of D would produce a helical-type magnetic structure [1.13-1.15].

In equilibrium $\mathcal{E}$ is at a minimum. Minimizing $\mathcal{E}$ with respect to the components of $\boldsymbol{m}$ at fixed $\boldsymbol{l}$, we get the equilibrium orientation of $\boldsymbol{m}$ with respect to $\boldsymbol{l}$:

$$\boldsymbol{m} = \left(\frac{D}{E - \frac{1}{3}b} l_y, \quad -\frac{D}{E - \frac{1}{3}b} l_x, \quad -\frac{c + f\left(9 l_z^{\,2} - 1\right)}{E + \frac{2}{3}b} \left(l_x^{\,2} - 3 l_y^{\,2} \right) l_x \right). \tag{1.14}$$

Obviously, m_z is negligible in comparison with m_x and m_y, so that we can put $m_z = 0$. Substituting the components of $\boldsymbol{m}$ in eq. (1.13), after simple transformations we get:

$$\begin{aligned} \mathcal{E} = {} & \tfrac{1}{2} \frac{D^2}{E - \frac{1}{3}b} \left(l_z^{\,2} - l^2 \right) + \tfrac{1}{6} a \left(3 l_z^{\,2} - l^2 \right) \\ & + d \left(3 l_x^{\,2} - l_y^{\,2} \right) l_y l_z + e \left(l_x^{\,4} - 14 l_x^{\,2} l_y^{\,2} + l_y^{\,4} \right) \left(l_x^{\,2} - l_y^{\,2} \right) \end{aligned} \tag{1.15}$$

The first and second terms on the right-hand side of this equation can be written as a sum of an isotropic term, $\mathcal{E}_{\text{iso}} = -\frac{1}{3} \frac{D^2}{E - \frac{1}{3}b} l^2$ and a uniaxial anisotropy term. Then eq. (1.15) becomes:

$$\mathcal{E} = \mathcal{E}_{\text{iso}} + \tfrac{1}{6} a_{\text{eff}} \left(3 l_z^{\,2} - l^2 \right) + d \left(3 l_x^{\,2} - l_y^{\,2} \right) l_y l_z + e \left(l_x^{\,4} - 14 l_x^{\,2} l_y^{\,2} + l_y^{\,4} \right) \left(l_x^{\,2} - l_y^{\,2} \right). \tag{1.16}$$

where we have introduced an effective constant of uniaxial anisotropy:

$$a_{\text{eff}} = \frac{D^2}{E - \frac{1}{3}b} + a\,. \tag{1.17}$$

Expressing

$$\boldsymbol{l} = l \left(\sin\vartheta \cos\varphi, \quad \sin\vartheta \sin\varphi, \quad \cos\vartheta \right), \tag{1.18}$$

eq. (1.16) becomes:

$$\mathcal{E} = \mathcal{E}_{\text{iso}} + \tfrac{1}{6} a_{\text{eff}} l^2 \left(3\cos^2\vartheta - 1 \right) + d l^4 \sin^3\vartheta \cos\vartheta \sin 3\varphi + e l^6 \sin^6\vartheta \cos 6\varphi. \tag{1.19}$$

We are interested in the orientation of $\boldsymbol{l}$ in a stable equilibrium, *i.e.* in a minimum of $\mathcal{E}(\vartheta, \varphi)$ function. The relevant condition of occurrence of critical points of this function is vanishing of the gradient $\nabla\mathcal{E}$. The components of the latter are as follows:

$$\frac{\partial \mathcal{E}}{\partial \vartheta} = \left[-a_{\text{eff}} \cos\vartheta + d l^2 \left(4\cos^2\vartheta - 1 \right) \sin\vartheta \sin 3\varphi + 6 e l^4 \sin^4\vartheta \cos\vartheta \cos 6\varphi \right] l^2 \sin\vartheta \tag{1.20}$$

and

$$\frac{1}{\sin\vartheta}\frac{\partial \mathcal{E}}{\partial \varphi} = 3\left(d\cos\vartheta - 4el^2\sin^3\vartheta\sin 3\varphi\right)l^4\sin^2\vartheta\cos 3\varphi\,. \tag{1.21}$$

The nature of a critical point, in accordance with the "second partial derivative test" [1.16], depends on the signs in this point of $\partial^2\mathcal{E}/\partial\vartheta^2$ and $\det(\boldsymbol{H})$, the determinant of the Hessian matrix

$$\boldsymbol{H} = \begin{pmatrix} \dfrac{\partial^2\mathcal{E}}{\partial\vartheta^2} & \dfrac{\partial}{\partial\vartheta}\dfrac{1}{\sin\vartheta}\dfrac{\partial\mathcal{E}}{\partial\varphi} \\ \dfrac{\partial}{\partial\vartheta}\dfrac{1}{\sin\vartheta}\dfrac{\partial\mathcal{E}}{\partial\varphi} & \dfrac{1}{\sin^2\vartheta}\dfrac{\partial^2\mathcal{E}}{\partial\varphi^2} + \operatorname{ctg}\vartheta\dfrac{\partial\mathcal{E}}{\partial\vartheta} \end{pmatrix}. \tag{1.22}$$

Namely, a critical point is a minimum or a maximum point of $\mathcal{E}$, if in this point $\det(\boldsymbol{H}) > 0$ and $\partial^2\mathcal{E}/\partial\vartheta^2 > 0$ or $\partial^2\mathcal{E}/\partial\vartheta^2 < 0$, respectively.

With eq. (1.19) only three different cases can occur where $\nabla\mathcal{E}(\vartheta,\varphi) = \mathbf{0}$:

(i) $\vartheta = 0$: in this point, $\boldsymbol{l}$ would be parallel to C_3, and $\boldsymbol{m}$ vanishes, *cf.* eqs. (1.18) and (1.14), *i.e.*, we would deal with an easy-axis antiferromagnet. However, iron borate is an easy-plane antiferromagnet [1.3]; therefore, this case does not occur. Note that in this point, $\det(\boldsymbol{H}) = a_{\text{eff}}{}^2 l^4$ while $\partial^2\mathcal{E}/\partial\vartheta^2 = -a_{\text{eff}}l^2$. Obviously, $\mathcal{E}$ would be at a minimum at this point, if a_{eff} were negative, which is not the case in iron borate, *cf.* Table 1.5.

(ii) $\vartheta = \frac{1}{2}\pi$: $\boldsymbol{l}$ is contained in the basal plane, so that eqs. (1.20) and (1.21) reduce to

$$\frac{\partial\mathcal{E}}{\partial\vartheta} = -dl^4\sin 3\varphi \quad ; \quad \frac{1}{\sin\vartheta}\frac{\partial\mathcal{E}}{\partial\varphi} = -6el^6\sin 6\varphi\,. \tag{1.23}$$

Obviously, $\nabla\mathcal{E}\left(\vartheta = \frac{\pi}{2}\right)$ vanishes for $\sin 3\varphi = 0$, *i.e.* $\varphi = \frac{1}{3}\pi n$, $n = 0, 1, \cdots, 5$. At these points,

$$\det(\boldsymbol{H}) = -9\left(4a_{\text{eff}}e + d^2\right)l^8 \quad ; \quad \partial^2\mathcal{E}/\partial\vartheta^2 = \left(a_{\text{eff}} - 6el^4\right)l^2\,. \tag{1.24}$$

In the latter equations as well as in the subsequent ones we have neglected higher than the first power in e terms, as far as such terms are small, *cf.* Table 1.5. $\mathcal{E}$ will be at a minimum at this point if $4a_{\text{eff}}e + d^2 < 0$. Obviously, this is possible only if $e < 0$. In this case $\boldsymbol{l}$ would be parallel to one of the C_2 axes and $\boldsymbol{m}$ would lie in the symmetry plane perpendicular to this axis, making a negligibly small angle $\approx \frac{e}{D} \sim 10^{-4} - 10^{-3}$ with the basal plane, *cf.* eqs. (1.18) and (1.14) and Figure 1.1.

(iii) The last possible case is that of $\cos 3\varphi = 0$, *i.e.* $\varphi = \frac{1}{6}(2n+1)\pi$, $n = 0, 1, \cdots, 5$.

In this case, the φ-component of $\nabla\mathcal{E}$ vanishes identically, *cf.* eq. (1.21), and ϑ should be chosen such that $\partial\mathcal{E}/\partial\vartheta$ vanishes as well. Since in iron borate, within the experimental

errors, $\boldsymbol{l}$ lies in the basal plane [1.3], we assume $\vartheta = \frac{1}{2}\pi + \delta$ where $\delta \ll \frac{1}{2}\pi$, and expanding $\partial\mathcal{E}/\partial\vartheta$ in Taylor series about $\vartheta = \frac{1}{2}\pi$ to the second order in δ, we get the following critical points:

$$\begin{aligned} \vartheta_+ &= \tfrac{1}{2}\pi + \begin{cases} \delta_1 \\ \delta_2 \end{cases} \quad ; \quad \varphi_+ = \tfrac{1}{6}\pi, \tfrac{5}{6}\pi, \tfrac{3}{2}\pi \\ \vartheta_- &= \tfrac{1}{2}\pi - \begin{cases} \delta_1 \\ \delta_2 \end{cases} \quad ; \quad \varphi_- = \tfrac{1}{2}\pi, \tfrac{7}{6}\pi, \tfrac{11}{6}\pi \end{aligned} \tag{1.25}$$

where

$$\begin{aligned} \delta_1 &= \frac{dl^2}{a_{\text{eff}}} \\ \delta_2 &= -\frac{a_{\text{eff}}}{5dl^2} - \frac{6el^2}{5d} - \frac{dl^2}{a_{\text{eff}}} \end{aligned} \tag{1.26}$$

In the latter equations as well as in the subsequent ones, we have neglected terms higher than the second power in d and higher than the first power in e as well as terms in the product de. Note that for the parameter values quoted in Table 1.5, δ_2 is well outside the domain of definition of ϑ, therefore only the nature of the critical points $\left(\vartheta_+ = \frac{1}{2}\pi + \delta_1 \quad ; \quad \varphi_+\right)$ and $\left(\vartheta_- = \frac{1}{2}\pi - \delta_1 \quad ; \quad \varphi_-\right)$ should be determined. For both of them we get:

$$\det(\boldsymbol{H}) = 9\left(4a_{\text{eff}}e + d^2\right)l^8; \quad \partial^2\mathcal{E}/\partial\vartheta^2 = a_{\text{eff}}l^2 + 2\left(4\frac{d^2}{a_{\text{eff}}} + 3e\right)l^6. \tag{1.27}$$

$\mathcal{E}$ will be at a minimum at this point if $4a_{\text{eff}}e + d^2 > 0$ and $\left(\vartheta_+, \varphi_+\right)$ and $\left(\vartheta_-, \varphi_-\right)$ are minima points of $\mathcal{E}(\vartheta, \varphi)$. In this case $\boldsymbol{l}$ is contained in the plane of symmetry m, making a small angle $\delta = \frac{dl^2}{a_{\text{eff}}}$ with the basal plane; $\boldsymbol{m}$ is parallel to the symmetry axis perpendicular to this plane and lies in the basal plane, *cf.* eqs. (1.18) and (1.14) and Figure 1.1.

We have seen that the magnetic state of iron borate depends on the sign of the quantity

$$e_{\text{eff}} = e + \tfrac{1}{4}\frac{d^2}{a_{\text{eff}}}, \tag{1.28}$$

viz. the cases (ii) and (iii) occur if $e_{\text{eff}} < 0$ and $e_{\text{eff}} > 0$, respectively. We refer to this quantity as the effective constant of hexagonal anisotropy. e_{eff} will be experimentally determined by AFMR, see Chapter 3, "Electron magnetic resonance of iron-gallium borate single crystals with $0.2 \leq x \leq 1$".

1.3 Conclusions

The crystal and magnetic structures of iron borate have been discussed in details. The magnetic energy of $FeBO_3$, $\mathcal{E}$ has been expanded in a series of products of tesseral harmonics of the components of unit vectors in the direction of $\boldsymbol{l}$ and $\boldsymbol{m}$ up to the sixth order and the equilibrium orientations of $\boldsymbol{l}$ and $\boldsymbol{m}$ have been determined for two possible magnetic states. In the first case, $\boldsymbol{l}$ is directed along one of C_2 and $\boldsymbol{m}$ lies in the symmetry plane perpendicular to this axis, making a negligibly small angle with the basal plane. In the second case, $\boldsymbol{l}$ lies in one of the symmetry planes making a small angle with the basal plane, and $\boldsymbol{m}$ is directed along the symmetry axis perpendicular to $\boldsymbol{l}$ and lies in the basal plane.

1.4 References

1.1 L. Bernal, C.W. Struck and T.G. White, *New transition metal borates with the calcite structure*, Acta Cryst. **16** (1963) 849-850

1.2 R. Diehl, *Crystal structure refinement of ferric borate* $FeBO_3$, Sol. St. Commun. **17** (1975) 743-745

1.3 R. Diehl, W. Jantz, B.I. Nolang and W. Wettling, *Growth and properties of iron borate,* $FeBO_3$, *in: Current Topics in Materials Science,* E. Kaldis ed., Elsevier, New-York, V. **11** (1984) 241-387

1.4 M. Pernet, D. Elmalch and T.G. Toubert, *Structure magnétique du métaborate de fer* $FeBO_3$, Sol. Stat. Com. **8** (1970) 1583-1587

1.5 М.П. Петров, Г.А. Смоленский, А.Г. Паугурт, С.А. Кижаев и М.К. Чижов, *Ядерный магнитный резонанс и слабый ферромагнетизм в* $FeBO_3$, Физика твердого тела **14** (1972) 109-113

1.6 J. Kanamori, *Anisotropy and magnetostriction of ferromagnetic and antiferromagnetic materials,* in: *Magnetism, a treatise on modern theory and material*, G.T. Rado, H. Suhl, ed., Acad. Press, v. **1** (1963) 127-203

1.7 V.D. Doroshev, I.M. Krygin, S.N. Lukin, A.N. Molchanov, A.D. Prokhorov, V.V. Rudenko and V.N. Seleznev, *Basal magnetic anisotropy of a weak ferromagnetic* $FeBO_3$ *crystal,* JETP Lett. **29** (1979) 257-260

1.8 URL: http://www2.cpfs.mpg.de/~rotter/homepage_mcphase/manual/node131.html

1.9 M. Eibshütz and M.E. Lines, *Sublattice magnetization of single crystals by Mössbauer effect,* Phys. Rev. B **7** (1973) 4907-4915

1.10 В.Д. Дорошев, Клочан В.А., Ковтун Н.М. и др., *Экспериментальное и теоретическое изучение температурной зависимости подрешеточной намагниченности слабого ферромагнетика* $FeBO_3$, Препринт Дон. ФТИАН УССР **7**(102), Донецк (1985) 60 с.

1.11 L.V. Velikov, A.S. Prokhorov, E.G. Rudashevskii and V.N. Seleznev, *Antiferromagnetic resonance in* $FeBO_3$, Soviet Physics JETP **39** (1974) 909-915

1.12 В.Н. Селезнев, *Магнитоупорядоченные бораты железа (физическиесвойства, применение, синтез)*, Диссертация, Симферопольский гос. университет (1988) 371 с.

1.13 J. Curély, *Theory of the magnetic properties of an infinite classical spin chain showing axial anisotropic couplings: Crossover phenomena*, Physica B **205** (1995) 31-40

1.14 J. Curély and R. Georges, *Exact solution for an infinite classical spin chain showing axial anisotropic couplings*, Phys. Lett. A **184** (1994) 310-314

1.15 J. Curély and R. Georges, *Theory of the magnetic properties of an infinite classical spin-chain showing axial anisotropic couplings: Low-temperature behaviour*, Phys. Rev. B **49** (1994) 12839-12847

1.16 URL: http://mathworld.wolfram.com/SecondDerivativeTest.html

2. Synthesis of iron-gallium borate single crystals

2.1 Introduction

In this chapter we describe the procedure of synthesizing $Fe_xGa_{1-x}BO_3$ single crystals with a part $(1 - x)$ of Fe^{3+} ions isomorphously substituted by Ga^{3+} ions.

As mentioned above in Introduction, the series of $Fe_xGa_{1-x}BO_3$ single crystals, synthesized in a wide range of compositions, allows detailed studies of transformation of various physical characteristics under the transition from magnetically ordered to paramagnetic state.

Iron borate crystals can be synthesized by two routes: (i) from gas phase and (ii) from solution in the melt [2.1, 2.2]. Using the gas phase technique, *bulk* single crystals of iron borate with large *non-basal* faces of optical quality are obtained. The occurrence of natural non-basal faces has allowed identifying and describing surface magnetism present on such faces and caused by specific surface anisotropy [2.3, 2.4]. Another effect observed only in bulk crystals is magnetic birefringence of sound [2.5].

The solution in the melt technique allows obtaining *thin* single crystals, 0.05 – 0.1 mm along the C_3 axis and up to 10 mm in the basal plane, (0001) in hexagonal coordinate system. Such crystals are of high structural perfection and are much less costly in manufacturing in comparison with those obtained from gas phase. For the purposes of the present work this technique has proved to be most appropriate.

To the best of our knowledge, the first synthesis of $FeBO_3$ single crystals was reported by Bernal *et al.* [2.6]. Later, $FeBO_3$ single crystals were obtained by cooling from 860 to 670 °C a solution melt with molar component ratio suggested by Bernal *et al.* It was concluded that the crystal growth should be carried out in the temperature range 860–670 °C, as a further decrease of temperature leads to decreasing crystal quality [2.7]. Boron-lead solvent B_2O_3-PbO-PbF_2 for synthesizing $FeBO_3$ was first used by Le Craw *et al.* [2.8]. Mixing of the solution melt and crystal synthesis on the seed holder were used by Bezmaternykh *et al.* [2.9].

Using the solution in the melt technique simplifies the crystal synthesis, allows obtaining materials with complex compositions and reduces the crystallization temperature of refractory compounds. Usually, crystallization regimes suitable for obtaining desired crystal phases are determined by trial and error, requiring significant time and financial resources. Hence, express methods of determining the ranges of stability of crystalline phases and temperature ranges of phase formation are desirable. In the present work for this purpose we have used differential thermal analysis (DTA) and probe methods.

After $Fe_xGa_{1-x}BO_3$ synthesis, a detailed characterization is required for further studies and applications of the samples. The exact crystal composition and parameters of the crystal lattice have been determined by XRF and XRD, respectively. Besides, EPR has been used to estimate local disorder in the $Fe_xGa_{1-x}BO_3$ crystals at low x values.

2.2 Crystal synthesis

The synthesis of $Fe_xGa_{1-x}BO_3$ crystals by solution in the melt technique is schematically represented in Figure 2.1.

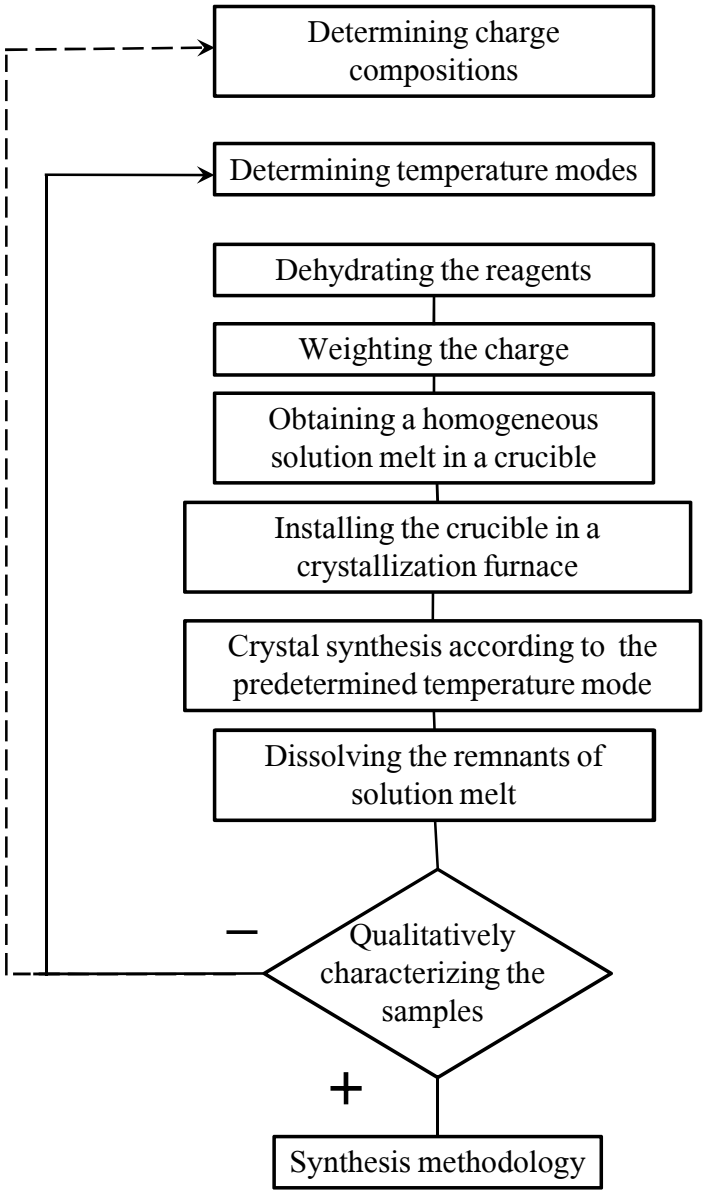

Figure 2.1 General scheme for the synthesis of $Fe_xGa_{1-x}BO_3$ single crystals by solution in the melt technique.

It includes the following steps:

- ✓ determining suitable charge compositions and temperature modes (by DTA and probe methods);
- ✓ dehydrating the reagents;
- ✓ weighting the charge;
- ✓ obtaining a homogeneous solution melt in a crucible;
- ✓ installing the crucible in a crystallization furnace;
- ✓ slow cooling of the solution according to a predetermined temperature mode;
- ✓ extracting the crucible from the furnace;
- ✓ dissolving the remnants of solution melt in 20 % solution of HNO_3 and extracting the crystals from the crucible.

2.2.1 Differential thermal analysis

Differential thermal analysis (DTA) can be applied to a wide range of substances; meanwhile, there have been only few DTA studies of the solution-melt systems. This can be explained by the fact that for diluted solutions, sensitivity of this technique is greatly reduced because of the smallness of the exothermic peak on the thermograms [2.10].

Therefore, we have developed a highly sensitive setting for rapid analysis of small amounts of the solution melts in the temperature range from 300 to 1150ºC. This setting allows detecting weak temperature change ΔT caused by crystal formation and determining temperature ranges of crystallization with sufficient accuracy [2.11, 2.12].

As a differential thermocouple for measuring ΔT, we have used two metallic crucibles of 1.5 cm^3 volume, allowing to detect ΔT values as small as ca. 0.01 °C.

We have carried out DTA studies of different charge compositions for synthesis of mixed iron gallium borate crystals. As an example, the DTA curve for the composition used to synthesize $FeBO_3$ is shown in Figure 2.2. As one can see, in the range of 835–737ºC a flat exothermic peak is observed. A detailed analysis of this temperature range, see Figure 2.3, has revealed the existence of two separate exothermic peaks, above and below ca. 817ºC. The high-temperature, 835–817ºC, and the low-temperature, 817–737ºC, peaks correspond to the emergence of Fe_3BO_6 and $FeBO_3$ phases, respectively.

The obtained DTA thermograms have proved highly efficient for studying phase transitions occurring in the course of crystal synthesis by solution in the melt route. In particular, they have allowed determining temperature ranges of forming $Fe_xGa_{1-x}BO_3$ crystals in the whole contents range, $0 \leqslant x \leqslant 1$.

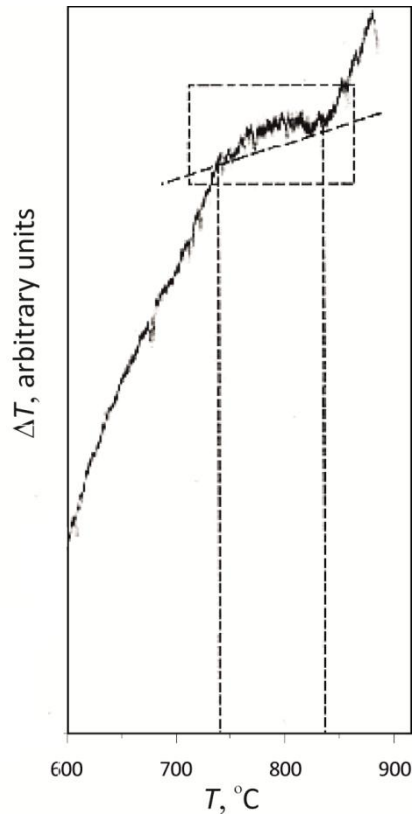

Figure 2.2 DTA curve for the composition used for the synthesis of $FeBO_3$ in wide temperature range.

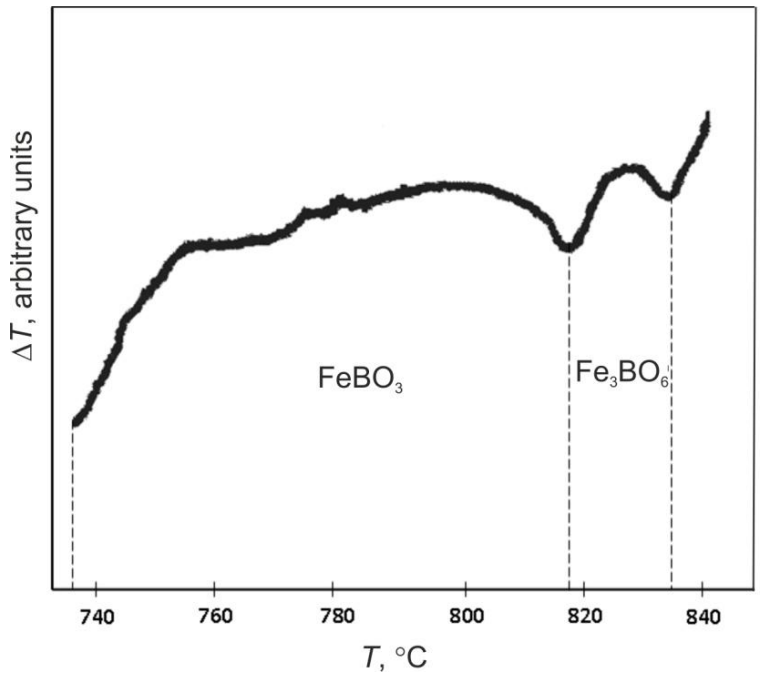

Figure 2.3 DTA curve for the composition used for the synthesis of $FeBO_3$ in the range of formation of $FeBO_3$ and Fe_3BO_6 crystal phases.

2.2.2 Probe method

Certain shortcomings of the DTA, namely, high crystallization rates required and impossibility of *in situ* control of emerging phases, require a complementary analysis technique. With this aim, the probe method has been applied for the same compositions as DTA. As a probe, a platinum wire of 0.5 mm in diameter, fixed on the lifting device, has been used. The probe was immersed into the melt, then the temperature was modified following a distinct regime in accordance with a predetermined program, and finally, the probe was removed. The microcrystals formed on the probe have been studied by scanning electron microscopies, see Figure 2.4. In this way, the emergence of the same crystalline phases in the same temperature ranges as those found with DTA has been confirmed.

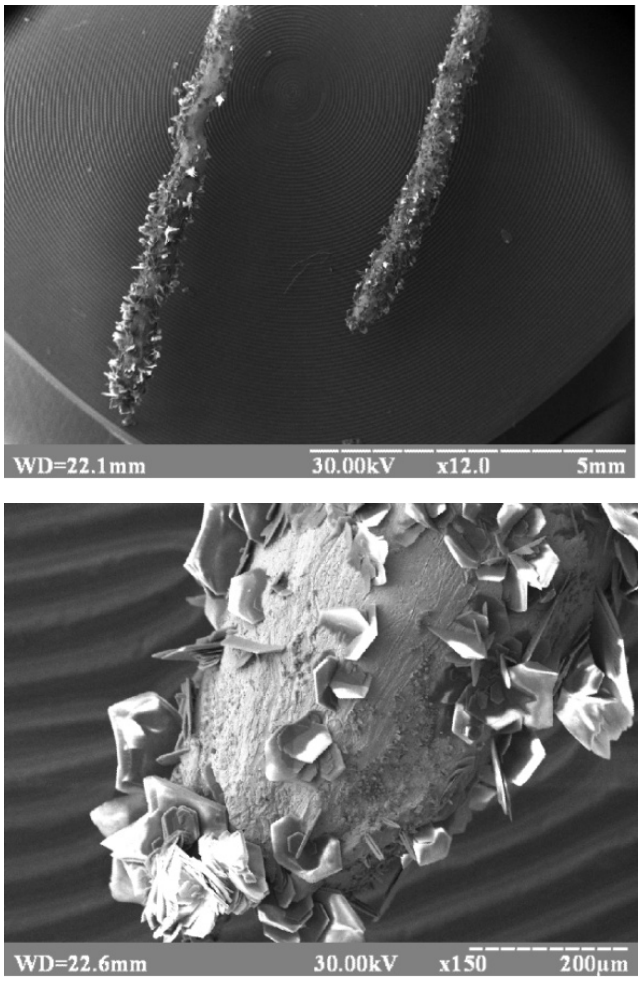

Figure 2.4 Electron microscope pictures showing $FeBO_3$ single crystals on the probes for two different magnifications.

2.2.3 Charge compositions

Crystallizations were carried out in the Ga_2O_3-Fe_2O_3-B_2O_3-PbO-PbF_2 system. Here the crystal-forming reagents are Ga_2O_3, and Fe_2O_3, PbO and PbF_2 serve as solvents and B_2O_3 is both crystal-forming reagent and solvent.

Examples of charge compositions used in the synthesis are shown in Table 2.1.

Table 2.1 Charge compositions used for synthesizing $Fe_xGa_{1-x}BO_3$crystals with different x values.

x	Ga_2O_3	Fe_2O_3	B_2O_3	PbO	PbF_2
	mass %				
0.00	18.60	0.00	42.40	27.30	11.70
0.02	18.52	0.08			
0.20	16.99	1.61			
0.30	14.49	4.11			
1.00	0.00	5.73	51.23	29.31	13.73

2.2.4 Preparing a solution

After determining a charge composition, all reagents have been dehydrated in a drying chamber at 150 °C during 24 hours. Next, the reagents have been weighted with a high-precision balance and mixed with a laboratory-developed device. An example of charge prepared for synthesis is shown in Figure 2.5.

For obtaining a homogeneous solution melt, small portions, about 5 g, of the charge have been successively adjoined to a metallic crucible and each time kept for 20 min in a muffle furnace at 900 °C. As an example, Figure 2.6 shows a crucible with the solution melt extracted from the furnace. As one can see, the solution used for $GaBO_3$ crystal synthesis is almost transparent.

Figure 2.5 Prepared charge used in synthesizing $Fe_xGa_{1-x}BO_3$ crystals of a definite composition.

Figure 2.6 Crucible with the solution melt used for synthesizing $GaBO_3$ crystals after extracting from the muffle furnace.

2.2.5 Crystallization

The crucible with the solution melt has been installed in the crystallization furnace with uniform temperature distribution. The crucible in the furnace before starting the crystallization process is shown in Figure 2.7. The crystallization setting consists of the following elements, see Figure 2.8:

(i) crystallization furnace;
(ii) lowering-rotating-lifting device;
(iii) seed holder;
(iv) temperature controller;
(v) managing thermocouple;
(vi) controlling thermocouple;
(vii) power unit;
(viii) computer.

Figure 2.7 Crucible with a solution melt in the furnace.

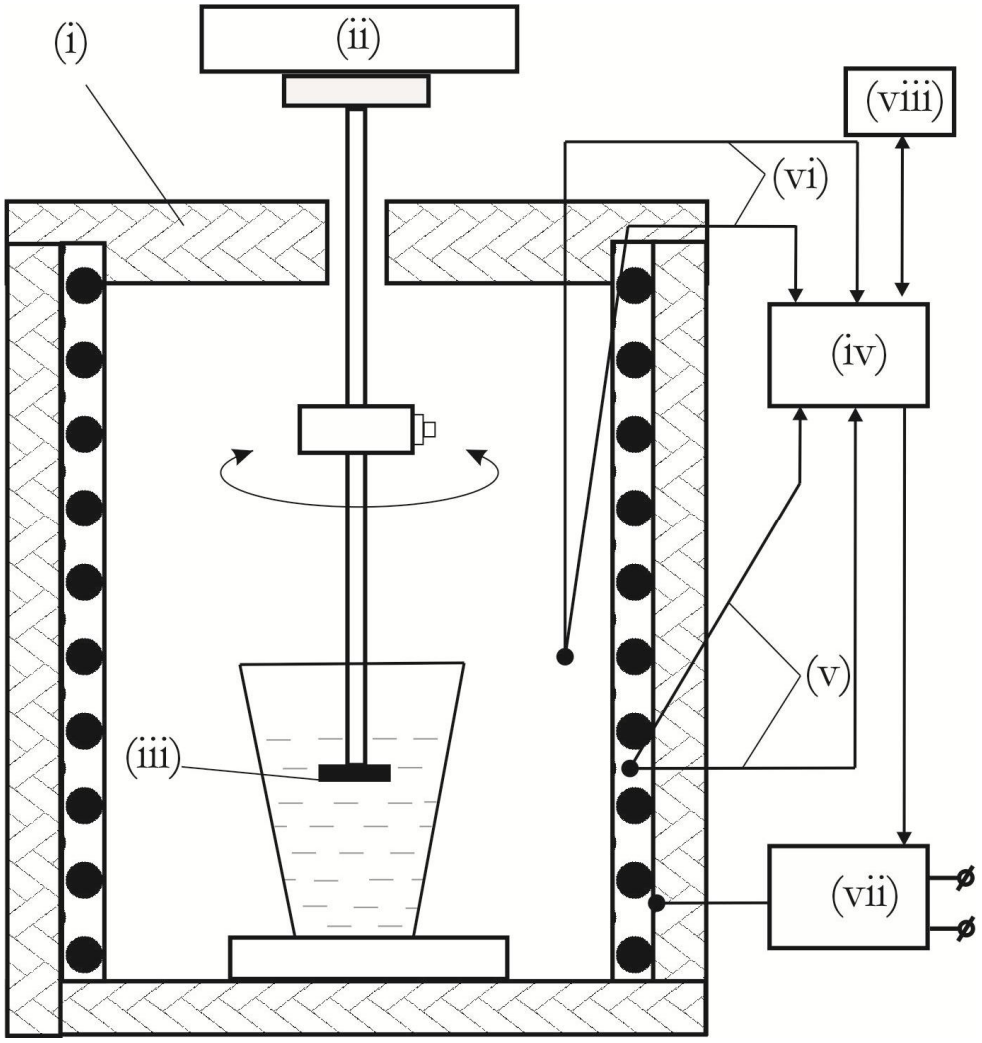

Figure 2.8 Scheme of the crystallization setting.

Figure 2.9 shows a typical temperature regime used in synthesizing crystals of a definite composition. It includes the following steps:

(i) heating of the furnace;

(ii) homogenization of the solution melt (at the beginning of this step, the seed holder is immersed in the solution melt and serves as a mixer);

(iii) sharp temperature dropping;

(iv) nucleation and crystal growth (using the seed holder during this step allows monitoring the emergence of $FeBO_3$ crystal phase; at the end of this step, the seed holder with the synthesized crystals is extracted from the solution melt);

(v) and (vi) cooling the furnace.

After the last step, a crucible has been removed from the furnace and boiled in 20 % solution of HNO_3 in order to dissolve the remnants of the solution melt, so that the crystals can be extracted.

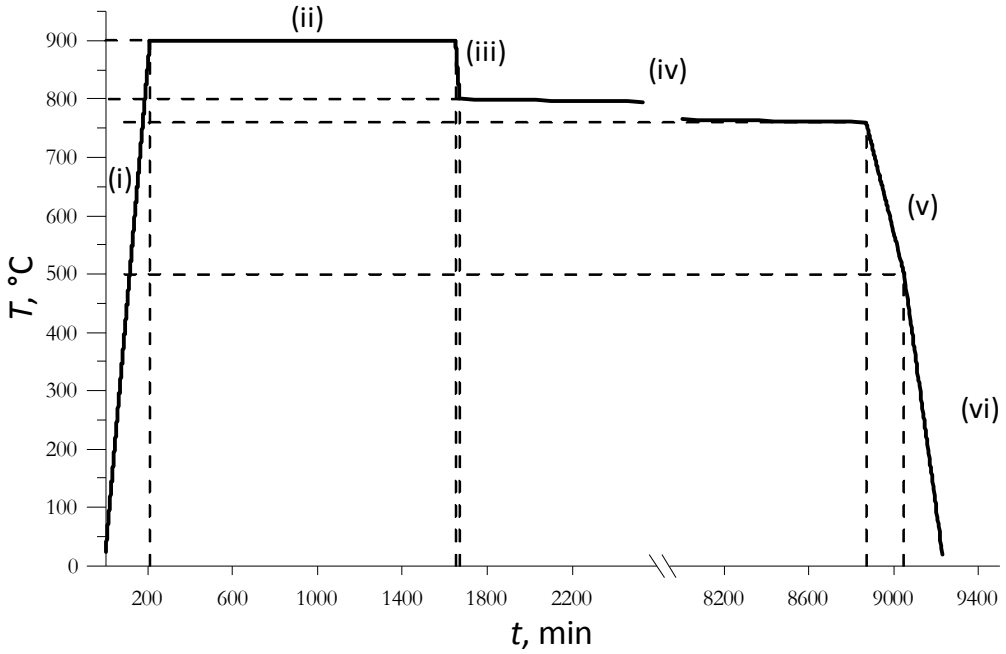

Figure 2.9 Temperature mode of crystallization used in synthesizing $Fe_xGa_{1-x}BO_3$ crystals of a definite composition.

2.2.6 Synthesized crystals

The synthesized $Fe_xGa_{1-x}BO_3$ crystals are shown in Figures 2.10 to 2.12. All crystals have the shape of hexagonal plates with the dimensions of a few millimeters in the basal plane and ca. 0.1 mm in the perpendicular direction. Gallium borate is colourless while iron borate is green. The aspect of $Fe_xGa_{1-x}BO_3$ crystals is gradually modified with the iron contents.

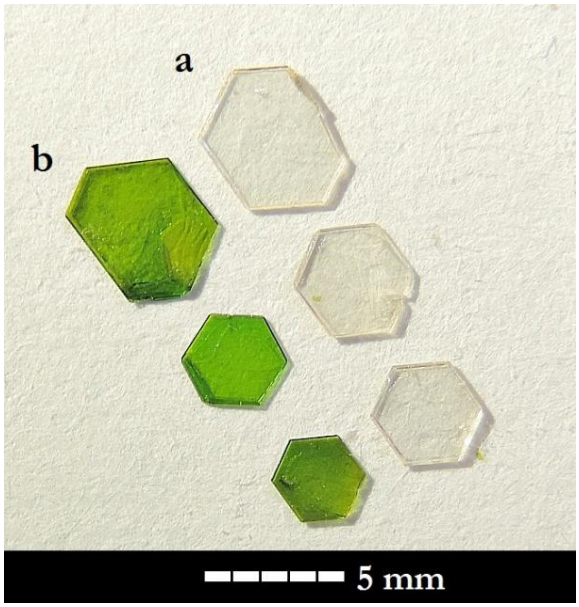

Figure 2.10 $GaBO_3$ (a) and $FeBO_3$ (b) single crystals.

Figure 2.11 $Fe_xGa_{1-x}BO_3$ single crystals with different *x*.

Figure 2.12 $GaBO_3$ crystals on the seed holder.

2.3 Characterization of synthesized crystals

2.3.1 Crystal composition: X-ray fluorescence analysis

In order to determine exact contents of iron in the synthesized crystals, $x_{crystal}$, we have carried out XRF analysis, a simple and accurate analytical method of determining the elemental composition of materials. The X-ray beam interacts with the atoms in the crystal in such a way that electrons are ejected from inner shells, leaving behind holes. Then the electrons from outer shells recombine with the holes, and the energy difference between the two states involved is released in the form of a photon. Since this energy difference is specific to each element, it is used to identify the latter. The concentration of a certain element is proportional to the intensity of the corresponding peak in the energy or wavelength spectrum.

Figure 2.13 shows the results of XRF analysis; as one can see, $x_{crystal}$, substantially differ from those in the charge, x_{charge}; besides, a considerable difference in iron contents occurs for different crystals extracted from the same crucible. For instance, for $x_{charge} = 0.01$, $x_{crystal}$ is in the range from 0.002 to 0.04.

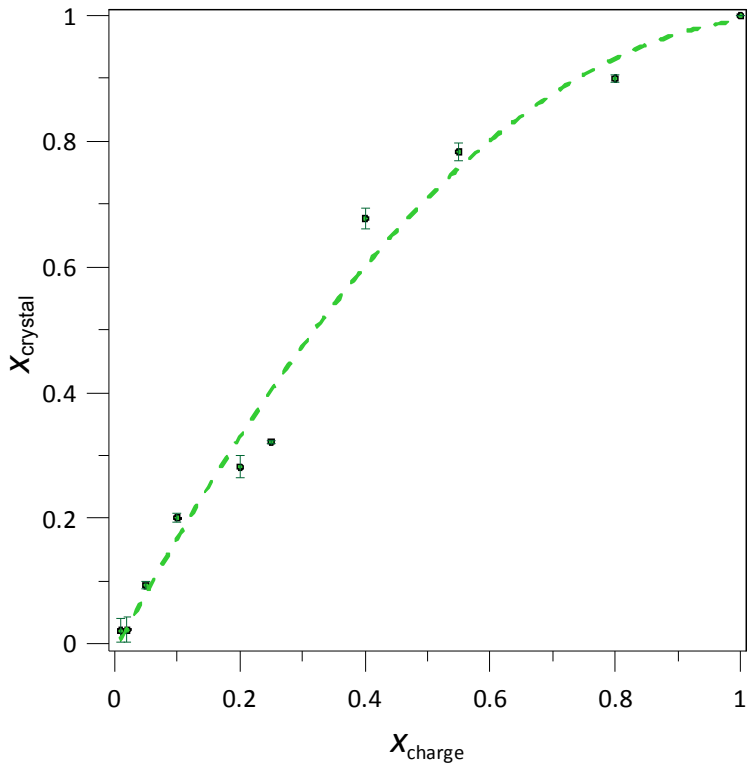

Figure 2.13 Iron contents in $Fe_xGa_{1-x}BO_3$ crystals *vs.* initial iron contents in the charge. The vertical bars show the spread of iron contents for the samples extracted from the same crucible. The dashed line is a guide for the eyes.

2.3.2 Crystal structure: X-ray diffraction studies

The parameters of crystal lattice in the series of $Fe_xGa_{1-x}BO_3$ crystals have been determined by XRD with a RigakuSmartLab diffractometer using copper radiation CuKα in the angle range of $5 < 2\vartheta < 100°$ with the step of 0.02° [2.12] *.

Figure 2.14 shows XRD powder patterns for $FeBO_3$ and $Fe_{0.05}Ga_{0.95}BO_3$ crystals. Diffraction angles for the observed lines in the XRD pattern of $FeBO_3$ and the corresponding planes are listed in Table 2.2 [2.12].

Table 2.2 Diffraction angles of the lines in XRD pattern of $FeBO_3$ and corresponding planes in the hexagonal system [2.13].

2ϑ, deg	(hkl)	2ϑ, deg	(hkl)
25.43	(012)	62.73	(122)
33.38	(104)	67.04	(214)
37.23	(006)	70.12	(208)
38.95	(110)	70.54	(300)
43.39	(113)	70.72	(119)
47.11	(202)	79.31	(0.0.12)
52.21	(024)	82.51	(306)
55.09	(116)	83.12	(128)
55.78	(018)	83.65	(223)
61.58	(211)	89.19	(312)

Isomorphous substitution of iron with gallium produces change of the lattice parameters manifesting itself in a shift of the XRD peaks from their positions in pure iron borate, see Figure 2.14. The hexagonal lattice parameters a and c can be calculated using the following expression [2.14]:

$$\frac{1}{d^2} = \frac{4}{3}\frac{h^2 + hk + k^2}{a^2} + \frac{l^2}{c^2} \qquad (2.1)$$

where d are interplanar spacings calculated using the Bragg's formula $d = \lambda/2\sin\vartheta$, and h, k and l represent the lattice planes.

* These results have been obtained in collaboration with E. Maksimova and I. Nauhatsky of the Physics and Technology Institute, Simferopol.

The lattice parameters in $Fe_xGa_{1-x}BO_3$ crystals have been calculated using the positions of the most "convenient" peaks, *e.g.*, (300) for *a*, and (006) and (0.0.12) for *c*. Next, these parameters have been refined by graphical extrapolation for all diffraction peaks in the angle range of $40 < 2\vartheta < 100°$. The dependences of *a* and *c* on the crystal composition are shown in Figure 2.15.

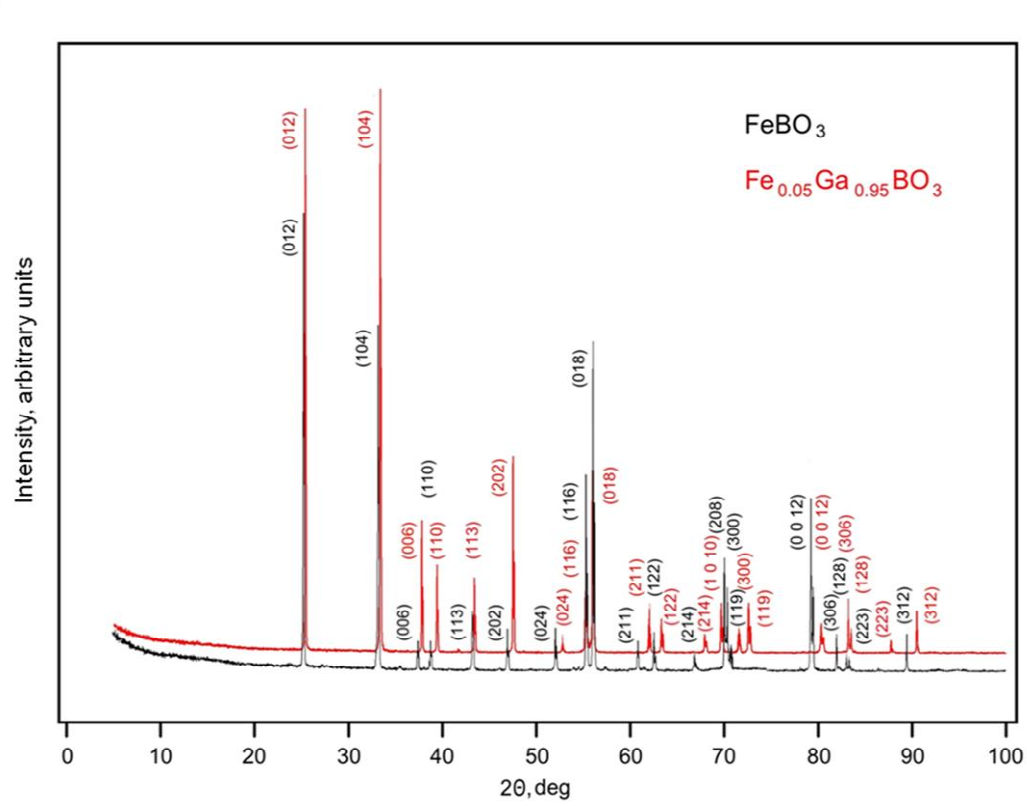

Figure 2.14 XRD patterns of $FeBO_3$ (bottom curve) and $Fe_{0.05}Ga_{0.95}O_3$ (top curve) [2.12].

According to Vegard's law [2.15], suggesting a linear relationship between the lattice parameters of a solid solution and concentrations of its constituent components, the following relation should hold for $Fe_xGa_{1-x}BO_3$ crystals:

$$\begin{aligned} a_{Fe_xGa_{1-x}BO_3} &= x_{crystal} a_{FeBO_3} + (1 - x_{crystal}) a_{GaBO_3}, \\ c_{Fe_xGa_{1-x}BO_3} &= x_{crystal} c_{FeBO_3} + (1 - x_{crystal}) c_{GaBO_3}. \end{aligned} \tag{2.2}$$

The dashed lines on Figure 2.15 are obtained by least square fitting to the experimental data to this relation. One can see that in the limits of errors, this relation quite adequately describes the experimental tendencies.

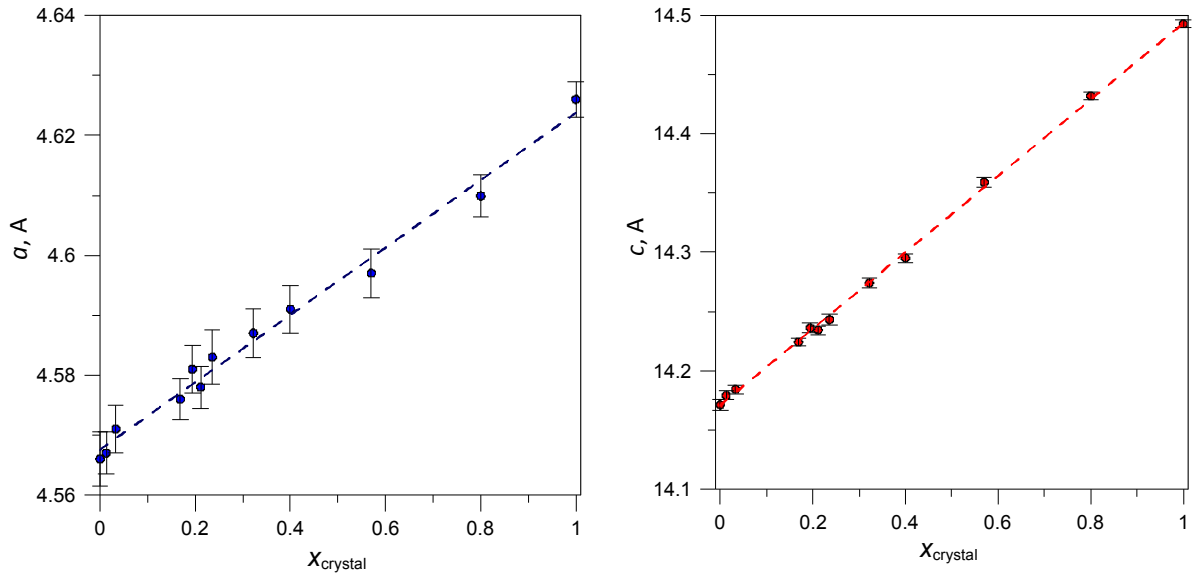

Figure 2.15 Concentration dependences of lattice parameters *a* (left) and *c* (right). Dashed lines : least square fittings [2.12].

2.3.3 Crystal quality: EPR studies

For estimating the quality of the synthesized crystals, we have chosen the EPR characterization, particularly sensitive to imperfections of local structure. At low x values, only the EPR of diluted Fe^{3+} in $GaBO_3$ lattice is observed; therefore, this ion can serve as a high-sensitive probe for evaluating the degree of structural disorder in crystals. A single crystal with $x = 0.003$ has been studied by EPR with an X-band Bruker spectrometer at 4 K and magnetizing fields up to 1 T. A detailed account of this study will be given below, *cf.* Chapter 4, "EPR of iron-gallium borate single crystals with low x".

The experimental EPR spectrum, curve a in Figure 2.16, is typical of isolated Fe^{3+} in oxygen environment. The spin Hamiltonian parameters have been determined by computer simulating the EPR spectra with a laboratory-made code. Besides, no characteristic line splitting has been detected, evidencing the absence of twinning in the crystals.

In order to numerically estimate the degree of local disorder, we have attributed different normal random site-to-site distributions to the Cartesian coordinates of the Fe^{3+} ligands, and calculated the spin Hamiltonian parameter distributions by means of the superposition model, see details in Chapter 4, "EPR of iron-gallium borate single crystals with low x". Figure 2.17 shows computer simulations of a chosen EPR line, for different degrees of local disorder estimated from the width, σ of the ligand coordinate distributions. Obviously, with increased disorder, the width of this line drastically increases and its amplitude decreases, so that the absorption intensity remains roughly the same. The best agreement between this experimental and computer-generated line profile is attained at $\sigma \approx 0.0003 - 0.0005$ Å. Besides, Figure 2.16 shows that with such parameter distributions, a good fitting, curve b, is achieved for the whole experimental spectrum.

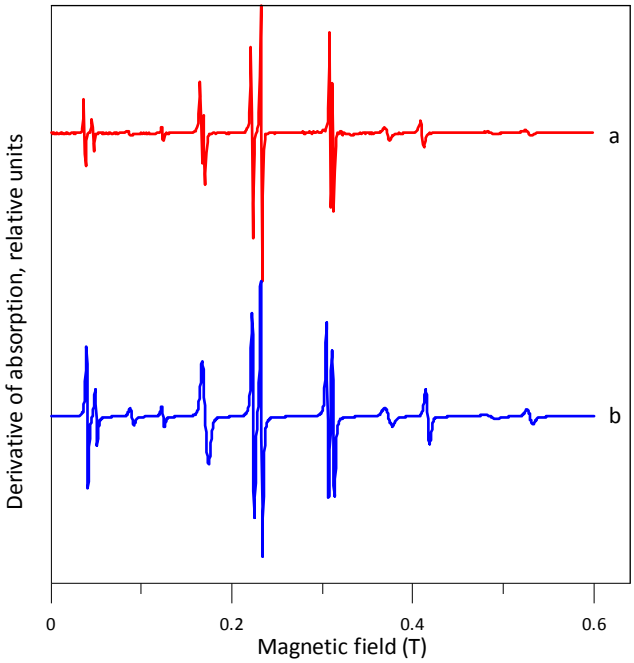

Figure 2.16 Experimental EPR spectrum of Fe^{3+} in $Fe_xGa_{1-x}BO_3$ crystal with $x = 0.003$ at 4 K (a) and corresponding computer-generated spectrum (b).

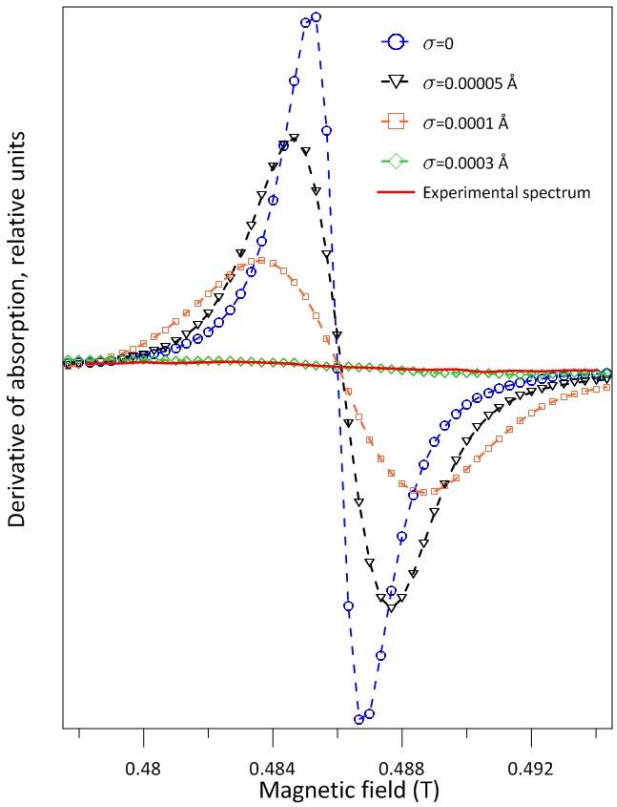

Figure 2.17 Experimental EPR line at ca. 0.486 T and the corresponding part of computer-generated spectrum for different distribution widths of the ligand coordinates.

2.4 Conclusions

We have succeeded in obtaining high-quality $Fe_xGa_{1-x}BO_3$ single crystals in the whole range of concentrations, using the solution in the melt technique for isomorphous substitution in iron-gallium borate system. By means of DTA and the probe method we have determined the component ratios in the charge and the corresponding temperature modes optimal for the crystal synthesis for different *x*.

The XRF analysis has revealed certain difference in Fe^{3+} ion contents in different crystals extracted from the same crucible. The XRD analysis has shown that in mixed iron gallium borates the modification of the crystal lattice parameters closely follows the Vegard's law.

The EPR studies have allowed evaluating the degree of local disorder. Its quantitative characteristic – distribution width of the ligand coordinates, $\sigma \approx 0.0003 - 0.0005$ Å, – confirms the high quality of the synthesised crystals.

2.5 References

2.1 А.К. Панкратов, М.Б. Стругацкий и С.В. Ягупов, *Газотранспортный синтез и морфология изометричных монокристаллов бората железа*, Уч. записки Таврического национального университета им. В. И. Вернадского, Сер. Физ. **20(59)** (2007) 64-73

2.2 М.Б. Стругацкий и С.В. Ягупов, *Раствор-расплавный синтез монокристаллов бората железа*, Уч. записки Таврического национального университета им. В. И. Вернадского, Сер. Физ. **19(58)** (2006) 76-78

2.3 V.E. Zubov, G.S. Krinchik, V.N. Seleznyov and M.B. Strugatsky, *Near-surface magnetic structures in iron borate*, J. Magn. Magn. Mater. **86** (1990) 105-114

2.4 E.M. Maksimova, I.A. Nauhatsky, M.B. Strugatsky and V.E. Zubov, *Surface magnetism of real iron borate monocrystals*, J. Magn. Magn. Mater. **322** (2010) 477-480

2.5 M.B. Strugatsky, K.M. Skibinsky, V.V. Tarakanov and V.I. Khizhnyi, *Fine structure of Gakel'-Turov oscillations in iron borate,* J. Magn. Magn. Mater. **241** (2002) 330-334

2.6 L. Bernal, C.W. Struck and T.G. White, *New transition metal borates with the calcite structure*, Acta Cryst. **16** (1963) 849-850

2.7 И.Г. Аваева, *Выращивание кристаллов метабората железа* $FeBO_3$, Тр. 4 Всесоюзн. совещ. по росту кристаллов, АН Арм. ССР, Ереван (1972) ч. 1, с. 147-148

2.8 R.C. Le Craw, R. Wolfe and J.W. Nielsen, *Ferromagnetic resonance in* $FeBO_3$, *a green room-temperature ferromagnet*, Appl. Phys. Lett. **14** (1969) 352-354

2.9 Л.Н. Безматерных, В.Г. Мащенко, В.А. Чихачев, В.С. Близняков, *Способ получения монокристаллов* $FeBO_3$ *из раствора-расплава*, А.С. 1059029, СССР, Бюл. 45 (1983)

2.10 В.А. Тимофеева, *Рост кристаллов из растворов-расплавов*, Наука, Москва (1978) 268 с.

2.11 С.В. Ягупов, М.Б. Стругацкий, Н.С. Постывей и С.С. Костулин, *Применение дифференциально-термического анализа для исследования раствор-расплавной кристаллизации*, Уч. записки Таврического национального университета им. В. И. Вернадского, Сер. Физ. - мат. **23(62)** (2010) 121-124

2.12 S. Yagupov, M. Strugatsky, K. Seleznyova, E. Maksimova, I. Nauhatsky, V. Yagupov, E. Milyukova and J. Kliava, $Fe_xGa_{1-x}BO_3$ *single crystals: Synthesis and characterization*, Appl. Phys. A **121** (2015) 179-185

2.13 R. Diehl, W. Jantz, B.I. Nolang and W. Wettling, *Growth and properties of iron borate,* $FeBO_3$, in*: Current Topics in Materials Science*, E. Kaldis ed., Elsevier, New-York, v. **11** (1984) pp. 241-387

2.14 H. Lipson and H. Stipl, *Interpretation of the powder x-ray patterns*, Macmillan, London, St. Martins Press, New York (1970) viii+335 pp.

2.15 L. Vegard, *Die Konstitution der Mischkristalle und die Raumffüllung der Atome*, Z. Phys. **5(1)** (1921) 17-26

3. Electron magnetic resonance of iron-gallium borate single crystals with 0.2≤x≤1

3.1 Basic formalism

A classical description of AFMR has first been given by Kittel in 1951 [3.1].

In a two-sublattice antiferromagnet the equilibrium orientation of the sublattice magnetizations $\mathcal{M}_1$ and $\mathcal{M}_2$ minimises the magnetic energy $\mathcal{E}$ of this system, *i.e.*, at equilibrium $\mathcal{M}_1$ and $\mathcal{M}_2$ are parallel to *effective* magnetic fields $\boldsymbol{H}_{\text{eff}\,1}$ and $\boldsymbol{H}_{\text{eff}\,2}$ acting on the first and second sublattices, respectively, and defined as:

$$\boldsymbol{H}_{\text{eff}\,1} = -\nabla_{M_1}\mathcal{E} \text{ and } \boldsymbol{H}_{\text{eff}\,2} = -\nabla_{M_2}\mathcal{E}. \tag{3.1}$$

The equations of precession of $\mathcal{M}_1$ and $\mathcal{M}_2$ about $\boldsymbol{H}_{\text{eff}\,1}$ and $\boldsymbol{H}_{\text{eff}\,2}$ in the absence of damping are [3.1, 3.2]:

$$\begin{aligned} \dot{\mathcal{M}}_1 &= -\gamma \mathcal{M}_1 \wedge \boldsymbol{H}_{\text{eff}\,1} \\ \dot{\mathcal{M}}_2 &= -\gamma \mathcal{M}_2 \wedge \boldsymbol{H}_{\text{eff}\,2} \end{aligned} \tag{3.2}$$

where γ is the gyromagnetic ratio defined as $\gamma = -\frac{1}{2}{}^{ge}\!/_{m}$, e is the electron charge, m is the electron mass and g is the electronic g-factor.

In a magnetic resonance experiment, one applies perpendicularly to $\boldsymbol{H}$ an oscillating magnetic field $\boldsymbol{h}$ (the magnetic component of an electromagnetic wave, typically in the microwave range), of a frequency ν and amplitude $h \ll H$. In most EMR spectrometers, ν is kept constant and H is linearly swept, so that the resonance occurs when ν is equal to the frequency of precession of magnetizations.

Considering weak precessions of $\mathcal{M}_1$ and $\mathcal{M}_2$ about their equilibrium orientations and solving eqs. (3.2), magnetic modes of the antiferromagnetic substance in the vicinity of the ground state can be found.

The subsequent analysis has been made for rhombohedral antiferromagnets with weak ferromagnetism [3.3]; thus, it is applicable to $FeBO_3$ as well as to (isomorphous) mixed crystals of the $Fe_xGa_{1-x}BO_3$ series. For $\boldsymbol{H}$ contained in the basal plane of the crystals, the expressions of the low-frequency (LF) and high-frequency (HF) AFMR modes are, respectively [3.3-3.5]:

$$\nu = \gamma\left[H\left(H + H_{\mathrm{D}}\right) + {H_{\Delta}}^{2} + 36H_{\mathrm{E}}H_{\mathrm{hex}}\cos 6\varphi\right]^{1/2}$$

and (3.3)

$$\nu = \gamma\left[2H_{\mathrm{a}}H_{\mathrm{E}} + H_{\mathrm{D}}\left(H + H_{\mathrm{D}}\right)\right]^{1/2}$$

(In what follows, we will consider only the LF AFMR mode.) Different parameters appearing in these equations are specified in Table 3.1, and φ is the angle between $\boldsymbol{H}$ and the *x*-axis. The definitions of the constants given in Table 3.1 are given in Chapter 1, "Crystal and magnetic structure of iron borate".

Clearly, using the AFMR, one can determine these parameters and get information on magnetic properties of the crystals.

Table 3.1 Parameters in eqs. (3.3) and their experimental values for $FeBO_3$, taken or calculated from the corresponding references.

Parameter	**Definition**	**Value** at 77 K
Dzyaloshinskii-Moriya field	$H_{\mathrm{D}} = \frac{1}{2}\frac{D}{\mathscr{M}_T}$ *	99.3±0.2 kOe [3.4, 3.6] 98.7±0.5 kOe [this work]
Exchange field	$H_{\mathrm{E}} = \frac{1}{4}\frac{E}{\mathscr{M}_T}$ *	$2.969\cdot 10^3$ kOe $3.01\cdot 10^3$ kOe ** [3.7]
Isotropic energy gap	${H_{\Delta}}^{2}$	4.25±0.25 kOe^2 [3.4, 3.6]
Hexagonal anisotropy field	$H_{\mathrm{hex}} = \frac{e_{\mathrm{eff}}}{\mathscr{M}_T}$ *	$1.826\cdot 10^{-5}$ kOe [this work]
Uniaxial anisotropy field	$H_{\mathrm{a}} = \frac{1}{2}\frac{a}{\mathscr{M}_T}$ *	3.1 kOe [3.4]

* $\mathscr{M}_T$ is the sublattice magnetization at a temperature T: $\mathscr{M}_0 = 520\,\mathrm{G}$ for $FeBO_3$ at 0 K and $\mathscr{M}_{77} = 512.876\,\mathrm{G}$ for $FeBO_3$ at 77 K [3.7]

** value at 0 K

In this chapter we describe the results of EMR studies of $Fe_xGa_{1-x}BO_3$ crystals for $0 < x \leqslant 1$ and report in more detail those for x = 0.85; 0.75; 0.65; 0.34 and 0.2.

3.2 Experimental results

EMR studies of $Fe_xGa_{1-x}BO_3$ single crystals have been carried out with two different spectrometers:

(i) a laboratory-developed spectrometer operating in the frequency range from 7 to 37.35 GHz and recording *absorption* spectra†, and

(ii) a commercial high-sensitivity X-band (9.464 GHz) Bruker spectrometer recording *derivative of absorption* spectra.

In both cases, the crystals were studied in the temperature range from 4 to 310 K and magnetizing fields up to 10 kOe applied in the basal plane.

3.2.1 EMR at different iron contents and temperatures

Depending on the iron contents and the temperature, several types of EMR have been observed in $Fe_xGa_{1-x}BO_3$ crystals. Figure 3.1 shows the transformation of spectra shapes with x at room temperature. At $x = 1$ (pure iron borate) only a low-field resonance is observed. In the microwave frequency and temperature ranges used in this work, only this resonance line is observed for $x = 1$. The EMR in pure iron borate has been earlier identified as AFMR [3.4]. At somewhat lower iron contents, $x = 0.75$, besides the low-field line, a new broad resonance at higher magnetic fields emerges with an effective g-factor $g_{\text{eff}} = 2.0$. As far as iron substitution for gallium occurs more or less randomly, such crystals are expected to contain regions with different local iron concentrations, implying different magnetic ordering. The low-field line observed in the mixed crystals, by analogy with iron borate [3.4], can be identified as AFMR line arising from magnetically ordered regions. The high-field line can be ascribed to Cluster Magnetic Resonance (CMR), *i.e.*, EMR arising from only partially magnetically ordered regions, or to superposition of CMR and EPR subsisting in the vicinity of the Néel temperature. At still lower iron contents, $x = 0.2$, the AFMR line disappears and the high-field line becomes more pronounced. For $x = 0.04$, the latter line disappears as well, and the EPR spectrum of diluted Fe^{3+} ions, broadened by dipole-dipole interactions, comes into view. At still lower iron contents, $x = 0.003$ this spectrum is spectacularly narrowed. A detailed account of the EPR studies of this crystal will be given below, *cf.* Chapter 4, "EPR of iron-gallium borate single crystals with low x".

† These results have been obtained in collaboration with A. Drovosekov and N. Kreines in the Kapitsa Institute for Physical Problems, Moscow.

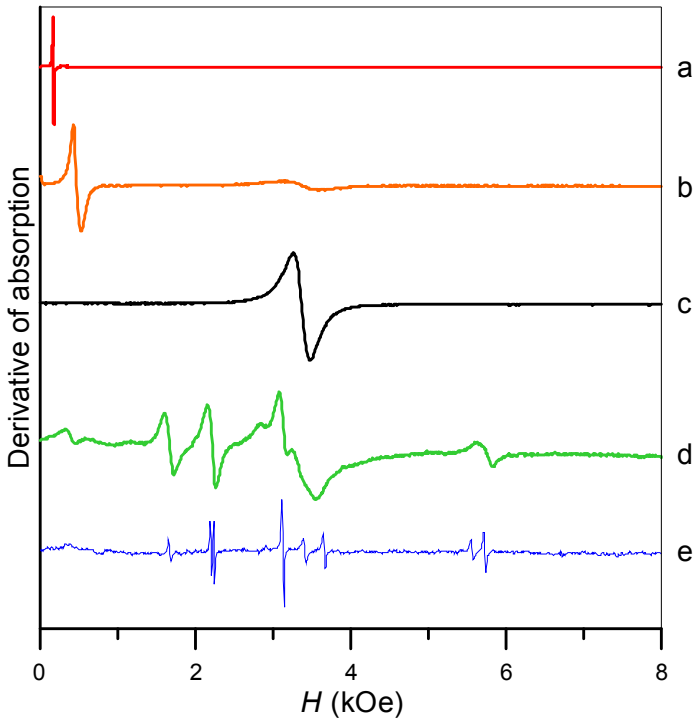

Figure 3.1 Normalized X-band room-temperature EMR spectra of $Fe_xGa_{1-x}BO_3$ crystals with different x: 1 (a), 0.75 (b), 0.2 (c), 0.04 (d) and 0.003 (e).

Figure 3.2 shows EMR spectra for $x = 0.85$ crystal at different temperatures. As one can see, at $T \gtrsim 304$ K only the high-field line is present; this temperature can be tentatively identified as an *effective* Néel temperature for this crystal (this assignment will further be corroborated by SQUID results). Obviously, the nature of this line can be only paramagnetic. At lower T, the AFMR line splits off the high-field one and gradually shifts towards lower fields; simultaneously, the relative intensity of the high-field line decreases. (Above room temperature, a second weak low-field line is also visible for this crystal; the nature of this line is not yet obvious.)

In order to prove or disprove the existence of a high-field line below T_N, we have carried out experiments with the high-sensitive Bruker spectrometer. Figure 3.3 shows the EMR spectra for $x = 0.85$ crystal at different temperatures in the magnetic field range corresponding to this line. Obviously, such a line is present in the whole temperature range; and below T_N it can be identified as CMR.

Similar transformations of the EMR spectra in the vicinity of T_N occur in $x = 0.75$, 0.65 and 0.34 crystals.

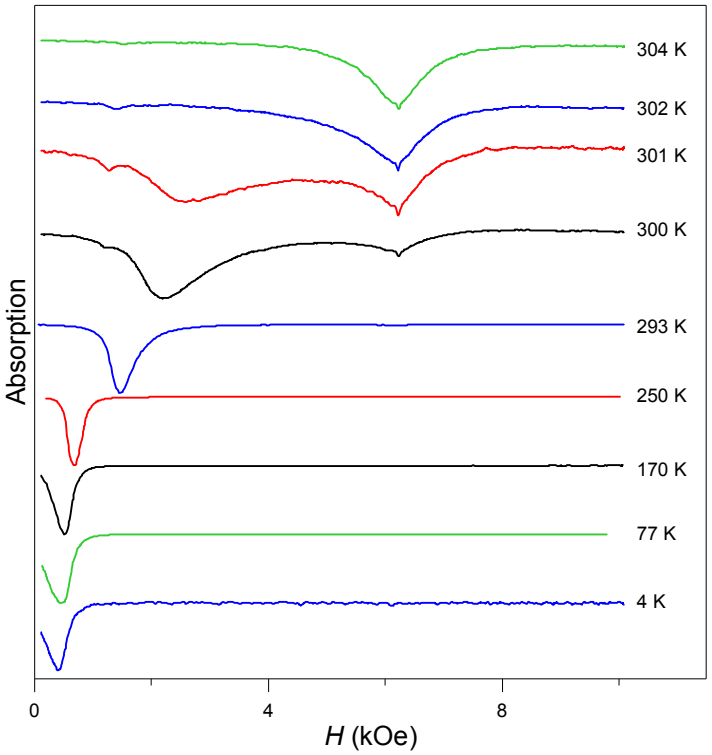

Figure 3.2 Normalized EMR absorption spectra series for x = 0.85 crystal at $\nu \approx 17\,\text{GHz}$ and different temperatures shown alongside the curves. The high-field line is superposed with a narrow signal from a probe with $g = 2.006$.

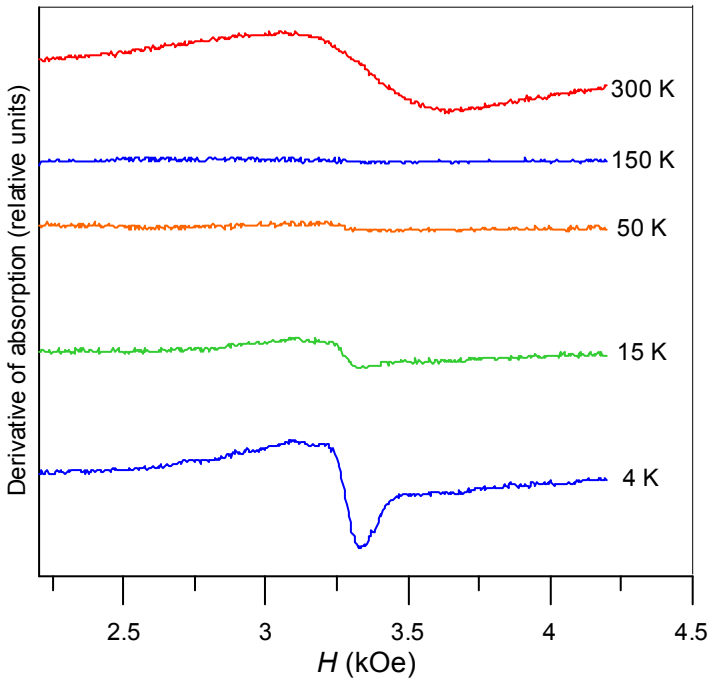

Figure 3.3 X-band EMR derivative of absorption spectra for x = 0.85 crystal at different temperatures shown alongside the curves.

For all crystals with $x \geqslant 0.34$ a splitting of the AFMR line in several more or less resolved components is observed. These components have different frequency dependences of their resonance fields (FDF). Figure 3.4 shows this line for x = 0.75 crystal at different frequencies; obviously, at higher frequencies this splitting becomes more pronounced. It can be caused either by a certain mesoscopic inhomogeneity of the crystals (the occurrence of regions with different local iron concentrations resulting in different magnetic properties) or by magneto-elastic effects due to random stresses [3.4]. In the case where such splitting was significant, we have defined the resonance field as the maximum of the most intense component.

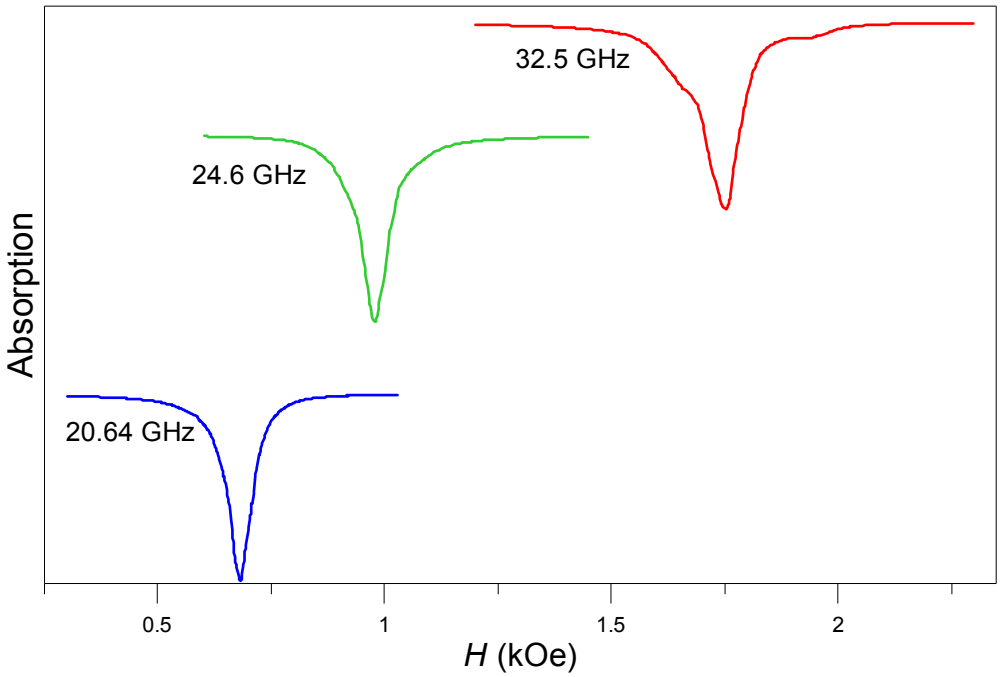

Figure 3.4 Normalized AFMR line for x = 0.75 crystal at different frequencies and T = 77 K.

Figures 3.5 and 3.6 show the temperature dependences of the resonance field of the AFMR line for two crystals with x = 0.65 and 0.34. Cooling the crystals down from T_N, the resonance field, first, sharply decreases, showing a transition from paramagnetic to magnetically ordered state. Next, this decrease is slowed down, and below a certain temperature — ca. 80 K for x = 0.65 crystal and ca. 20 K for x = 0.34 crystal — the tendency is reversed, *viz.*, the resonance shifts upfield. Figure 3.7 shows EMR spectra for x = 0.34 crystal at different temperatures. With lowering T from the Néel temperature (77 K in this crystal) to ca. 20 K, the AFMR line slightly shifts downfield. Meanwhile, a further cooling to 4 K results in a pronounced upfield shift and broadening of this line. In contrast, the high-field line decreases in intensity with lowering T; however, it again becomes obvious at 4 K. All these transformations suggest the occurrence of one more magnetic transition at low temperatures.

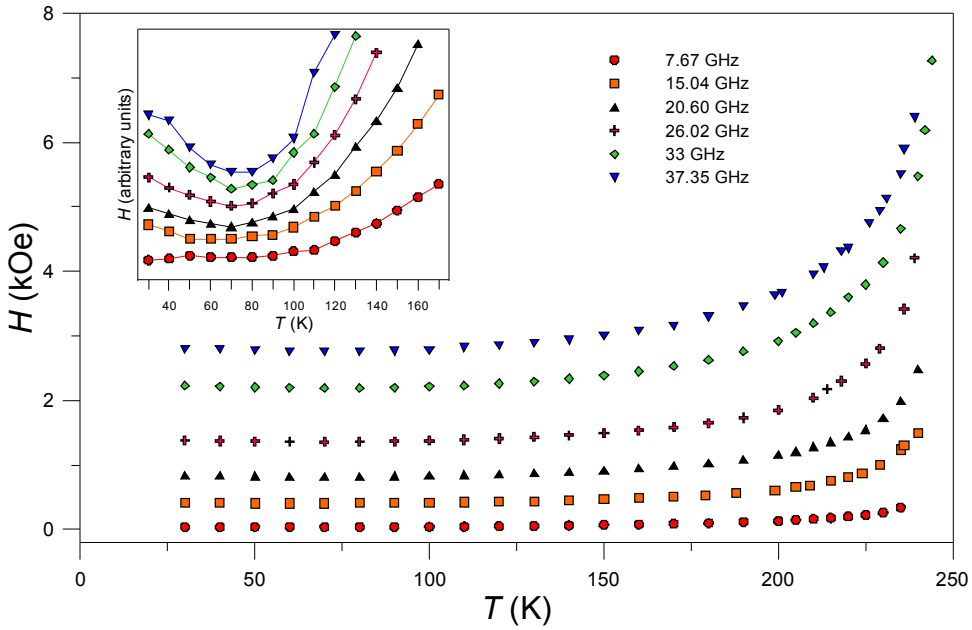

Figure 3.5 Temperature dependence of the resonance field of the AFMR line for $x = 0.65$ crystal measured at different microwave frequencies. The inset shows a vertical zoom in the low temperature region, with different curves arbitrarily shifted along the vertical axis.

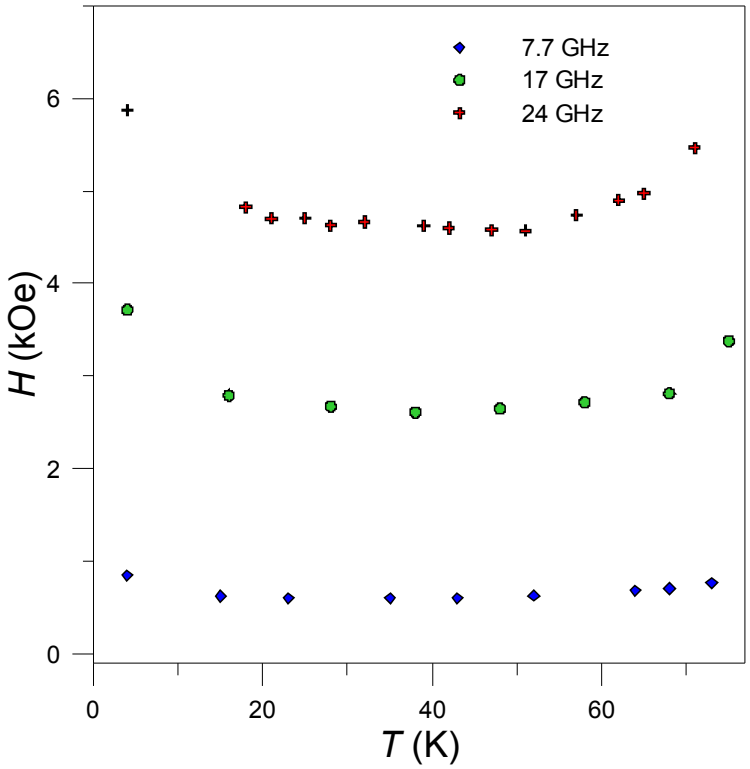

Figure 3.6 Temperature dependence of the resonance field of the AFMR line for $x = 0.34$ crystal measured at different microwave frequencies.

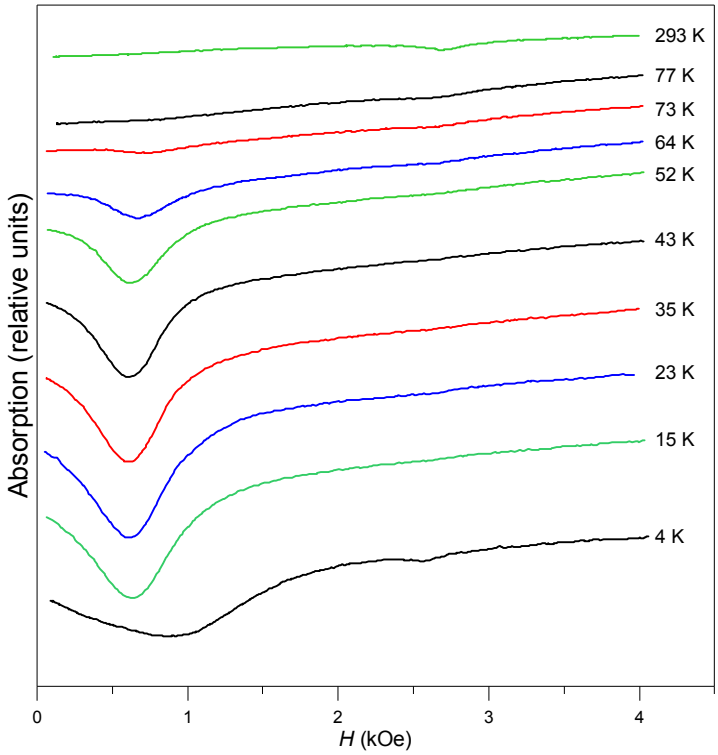

Figure 3.7 EMR absorption spectra at $\nu \approx 7.7\,\mathrm{GHz}$ for $x = 0.34$ crystal at different temperatures shown alongside the curves.

Such a transition does not occur in pure iron borate; however, an apparently similar transition has been observed in hematite α-Fe_2O_3 by Morin [3.8] and Morrison *et al.* [3.9]. As in iron-gallium borates, in hematite the LF and HF AFMR modes occur in the temperature range between the Néel temperature and the Morin's temperature T_M. For the LF mode in hematite, Morrison *et al.* have found that with decreasing temperature in the vicinity of T_M the resonance field rapidly increases (see Figure 9 in their paper), similarly to what we observe in mixed iron-gallium borates, see Figures 3.5 and 3.6. Besides, in hematite doped with Ga, Ti and Al the Morin's temperature is lowered in comparison with pure α-Fe_2O_3 [3.10, 3.11], similarly as in our case with decreasing iron content the supposed transition temperature decreases.

Thus, we assume that $Fe_xGa_{1-x}BO_3$ crystals with $x = 0.34$ and 0.65 undergo the Morin's transition at temperatures T_M below 20 K and 80 K, respectively. Above T_M crystals are easy-plane antiferromagnets with a weak in-plane ferromagnetism; the sublattice magnetizations lie in the basal plane and are slightly tilted (as occurs in $FeBO_3$ in the whole temperature range below T_N, *cf.* Chapter 1, "Crystal and magnetic structure of iron borate"). Below T_M the weak ferromagnetism vanishes and the crystals become pure easy-axis antiferromagnets, the sublattice magnetizations lying along the trigonal axis.

Obviously, in order to confirm this assumption, additional measurements, *e.g.* that of the dependence of the magnetization on the temperature, are required.

The EMR spectra for x = 0.2 crystal, see Figure 3.8, consist of a single line at $g \approx 2$, quite similar to the high-field line observed for higher x; consequently, the antiferromagnetic regions in this case are absent in the whole temperature range. At lower T this line considerably broadens, and Figure 3.9 (left) shows that its intensity does not follow the T^{-1} Curie law; therefore it cannot be a usual EPR line. We assume that this line is due to magnetic clusters.

As far as, except at very low x values, the EMR line at $g \approx 2$ is present in all crystals with $x < 1$, *cf.* Figures 3.1, 3.3 and 3.7, we can conclude that in such crystals long-range and short-range (cluster-type) magnetic ordering coexist. Figure 3.9 (right) shows the temperature dependence of the CMR line intensity for x = 0.65, confirming that the Curie law for this resonance is not respected.

Figure 3.10 shows the decrease of T_N, determined by AFMR, with the decrease in x. The AFMR data have been corroborated by SQUID. For comparison, data on T_N in similar crystals obtained by magnetometry and Mössbauer spectroscopy [3.12] are included‡. Obviously, the results of different determinations are in good agreement with each other.

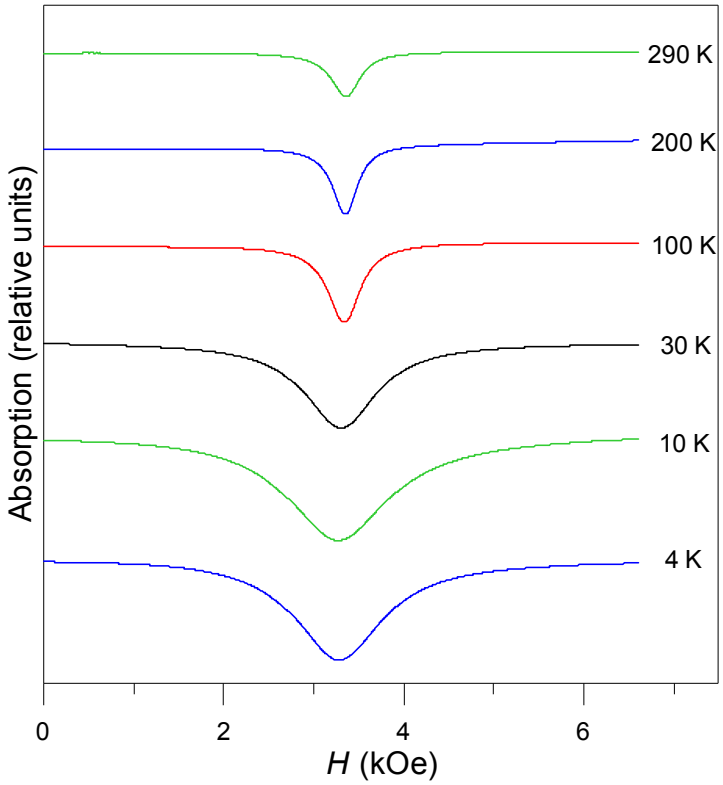

Figure 3.8 Integrated X-band derivative of absorption spectra for the x = 0.2 crystal at different temperatures shown alongside the curves.

‡In the original paper Kamzin *et al.* [3.12] erroneously refer to their crystals as $Fe_{1-x}Ga_xBO_6$.

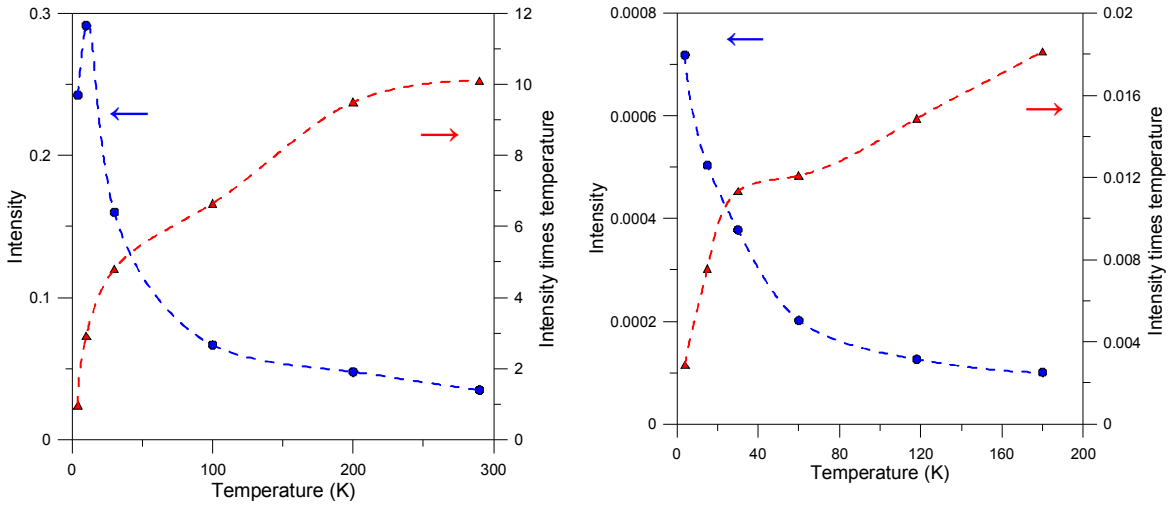

Figure 3.9 Temperature dependence of the intensity of the resonance line (circles, blue) and of the product intensity times temperature (triangles, red) for $x = 0.2$ (left) and $x = 0.65$ (right) crystals at $\nu \approx 9.5\,\mathrm{GHz}$. The dashed lines are guides for the eye.

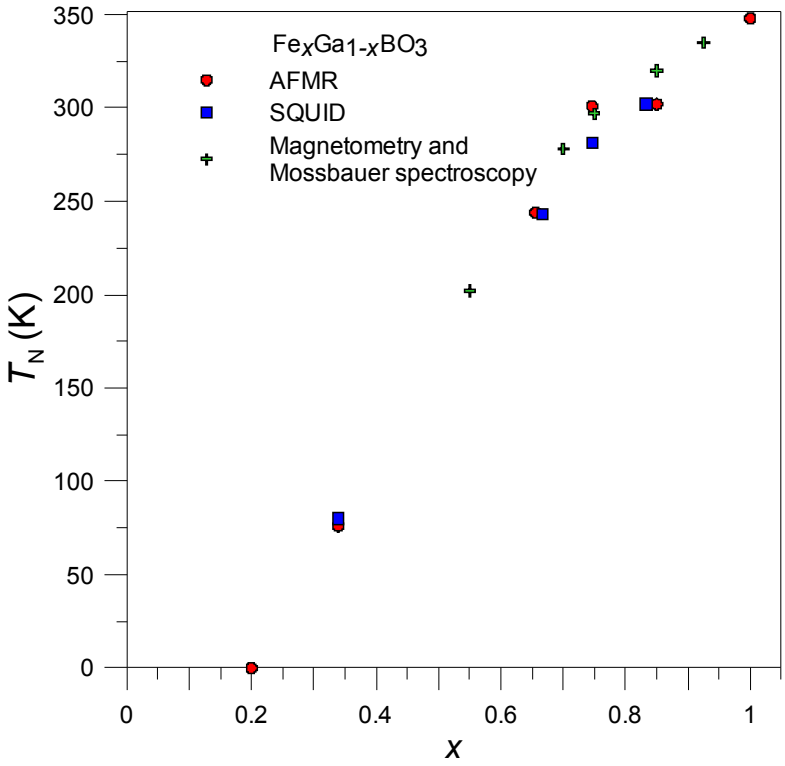

Figure 3.10 Néel temperature *vs.* x determined from AFMR and SQUID measurements. For comparison, magnetometry and Mössbauer spectroscopy data [3.12] are included.

3.2.2 Relationship between antiferromagnetic resonance frequency and magnetizing field

Field-sweep EMR spectra recordings at different microwave frequencies allow obtaining the FDF. Figure 3.11 shows these dependences at different temperatures for x = 1 crystal. With decreasing T, the FDF for $FeBO_3$ shifts downfield.

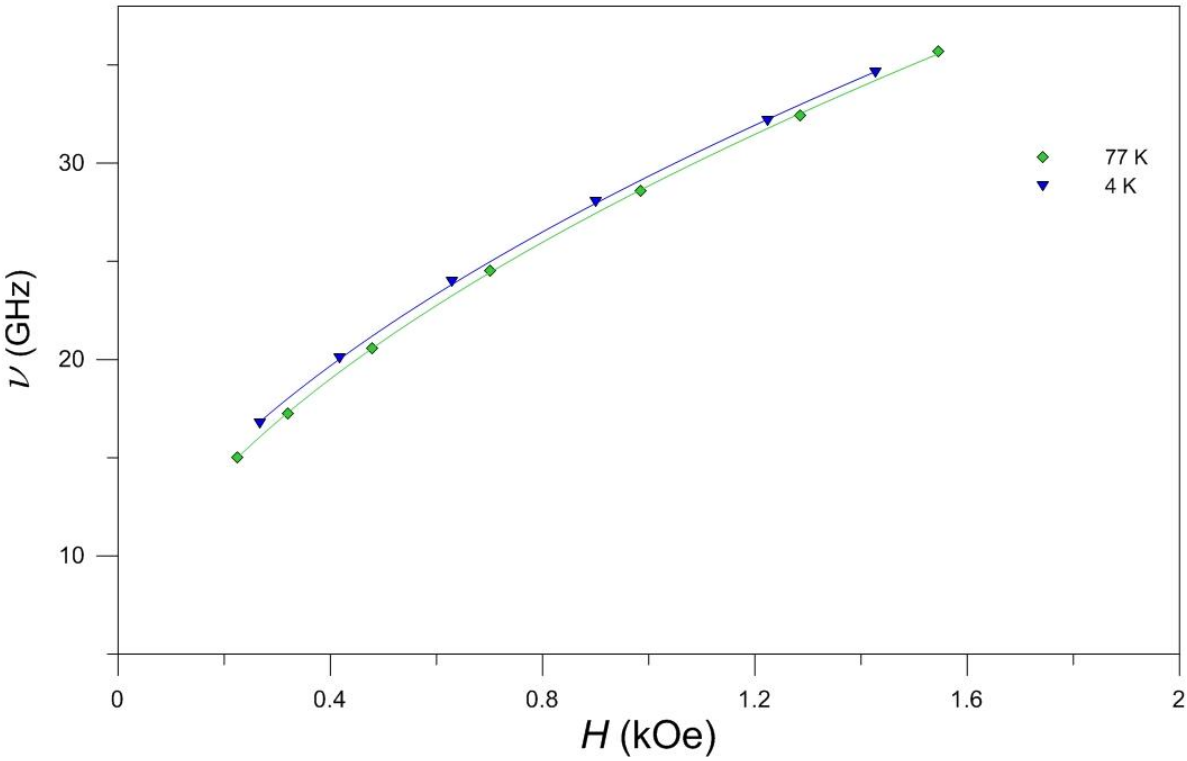

Figure 3.11 FDFs for $x = 1$ crystal at different temperatures. The solid curves are fittings according to eq (3.3).

FDFs for crystals with $x < 1$ show somewhat different behaviour. Figure 3.12 and 3.13 illustrate these dependences at different temperatures for x = 0.85 and 0.34 crystals, respectively. With decreasing T, the FDF, first, shifts downfield and next, shows an opposite tendency. In a greater or lesser extent, this behaviour is characteristic of all crystals with $x < 1$; the most pronounced shift is observed for x = 0.34 crystal, see Figure 3.13.

Fitting the FDF with eq. (3.3) using the least-squares method, allows one to determine the H_D, as well as the isotropic and anisotropic, $H_E H_{hex}$, energy gaps.

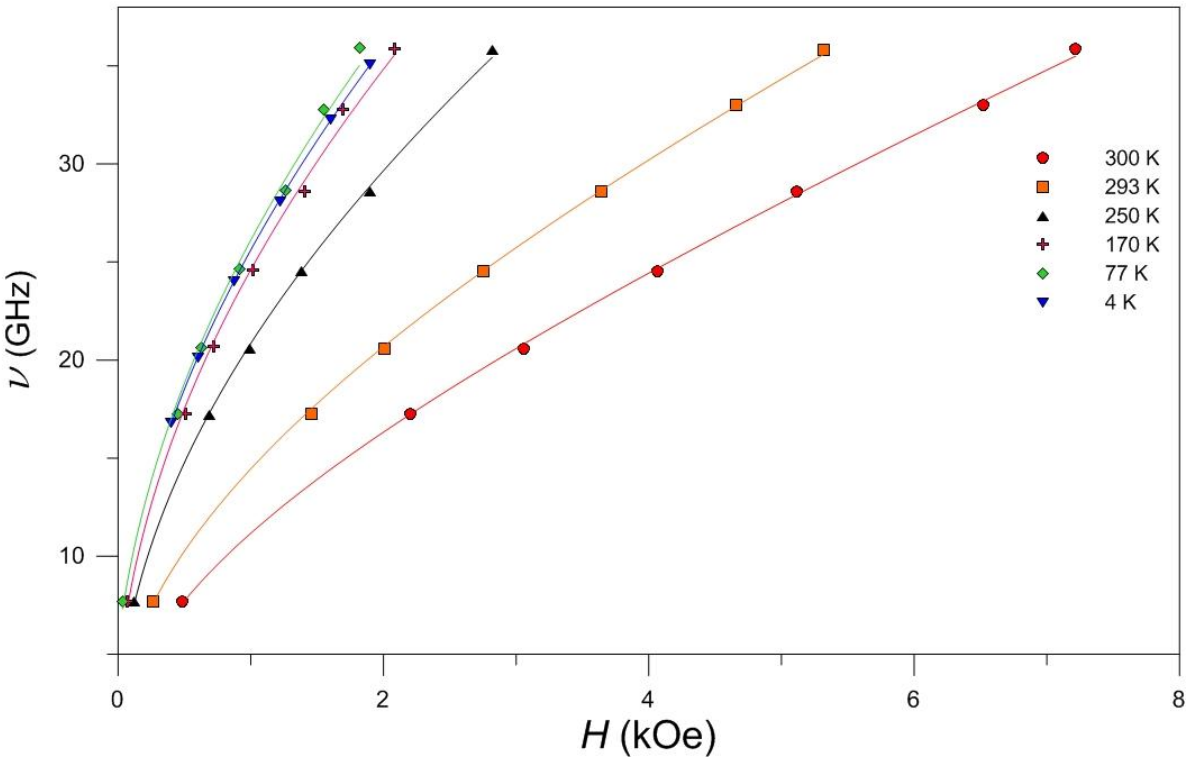

Figure 3.12 FDFs for $x = 0.85$ crystal at different temperatures. The solid curves are fittings according to eq. (3.3).

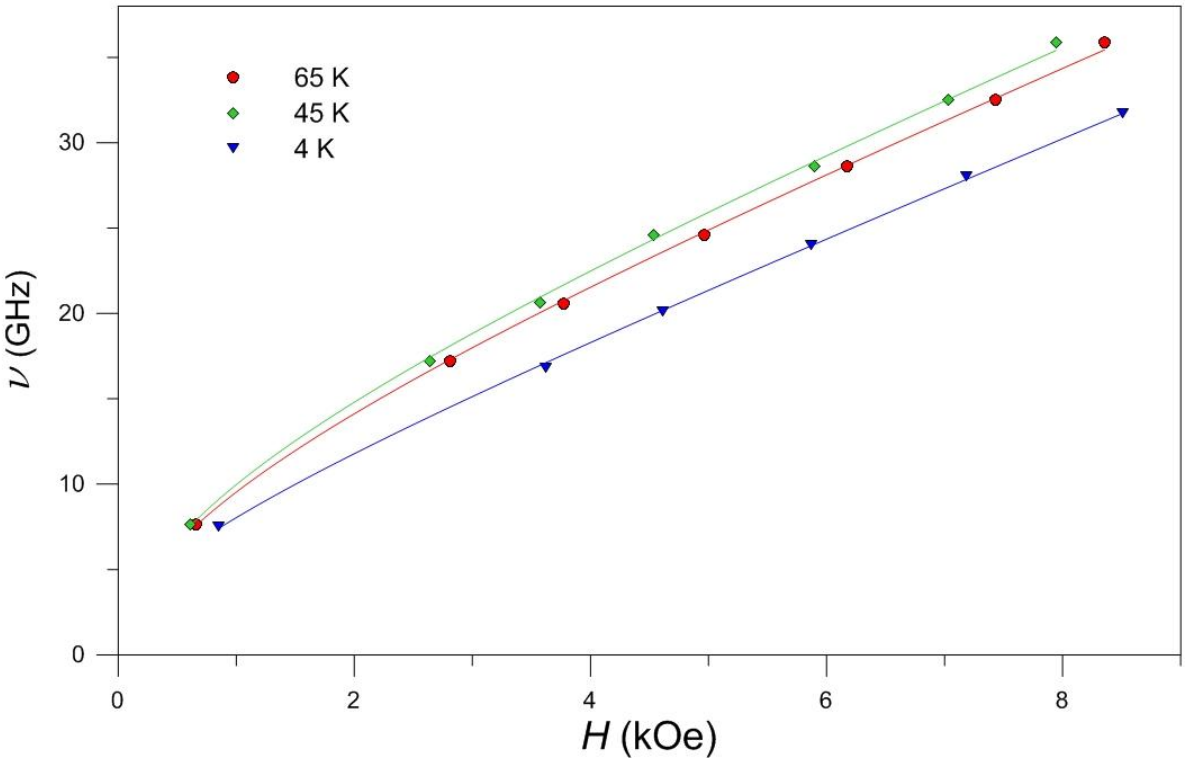

Figure 3.13 FDFs for $x = 0.34$ crystal at different temperatures. The solid curves are fittings according to eq. (3.3).

3.2.3 Dzyaloshinskii-Moriya field

Data on H_D for different crystals at different temperatures are summarized in Table 3.2.

Table 3.2 H_D (in kOe) for different x at different temperatures.

T, K	x				
	0.34	**0.65**	**0.75**	**0.85**	**1.0**
4	6.50±0.15	55.55±0.60	72.85±0.45	78.4±0.5	101.2±0.1 [3.4, 3.6] 99.3±0.5
45	12.25±0.25				
65	10.85±0.15				
77		59.2±0.4	74.10±0.25	88.2±3.0	99.3±0.2 [3.4, 3.6] 98.7±0.5
130		56.50±0.25			
170		51.6±0.2		74.55±1.50	
190		47.1±0.1	64.0±0.2		
200		44.20±0.15			89.7±0.1 [3.4, 3.6]
230		29.9±0.2			
250				54.0±0.5	
260			42.5±0.5		
273					72.0±0.1 [3.4, 3.6]
290			28.5±0.5		
293				24.9±0.2	
300				15.1±0.3	62.0±0.5 [3.4, 3.6]

A detailed study of the temperature dependence of H_D has been carried out for x = 0.65 crystal, see Figure 3.14. In cooling from the Néel temperature, H_D increases, passes through a maximum at ca. 80 K and then decreases. A similar behaviour is observed for all crystals with $0.34 \leqslant x \leqslant 0.85$, see Table 3.2. These findings corroborate the idea of the existence of the magnetic transition described above.

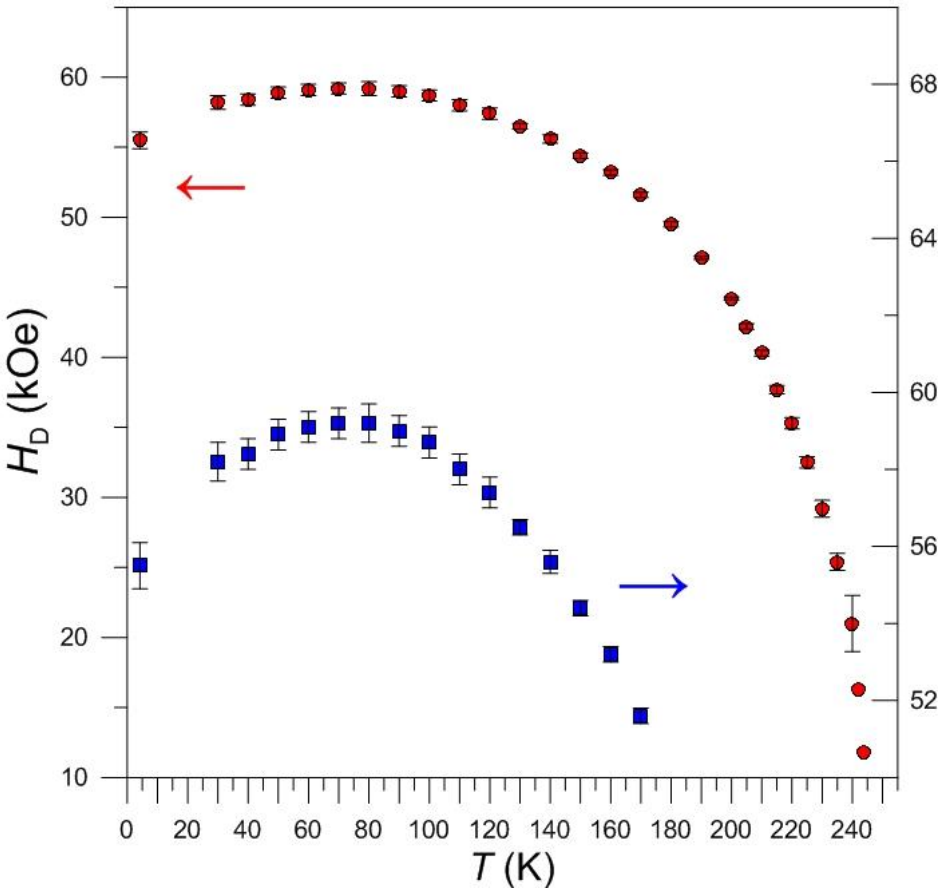

Figure 3.14 Temperature dependence of the effective Dzyaloshinskii-Moriya field for x = 0.65 crystal.

3.2.4 Isotropic energy gap

H_Δ^2 for different crystals at different temperatures, determined from fitting to eq. (3.3) of the corresponding FDFs, are shown in Table 3.3.

With increasing T from 4 K up to the Néel temperature, H_Δ^2 decreases, see Figure 3.15. In the temperature range from 4 to ca. 80 K a slow decrease is observed, while at higher temperatures this decrease is drastically accelerated.

The fact that H_Δ^2 becomes negative in the vicinity of the Neel temperature may be an artefact caused by non-validity of eq. (3.3) in this temperature range [3.13].

Table 3.3 H_Δ^2 (in kOe^2) for different x at different temperatures.

T, K	x				
	0.34	**0.65**	**0.75**	**0.85**	**1.0**
4	0.75±0.45	5.20±0.45	6.02±0.45	4.3±0.5	4.9±0.2 [3.4, 3.6]
45	-0.55±0.65				
65	-0.25±0.50				
77		4.90±0.30	5.00±0.15	3.9±1.2	4.25±0.25 [3.4, 3.6] 6.543 ±0.032
130		4.2±0.1			
170				1.65±1	
190			0.7±0.2		
200		1.65±0.10			1.6±0.2 [3.4, 3.6]
230		-0.3±0.5			
250				0.70±0.55	
260			-1.7±1		
273					0.6±0.2 [3.4, 3.6]
290			-1.65±0.45		
293				0.70±0.35	
300				-0.2±0.5	0.6±0.5 [3.4, 3.6]

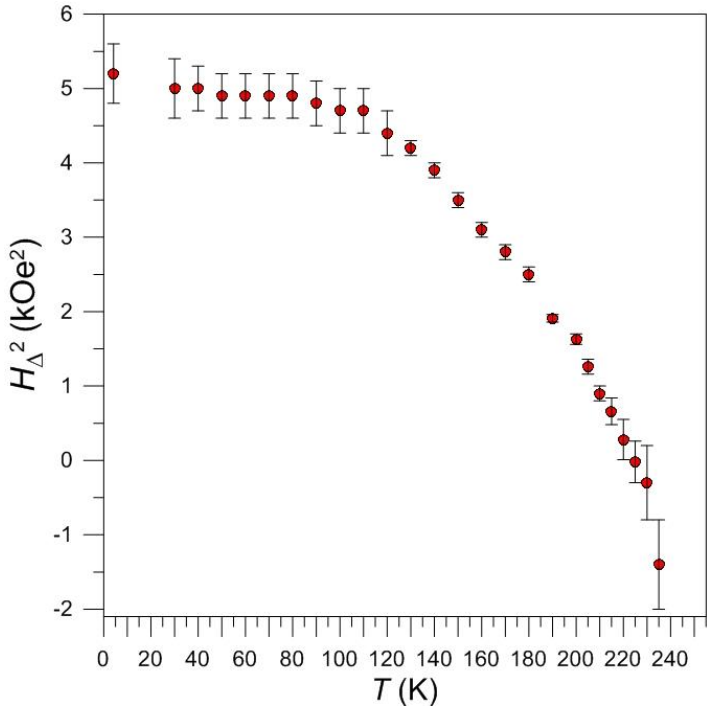

Figure 3.15 Isotropic energy gap *vs.* temperature for x = 0.65 crystal.

3.2.5 Anisotropic energy gap for iron borate

Using the values of H_D from Table 3.2, we have determined $H_E H_{hex}$, see eq. (3.3), from the measurements at a fixed ν carried out by rotating $\boldsymbol{H}$ in the basal plane of the crystal. Figure 3.16 shows the angular dependence of the quantity $\left(\nu/\gamma\right)^2 - H\left(H+H_D\right)$ for $x = 1$ crystal at 77 K. One can see that this dependence can be accounted for by a superposition of hexagonal and uniaxial anisotropies in basal plane. The occurrence of uniaxial anisotropy in this case can be due to a slight deviation of $\boldsymbol{H}$ from the basal plane or caused by mechanical stresses [3.14]. Therefore, the angular dependence of the resonance field has been fitted by the following expression, *cf.*eq. (3.3):

$$\left(\frac{\nu}{\gamma}\right)^2 - H\left(H+H_D\right) = H_\Delta{}^2 + 36 H_E H_{hex}\cos 6\varphi + p\cos 2\varphi \qquad (3.4)$$

where $H_\Delta{}^2$, $H_E H_{hex}$ and p are fitting parameters, the term in p describing the uniaxial component. The best-fit parameters in this equation are listed in Table 3.4.

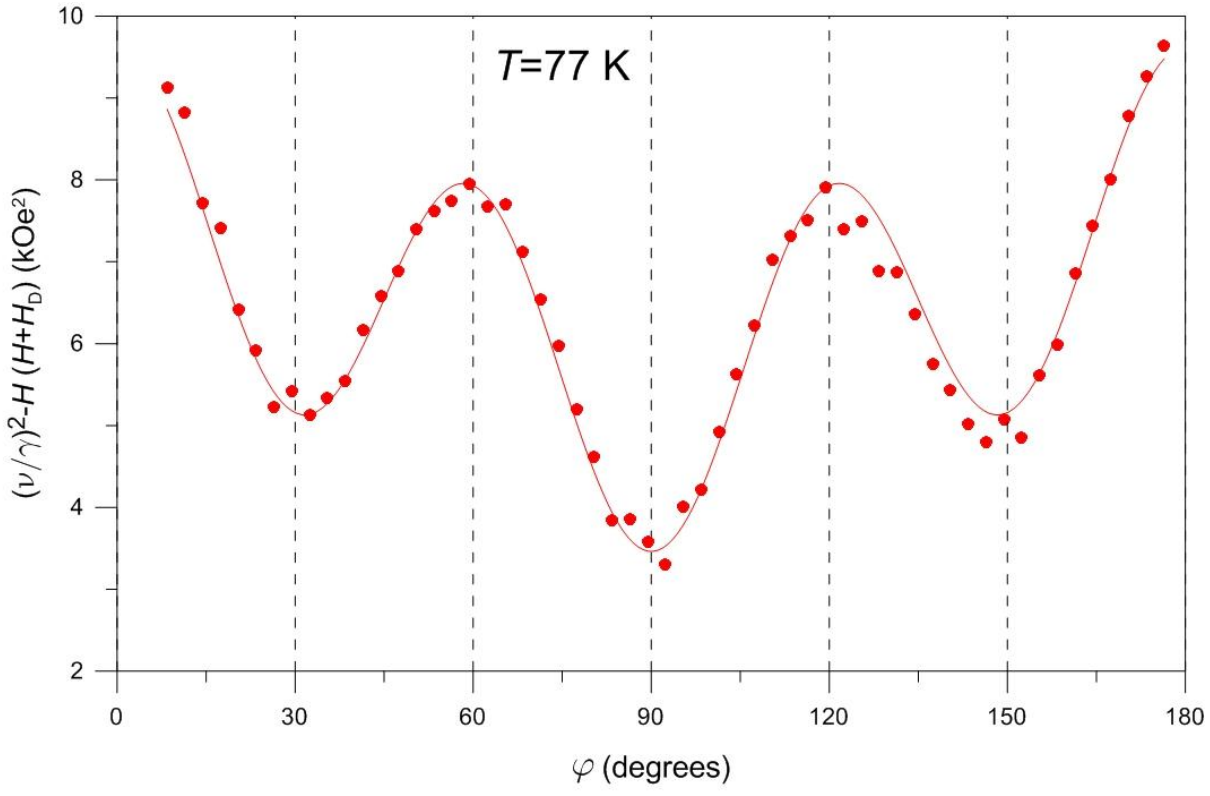

Figure 3.16 Dependence of $\left(\nu/\gamma\right)^2 - H\left(H+H_D\right)$ on the azimuthal angle φ at 77 K. The curve is a fitting according to eq. (3.4).

Table 3.4 Best-fit parameters in eq. (3.4)

Parameter	Value, in kOe²
$H_\Delta{}^2$	6.55±0.05
$H_E H_{hex}$	0.0542 ± 0.0013
p	1.13 ±0.05

From $H_E H_{hex}$ and H_E, *cf.* Tables 3.1 and 3.4, we get $H_{hex} = 1.826 \cdot 10^{-5}$ kOe; then, using the definition of H_{hex} given in Table 3.1, we get the effective constant of hexagonal anisotropy $e_{eff}^{exp} = 0.936$ Jm^{-3}. The $H_{hex} = -0.9 \cdot 10^{-5}$ kOe value at 77 K, reported earlier by Doroshev *et al.* [3.5], is negative and about twice as small in absolute value as our result. Such a discrepancy is mainly due to different definitions of H_{hex} and φ used by these authors.

3.3 Conclusions

With decreasing *x*, the EMR spectra show a gradual passage from the low-frequency AFMR mode at $x = 1$ towards the EPR of diluted iron ions at $x \ll 1$, going through a coexistence of AFMR and CMR arising, respectively, from magnetically ordered and partially disordered crystal regions for $0.34 \leqslant x \leqslant 0.85$, and CMR only for $x < 0.34$.

The Néel temperatures for crystals with $0.34 \leqslant x \leqslant 0.85$ have been determined by EMR and SQUID techniques. With decreasing *x*, T_N substantially decreases.

With decreasing *x*, both H_D and H_Δ^2 decrease. For $x < 1$ crystals, in cooling from T_N, H_D first increases, passes through a maximum and then decreases. The temperature dependences of H_D and the resonance field for the AFMR line suggest an occurence of another magnetic transition at ca. 80 and 20 K for $x = 0.65$ and 0.34 crystals, respectively. We assume that this transition is of Morin's type. Basing on the data on the temperature dependence of H_D it is reasonable to suppose that such transition occur for all crystals with $0.34 \leqslant x \leqslant 0.85$.

The intensity of the high-field line observed in all crystals with $x < 1$ except at very low *x*-values, does not follow the T^{-1} Curie law, suggesting that this line is due to magnetic clusters.

The anisotropic energy gap, determined for $x = 1$ crystal at 77 K, has allowed to calculate the effective constant of hexagonal anisotropy; the latter will be further used in the analysis of basal magnetocrystalline anisotropy in Chapter 6, "Magnetocrystalline anisotropy of iron borate and iron-gallium borates".

3.4 References

3.1 C. Kittel, Theory of antiferromagnetic resonance, Phys. Rev. 82 (1951) 565

3.2 C. Kittel, Introduction to solid state physics, 8th ed., Wiley, Hoboken, NJ, (2005) 680 pp.

3.3 E.A. Turov and N.G. Guseĭnov, Magnetic resonance in rhombohedral weak ferromagnetic, Soviet Physics JETP 11 (1960) 955-958

3.4 L.V. Velikov, A.S. Prokhorov, E.G. Rudashevskii and V.N. Seleznev, Antiferromagnetic resonance in FeBO3, Soviet Physics JETP 39 (1974) 909-915

3.5 V.D. Doroshev, I.M. Krygin, S.N. Lukin, A.N. Molchanov, A.D. Prokhorov, V.V. Rudenko and V.N. Seleznev, Basal magnetic anisotropy of a weak ferromagnetic FeBO3 crystal, JETP Lett. 29 (1979) 257-260

3.6 В.Н. Селезнев, Магнитоупорядоченные бораты железа (физические свойства, применение, синтез), Диссертация, Симферопольский гос. университет (1988) 371 с.

3.7 В.Д. Дорошев, Клочан В.А., Ковтун Н.М. и др., Экспериментальное и теоретическое изучение температурной зависимости подрешеточной намагниченности слабого ферромагнетика FeBO3, Препринт Дон. ФТИАН УССР 7(102), Донецк (1985) 60 с.

3.8 F.J. Morin, Magnetic susceptibility of αFe2O3 and αFe2O3 with added titanium, Phys. Rev 78 (1950) 819-820

3.9 B.R. Morrison, A.H. Morrish and G.J. Troup, High-field antiferromagnetic resonance in α-Fe2O3, Phys. Stat. Sol. (b) 56 (1973) 183-195

3.10 P.J. Besser, A.H. Morrish and C.W. Searle, Magnetocrystalline anisotropy of pure and doped hematite, Phys. Rev. 153 (1967) 632-640

3.11 J.K. Srivastaya and R.P. Sharma, Magnetic dilution effects on Morin phase transition in hematite, Phys. Stat. Sol. (b) 49 (1972) 135-146

3.12 A.S. Kamzin, L.P. Ol'khovik and E.V. Snetkova, Preparation and investigation of weakly ferromagnetic Fe1-xGaxBO3 single crystals, Physics of the Solid State 45 (2003) 2128–2130

3.13 Л.В. Великов, Е.Г. Рудашевский и В.Н. Селезнев, Наблюдение антиферромагнитного резонанса в борате железа выше температуры Нееля, Известия АН СССР, Сер. физ. 36 (1972) 1531-1534

3.14 M.B. Strugatsky, K.M. Skibinsky, V.V. Tarakanov and V.I. Khizhnyi, Fine structure of Gakel'-Turov oscillations in iron borate, J. Magn. Magn. Mater. 241 (2002) 330-334

4. EPR of iron-gallium borate single crystals with low x

4.1 Principles of computer-assisted EPR spectroscopy

4.1.1 Basic formalism

Electron Paramagnetic Resonance (EPR), first observed in 1944 by Zavoisky, has become a powerful tool for studying intimate physical characteristics of solids.

In condensed state, free atoms or ions form bonds (typically, ionic or covalent) and thus lose their magnetic moments; as a result, the substance becomes diamagnetic. Paramagnetism in condensed state exists due to some exceptions to this rule, where one or several unpaired electrons are maintained. These exceptions are: structure defects, impurity ions as well as ions with partially filled electron shells, *i.e.* transition elements and rare-earths; a generic term for all these entities is "paramagnetic species". Each representative of such species has an electronic spin $\boldsymbol{S}$, either integer or half-integer, its projection along a quantification axis taking $2S+1$ values: $M_S = -S, -S+1, \cdots, S$. Besides, it can possess an orbital moment $\boldsymbol{L}$ quantified by a quantum number $M_L = -L, -L+1, \cdots, L$. Finally, in the case of the Russell–Saunders coupling, the resulting angular moment $\boldsymbol{J} = \boldsymbol{L} + \boldsymbol{S}$ occurs, taking the values $J = L+S, L+S-1, \cdots, |L-S|$, and each of these states is quantified by a corresponding quantum number $M_J = -J, -J+1, \cdots, J$.

The magnetic moment associated with a given $\boldsymbol{J}$ is:

$$\boldsymbol{\mu} = -g_J \beta \boldsymbol{J} \tag{4.1}$$

where β is the Bohr magneton and g_J is the Landé factor:

$$g_J = 1 + \frac{J(J+1) - L(L+1) + S(S+1)}{2J(J+1)} \tag{4.2}$$

Note that in the case of a pure orbital moment and a pure spin, g_J becomes: $g_L = 1$ and $g_S = 2$, respectively. (The exact value of g_S in the latter case, $g_S = 2.002319$, is explained by quantum electrodynamics.)

In a magnetizing field $\boldsymbol{B}$, $\boldsymbol{\mu}$ is quantified along the direction of $\boldsymbol{B}$, so that the state with a given J splits into $2J+1$ substates called Zeeman sublevels:

$$\mathcal{E} = -\boldsymbol{\mu}\cdot\boldsymbol{B} = g_J\beta\boldsymbol{J}\cdot\boldsymbol{B} = g_J\beta BM_J\,. \tag{4.3}$$

This splitting in the case $J = \frac{5}{2}$ is shown in Figure 4.1.

In EPR, magnetic dipole transitions between the Zeeman sublevels are aroused under the action of an electromagnetic wave. The resonance occurs when the electromagnetic energy quantum $h\nu$ matches the energy difference between the Zeeman sublevels:

$$h\nu = \Delta\mathcal{E} = g_J\beta B\Delta M_J \tag{4.4}$$

In accordance with the selection rules, in the first approximation only transitions between adjacent sublevels are allowed, $\Delta M_J = \pm 1$. Thus the condition of EPR becomes:

$$h\nu = g_J\beta B \tag{4.5}$$

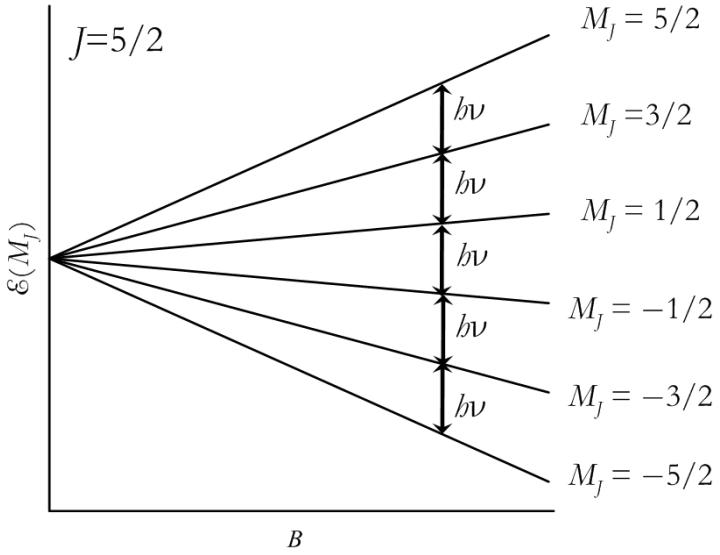

Figure 4.1 Zeeman sublevels for $J = \frac{5}{2}$ in a magnetic field

4.1.2 Calculating the EPR spectra

Many paramagnetic species, in particular, the transition elements, possess only the spin S. This occurs for the d^5 configuration where $L = 0$ as well as for other configurations, if L is "frozen". In these cases the g-factor is almost isotropic and its value is close to g_S. If L is not completely frozen, in order to describe the spin state an effective spin S taking into account the orbital contribution is introduced.

The spin Hamiltonian including the Zeeman coupling $\mathcal{H}_Z$ and coupling between S and the electrostatic field of surrounding atoms $\mathcal{H}_C$ (so-called fine structure) can be expressed as follows:

$$\mathcal{H} = \mathcal{H}_Z + \mathcal{H}_C \tag{4.6}$$

where

$$\mathcal{H}_{\tilde{z}} = B \sum_{i=x,y,\tilde{z}} l_i \sum_{n=1,3,5,7} \sum_{m=-n}^{n} B_{ni}^{m} O_n^m , \tag{4.7}$$

and

$$\mathcal{H}_C = \sum_{n=2,4} \sum_{m=-n}^{n} B_n^m O_n^m \tag{4.8}$$

In eqs. (4.7), (4.8) O_n^m are extended Stevens operators [4.1] and l_i are direction cosines of $\boldsymbol{B}$:

$$l_x = \sin\vartheta\cos\varphi; \quad l_y = \sin\vartheta\sin\varphi; \quad l_{\tilde{z}} = \cos\vartheta , \tag{4.9}$$

ϑ and φ being the polar and azimuthal angles, respectively.

$\mathcal{H}_C$ gives non-trivial contributions to the Zeeman sublevel energies only for $S \geqslant 1$.

The spin Hamiltonian parameters B_{ni}^{m} and B_n^m are assumed to only depend on local structure and not on the field *B*. This means that *B* should be low enough for the splitting between the Zeeman sublevels to be much smaller than that between the spin multiplets of the ground and the first excited state of S.

$\mathcal{H}$ should comprise all terms consistent with symmetry, including time reversal symmetry.

Linear in *S* terms in eq. (4.7) can be expressed as $\beta \boldsymbol{B} \cdot \boldsymbol{g} \cdot \boldsymbol{S}$ where $\boldsymbol{g}$ is the g-matrix [4.2]:

$$\boldsymbol{g} = \begin{pmatrix} g_{xx} & g_{xy} & g_{x\tilde{z}} \\ g_{yx} & g_{yy} & g_{y\tilde{z}} \\ g_{\tilde{z}x} & g_{\tilde{z}y} & g_{\tilde{z}\tilde{z}} \end{pmatrix} = \frac{1}{\beta} \begin{pmatrix} B_{1x}^{1} & B_{1x}^{-1} & B_{1x}^{0} \\ B_{1y}^{1} & B_{1y}^{-1} & B_{1y}^{0} \\ B_{1\tilde{z}}^{1} & B_{1\tilde{z}}^{-1} & B_{1\tilde{z}}^{0} \end{pmatrix}. \tag{4.10}$$

Similarly, second-order fine structure terms in eq. (4.7) can be expressed as $\boldsymbol{S} \cdot \boldsymbol{D} \cdot \boldsymbol{S}$ where the *D*-tensor

$$\boldsymbol{D} = \begin{pmatrix} D_{xx} & D_{xy} & D_{x\tilde{z}} \\ D_{yx} & D_{yy} & D_{y\tilde{z}} \\ D_{\tilde{z}x} & D_{\tilde{z}y} & D_{\tilde{z}\tilde{z}} \end{pmatrix} = \begin{pmatrix} B_2^2 - B_2^0 & B_2^{-2} & \frac{1}{2}B_2^1 \\ B_2^{-2} & -B_2^2 - B_2^0 & \frac{1}{2}B_2^{-1} \\ \frac{1}{2}B_2^1 & \frac{1}{2}B_2^{-1} & 2B_2^0 \end{pmatrix} \tag{4.11}$$

is symmetric and traceless, consequently it can be diagonalized by appropriately turning the $x, y, \tilde{z}$ frame:

$$\boldsymbol{D} = \begin{pmatrix} D_x & 0 & 0 \\ 0 & D_y & 0 \\ 0 & 0 & D_{\tilde{z}} \end{pmatrix} \tag{4.12}$$

Thus, only two parameters are necessary to completely define $\boldsymbol{D}$:

$$D = \tfrac{3}{2} D_{\tilde{z}} \quad \text{and} \quad E = \tfrac{1}{2}\left(D_x - D_y\right) \tag{4.13}$$

D and E are, respectively, axial and rhombic second-order fine structure constants, and the "rhombicity" parameter is defined as

$$\lambda = \frac{E}{D} = \frac{D_x - D_y}{3D_z} \tag{4.14}$$

Usually, the x, y, z axes are chosen within the convention that $|D_x| \leqslant |D_y| \leqslant |D_z|$ [4.3], in which case

$$0 \leqslant \lambda \leqslant \tfrac{1}{3} \tag{4.15}$$

The lower and upper limits of λ correspond to axial $(E = 0)$ and orthorhombic $\left(E/D = 1/3\right)$ symmetry, respectively.

For the fourth-order fine structure parameters, the following notation is sometimes used: a (cubic), F (axial), H and G (rhombic).

If the local symmetry is not lower the rhombic, in the x, y, z frame where $\boldsymbol{D}$ is diagonal, the g-matrix is also diagonal [4.2]:

$$\boldsymbol{g} = \begin{pmatrix} g_x & 0 & 0 \\ 0 & g_y & 0 \\ 0 & 0 & g_z \end{pmatrix} \tag{4.16}$$

so that the x, y, z axes can be considered as local magnetic axes.

By diagonalizing the spin Hamiltonian matrix, the Zeeman sublevel energies $\mathcal{E}_i$ (eigenvalues) and the corresponding wave functions Ψ_i (eigenvectors) are obtained.

The transitions between the Zeeman sublevels are of magnetic dipolar nature; therefore they are induced by coupling between the magnetic field $\boldsymbol{B}_1$ of the electromagnetic wave of a frequency ν and the magnetic dipole moment with components

$$\left(\beta g S\right)_i = \beta \sum_i g_i S_i, \quad i = x, y, z \tag{4.17}$$

In most commercial EPR spectrometers the two magnetic fields are orthogonal, $\boldsymbol{B}_1 \perp \boldsymbol{B}$; besides, in the experiment the condition that $B_1 \ll B$ usually holds. Hereinafter, both these conditions are assumed to be satisfied.

The matrix element of the perturbation operator is [4.2]

$$\mu_{pq} = \beta \left\langle \Psi_p \middle| \boldsymbol{B}_1 \cdot \boldsymbol{g} \cdot \boldsymbol{S} \middle| \Psi_q \right\rangle \tag{4.18}$$

where Ψ_p and Ψ_q are wave functions of the Zeeman sublevels with energies $\mathcal{E}_p$ and $\mathcal{E}_q$, respectively. The transition intensity, proportional to the number of transitions per unit time between the p and q states, can be expressed as [4.2]

$$W_{pq} \propto \nu^2 \left|\mu_{pq}\right|^2 \tag{4.19}$$

W_{pq} depends on the orientations of both $\boldsymbol{B}$ (through Ψ_p and Ψ_q) and $\boldsymbol{B}_1$ (explicitly). These orientations can be described as follows. (We assume for simplicity that the x, y, z frame

coincides with the crystallographic frame x_c, y_c, z_c.) In the laboratory frame x_l, y_l, z_l, defined by the configuration of the microwave cavity and its disposition with respect to the poles of the electromagnet of the EPR spectrometer, we choose $\boldsymbol{B} \parallel z_l$ and $\boldsymbol{B}_1 \parallel y_l$.

The relative orientations of the laboratory and crystallographic frames can be described by the following matrix [4.4]:

$$\boldsymbol{A}_{cl} = \begin{pmatrix} -\cos\psi\cos\vartheta\cos\varphi - \sin\psi\sin\varphi & -\sin\psi\cos\vartheta\cos\varphi + \cos\psi\sin\varphi & \sin\vartheta\cos\varphi \\ -\cos\psi\cos\vartheta\sin\varphi + \sin\psi\cos\varphi & -\sin\psi\cos\vartheta\sin\varphi - \cos\psi\cos\varphi & \sin\vartheta\sin\varphi \\ \cos\psi\sin\vartheta & \sin\psi\sin\vartheta & \cos\vartheta \end{pmatrix} \quad (4.20)$$

where $\vartheta, \varphi, \pi - \psi$ are the Euler angles shown in Figure 4.2. Obviously, with such a definition, in the x_c, y_c, z_c frame ϑ and φ are spherical angles of $\boldsymbol{B}$ and ψ describes the orientation of $\boldsymbol{B}_1$ in the plane perpendicular to $\boldsymbol{B}$.

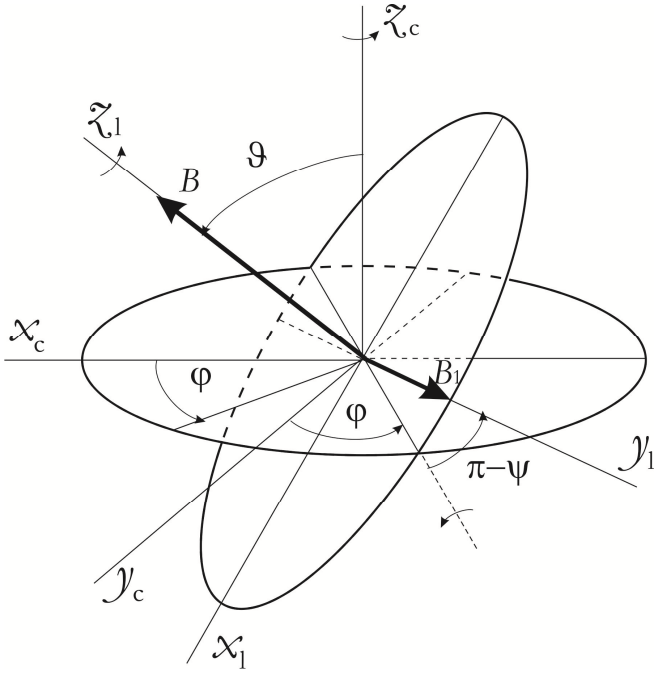

Figure 4.2 Euler angles between the crystallographic frame x_c, y_c, z_c and the laboratory frame x_l, y_l, z_l.

Thus, the unit vectors of $\boldsymbol{B}$ and $\boldsymbol{B}_1$ are, respectively, in the laboratory frame:

$$\boldsymbol{l}_l = \begin{pmatrix} 0 \\ 0 \\ 1 \end{pmatrix} \quad \text{and} \quad \boldsymbol{l}_{1l} = \begin{pmatrix} 0 \\ 1 \\ 0 \end{pmatrix} \quad (4.21)$$

and in the crystallographic frame:

$$\boldsymbol{l} = \boldsymbol{A}_{\mathrm{cl}}\boldsymbol{l}_{\mathrm{l}} = \begin{pmatrix} \sin\vartheta\cos\varphi \\ \sin\vartheta\sin\varphi \\ \cos\vartheta \end{pmatrix} \quad \text{and} \quad \boldsymbol{l}_{\mathrm{l}} = \boldsymbol{A}_{\mathrm{cl}}\boldsymbol{l}_{\mathrm{ll}} = \begin{pmatrix} -\sin\psi\cos\vartheta\cos\varphi + \cos\psi\sin\varphi \\ -\sin\psi\cos\vartheta\sin\varphi - \cos\psi\cos\varphi \\ \sin\psi\sin\vartheta \end{pmatrix} \tag{4.22}$$

With this definition, the matrix element of the perturbation operator becomes:

$$\mu_{pq} = \beta B_{\mathrm{l}} \left\langle \Psi_p(\vartheta,\varphi) \middle| \boldsymbol{l}_{\mathrm{l}}(\vartheta,\varphi,\psi)\cdot\boldsymbol{g}\cdot\boldsymbol{S} \middle| \Psi_q(\vartheta,\varphi) \right\rangle \tag{4.23}$$

In the usual field-sweep EPR spectroscopy, the resonance condition can be expressed as follows:

$$\left|\mathcal{E}_q - \mathcal{E}_p\right| = g_{\mathrm{eff}}\beta B_{pq} = h\nu \tag{4.24}$$

where g_{eff} is the effective g-factor, B_{pq} is the corresponding resonance field.

In reality, the resonance occurs within a certain field range about B_{pq}, and its intensity is described by a lineshape function $F_{pq}\left(B - B_{pq}, \Delta B_{pq}\right)$ with a linewidth ΔB_{pq}, normalized by the condition

$$\int_{-\infty}^{\infty} F_{pq}\left(B - B_{pq}, \Delta B_{pq}\right)\mathrm{d}B = 1 \tag{4.25}$$

Most often, F_{pq} is assumed to have either Lorentzian, F_{L} or Gaussian, F_{G} shape:

$$\begin{aligned} F_{\mathrm{L}} &= \left(B - B_{pq}, \Delta B_{pq}\right) = \frac{1}{\pi\Delta B_{pq}}\left(1 + \frac{\left(B - B_{pq}\right)^2}{\Delta B_{pq}{}^2}\right)^{-1} \\ F_{\mathrm{G}} &= \left(B - B_{pq}, \Delta B_{pq}\right) = \frac{1}{\sqrt{2\pi}\Delta B_{pq}}\mathrm{e}^{-\frac{\left(B - B_{pq}\right)^2}{2\Delta B_{pq}{}^2}} \end{aligned} . \tag{4.26}$$

F_{L} is applicable in the case of broadening caused by relaxation processes, whereas F_{G} describes broadening due to static disorder.

4.1.3 Computer treatment of the EPR spectra

An important facet of the EPR studies is numerical analysis (computer simulation) of experimental spectra. Indeed, extracting meaningful physical information from the experimental results requires accurate spectra fitting. The fitting procedure, called spectra parameterization, consists in determining numerical values of the spin Hamiltonian parameters providing a complete description of the paramagnetic species. Such a description will only be satisfactory if the spin Hamiltonian includes all essential interactions contributing to the genesis of the EPR spectrum.

The computer-assisted treatment of the EPR spectra includes the following steps shown in Figure 4.3:

- ✓ Recording an experimental derivative-of-absorption spectrum.
- ✓ Developing a physical model of the paramagnetic species.
- ✓ Choosing an adequate form of the spin Hamiltonian and assuming tentative values of its parameters.
- ✓ Diagonalizing the spin Hamiltonian; calculating resonance fields and transition intensities; and generating a theoretical EPR spectrum.
- ✓ Comparing iteratively the experimental and computer-generated spectra; determining the best-fit parameter set or improving the initial model.

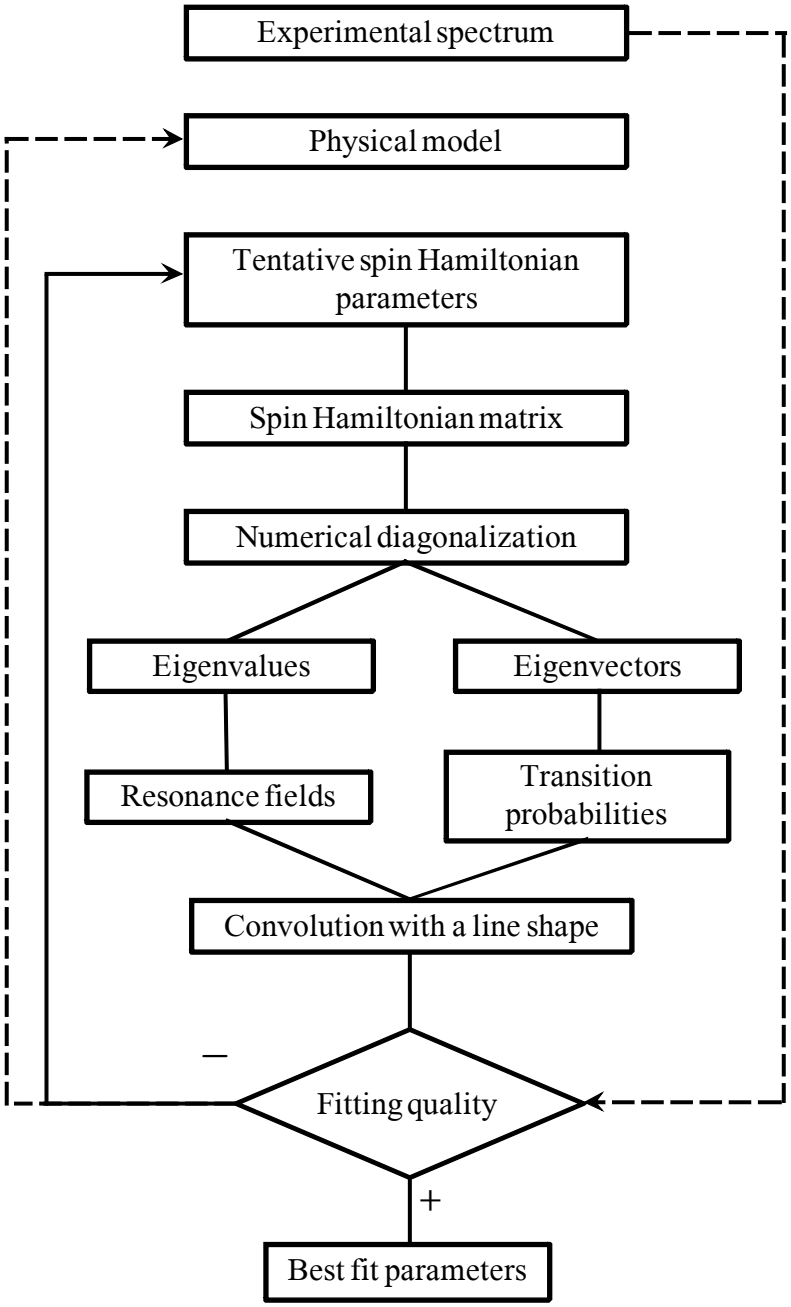

Figure 4.3 General scheme of numerical analysis of experimental EPR spectra.

4.2 Experimental results

$Fe_xGa_{1-x}BO_3$ single crystals with $x < 0.01$ were studied by EPR with an X-band (9.464 GHz) spectrometer (Bruker) in the temperature range from 4 to 290 K and magnetizing field up to 1 T.

Figure 4.4 shows the EPR spectra for $Fe_{0.003}Ga_{0.997}BO_3$ at 4 K for different orientations of $\boldsymbol{B}$, described by the polar angle ϑ with respect to the C_3 axis and the azimuthal angle φ with respect to C_2. Because of small crystal sizes, exact orientations could be determined only through careful trial and error computer fittings to the experimental spectra. Figure 4.5 shows the actual relation between ϑ and φ in rotating the crystal.

For all crystal orientations with the exception of the basal plane, strong anisotropy of the resonance fields and pronounced angular dependence of the corresponding linewidths have been observed.

No temperature dependence of the resonance magnetic fields has been found, and the integral spectra intensities at different temperatures closely followed the T^{-1} Curie law.

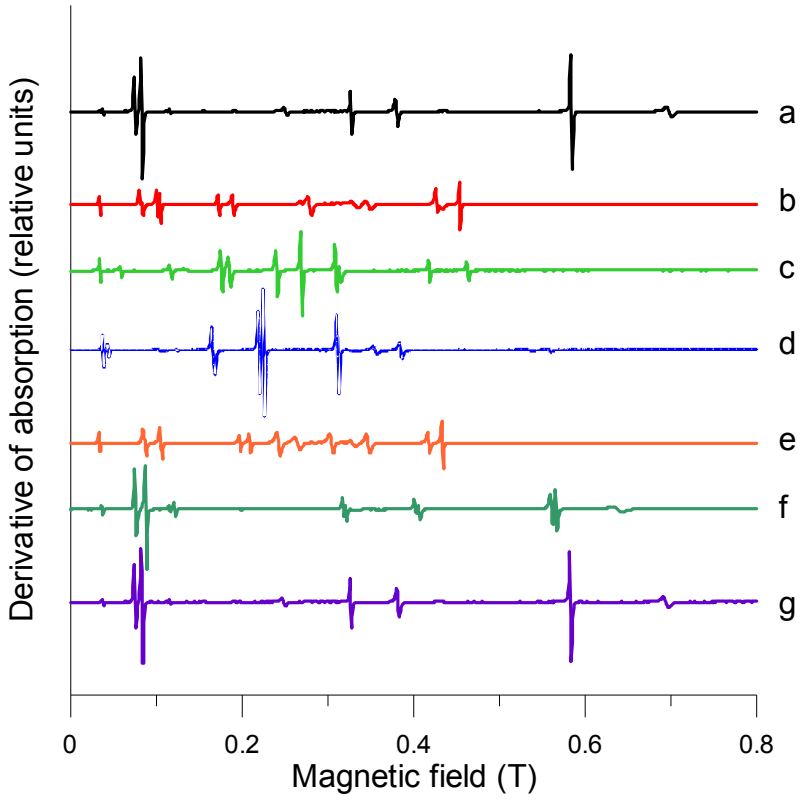

Figure 4.4 Experimental EPR spectra of $Fe_xGa_{1-x}BO_3$ crystal with $x = 0.003$ at 4 K for different orientations of $\boldsymbol{B}$: $\vartheta = 11$, $\varphi = 270°$ (a); $\vartheta = 37$, $\varphi = 300°$ (b); $\vartheta = 66$, $\varphi = 307°$ (c); $\vartheta = 96$, $\varphi = 311°$ (d); $\vartheta = 135$, $\varphi = 318°$ (e); $\vartheta = 164$, $\varphi = 339°$ (f) and $\vartheta = 169$, $\varphi = 30°$ (g).

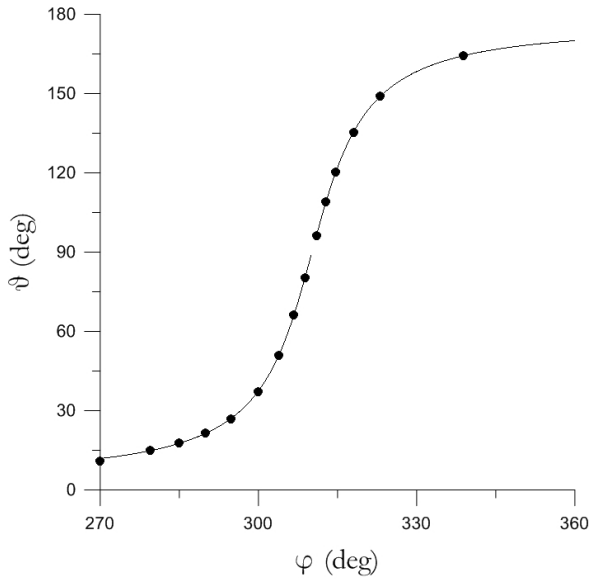

Figure 4.5 Relationship between the spherical angles in the course of rotation of the crystal when recording the spectra shown in Figure 4.4. Circles: results of spectra simulations; full line: the best-fit curve described by the equation $\tan\vartheta = -0.12/(0.57\sin\varphi + 0.68\cos\varphi)$.

With increasing iron contents in the crystals, the EPR spectra experience dipole-dipole broadening, see Figure 4.6.

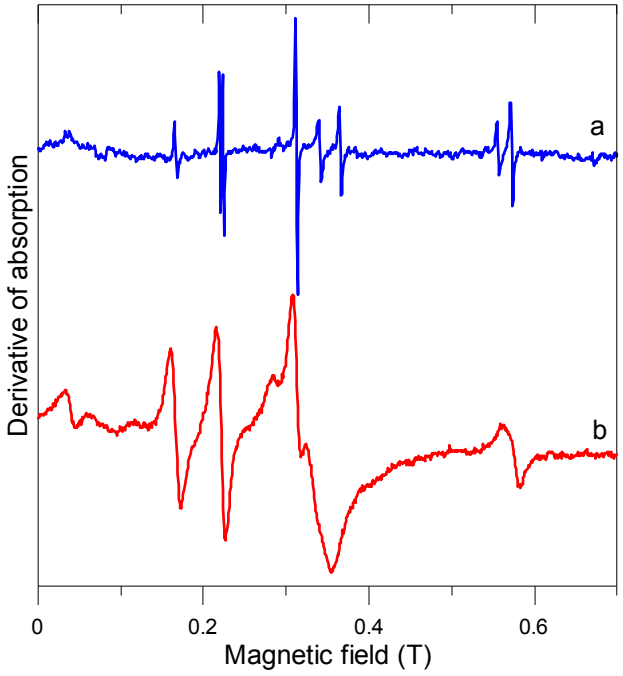

Figure 4.6 Normalized experimental room-temperature EPR spectra of $Fe_{0.003}Ga_{0.997}BO_3$ (a, blue) and $Fe_{0.042}Ga_{0.958}BO_3$ (b, red). In both cases $\vartheta = 87$, $\varphi = 285°$.

4.3 Discussion

4.3.1 Conventional spin Hamiltonian: spectra parametrization

In order to determine the EPR parameters, detailed computer simulations of the EPR spectra recorded at different orientations of $\boldsymbol{B}$ have been carried out using a laboratory-developed code based on the conventional spin Hamiltonian of trigonal symmetry, containing Zeeman as well as second- and fourth-order fine structure terms [4.5, 4.6]:

$$\mathcal{H} = g\beta \boldsymbol{B}\cdot\boldsymbol{S} + \tfrac{1}{3}DO_2^0 - \tfrac{1}{180}(a-F)O_4^0 + \tfrac{\sqrt{2}}{9}a\left(\mp O_4^3 \sin 3\alpha + O_4^{-3}\cos 3\alpha\right) \qquad (4.27)$$

where the various symbols have been defined previously. In the actual case, $S = 5/2$ and the extended Stevens operators O_2^0, O_4^0, O_4^3 and O_4^{-3} are defined as in the textbook by Al'tshuler and Kozyrev [4.1]. Note that instead of O_4^{-3} the notations $\tilde{O}_4^3$ [4.6], O_4^{3*} [4.5] and Ω_4^3 [4.1] have also been used. The $\mp$ signs in eq. (4.27) refer to two non-equivalent Fe^{3+} sites with local magnetic axes rotated through the angle $\mp\alpha$ about the C_3 axis [4.5, 4.6], see Figure 1.3 in Chapter 1, "Crystal and magnetic structure of iron borate". Note that in the spin Hamiltonian in the paper by Lukin *et al.* [4.6] the coordinate system is turned in such a way that x-axis lies in the symmetry plane m .

First, we have focused on determining the sign of D, the leading parameter in eq.(4.27). This could be achieved by following the temperature dependences of relative intensities of different resonance lines identified with transitions between distinct Zeeman sublevels. Figure 4.7 shows computer-generated spectra corresponding to different temperatures, with a and F parameters set to zero in order to simplify the analysis.

The various resonance lines in Figure 4.7 are identified by the numbers of Zeeman sublevels involved in the corresponding transitions. This identification is straight forward with our simulation code, separating contributions of transitions between each pair of levels. Figure 4.8 shows the energy levels and possible EPR transitions for positive and negative signs of D; expectedly, with changing the sign the order of levels in low and intermediate magnetizing field is inversed. As one can see, for positive D the transitions occur between lower, occupied, Zeeman sublevels, whereas for negative D the transitions can take place only between higher Zeeman sublevels, which are empty at low temperatures.

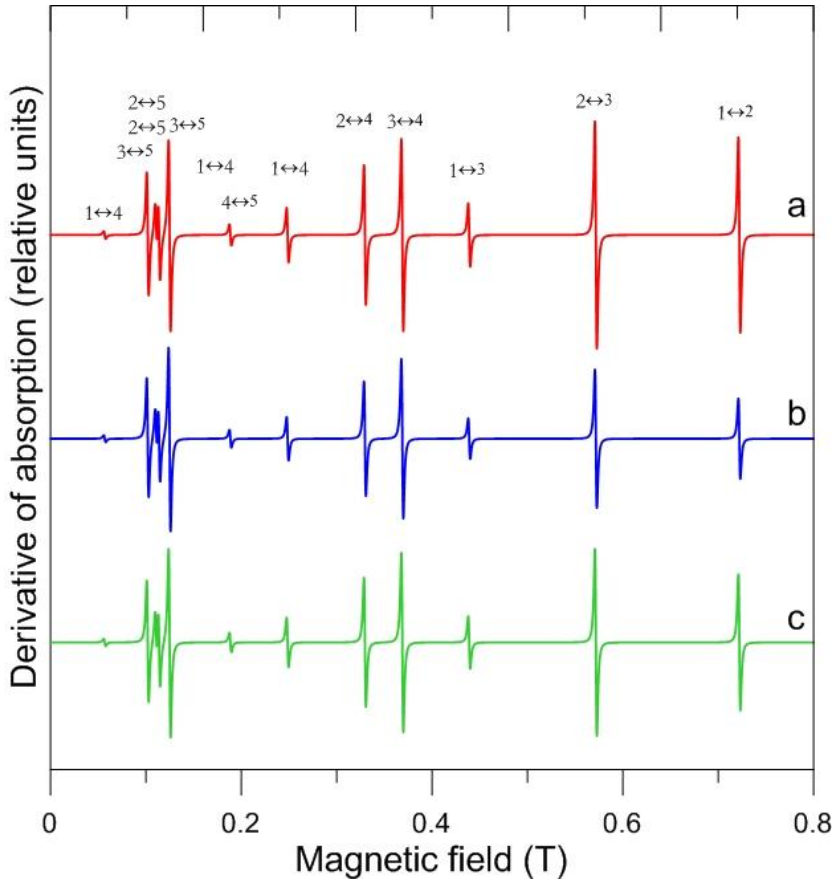

Figure 4.7 Computer-generated EPR spectra at 4 K with $D > 0$ (a, red) and $D < 0$ (b, blue) and at 300 K (c, green). The parameters a and F are set to zero and the spectra intensities are multiplied by the absolute temperature. The numbering from 1 to 6 of the Zeeman sublevels involved is in ascending order for $D > 0$ and in descending order for $D < 0$.

In Figure 4.7 it is apparent that the most pronounced temperature dependence of the relative intensity occurs for the line at 0.5717 T. As the temperature decreases, the intensity of this line increases for $D > 0$ and decreases for $D < 0$. Figure 4.9 (top) shows a zoom of computer-generated spectra for positive D at two different temperatures. The comparison with the corresponding experimental spectra, see Figure 4.9 (bottom), allows concluding that the sign of D is, indeed, positive. (The splitting in Figure 4.9 (bottom), instead of the single line in Figure 4.9 (top), is observed because of the presence of two non-equivalent iron sites.)

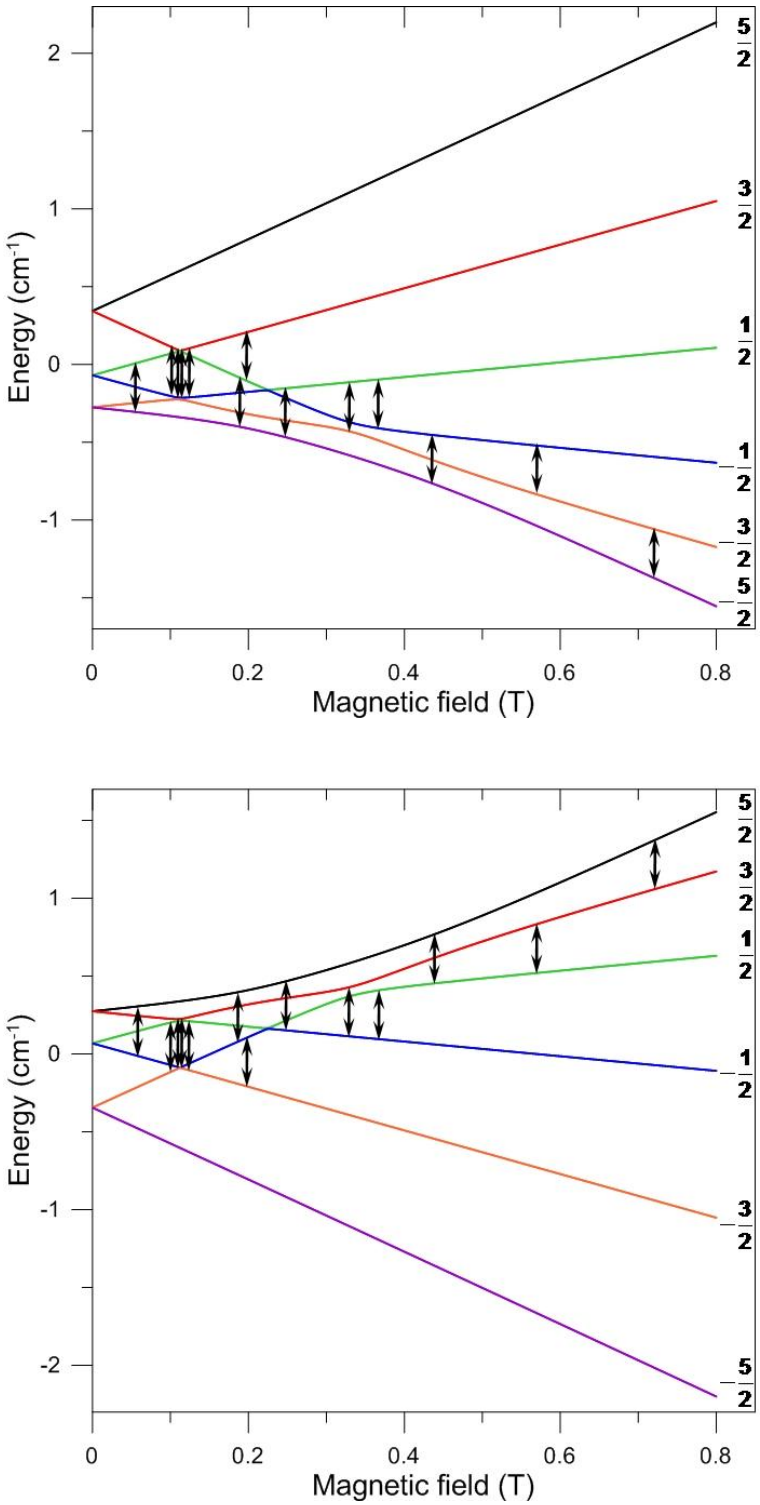

Figure 4.8 Energy diagrams for $D > 0$ (top) and $D < 0$ (bottom) for $\vartheta = 10$ and $\varphi = 278^{o}$, showing various resonance transitions for energy quanta of $0.316\,\mathrm{cm}^{-1}$. The different Zeeman sublevels are identified by their quantum numbers M_S in the high magnetizing field approximation.

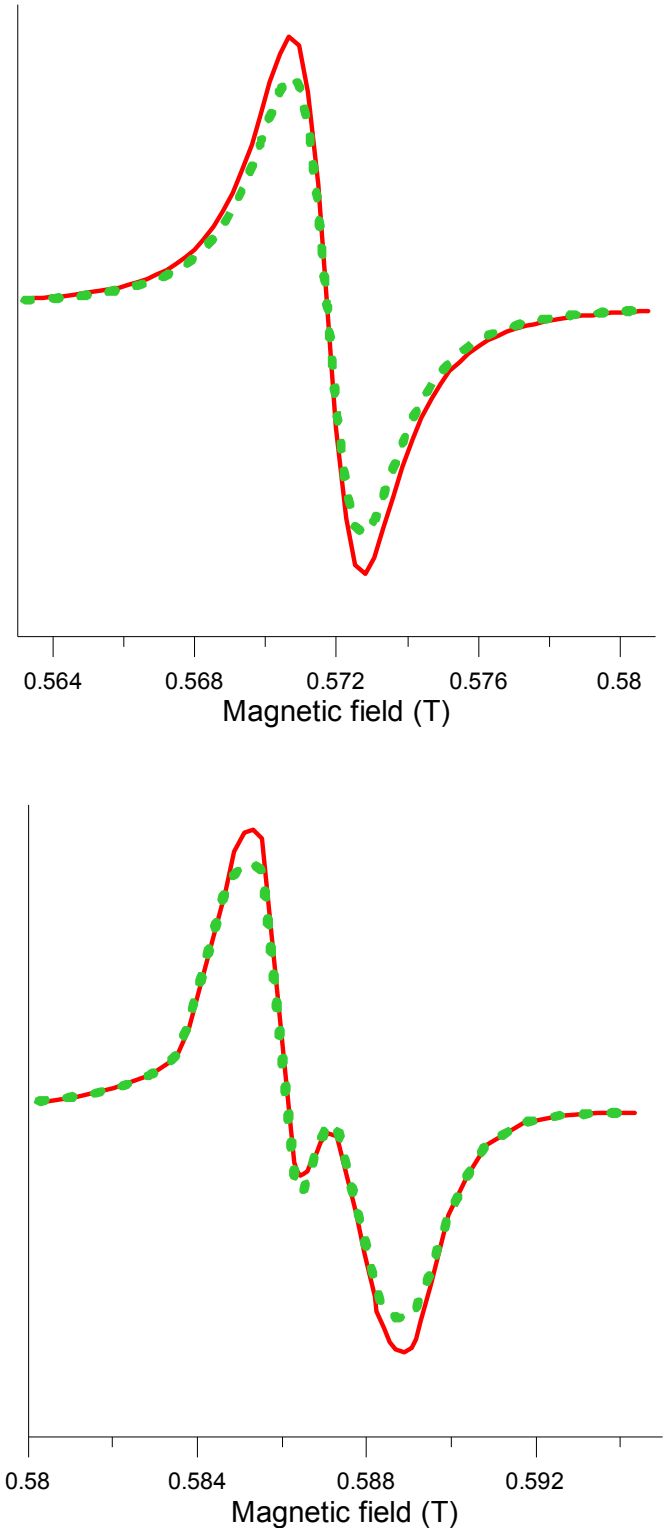

Figure 4.9 Zooms of computer-generated (top) and experimental (bottom) EPR spectra for $\vartheta = 10$ and $\varphi = 278\,°$ at 4 (continuous, red) and 30 K (dashed, green). The spectra intensities have been multiplied by the absolute temperature.

After specifying the sign of D, its absolute value as well as exact values of a and F could be determined by accurate computer simulations of the experimental EPR spectra at different orientations of $\boldsymbol{B}$, *e.g.*, see Figures 4.10 and 4.11. As the result, two different best-fit parameter sets have been obtained, as given in Table 4.1. The set I parameters are in a reasonably good agreement with those obtained by Lukin *et al.* [4.6] and Seleznev [4.7] for a crystal of nominal composition $Fe_{0.005}Ga_{0.995}BO_3$ studied by EPR at Q- and V-bands (ca. 36 and 75 GHz, respectively).

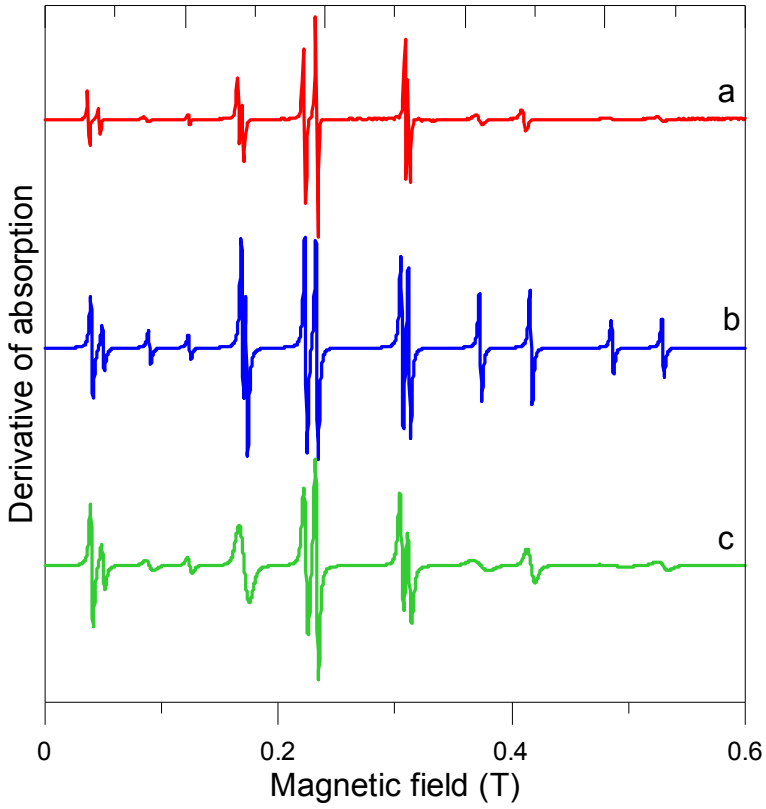

Figure 4.10 Normalized experimental EPR spectrum of $Fe_{0.003}Ga_{0.997}BO_3$ at 4 K (a, red), the best-fit computer generated spectra for $\vartheta = 80$ and $\varphi = 309\,°$ without (b, blue) and with parameter distributions (c, green).

As one can see from Figures 4.10 (a and b) and 4.11 (left), the positions of different resonance lines are perfectly fitted to. Meanwhile, the relative amplitudes of certain lines are not satisfactorily reproduced in the simulations, in spite of the fact that both the positions and intensities of all resonance lines have been calculated from eigenvalues and eigenvectors determined within the same diagonalization procedure of the spin Hamiltonian matrix. This discrepancy will be discussed below.

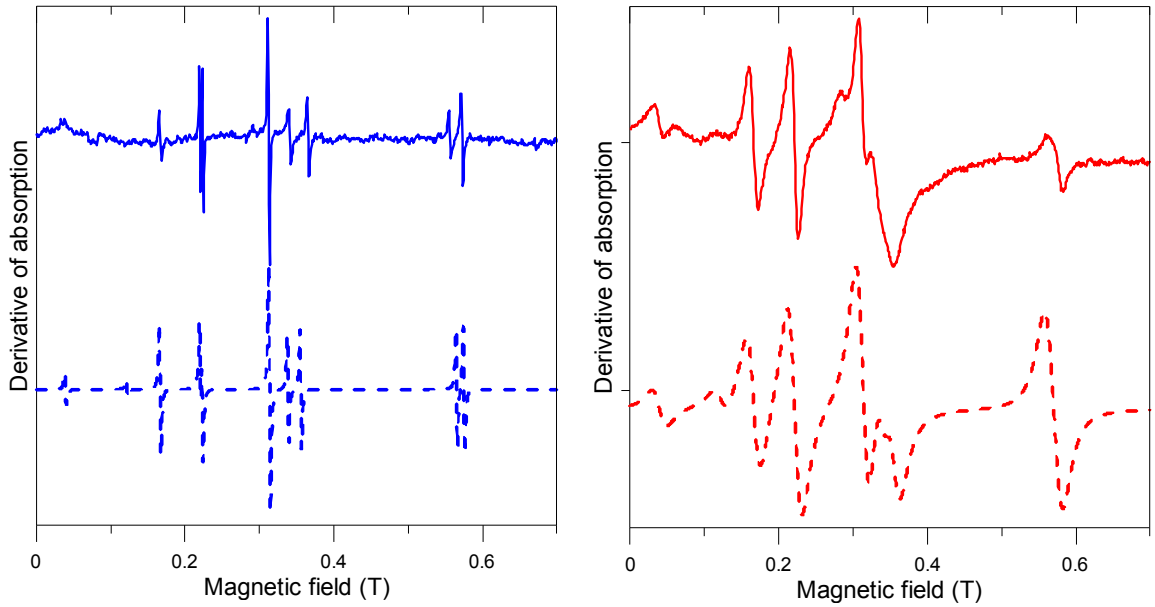

Figure 4.11 Normalized experimental room temperature EPR spectra, see curves a, b in Figure 4.6 (full lines) and corresponding computer-generated spectra (dashed lines). The linewidth ΔB, as deduced from the simulations, is 0.001 T for $x = 0.003$ (left) and 0.0097 T for $x = 0.042$ (right).

Table 4.1 Spin Hamiltonian parameters for Fe^{3+} ions in $GaBO_3$[*].

Parameter	This work		Lukin *et al.* [4.6], Seleznev [4.7]
	Set I	Set II	
D[**]	0.1032±0.0005		0.0989±0.0049
a[**]	0.0158±0.002	−0.0158±0.002	0.0146±0.002
F[**]	−0.0052±0.002	−0.0368±0.002	−0.0052±0.003
α, deg	24	36	24

[*] $g \approx 2.0023$

[**] in cm^{-1}.

4.3.2 General spin Hamiltonian: superposition model analysis

As far as both spin Hamiltonian parameter sets, see Table 4.1, result in one and the same spin Hamiltonian matrix, they can be considered as equivalent at least, from the mathematical viewpoint. Meanwhile, they may not necessarily be so from the physical viewpoint.

In order to elucidate this issue, we have tested the compatibility of both sets of parameters with the predictions of the Newman superposition model [4.8]. For this purpose, we have put forward a simulation code based on the general spin Hamiltonian for Fe^{3+} [4.1]:

$$\mathcal{H} = g\beta \boldsymbol{B}\cdot\boldsymbol{S} + \sum_{i=-2}^{2} B_2^i O_2^i + \sum_{i=-4}^{4} B_4^i O_4^i \tag{4.28}$$

where O_2^i and O_4^i are the extended Stevens operators of appropriate superscripts. The second- and fourth-order fine structure parameters of the spin Hamiltonians (4.28) and (4.27) are related to each other, respectively, as:

$$B_2^0 = \tfrac{1}{3}D \quad ; \quad B_2^2 = E \tag{4.29}$$

and

$$B_4^0 = \tfrac{1}{180}(F-a) \quad ; \quad B_4^3 = \mp\tfrac{\sqrt{2}}{9}a\sin 3\alpha \quad ; \quad B_4^{-3} = \tfrac{\sqrt{2}}{9}a\cos 3\alpha \tag{4.30}$$

In the framework of the Newman model, the B_l^i parameters are evaluated on the basis of a structural model of the paramagnetic site, as follows [4.8, 4.9]:

$$B_l^m = \sum_{j=1}^{n} b_l\left(r_j\right) K_l^m\left(\vartheta_j, \varphi_j\right) \tag{4.31}$$

In eq. (4.31) j enumerates the nearest neighbours of the paramagnetic ion (ligands) with spherical coordinates r_j, ϑ_j and φ_j, $b_l\left(r_j\right)$ are radial functions and $K_l^m\left(\vartheta_j, \varphi_j\right)$ are coordination factors proportional to tesseral harmonics with the corresponding l and m indices. The radial functions are expressed as power functions of the metal-to-ligand distances:

$$b_l\left(r_j\right) = \overline{b}_l \times \left(r_0 / r_j\right)^{t_l} \tag{4.32}$$

where the intrinsic parameters $\overline{b}_l$ and the power exponents t_l are considered as fitting parameters.

In applying eqs. (4.31) and (4.32), the iron ligand coordinates have been calculated with structural parameters for both $FeBO_3$ and $GaBO_3$, reported by Diehl [4.10] and Seleznev [4.7], respectively. Meanwhile, as far as results of determination of $\overline{b}_l$ and t_l obtained in both cases have been very close to each other, we have chosen to give all these results for ligand coordinates averaged between the $FeBO_3$ and $GaBO_3$ structures.

For Fe^{3+} in sixfold coordination, several second-rank intrinsic parameter values are quoted in the literature. For the reference distance $r_0 = 2.101$ Å (corresponding to the average Fe-O

distance in MgO [4.11]), most often $\overline{b}_2 = -0.412$ cm^{-1} is taken [4.11, 4.12]. Meanwhile, a positive $\overline{b}_2 = 0.412$ cm^{-1} value has been assumed by Acıkgöz *et al.* [4.13, 4.14]. The latter value has been adopted in the present case, as far as taking $\overline{b}_2 < 0$ would result in a negative D value, in disagreement with the experimental results. Figure 4.12 shows that for this choice the agreement between the experimental and theoretical D values is attained with the second-rank power exponent $t_2 = 8.7$, in reasonably good accord with the value $t_2 = 8$ usually quoted for Fe^{3+} in oxygen environment [4.11, 4.12]. The calculated E values are close to zero, in accordance with the experimental results.

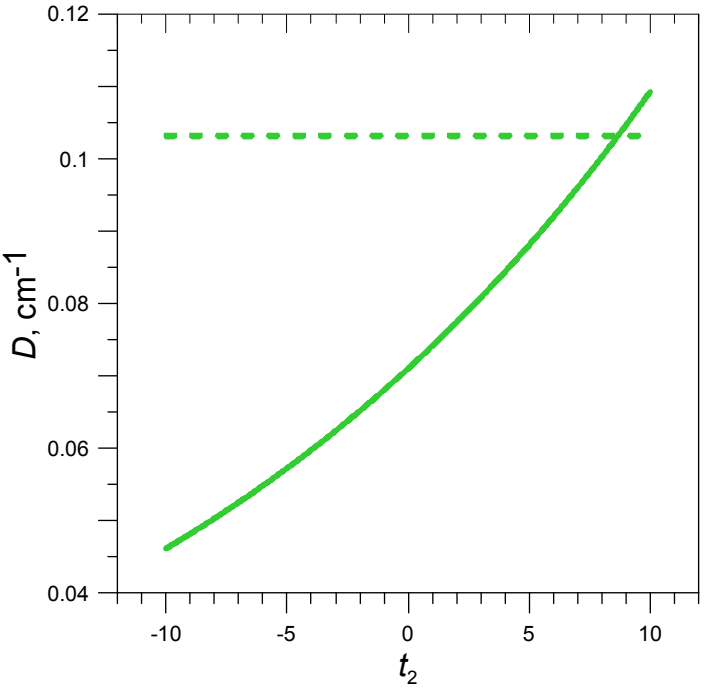

Figure 4.12 D values *vs.* the power exponent t_2. The dashed line is the D value determined from the experimental data, see Table 4.1.

As only few references to the fourth-rank intrinsic parameter values could be found in the literature [4.12, 4.15, 4.16], a large range of values has been tested for both $\overline{b}_4$ and t_4 parameters. No consistent results could be obtained with negative $\overline{b}_4$ values. Figure 4.13 shows the dependence of a and F on t_4 calculated for $\overline{b}_4 = 3.1 \cdot 10^{-5}$ cm^{-1}. (This value of $\overline{b}_4$ is in a reasonable agreement with the value $\overline{b}_4 = 2.45 \cdot 10^{-5}$ cm^{-1} for Fe^{3+} in calcite [4.12].) Obviously, within the framework of the Newman model the set I parameters cannot be fitted to in the whole range of t_4 values tested (Figure 4.13, top). In contrast, for the set II parameters, consistent results can be obtained with $t_4 \approx 5$ for a and $t_4 \approx 8$ for F (Figure 4.13, bottom).

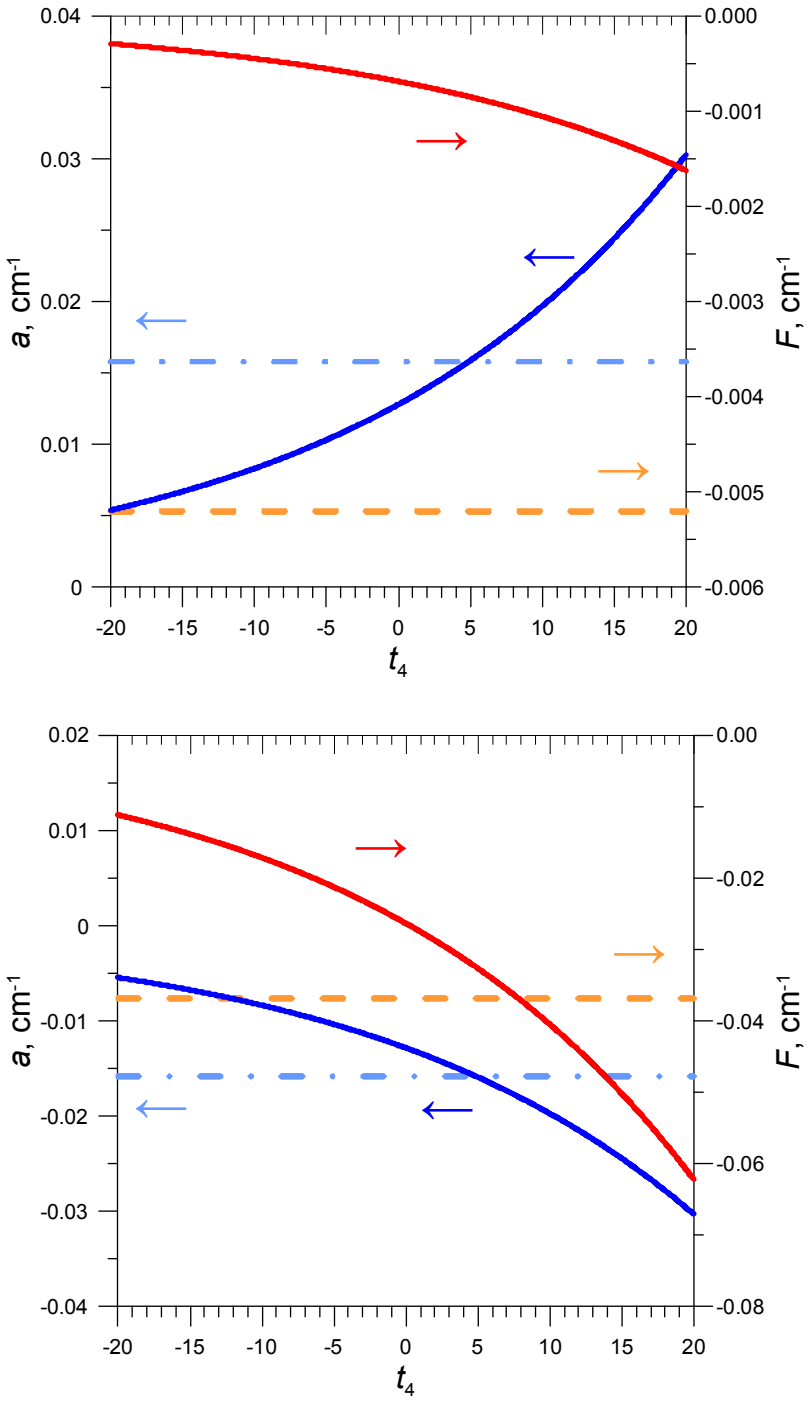

Figure 4.13 Dependences of a (continuous, blue) and F (continuous, red) on the power exponent t_4 for set I (top) and set II parameters (bottom). The experimental a and F values, see Table 4.1, are shown by the dash-dotted (light blue) and the dashed lines (orange), respectively.

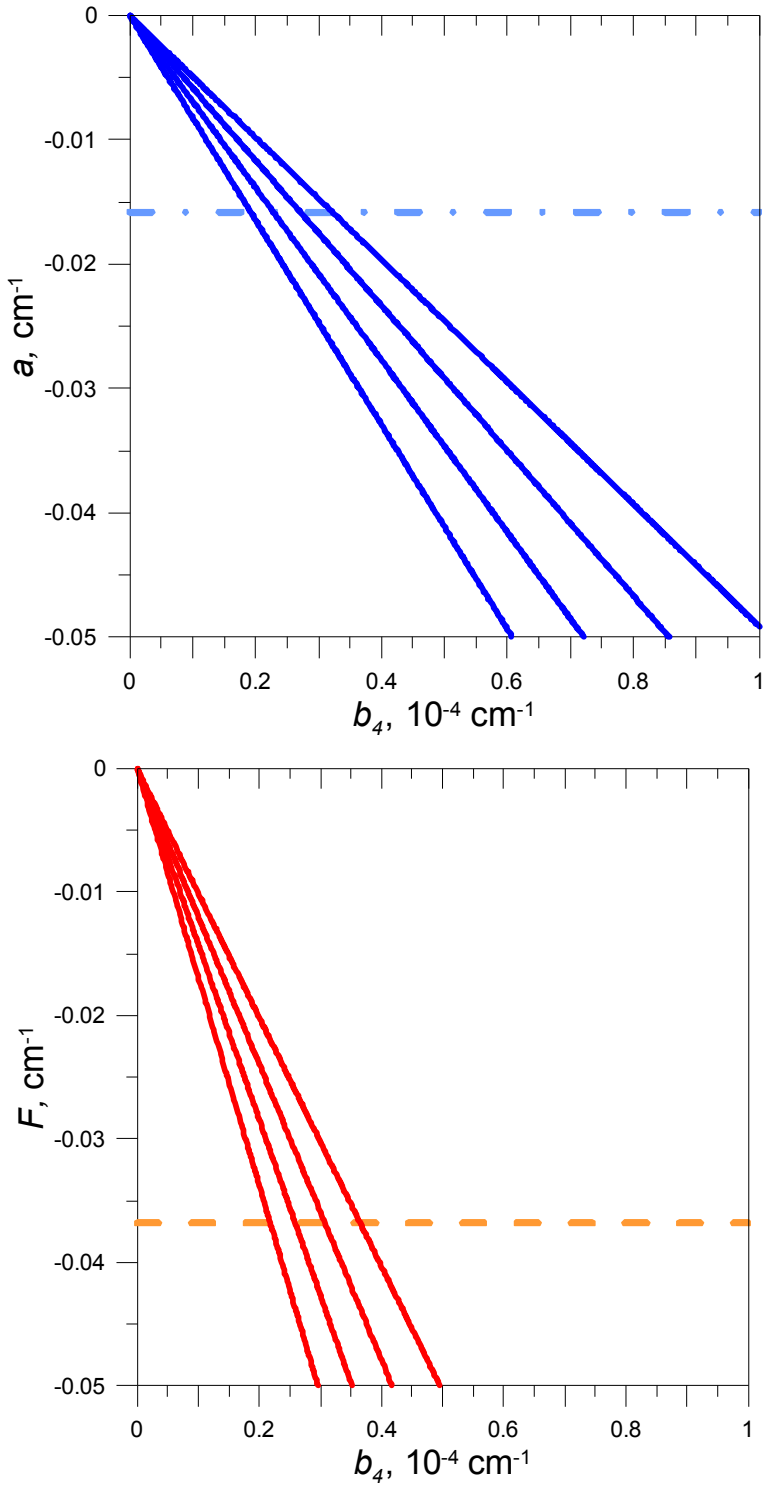

Figure 4.14 Dependences of a (top) and F (bottom) on the intrinsic parameter $\overline{b}_4$ for different t_4 values (4, 8, 12 and 16 from right to left, respectively) calculated with set II spin Hamiltonian parameters. The horizontal lines show the set II values of a (dash-dotted, light blue) and F (dashed, orange).

Figure 4.14 shows the dependences of a and F on the intrinsic parameter $\overline{b}_4$ for different t_4. Once again, the set II a and F parameters can be satisfactorily accounted for with close Newman model parameters; on the other hand, no agreement can be found for the set I parameters. One can conclude that the set I fourth-order fine structure parameters are totally incompatible with the predictions of the superposition model. In contrast, the set II parameters can be quite consistently accounted for by this model. Thus, the spin Hamiltonian of eq. (4.27) is seen to be ambiguous; therefore, its use should be avoided. On the other hand, the spin Hamiltonian of eq. (4.28) has no such drawback.

4.3.3 Tesseral spin Hamiltonian: local disorder

We return to the discrepancy in relative line intensities in experimental and computer-generated spectra, see Figure 4.10. This effect can be due to local disorder present in the crystals and resulting in statistical site-to-site distributions of the spin Hamiltonian parameters. As a consequence, a more or less pronounced broadening and concomitant amplitude decrease are observed for the lines with a stronger or weaker dependence of their resonance fields on these parameters. From the viewpoint of the magnetic resonance spectroscopist (both electronic and nuclear, *vide infra*) different degree of local disorder gives rise to more or less broad distributions of relevant spectroscopic parameters. Therefore, in most cases, the degree of disorder can be defined with respect to the ratio distribution width/mean value for the most representative parameters. Typically, low local disorder occurs in high quality crystals possessing low concentrations of structure defects while high local disorder is observed in non-crystalline, in particular glassy solids [4.17] as well as in crystals with highly flawed structure [4.18, 4.19]. In what follows, we shall refer to low and high degree of disorder in accordance with the above-mentioned criterion.

In order to provide a more quantitative estimate of line broadening in the experimental EPR spectra, we have assumed that all the ligand coordinates undergo random site-to-site distributions. As a result, the spin Hamiltonian parameters will also be distributed. However, the latter distribution cannot be analyzed in the framework of eq. (4.27) because of the fact that in this case the local symmetry is lower than trigonal one. Moreover, strictly speaking, neither can it be analyzed in the framework of eq. (4.28) because the spin Hamiltonian expressed by means of the extended Stevens operators do not possess sufficient symmetry [4.20]. In order to overcome this difficulty, we have used the general spin Hamiltonian expressed by means of two-vector tesseral spherical tensor operators $\mathcal{T}_{lm}^{l_B l_S}(\boldsymbol{n},\boldsymbol{S})$ [4.20]. Here $\boldsymbol{n}$ is the unit vector of the direction of $\boldsymbol{B}$, l_B and l_S are powers of $\boldsymbol{B}$ and of the spin operators, respectively.

The spin Hamiltonian form needed can be adapted from eq. (4) in the paper by Tennant *et al.* [4.21], see the review article by Kliava and Berger [4.9]:

$$\mathcal{H} = \sum_{l=2,4}\sum_{m=-l}^{l} \mathcal{B}_{lm}^{0l}\mathcal{T}_{lm}(\boldsymbol{S}) + g_e\beta B \sum_{l_S=1,3,5}\sum_{l=\begin{cases}l_S-1\\l_S+1\end{cases}}\sum_{m=-l}^{l} \mathcal{B}_{lm}^{1l_S}\mathcal{T}_{lm}^{1l_S}(\boldsymbol{n},\boldsymbol{S}) \tag{4.33}$$

Here the first and second terms in the right-hand side are, respectively, zero-field ($l_B = 0$) and *linear* Zeeman $l_B = 1$ spin Hamiltonians, and l must be even to preserve time-inversion invariance. The $\mathcal{B}_{lm}^{0l}$ parameters in this equation are proportional to the corresponding Stevens parameters B_l^m [4.20], and the procedure of calculating the $\mathcal{B}_{lm}^{1l_S}$ parameters is described in detail in the same work.

As far as $\mathcal{B}_{lm}^{l_B l_S}$ are components of rank l irreducible tensors [4.20, 4.21], they can be consistently expressed within the superposition model, as follows [4.9]:

$$\mathcal{B}_{lm}^{l_B l_S} = \sum_{j=1}^{n} \overline{b}_{lm}^{l_B l_S}\left(r_j\right) C_l^m\left(\vartheta_j,\varphi_j\right) \tag{4.34}$$

For simplicity, we assume that the radial functions in the latter equation depend only on l_B and l_S and have the radial dependence described in eq. (4.32). The tesseral coordination factors $C_l^m\left(\vartheta_j,\varphi_j\right)$ are given in Table 4.2.

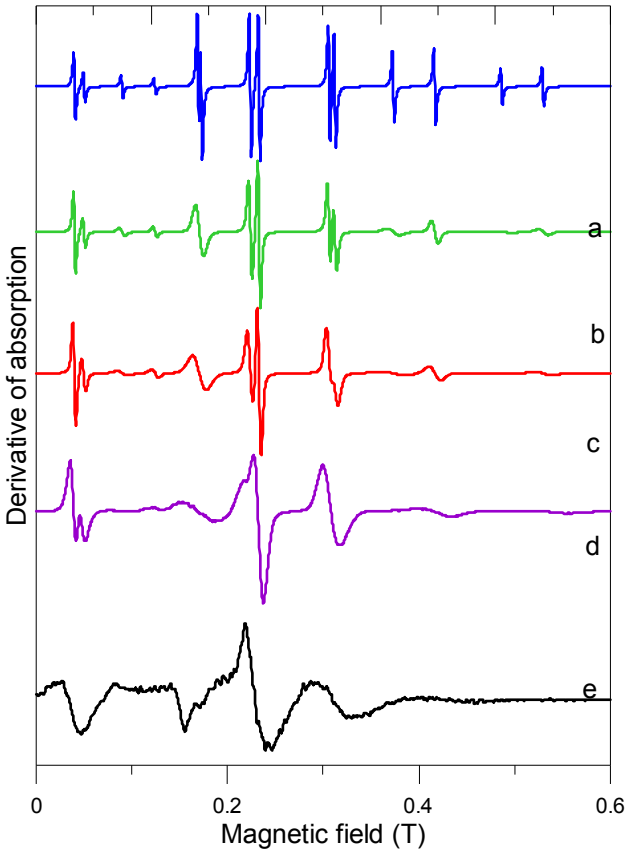

Figure 4.15 Normalized EPR spectra computed with $\sigma = 0$ (a), $\sigma = 0.0005$ (b), $\sigma = 0.001$ (c), $\sigma = 0.003$ (d) and $\sigma = 0.01$ (e) Å.

Table 4.2 Tesseral coordination factors used in eq. (4.34); x, y and z are the corresponding components of $\boldsymbol{n}$ (the unit vector of the direction of $\boldsymbol{B}$).

l	m	C_{lm}	l	m	C_{lm}
2	0	$\frac{\sqrt{6}}{2}(3z^2-1)$	6	0	$\frac{\sqrt{231}}{4}(231z^6-315z^4+105z^2-5)$
	1	$3\sqrt{2}zx$		1	$6\sqrt{11}(33z^4-30z^2+5)zx$
	−1	$3\sqrt{2}zy$		−1	$6\sqrt{11}(33z^4-30z^2+5)zy$
	2	$\frac{3}{\sqrt{2}}(x^2-y^2)$		2	$\frac{21\sqrt{110}}{8}(33z^4-18z^2+1)(x^2-y^2)$
	−2	$3\sqrt{2}xy$		−2	$\frac{21\sqrt{110}}{4}(33z^4-18z^2+1)xy$
4	0	$\frac{\sqrt{70}}{4}(35z^4-30z^2+3)$		3	$\frac{21\sqrt{110}}{4}(x^2-3y^2)(11z^2-3)zx$
	1	$5\sqrt{7}(7z^2-3)zx$		−3	$\frac{21\sqrt{110}}{4}(3x^2-y^2)(11z^2-3)zy$
	−1	$5\sqrt{7}(7z^2-3)zy$		4	$\frac{21\sqrt{33}}{4}(x^4-6x^2y^2+y^4)(11z^2-1)$
	2	$5\sqrt{\frac{7}{2}}(7z^2-1)(x^2-y^2)$		−4	$21\sqrt{33}(x^2-y^2)(11z^2-1)xy$
	−2	$5\sqrt{14}(7z^2-1)xy$		5	$\frac{231\sqrt{6}}{4}(x^4-10x^2y^2+5y^4)zx$
	3	$35(x^2-3y^2)zx$		−5	$\frac{231\sqrt{6}}{4}(5x^4-10x^2y^2+y^4)zy$
	−3	$35(3x^2-y^2)zy$		6	$\frac{231\sqrt{2}}{8}(x^4-14x^2y^2+5y^4)(x^2-y^2)$
	4	$\frac{35\sqrt{2}}{4}(x^4-6x^2y^2+y^4)$		−6	$\frac{21\sqrt{110}}{4}(x^2-3y^2)(11z^2-3)zx$
	−4	$35\sqrt{2}(x^2-y^2)xy$			

The approach described above has the advantage of automatically taking into account the symmetry lowering brought by fluctuations of the ligand coordinates. We have carried out simulations of the EPR spectra using a laboratory-developed computer code taking into account distributions of the ligand coordinates supposed to be Gaussian with standard deviation σ. The distributions have been generated using the Monte Carlo technique [4.22]; 10^5 computer-generated curves have been accumulated for each resulting spectrum. As one can see in Figure 4.15, this number is quite sufficient for producing smooth theoretical spectra; a considerable noise occurs only at the highest distribution width.

Figure 4.15 clearly shows the effect of the site-to-site distributions of ligand coordinates: with increasing local disorder (the σ value) the spectral features are broadened. Note that this broadening cannot be reproduced by a simple convolution with a certain linewidth, in which case, all features would broaden to more or less one and the same extent. In contrast, explicitly taking into account the parameter distribution, the broadening of the spectral features is determined by the dependence of the corresponding resonance field on the distributed spin Hamiltonian parameters. The latter approach yields a more realistic picture of the real physical situation; therefore, it much better accounts for amplitudes and widths of different resonance lines. In particular, curve b in Figure 4.15 showing the spectrum generated with $\sigma =$ 0.0005 Å, represents the best fit to the experimental EPR spectrum of $Fe_{0.003}Ga_{0.997}BO_3$ at 4 K, *vide supra*, Figure 4.10 (curves a and c). We have used the following superposition model parameters, see eq. (4.32):

$$\begin{gathered} \overline{b}_2 = 0.408\,\mathrm{cm}^{-1},\ t_2 = 8 \\ \overline{b}_4 = 3.1\cdot 10^{-5}\,\mathrm{cm}^{-1},\ t_4 = 5 \\ \text{and} \\ \overline{b}_5 = -4.0\cdot 10^{-6}\,\mathrm{cm}^{-1},\ t_5 = 7. \end{gathered} \tag{4.35}$$

The $\overline{b}_3$ parameters are very small and have not been taken into account.

More sophisticated models of local disorder are expected to further improve the quality of fitting to the experimental EPR spectra. In any case, detailed computer simulations of the experimental EPR spectra unambiguously demonstrate the presence of a certain degree of disorder in the environment of Fe^{3+} in gallium borate crystals.

4.4 Conclusions

The experimental EPR spectra of $Fe_xGa_{1-x}BO_3$ single crystals are typical of Fe^{3+} in the case where the Zeeman interaction is comparable with the second-order fine structure. The iron ions are located in trigonal symmetry sites and are surrounded by six oxygen atoms.

Detailed computer simulations of the EPR spectra have been carried out in order to determine the spin Hamiltonian parameters. First, we have put forward a simulation code based on the conventional spin Hamiltonian. It has allowed to obtain good fittings to the experimental spectra and to determine the sign of the fine structure parameter D.

Meanwhile, we have found that two different best-fit parameter sets are possible, respectively with positive and negative values of the fourth-order fine structure parameter a, both yielding one and the same spin Hamiltonian matrix. This dichotomy has been resolved through testing the consistency of both sets with the predictions of the Newman superposition model. For this purpose we have used the general spin Hamiltonian for trigonal symmetry. The tests have unambiguously shown that only one best-fit parameter set was compatible with the Newman model. Therefore, we highly recommend using the general spin Hamiltonian instead of the conventional spin Hamiltonian.

Applying the best-fit parameter set II, see Table 4.1, we have obtained good fits of the resonance lines positions. Nevertheless, a certain discrepancy in the amplitudes of different lines between the experimental and computer-generated spectra was obvious. To elucidate this issue, we have assumed the existence of local disorder in the crystals. Using the general spin Hamiltonian expressed through the tesseral spherical tensor operators allowed us to establish relations between the distributions of coordinates of the oxygen ligands, on the one hand, and of the spin Hamiltonian parameters, on the other hand. Computer simulations carried out with a code based on this model have yielded high-quality fittings to the experimental spectra, thus confirming our assumption of presence of local disorder in the crystals.

The superposition model parameters for Fe^{3+} ion determined by EPR will be further used in the analysis of the crystal field contribution to surface magnetocrystalline anisotropy, see Chapter 7, "Surface magnetocrystalline anisotropy of iron borate single crystals".

4.5 References

4.1 S.A. Al'tshuler and B.M. Kozyrev, *EPR in compounds of transition elements*, 2nd ed., Wiley, New York, Toronto, Jerusalem, London (1974) 512 pp.

4.2 A. Abragam and B. Bleaney, *Electron Paramagnetic resonance of transition ions*, Clarendon Press, Oxford (1970) 911 pp.

4.3 P.L. Hall, B.R. Angel and J.P.E. Jones, *Dependence of spin Hamiltonian parameters E and D on labeling of magnetic axes: Application to ESR of high-spin* Fe^{3+}, J. Magnetic Resonance **15** (1974) 64-68

4.4 G. Korn and T. Korn, *Mathematical handbook for scientists and engineers,* Dover Publications, Mineola, New York (2000) 1130 pp.

4.5 V. Lupei, A. Lupei and I. Ursu, *Spin Hamiltonian description of the ESR spectra of the* $^0S_{5/2}$ *ions of trigonal crystalline fields*, Rev. Roum. Phys. **18** (1968) 327-336

4.6 С.Н. Лукин, В.В. Руденко, В.Н. Селезнев и Г.А. Цинцадзе, *ЭПР ионов в гомологическом ряду боратов со структурой кальцита*, Физика Твердого Тела (1980) **22** 51-56

4.7 В.Н. Селезнев, *Магнитоупорядоченные бораты железа (физические свойства, применение, синтез)*, Диссертация, Симферопольский гос. университет (1988) 371 с.

4.8 D.J. Newman and W.Urban, *A new interpretation of the ground state splitting in* Gd^{3+}, J. Phys. C: Solid St. Phys **5** (1972) 3101-3109

4.9 J. Kliava and R. Berger, *Magnetic resonance spectroscopy of iron-doped glasses: From isolated ions to clusters and nanoparticles, Recent Res. Devel. Non Crystalline Solids* **3**, Transworld Research Network, Kerala (2003) pp. 41-84

4.10 R. Diehl, W. Jantz, B.I. Nolang and W. Wettling, *Growth and properties of iron borate,* $FeBO_3$*,* in*: Current Topics in Materials Science*, E. Kaldis ed., Elsevier, New-York, v. **11** (1984) pp. 241-387

4.11 E. Siegel and K.A. Muller, *Structure of transition-metal-oxygen-vacancy pair centers*, Phys. Rev. B **19** (1979) 109-120

4.12 D.J. Newman and E. Siegel, *Superposition model analysis of* Fe^{3+} *and* Mn^{2+} *spin-Hamiltonian parameters*, J. Phys. C: Solid St. Phys. **9** (1976) 4285-4292

4.13 M. Acıkgöz, P. Gnutek and C. Rudowicz, *The calculation of zero-field splitting parameters for* Fe^{3+} *ions doped in rutile* TiO_2 *crystal by superposition model analysis*, Chem. Phys. **402** (2012) 83-90

4.14 M. Acıkgöz, P. Gnutek and C. Rudowicz, *Modeling zero-field splitting parameters for dopant* Mn^{2+} *and* Fe^{3+} *ions in anatase* TiO_2 *crystal using superposition model analysis*, Chem. Phys. Let. **524** (2012) 49-55

4.15 T.H. Yeom, *Superposition model calculation of zero-field splitting of* Fe^{3+} *in* $LiTaO_3$ *crystal*, J. Phys.: Condens. Matter **13** (2001) 10471-10476

4.16 O. Rubio, S. Murrieta and S. Aguilar, *Superposition model analysis of the cubic spin-Hamiltonian parameters for* Mn^{2+} *and* Fe^{3+} *in the alkaline earth oxides, fluoroperovskite, and* II–VI *compounds*, J. Chem. Phys. **71** (1979) 4112-4122

4.17 J. Kliava, *EPR of impurity ions in disordered solids*, Phys. Stat. Sol. B **134** (1986) 411-455

4.18 J.-B. d'Espinose de Lacaillerie, C. Fretigny and D. Massiot, *MAS NMR spectra of quadrupolar nuclei in disordered solids: The Czjzek model*, J. Magn. Reson. (2008) **192** 244-251

4.19 A. Bals, S.I. Gorbachuk, J. Kliava and N.G.Kakazei, *EPR Study of the Structure of Disordered Polycrystals* Mn^{2+} *in Lithographic Stone*, Phys. Status Sol. (a) (1989) **114** 305-314

4.20 D.G. McGavin, W.C. Tennant and J.A. Weil, *High-spin Zeeman terms in the spin Hamiltonian*, J. Magn. Reson. **87** (1990) 92-109

4.21 W.C. Tennant, C.J. Walsby, R.F.C. Claridge and D.G. McGavin, *Rotation matrix elements and further decomposition functions of two-vector tesseral spherical tensor operators; their uses in electron paramagnetic resonance spectroscopy*, J. Phys.: Condens. Matter **12** (2000) 9481-9495

4.22 L. Devroye, *Non-Uniform Random Variate Generation*, Springer, New York, Berlin, Heidelberg, Tokyo (1986) 843 pp.

5. NMR studies of iron-gallium borates

5.1 Basic formalism

Nuclear magnetic resonance (NMR) was first observed in molecular beams by Isidor Rabi in 1938. In 1946, Felix Bloch and Edward Mills Purcell extended NMR to liquids and solids.

Individual neutrons and protons possess a nuclear spin $I = \frac{1}{2}$; certain atomic nuclei isotopes also have an overall spin of integer or semi-integer quantum number I. The angular momentum associated with nuclear spin is quantified by a quantum number having $2I+1$ values $m_I = -I, -I+1, \cdots, I$.

A non-zero I is associated with a magnetic moment

$$\boldsymbol{m}_{\mathrm{n}} = \gamma\hbar\boldsymbol{I} = g_{\mathrm{n}}\beta_{\mathrm{n}}\boldsymbol{I} \tag{5.1}$$

where

$$\gamma = g_{\mathrm{n}}\,\beta_{\mathrm{n}}/\hbar = \tfrac{1}{2}g_{\mathrm{n}}\,e/m_{\mathrm{p}} \tag{5.2}$$

is the gyromagnetic ratio, g_{n} is the nuclear g-factor and $\beta_{\mathrm{n}} = \frac{1}{2}e\hbar/m_{\mathrm{p}}$ is the nuclear magneton, e, m_{p} and $\hbar$ being, respectively, the elementary charge, proton mass and reduced Planck constant.

In an applied magnetizing field $\boldsymbol{B}$, $\boldsymbol{m}_{\mathrm{n}}$ has the energy

$$\mathcal{E} = -\boldsymbol{m}_{\mathrm{n}}\cdot\boldsymbol{B} = -\gamma\hbar B m_I = -g_{\mathrm{n}}\beta_{\mathrm{n}}B m_I\,. \tag{5.3}$$

The splitting of the nuclear spin state into nuclear Zeeman sublevels, described by eq. (5.3), is shown in Figure 5.1. It allows observing NMR spectra due to transitions between different sublevels induced by the magnetic component of the electromagnetic radiation. The resonance occurs when electromagnetic energy quantum $h\nu$ matches the energy difference between the Zeeman sublevels:

$$h\nu = \Delta\mathcal{E} = \gamma\hbar B\Delta m_I = g_{\mathrm{n}}\beta_{\mathrm{n}}B\Delta m_I\,. \tag{5.4}$$

In usual NMR conditions, only transitions between adjacent sublevels are allowed, resulting in the selection rule $\Delta m_I = \pm 1$; hence, the NMR condition on the energy quanta is:

$$h\nu = \Delta\mathcal{E} = \gamma\hbar B = g_{\mathrm{n}}\beta_{\mathrm{n}}B\,. \tag{5.5}$$

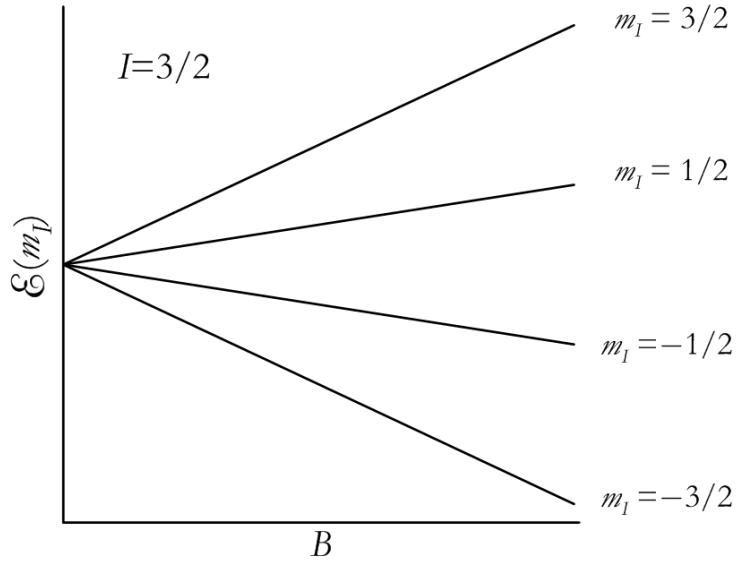

Figure 5.1 Zeeman sublevels for the nuclear spin $I = \frac{3}{2}$ in a magnetic field.

An assembly of non-interacting identical nuclei will resonate at the same frequency. Meanwhile, in the solid state, various a priori anisotropic interactions perturb the spin state energies and shift the resonance lines. Static disorder will therefore manifest itself in NMR spectra broadening. This makes the NMR spectroscopy a powerful research tool allowing to obtain detailed information on structure and physical properties of crystalline and non-crystalline, *e.g.*, glassy materials. In particular, solid-state NMR of quadrupolar nuclei (with $I > ½$) has become a helpful accurate technique of structural analysis [5.1].

In applying the solid state NMR spectroscopy, the major difficulty is spectra broadening mainly caused by static disorder, anisotropic chemical shielding, *vide infra*, but also by dipole-dipole interactions between different magnetic moments. A number of methods have been put forward in order to minimize the latter. In particular, the dipole-dipole broadening can be effectively removed by magic angle spinning (MAS), first described by Andrew, Bradbury, and Eades [5.2] in 1958 and independently by Lowe [5.3] in 1959. This technique consists in rotating the sample through the "magic" angle $\vartheta_m = \arccos\sqrt{⅓} \approx 54.74^\circ$ with respect to the field $\boldsymbol{B}$, see Figure 5.2. As far as the dipole-dipole interactions vary as $3\cos^2\vartheta - 1$, and the chemical shielding has anisotropic contributions with the same angular dependence, the former are averaged to zero, and the latter is averaged to its isotropic value.

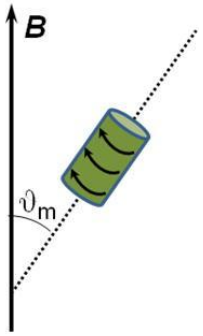

Figure 5.2 Magic-angle sample spinning.

Besides, in the solid-state NMR spectroscopy, it is essential to remove or, at least, minimize relaxation-induced line broadening. Two relaxation processes are effective: the spin-lattice (or

longitudinal) relaxation and the spin-spin (or transverse relaxation) with characteristic time constants T_1 and T_2, respectively. T_1 is a mean return time of an excited spin system to equilibrium with the thermal reservoir (solid lattice), and T_2 is a mean return time to equilibrium within the spin system itself. As a result of the difference in relaxation mechanisms involved, T_1 is usually longer than T_2; therefore, the spin-spin relaxation is the most important cause of broadening of the resonance.

In modern NMR spectroscopy, multiple pulse techniques are employed in order to reduce this broadening. In the experiment series described in this chapter, the Hahn two-pulse echo sequence has been used [5.4, 5.5]. The corresponding pulse sequence $90° - \tau - 180° - \tau - acquisition$, schematically illustrated in Figure 5.3, includes the following steps:

(i) All magnetic moments are in thermal equilibrium, aligned on the magnetizing field.

(ii) A 90° radiofrequency pulse turns the magnetization through the corresponding angle. The magnetic moments now are out of equilibrium. Because of inhomogeneity of the local magnetic field, dephasing of moments occurs, leading to a decay of magnetization.

(iii) Next, a 180° pulse is applied; the magnetization is inversed, so that the magnetic moments are refocused (the inhomogeneous dephasing is removed).

(iv) A return to equilibrium of the magnetic moments produces a free induction decay (FID), or "echo", containing useful information on the system. A subsequent Fourier transformation of this signal yields a narrowed frequency-swept NMR spectrum.

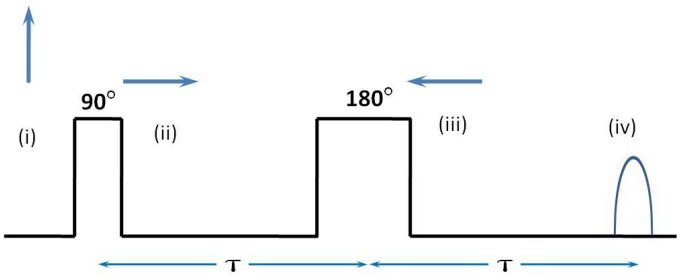

Figure 5.3 Scheme of the Hahn two-pulse echo sequence.

The MAS NMR of ^{11}B and ^{71}Ga has been used to study iron-doped gallium borates, $Fe_xGa_{1-x}BO_3$ ($x = 0$; 0.01; 0.02).

5.2 Spin Hamiltonian

The conditions of MAS NMR are determined by interactions between the nuclear spin and the magnetizing field (Zeeman coupling) as well as between the nuclear electric quadrupole moment and the electric field gradient (EFG) produced by the surrounding of the nucleus (quadrupole coupling) [5.6, 5.7]. The nuclear spin Hamiltonian can be expressed as follows [5.6]:

$$\mathcal{H} = \mathcal{H}_z + \mathcal{H}_{cs} + \mathcal{H}_Q$$

or (5.6)

$$\mathcal{H} = -\gamma\hbar \boldsymbol{I}\cdot\boldsymbol{B} - \gamma\hbar\delta_{iso}\boldsymbol{I}\cdot\boldsymbol{B} + \boldsymbol{I}\cdot\boldsymbol{V}\cdot\boldsymbol{I}$$

where the first two terms account for the Zeeman coupling, the second term describing the chemical shift, isotropic in the MAS conditions, and the third term corresponds to the quadrupole coupling.

The EFG is proportional to a second rank tensor $\boldsymbol{V}$ with principal components V_x, V_y and V_z subjected to the restriction [5.6]

$$V_x + V_y + V_z = 0. \tag{5.7}$$

Therefore, similarly to the case of the D-tensor in EPR, *cf.* Chapter 4, "EPR of iron-gallium borate single crystals with low *x*", to fully describe this tensor we need only two parameters: in the actual case, V_z and

$$\eta = \frac{V_x - V_y}{V_z}. \tag{5.8}$$

Here η, called asymmetry parameter, is confined in the range $0 \leqslant \eta \leqslant 1$ with the convention $|V_z| \geqslant |V_y| \geqslant |V_x|$ *cf. infra.* The parameter V_z is proportional to the coupling constant C_Q between the nuclear electric quadrupole moment and the EFG [5.7, 5.8].

The quadrupole coupling is usually small with respect to the Zeeman coupling; therefore, its contribution to the nuclear Zeeman sublevel energies can be deduced through a perturbation calculation. In the first order, it has an effect only on non-central NMR transitions $\pm\frac{1}{2} \leftrightarrow \pm\frac{3}{2}$ and $\pm\frac{3}{2} \leftrightarrow \pm\frac{5}{2}$ [5.7]. Consequently, the central transition $\pm\frac{1}{2} \leftrightarrow \mp\frac{1}{2}$ yields much narrower and therefore much more conspicuous NMR spectra. The MAS has no "magic" properties on the second-order quadrupole coupling, therefore the latter is not averaged. Thus, in the MAS experiments on powdered samples only the central transition is usually observed [5.7].

5.3 Computer treatment of the MAS NMR spectra

Extracting meaningful physical information from the experimental MAS NMR spectra requires detailed computer fitting.

In order to simulate the experimental spectra, first of all, we need an expression of the resonance frequency ν_r. For the central transition, the expression of ν_r as a function of the spin Hamiltonian parameters and the polar angle ϑ with respect to the C_3 axis and the azimuthal angle φ with respect to the C_2 axis, is [5.9, 5.10]:

$$\nu_r = \nu_L\left(1+\delta_{iso}\right) - \tfrac{1}{6}\frac{\nu_Q^{\,2}}{\nu_L}\left[I\left(I+1\right)-\tfrac{3}{4}\right]\left[\tfrac{1}{5}\left(1+\tfrac{1}{3}\eta^2\right)+A\cos^4\vartheta+B\cos^2\vartheta+C\right] \qquad (5.9)$$

where ν_L is the Larmor frequency,

$$\nu_Q = \tfrac{3}{2}\frac{C_Q}{I\left(2I-1\right)} \qquad (5.10)$$

is the quadrupole frequency, and A, B and C are functions of the parameter η and the angle φ [5.9, 5.10]:

$$\begin{aligned} A &= \tfrac{21}{16} - \tfrac{7}{8}\eta\cos 2\varphi + \tfrac{7}{48}\eta^2\cos^2 2\varphi \\ B &= -\tfrac{9}{8} + \tfrac{1}{12}\eta^2 + \eta\cos 2\varphi - \tfrac{7}{24}\eta^2\cos^2 2\varphi \\ C &= \tfrac{9}{80} - \tfrac{1}{15}\eta^2 - \tfrac{1}{8}\eta\cos 2\varphi + \tfrac{7}{48}\eta^2\cos^2 2\varphi. \end{aligned} \qquad (5.11)$$

It should be noted that erroneous expressions of A, B and C are quoted in a number of bibliographical sources, *e.g.*, in the review paper by Freude [5.7].

Tentative simulations of the experimental spectra have allowed estimating chemical shifts and quadrupole parameters; however, relative amplitudes and widths of the spectra features could not be satisfactorily reproduced. Besides, our challenge was to account for the observed broadening of the experimental spectra with increasing iron concentration. Therefore, we have been bound to assume the existence of a certain local disorder in the environment of the paramagnetic nuclei.

5.3.1 Local disorder

In disordered solids, the spin Hamiltonian parameters are expected to be statistically distributed, *cf.* Chapter 4, "EPR of iron-gallium borate single crystals with low *x*". The existence of disorder in the environment of paramagnetic nuclei manifests itself in broadening of the NMR spectra. As a consequence, relative amplitudes and widths of spectra features can be satisfactorily reproduced in the simulations only if local disorder is explicitly taken into account in the simulation code, allowing for statistical distributions of the NMR parameters, in particular of the quadrupole parameters.

This issue was first raised by Czjzek in the framework of a random-packing model of amorphous materials [5.11, 5.12]. As far as the quadrupole parameters are related to components of the EFG tensor, Czjzek *et al.* suggested a joint distribution density (JDD) of these parameters. Later, Le Caër *et al.* [5.13] have provided a more general justification of the Czjzek's JDD; indeed, they have shown that it holds if all components of the EFG tensor (in NMR) or of the quadrupole fine structure tensor (in EPR) tensor are subjected to normal (Gaussian) random distributions. The Czjzek's JDD has been extensively used in both NMR and EPR studies of amorphous materials [5.14-5.16] and also applied to simulate the NMR spectra of some disordered crystals [5.17]. Yet, the major drawback of this JDD is to completely disregard symmetry and local structure persisting to a certain extent in only partially disordered crystals.

With the aim of describing a randomly distorted structure preserving, to a certain extent, local ordering, a more elaborated JDD of the quadrupole parameters has been suggested by Maurer [5.18] and Le Caër and Brand [5.13]. For brevity, we refer to this JDD as the Maurer's one, although Le Caër and Brand have provided a more detailed theoretical analysis of this model. Interestingly, a similar model has been put forward to describe the JDD of nanoparticle size and shape distribution [5.19].

Below we evaluate the applicability of the Czjzek's and Maurer's JDDs to NMR studies of only slightly disordered crystals.

5.3.2 Czjzek's distribution

In a disordered solid, all components of $\boldsymbol{V}$ are expected to be statistically distributed. In order to satisfy the requirements of diagonal symmetry and tracelessness, as well as of rotational invariance, these components are calculated as linear combinations of five normally distributed random quantities U_i, $i=1,\ldots,5$, with zero mean values and equal standard deviations $\frac{1}{2}\sigma$ [5.11, 5.13, 5.20]. (Here the $\frac{1}{2}$ factor has been introduced in order that the subsequent formulae could be expressed in their habitual form [5.11-5.13, 5.18, 5.20].) Thus, we get:

$$\boldsymbol{V}=\sqrt{3}\begin{pmatrix} -\frac{1}{\sqrt{3}}U_1+U_5 & U_4 & U_2 \\ U_4 & -\frac{1}{\sqrt{3}}U_1-U_5 & U_3 \\ U_2 & U_3 & \frac{2}{\sqrt{3}}U_1 \end{pmatrix}. \tag{5.12}$$

Note that with this definition σ represents the standard deviation of $V_{\tilde{z}}$, the principle $\tilde{z}$-component of $\boldsymbol{V}$.

With these assumptions, the Czjzek's JDD takes the form [5.11, 5.13]:

$$P\left(V_{\tilde{z}},\eta\right)=\frac{1}{\sqrt{2\pi}}\frac{V_{\tilde{z}}^{4}}{\sigma^{5}}\eta\left(1-\tfrac{1}{9}\eta^{2}\right)\mathrm{e}^{-\frac{1}{2}\frac{V_{\tilde{z}}^{2}}{\sigma^{2}}\left(1+\frac{1}{3}\eta^{2}\right)} \tag{5.13}$$

with marginal distributions for $-\infty<V_{\tilde{z}}<\infty$ and $0\leqslant\eta\leqslant 1$, respectively:

$$P_{\mathrm{m}}\left(V_{zz}\right)=\sqrt{\frac{2}{\pi}}\frac{1}{\sigma}\left[\left(\frac{3}{2}\frac{V_{zz}^{2}}{\sigma^{2}}-1\right)\mathrm{e}^{-\frac{1}{2}\frac{V_{zz}^{2}}{\sigma^{2}}}-\left(\frac{4}{3}\frac{V_{zz}^{2}}{\sigma^{2}}-1\right)\mathrm{e}^{-\frac{2}{3}\frac{V_{zz}^{2}}{\sigma^{2}}}\right];$$
$$P_{\mathrm{m}}\left(\eta\right)=3\eta\frac{1-\frac{1}{9}\eta^{2}}{\left(1+\frac{1}{3}\eta^{2}\right)^{5/2}}. \tag{5.14}$$

Alternatively, instead of V_{zz} and η the following parameters can be introduced:

$$\Delta=\left|V_{zz}\right|\sqrt{1+\tfrac{1}{3}\eta^{2}} \tag{5.15}$$

and

$$\psi=\begin{cases}\frac{1}{6}\pi-\arctan\frac{1}{\sqrt{3}}\eta & \text{for } V_{zz}>0\\ -\frac{1}{6}\pi+\arctan\frac{1}{\sqrt{3}}\eta & \text{for } V_{zz}<0\end{cases}. \tag{5.16}$$

For the corresponding form of the Czjzek's JDD one gets [5.12]:

$$P\left(\Delta,\psi\right)=\frac{1}{\sqrt{2\pi}}\frac{\Delta^{4}}{\sigma^{5}}\cos 3\psi\,\mathrm{e}^{-\frac{1}{2}\frac{\Delta^{2}}{\sigma^{2}}} \tag{5.17}$$

with the marginal distributions, for $0\leqslant\Delta<\infty$ and $-\frac{\pi}{6}\leqslant\psi\leqslant\frac{\pi}{6}$, respectively:

$$P_{\mathrm{m}}\left(\Delta\right)=\tfrac{1}{3}\sqrt{\frac{2}{\pi}}\frac{\Delta^{4}}{\sigma^{5}}\mathrm{e}^{-\frac{1}{2}\frac{\Delta^{2}}{\sigma^{2}}};\ P_{\mathrm{m}}\left(\psi\right)=\tfrac{3}{2}\cos 3\psi\,. \tag{5.18}$$

The major drawback of the Czjzek's distribution is that it completely disregards symmetry and local structure existing in the perfect crystal. Not surprisingly, this distribution yields good simulation results when describing magnetic resonance spectra of amorphous and heavily disordered materials.

5.3.3 Numerical Maurer's distribution

In the Maurer's and Le Caër's *et al.* approach [5.13, 5.18, 5.20], the EFG tensor is represented as a sum of two tensors, $\boldsymbol{V}_0+\boldsymbol{V}$ where $\boldsymbol{V}$ is the random tensor defined above, and $\boldsymbol{V}_0$ is a fixed traceless tensor describing a "perfect crystal" and characterized by parameters V_{z0} and η_0. In the coordinate frame where $\boldsymbol{V}_0$ is diagonal,

$$\boldsymbol{V}_0=V_{z0}\begin{pmatrix}\frac{1}{2}\left(\eta_0-1\right) & 0 & 0\\ 0 & -\frac{1}{2}\left(\eta_0+1\right) & 0\\ 0 & 0 & 1\end{pmatrix} \tag{5.19}$$

where

$$\eta_0=\frac{V_{x0}-V_{y0}}{V_{z0}}. \tag{5.20}$$

The parameters Δ_0 and ψ_0 are introduced by means of eqs. (5.15) and (5.16), respectively, replacing in the latter V_z by V_{z0} and η by η_0.

(Note that in the Maurer's approach all components of the $\boldsymbol{V}$-tensor are assumed to be normally distributed with zero mean values and equal standard deviations [5.18]. However, such an assumption does not satisfy the above-mentioned requirements for this tensor.)

We have put forward a simulation code implementing the above model. This code

(i) generates the normal random quantities U_i, $i=1,\ldots,5$, *vide supra*;

(ii) using eqs. (5.12) and (5.19) computes and diagonalizes the $\boldsymbol{V}_0+\boldsymbol{V}$-tensor;

(iii) for each set of main values of the latter, respecting the above-mentioned convention $|V_z|\geqslant|V_y|\geqslant|V_x|$ and using eqs.(5.8), (5.15) and (5.16) calculates Δ and ψ;

(iv) builds marginal distribution densities of Δ and ψ as well as the JDD $P(\Delta,\psi)$ for the $\boldsymbol{V}_0+\boldsymbol{V}$-tensor;

(v) computes the mean values $\langle\Delta\rangle,\langle\psi\rangle$, the standard deviations $\sigma_\Delta,\sigma_\psi$ and the correlation coefficient ρ of Δ and ψ.

Figures 5.4 to 5.6 illustrate variations of the latter parameters with σ for different Δ_0 and ψ_0.

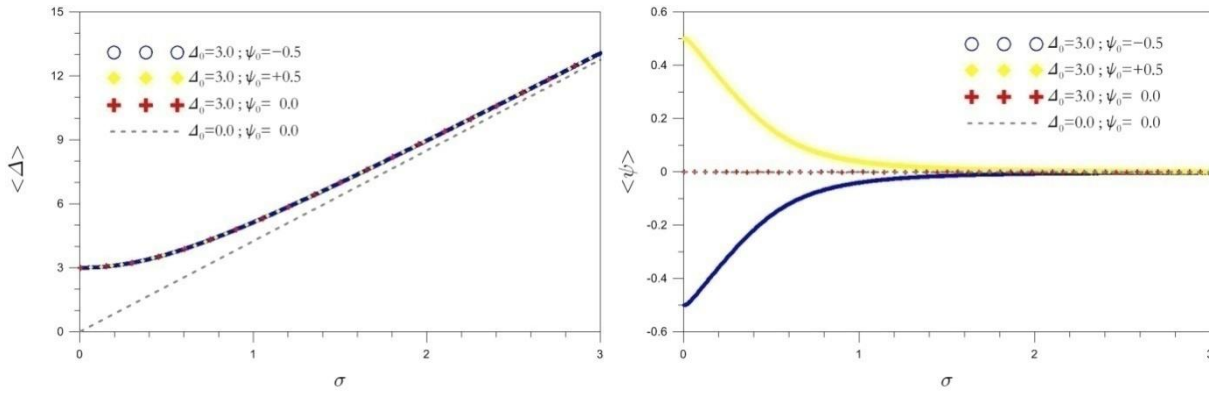

Figure 5.4 Dependences on σ of $\langle\Delta\rangle$ (left) and $\langle\psi\rangle$ (right) for different Δ_0 and ψ_0. The dashed line in the left part of the figure corresponds to eq. (5.21). Δ_0, σ and $\langle\Delta\rangle$ are in arbitrary units (a.u.).

The graph of $\langle\Delta\rangle$ *vs.* σ is shown in Figure 5.4 (left). For $\Delta_0=0$ (this corresponds to the Czjzek's JDD; obviously, in this case $\psi_0=0$ as well) the increase of $\langle\Delta\rangle$ with an increase of σ is strictly linear, corresponding to the relationship obtained using the marginal distribution $P_{\mathrm{m}}(\Delta)$, see eq. (5.18):

$$\langle \Delta \rangle = \tfrac{16}{3}\sqrt{\tfrac{2}{\pi}}\sigma \approx 4.2554\sigma \,. \tag{5.21}$$

For $\Delta_0 \neq 0$ and different values of ψ_0, $\langle \Delta \rangle$ tends to Δ_0 when σ tends to 0, and for $\sigma \gg \Delta_0$ asymptotically reaches the trend given by eq. (5.21).

From Figure 5.4 (right) one can see that $\langle \psi \rangle$ tends to ψ_0 when σ tends to 0 and tends to zero for $\sigma \gg \Delta_0$. If $\psi_0 = 0$, $\langle \psi \rangle$ is always zero, including the case $\Delta_0 = 0$, corresponding to the Czjzek's JDD.

With an increase of σ, both σ_Δ and σ_ψ increase, see Figure 5.5. For $\Delta_0 = 0$ (the Czjzek's JDD) one can readily show that

$$\sigma_\Delta = \tfrac{2}{3}\sqrt{45 - \tfrac{128}{\pi}}\,\sigma \approx 1.3754\sigma \,. \tag{5.22}$$

For $\Delta_0 \neq 0$ the relationship between σ_Δ and σ becomes non-linear, and the trend given by eq. (5.22) is reached asymptotically for $\sigma \gg \Delta_0$. In the latter case, as shown in Figure 5.5 (right), σ_ψ tends to its limiting value, corresponding to that of the Czjzek's JDD. Using the marginal distribution $P_{\mathrm{m}}(\psi)$, see eq. (5.18), one gets:

$$\lim_{\sigma\to\infty} \sigma_\psi = \tfrac{1}{6}\sqrt{\pi^2 - 8} \approx 0.2279 \,. \tag{5.23}$$

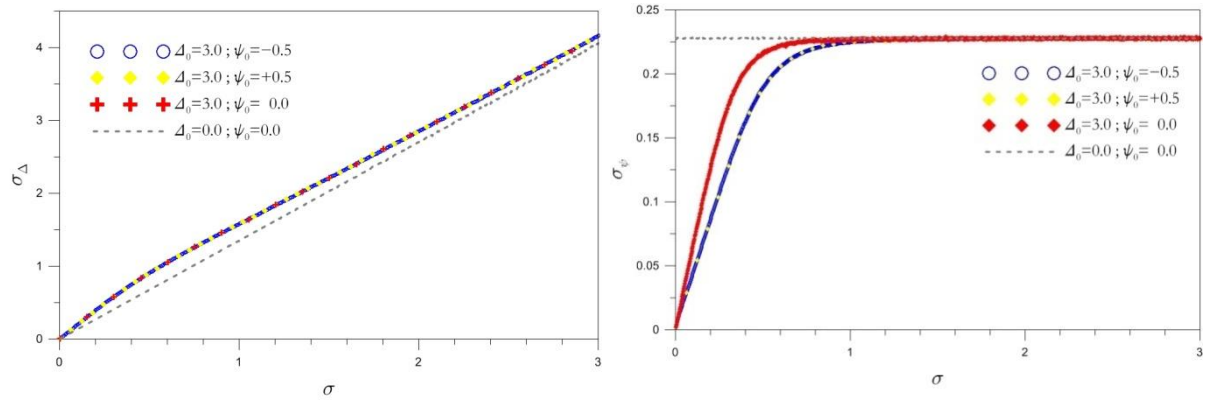

Figure 5.5 Dependences on σ of σ_Δ (left) and σ_ψ (right) for different Δ_0 and ψ_0. The dashed lines in the left and right parts correspond to eqs. (5.22) and (5.23), respectively. Δ_0, σ and σ_Δ are in arbitrary units (a.u.).

Figure 5 in the Maurer's paper suggests that the correlation between Δ and ψ tends to decrease with increasing departure from axial symmetry (*i.e.*, increasing η_0) and with lowering the degree of disorder (*viz.*, increasing the Δ_0/σ ratio) [5.18]. However, Figure 5.6 below shows that this is only a part of a more general trend: indeed, ρ vanishes for any degree of disorder if $\psi_0 = 0$ (*i.e.*, at maximal rhombic distortion) as well as in the limits of both low and high disorder.

The absolute value of ρ attains a maximal value of *ca.* 0.21 for $\psi_0 = \pm\pi/6$ (*i.e.*, for axial symmetry) at intermediate disorder. The corresponding value of σ, σ_{max} is proportional to Δ_0; numerical calculations result in the following relationship between these parameters:

$$\sigma_{max} \approx 0.16\Delta_0 . \tag{5.24}$$

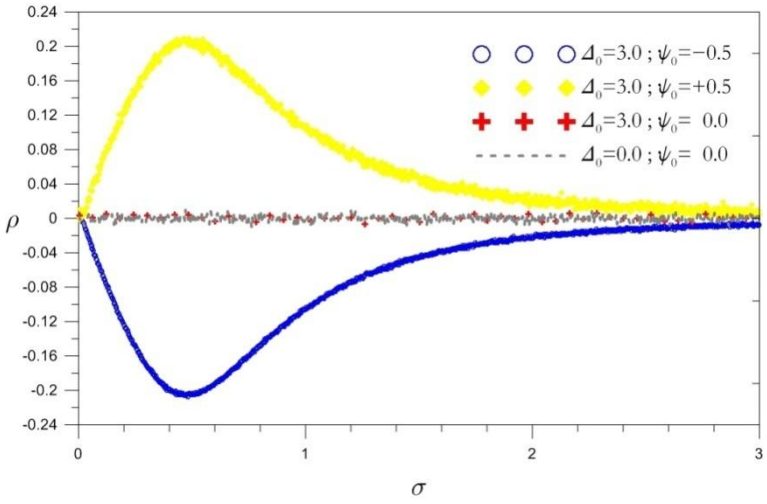

Figure 5.6 Relationships between ρ and σ for different Δ_0 (in a.u.) and ψ_0.

5.3.4 Analytical Maurer's distribution

Besides, Maurer [5.18] has introduced an empirical analytical JDD by associating the marginal distribution of $\delta = \Delta/\sigma$, derived from a non-central χ^2 distribution with five degrees of freedom, with a semi-heuristic marginal distribution of ψ and allowing for a certain correlation between both random variables. Here we prefer using σ_Δ instead of σ; indeed, such a choice seems more appropriate for a bivariate JDD $P(\Delta,\psi)$. After amending for a clerical error, this JDD becomes:

$$P(\Delta,\psi) \propto \frac{\Delta}{\sigma_\Delta} g(x) \cos 3\psi \, \mathrm{e}^{-\frac{1}{2}\frac{1}{1-\rho^2}\left[\frac{(\Delta-\Delta_0)^2}{{\sigma_\Delta}^2}+\frac{(\psi-\psi_0)^2}{{\sigma_\psi}^2}-2\rho\frac{(\Delta-\Delta_0)(\psi-\psi_0)}{\sigma_\Delta\sigma_\psi}\right]} \tag{5.25}$$

where

$$g(x) = x - 1 + (x+1)e^{-2x} \text{ and } x = \frac{\Delta\Delta_0}{{\sigma_\Delta}^2} . \tag{5.26}$$

Of course, the use of an analytical JDD considerably simplifies the analysis of the experimental results; yet, the limits of its applicability should be carefully evaluated. With this aim in view we have examined relations between the "input" parameters Δ_0, ψ_0 and ρ occurring in eq. (5.25) and the corresponding "output" parameters Δ_0^{cal}, ψ_0^{cal} and ρ^{cal}, *i.e.*, the characteristics of

$P(\Delta,\psi)$, calculated for different Δ_0/σ_Δ ratios. As far as σ and σ_ψ are interrelated, the values of the latter parameter have been taken in accordance with the relationships shown in Figure 5.5. The values of ρ have been chosen from the data displayed in Figure 5.6.

Figures 5.7 and 5.8 show the results of this analysis.

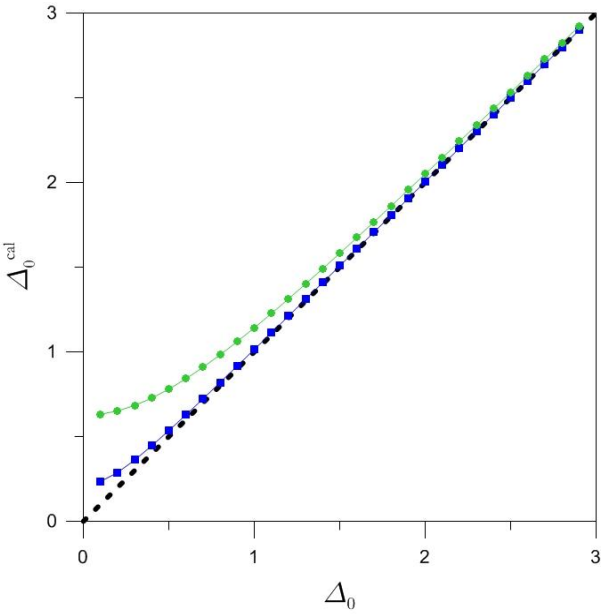

Figure 5.7 Relationships between Δ_0 and Δ_0^{cal} for $\psi_0 = 0.5$; $\sigma_\Delta = 0.102$ a.u., $\sigma_\psi = 0.024$, $\rho = 0.033$ (squares, blue) and $\sigma_\Delta = 0.303$ a.u., $\sigma_\psi = 0.066$, $\rho = 0.097$ (circles, green). The dashed line corresponds to $\Delta_0^{cal} = \Delta_0$.

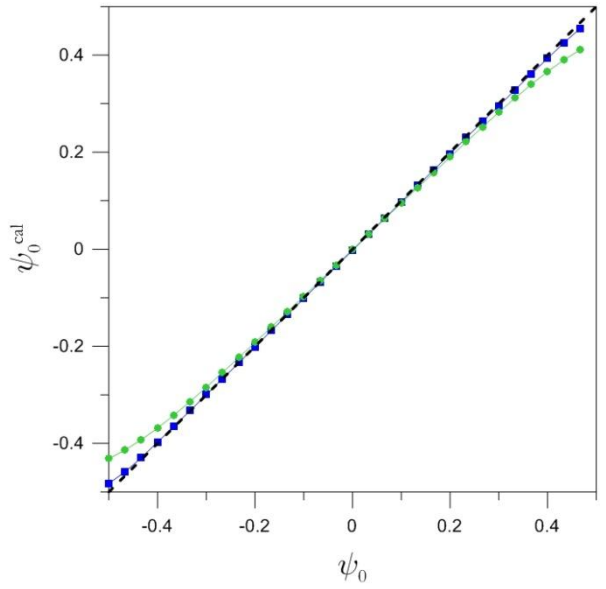

Figure 5.8 Relationships between ψ_0 and ψ_0^{cal} for $\Delta_0 = 3.0$ a.u.; $\sigma_\Delta = 0.102$ a.u., $\sigma_\psi = 0.024$, $\rho = 0.033$ (squares, blue) and $\sigma_\Delta = 0.303$ a.u., $\sigma_\psi = 0.066$, $\rho = 0.097$ (circles, green). The dashed line corresponds to $\psi_0^{cal} = \psi_0$.

As one can see, for relatively low disorder, $\Delta_0/\sigma_\Delta \approx 30$, the "input" and "output" parameters are in good agreement; however, at higher disorder, *i.e.*, already at $\Delta_0/\sigma_\Delta \approx 10$ these parameters considerably differ from each other. In Figures 5.7 and 5.8 we show the results for $\psi_0 = 0.5$ as far as in the low disorder case those for $\psi_0 = 0$ and $\psi_0 = -0.5$ are almost the same. For higher disorder, the results for $\psi_0 = \pm 0.5$ are still very close to each other and for $\psi_0 = 0$ the discrepancy between the "input" and "output" parameters becomes even more pronounced, but in any case we are outside the limits of applicability of the analytical Maurer's JDD.

One can conclude that the analytical Maurer's JDD satisfactorily accounts for local disorder only at low local disorder.

The Maurer's JDD, eq. (5.25) has relatively simple form; meanwhile, its disadvantage is not to include "physical" parameters featuring in the spin Hamiltonian, eq. (5.6). Therefore, we have developed an alternative form of the Maurer's JDD in the variables $V_{\tilde{z}}$ and η which is much more complicate:

$$P\left(V_{\tilde{z}},\eta\right) = \frac{\left(1-\frac{1}{9}\eta^2\right)}{\left(1+\frac{1}{3}\eta^2\right)^{\frac{3}{2}}}\frac{V_{\tilde{z}}\eta}{\sigma_\Delta}\, g_{V_{\tilde{z}}\eta}\, \mathrm{e}^{-\frac{1}{2}\frac{1}{1-\rho^2}\left[\frac{\left(V_{\tilde{z}}\sqrt{1+\frac{1}{3}\eta^2}-V_{\tilde{z}0}\sqrt{1+\frac{1}{3}\eta_0^2}\right)^2}{\sigma_\Delta^2}+\frac{\left(\arctan\frac{\eta}{\sqrt{3}}-\arctan\frac{\eta_0}{\sqrt{3}}\right)^2}{\sigma_\psi^2}+2\rho\frac{\left(V_{\tilde{z}}\sqrt{1+\frac{1}{3}\eta^2}-V_{\tilde{z}0}\sqrt{1+\frac{1}{3}\eta_0^2}\right)\left(\arctan\frac{\eta}{\sqrt{3}}-\arctan\frac{\eta_0}{\sqrt{3}}\right)}{\sigma_\psi\sigma_\Delta}\right]} \tag{5.27}$$

where

$$g_{V_{\tilde{z}}\eta} = \frac{V_{\tilde{z}}\sqrt{1+\frac{1}{3}\eta^2}\, V_{\tilde{z}0}\sqrt{1+\frac{1}{3}\eta_0^2}}{\sigma_\Delta^2} - 1 + \left(\frac{V_{\tilde{z}}\sqrt{1+\frac{1}{3}\eta^2}\, V_{\tilde{z}0}\sqrt{1+\frac{1}{3}\eta_0^2}}{\sigma_\Delta^2}+1\right)\mathrm{e}^{-2\frac{V_{\tilde{z}}\sqrt{1+\frac{1}{3}\eta^2}\, V_{\tilde{z}0}\sqrt{1+\frac{1}{3}\eta_0^2}}{\sigma_\Delta^2}}$$

and

$$\sigma_\Delta = \frac{1}{3}\frac{\sigma_{V_{\tilde{z}}}\sigma_\eta}{\sqrt{1+\frac{1}{3}\eta_0^2}}\sqrt{\frac{V_{\tilde{z}0}^2\eta_0^2}{\sigma_{V_{\tilde{z}}}^2}+9\frac{\left(1+\frac{1}{3}\eta_0^2\right)^2}{\sigma_\eta^2}+6\rho_{V_{\tilde{z}}\eta}V_{\tilde{z}0}\eta_0\frac{1+\frac{1}{3}\eta_0^2}{\sigma_{V_{\tilde{z}}}\sigma_\eta}}$$

$$\sigma_\psi = \frac{1}{\sqrt{3}}\frac{\sigma_\eta}{\sqrt{1+\frac{1}{3}\eta_0^2}} \tag{5.28}$$

$$\rho = \frac{\frac{V_{\tilde{z}0}\eta_0}{\sigma_{V_{\tilde{z}}}}+\frac{3\rho_{V_{\tilde{z}}\eta}}{\sigma_\eta}\left(1+\frac{1}{3}\eta_0^2\right)}{\sqrt{\frac{V_{\tilde{z}0}^2\eta_0^2}{\sigma_{V_{\tilde{z}}}^2}+9\frac{\left(1+\frac{1}{3}\eta_0^2\right)^2}{\sigma_\eta^2}+6\rho_{V_{\tilde{z}}\eta}V_0\eta_0\frac{1+\frac{1}{3}\eta_0^2}{\sigma_{V_{\tilde{z}}}\sigma_\eta}}}$$

Unfortunately, the marginal distributions of the Maurer's JDD cannot be analytically evaluated; they can be computed only numerically. Nevertheless, one can see from eq. (5.28) that

the quantities $V_{z0}\sqrt{1+\frac{1}{3}\eta_0^{\,2}}$ and $\arctan\frac{\eta_0}{\sqrt{3}}$ can be interpreted as mean values of $V_z\sqrt{1+\frac{1}{3}\eta^2}$ and $\arctan\frac{\eta}{\sqrt{3}}$, respectively.

The relation between the distribution widths and correlation coefficients featuring in the two forms of the Maurer's JDD can be found from the general formula relating the characteristics of different interrelated JDDs [5.21, pp. 64 ff]. We get:

$$\sigma_\eta = \sqrt{3}\frac{\Delta_0^{\,2}}{V_{z0}^{\,2}}\sigma_\psi$$

$$\sigma_{V_z}^{\,2} = \sin^2\left(\tfrac{1}{3}\pi+\psi_0\right)\sigma_\Delta^{\,2} + \Delta_0^{\,2}\cos^2\left(\tfrac{1}{3}\pi+\psi_0\right)\sigma_\psi^{\,2} + \Delta_0\sin 2\left(\tfrac{1}{3}\pi+\psi_0\right)\sigma_\Delta\sigma_\psi\rho \qquad (5.29)$$

$$\rho_{V_z\eta} = -\sqrt{3}\frac{\Delta_0}{V_{z0}}\frac{\sigma_\Delta\sigma_\psi}{\sigma_{V_z}\sigma_\eta}\rho - \sqrt{3}\frac{\Delta_0^{\,3}}{V_{z0}^{\,2}}\frac{\sigma_\psi^{\,2}}{\sigma_{V_z}\sigma_\eta}\cos\left(\tfrac{1}{3}\pi+\psi_0\right)$$

In the actual case, the EPR studies described in Chapter 4, "EPR of iron-gallium borate single crystals with low x" show that $Fe_xGa_{1-x}BO_3$ crystals are sufficiently well-ordered. Let us compare the appropriateness of using the Czjzek's and Maurer's JDD for our crystals.

5.3.5 Comparison with experimental data

The spectra are computed by integrating the resonance absorption over distributed values of the spin Hamiltonian parameters and random orientations of crystallites:

$$\mathcal{A}(\nu) \propto \int_0^{2\pi}\int_0^{\pi}\int_0^{\pi/6}\int_0^{\infty} P(\Delta,\psi)\,F(\nu-\nu_r,\sigma_\nu)\sin\vartheta\,\mathrm{d}\Delta\,\mathrm{d}\psi\,\mathrm{d}\vartheta\,\mathrm{d}\varphi\,. \qquad (5.30)$$

Here $F(\nu-\nu_r,\sigma_\nu)$ is an intrinsic lineshape with a linewidth σ_ν. In the case of line broadening due to distributions of the spin Hamiltonian parameters, one gets [5.22]:

$$\sigma_\nu^{\,2} = \left(\frac{\partial\nu_r}{\partial\Delta}\right)^2\sigma_\Delta^{\,2} + \left(\frac{\partial\nu_r}{\partial\psi}\right)^2\sigma_\psi^{\,2} + 2\frac{\partial\nu_r}{\partial\Delta}\frac{\partial\nu_r}{\partial\psi}\sigma_\Delta\sigma_\psi\rho \qquad (5.31)$$

where

$$\frac{\partial\nu_r}{\partial\Delta} = -\tfrac{1}{20}\frac{\Delta}{\nu_L}\left\{1+\tfrac{1}{16}\left[\begin{array}{c} 35\sin^2\left(\frac{\pi}{3}+\psi\right)\cos^2\vartheta\left(3\cos^2\vartheta-2\right) \\ +5\sqrt{3}\sin 2\left(\frac{\pi}{3}+\psi\right)\sin^2\vartheta\left(7\cos^2\vartheta-1\right)\cos 2\varphi \\ +20\cos 2\left(\frac{\pi}{3}+\psi\right)\cos^2\vartheta + 35\cos^2\left(\frac{\pi}{3}+\psi\right)\sin^4\vartheta\cos^2 2\varphi \\ -25\cos^2\left(\frac{\pi}{3}+\psi\right)+9 \end{array}\right]\right\} \qquad (5.32)$$

and

$$\frac{\partial \nu_r}{\partial \psi} = -\frac{1}{640}\frac{\Delta^2}{\nu_L}\begin{bmatrix} 35\sin 2\left(\frac{\pi}{3}+\psi\right)\cos^2\vartheta\left(3\cos^2\vartheta-2\right) \\ +10\sqrt{3}\cos 2\left(\frac{\pi}{3}+\psi\right)\sin^2\vartheta\left(7\cos^2\vartheta-1\right)\cos 2\varphi \\ -40\sin 2\left(\frac{\pi}{3}+\psi\right)\cos^2\vartheta-35\sin 2\left(\frac{\pi}{3}+\psi\right)\sin^4\vartheta\cos^2 2\varphi \\ +25\sin 2\left(\frac{\pi}{3}+\psi\right) \end{bmatrix}. \tag{5.33}$$

To illustrate the contribution of different crystallite orientations in the "powder" NMR spectra, we have computed and displayed in Figure 5.9 the spectra for $\vartheta = 0^\circ$, $\vartheta = 90^\circ$ and $\vartheta = 54.74^\circ$ as well as the best-fit simulation of a whole experimental spectrum (*vide infra* for a detailed account of experimental results). One can see two sharp features corresponding to the "magic" and equatorial orientations; the contribution of the polar orientation $\vartheta = 0^\circ$ is weak because of small relative number of such crystallites.

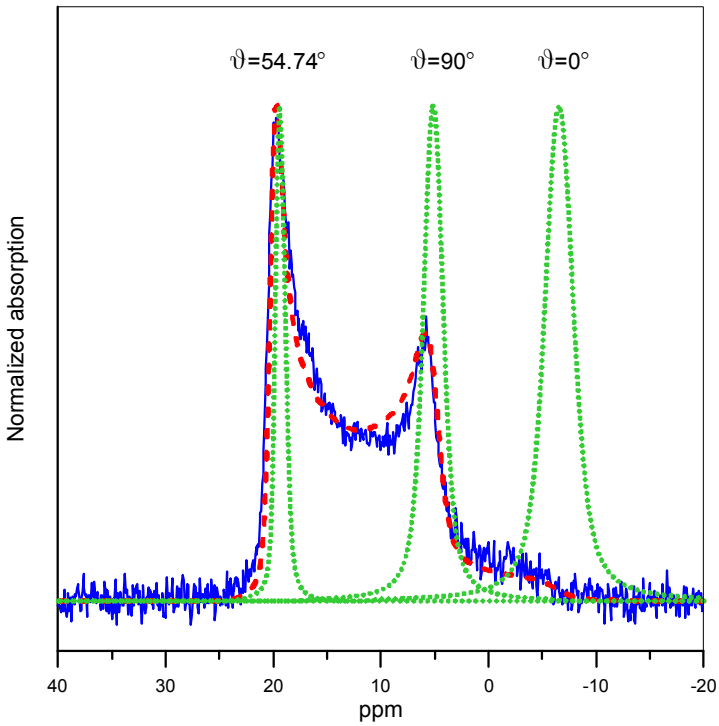

Figure 5.9 Experimental MAS NMR spectrum of ^{11}B in $Fe_xGa_{1-x}BO_3$ with $x = 0.01$ (continuous, blue) and computer-generated spectra for randomly oriented crystallites (dashed, red) and for chosen orientations indicated (dotted, green).

Figure 5.10 shows the marginal distributions of Δ for the Maurer's and Czjzek's models. For the former, the set of parameters corresponds to the best fit to the experimental spectrum, see Table 5.1 below, and for the latter two different σ values have been used. As one can see from Figure 5.10 (left), in order to obtain $\langle\Delta\rangle$ values close to $\Delta_0 \approx 2.86\,\text{MHz}$, in the Czjzek's model one should choose an unrealistically broad distribution of Δ. On the other hand, taking the same distribution widths of Δ as those determined with the Maurer's JDD, $\sigma_\Delta \approx 0.04\,\text{MHz}$,

in the case of the Czjzek's JDD would result in very low mean Δ value, 0.08 MHz, see Figure 5.10 (right).

The Czjzek's JDD, as expected from eq. (5.18), regardless of the σ value, always gives one and the same, extremely broad marginal distribution of ψ. Figure 5.11 illustrates this behaviour for two σ values used to calculate the distributions shown in Figure 5.10. Obviously, such a distribution is incompatible with only slightly perturbed axial site symmetry in the crystal. On the other hand, as one can also see in Figure 5.11, the Maurer's JDD can produce quite narrow marginal distributions of ψ, describing weak random distortions from the perfect structure.

Figure 5.12 shows three-dimensional JDD for the Czjzek's model, and Figure 5.13 shows computer simulated NMR spectra for both Czjzek's and Maurer's models. Clearly, the spectra calculated within the former model are unable to describe the experimental spectrum. In contrast, the Maurer's model provides quite satisfactory fits to the experiment using reasonable parameter values. One can conclude that the Czjzek's model should not be used to fit NMR spectra of materials with weak local disorder.

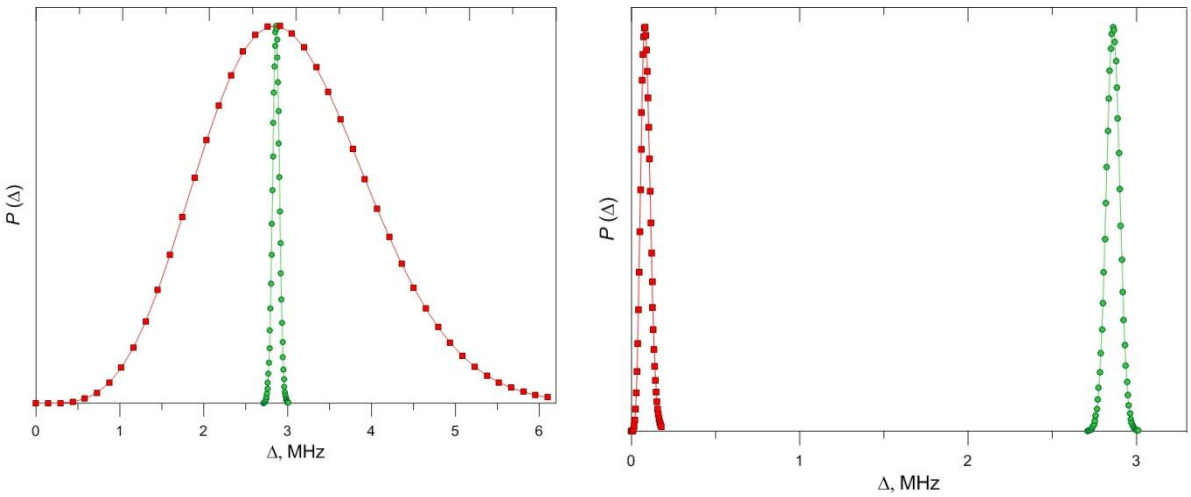

Figure 5.10 Marginal distributions of Δ obtained from the Maurer's (points, green) and Czjzek's (squares, red) models. The simulation parameters are: $\delta_{iso} = 24.5\,\text{ppm}$, $\Delta_0 = 2.86\,\text{MHz}$, $\sigma_\Delta = 0.04\,\text{MHz}$, $\psi_0 = \frac{\pi}{6}$, $\sigma_\psi = 0.015$ and $\rho = 0.2$ for the Maurer's model and $\delta_{iso} = 24.5\,\text{ppm}$ and $\sigma = 1.42$ (left) and $\sigma = 0.04\,\text{MHz}$ (right) for the Czjzek's model.

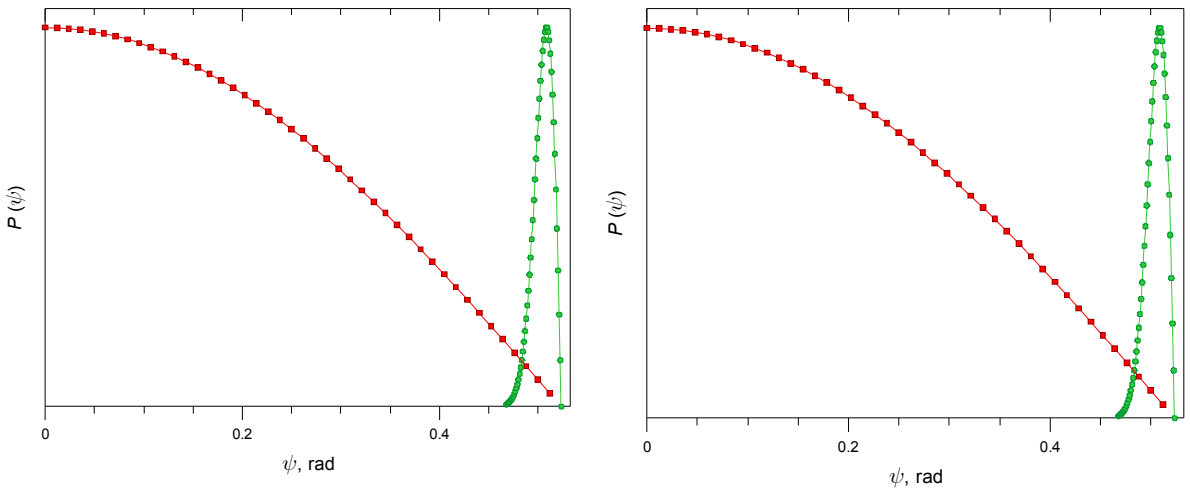

Figure 5.11 Marginal distributions of ψ obtained from the Maurer's (points, green) and Czjzek's (squares, red) models. The simulation parameters are: $\delta_{iso} = 24.5\,\text{ppm}$, $\Delta_0 = 2.86\,\text{MHz}$, $\sigma_\Delta = 0.04\,\text{MHz}$, $\psi_0 = \frac{\pi}{6}$, $\sigma_\psi = 0.015$ and $\rho = 0.2$ for the Maurer's model and $\delta_{iso} = 24.5\,\text{ppm}$ and $\sigma = 1.42$ (left) and $\sigma = 0.04\,\text{MHz}$ (right) for the Czjzek's model.

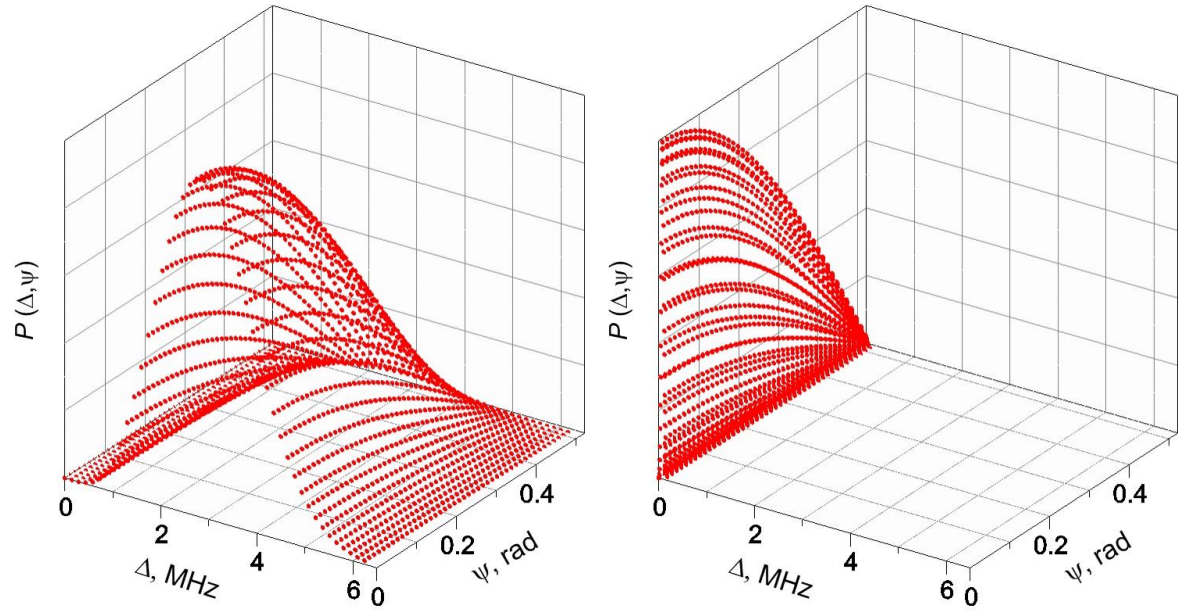

Figure 5.12 Normalized JDD for the Czjzek's model computed with $\delta_{iso} = 24.5\,\text{ppm}$ and $\sigma = 1.42$ (left) and $\sigma = 0.04\,\text{MHz}$ (right).

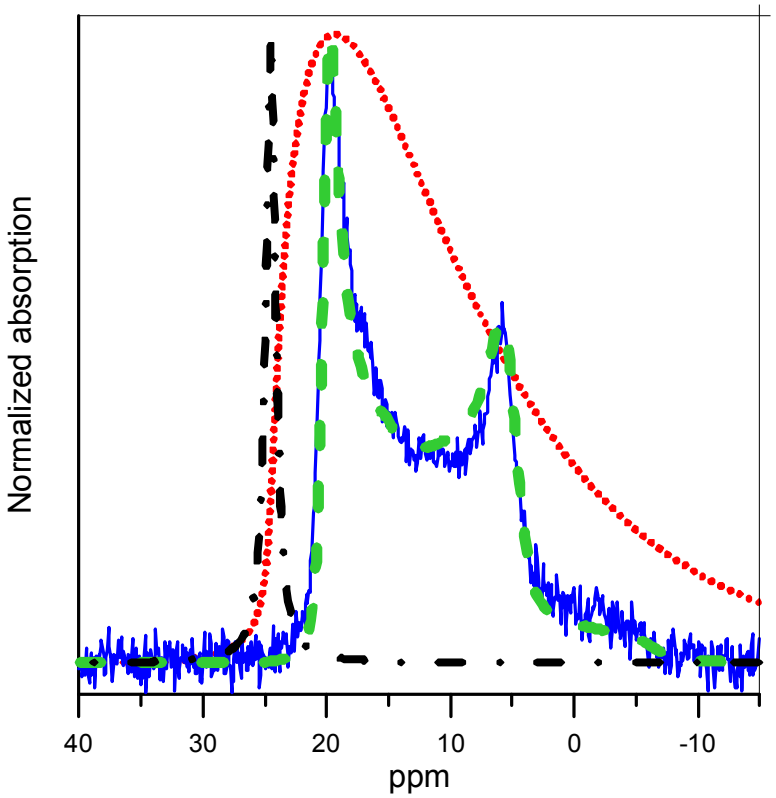

Figure 5.13 Experimental (solid, blue) and computer simulated NMR spectra for the Maurer's model (dashed, green) and the Czjzek`s model (dotted, red, and dashed-dotted, black). The simulation parameters are: $\delta_{iso} = 24.5\,\text{ppm}$, $\Delta_0 = 2.86\,\text{MHz}$, $\sigma_\Delta = 0.04\,\text{MHz}$, $\psi_0 = \frac{\pi}{6}$, $\sigma_\psi = 0.015$ and $\rho = 0.2$ for the Maurer's model, and $\delta_{iso} = 24.5\,\text{ppm}$ and $\sigma = 1.42$ (dotted, red) and $\sigma = 0.04\,\text{MHz}$ (dashed-dotted, black) for the Czjzek's model.

The JDD surfaces for the Maurer's model calculated for different parameters σ_Δ, σ_ψ and $\rho_{\Delta\psi}$, are displayed in Figures 5.14 to 5.16, respectively. As one can see, increasing σ_Δ results simply in broadening the JDD with no shift of the mean Δ value. The behavior of the JDD with increasing σ_ψ is more complicated. At low σ_ψ values the JDD is concentrated near the limiting value $\psi = \frac{\pi}{6}$ corresponding to axial local symmetry. At higher σ_ψ, the JDD not only broadenes but also shifts to lower ψ, manifesting a certain rhombic distortion. The $\psi = 0$ case corresponds to "orthorhombic" distortion when the EFG tensor has two eigenvalues equal in absolute value and opposite in sign. The transformation of the JDD with ρ can be accounted for as a rotation about its vertical axis.

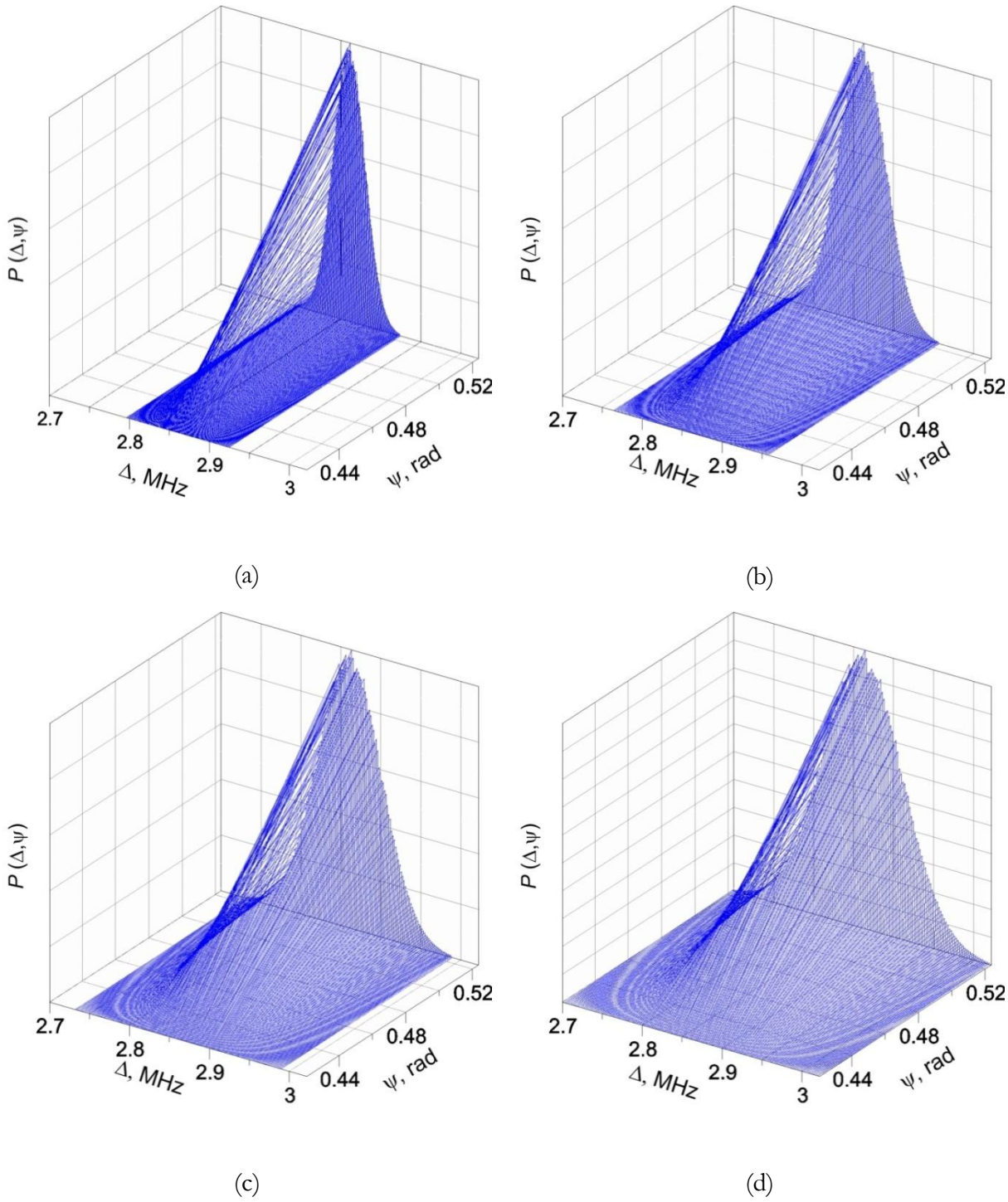

Figure 5.14 Normalized JDD for the Maurer's model computed with simulation parameters: $\delta_{iso} = 24.5\,\text{ppm}$, $\Delta_0 = 2.86\,\text{MHz}$, $\psi_0 = \frac{\pi}{6}$, $\sigma_\psi = 0.0001$, $\rho = 0$ and $\sigma_\Delta = 0.02, 0.03, 0.04$ and 0.05 MHz for (a), (b), (c) and (d), respectively.

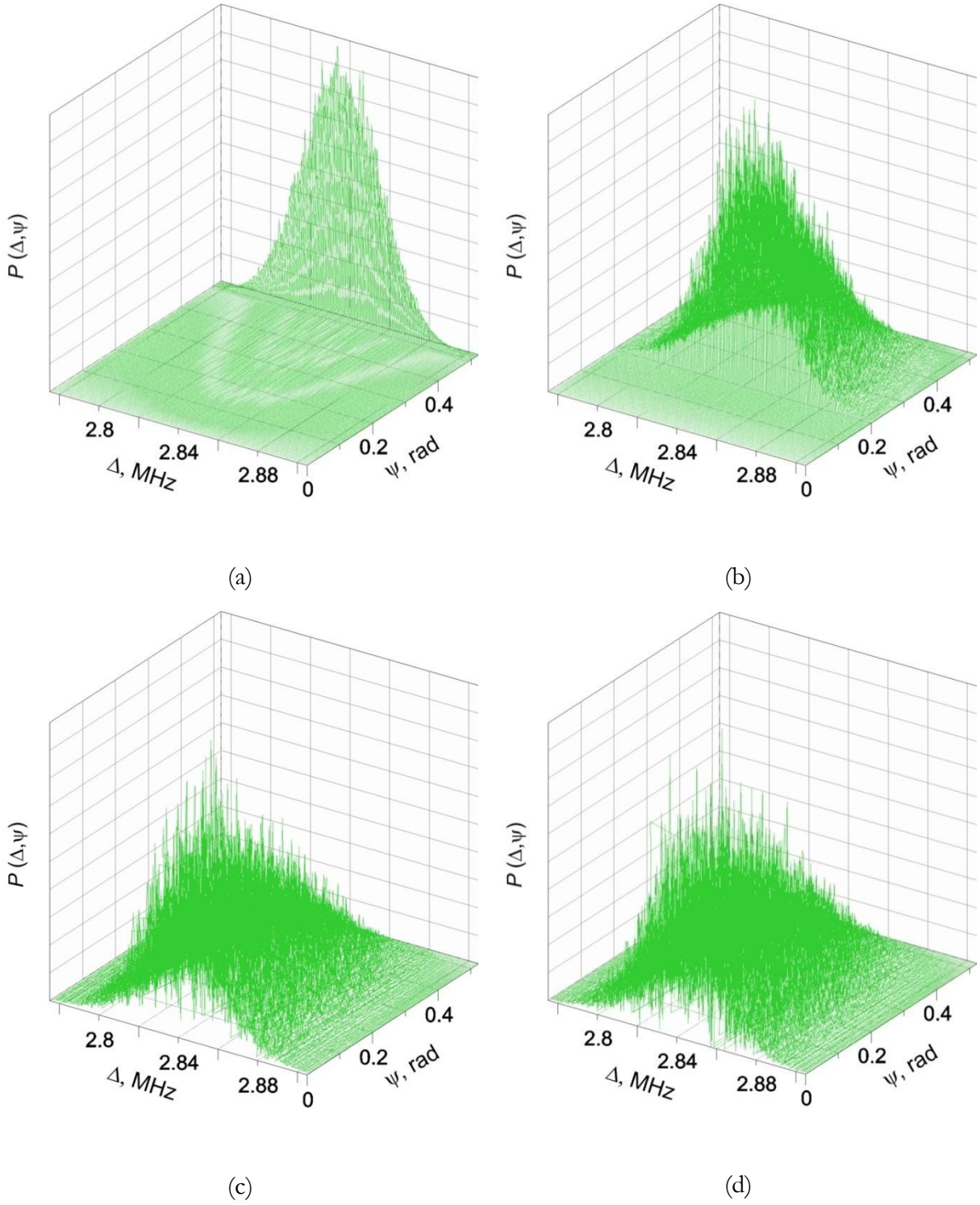

Figure 5.15 Normalized JDD for the Maurer's model computed with simulation parameters: $\delta_{iso} = 24.5\,\text{ppm}$, $\Delta_0 = 2.86\,\text{MHz}$, $\sigma_\Delta = 0.02\,\text{MHz}$, $\psi_0 = \frac{\pi}{6}$, $\rho = 0$ and $\sigma_\psi = 0.01, 0.1, 0.2$ and 0.3 for (a), (b), (c) and (d), respectively.

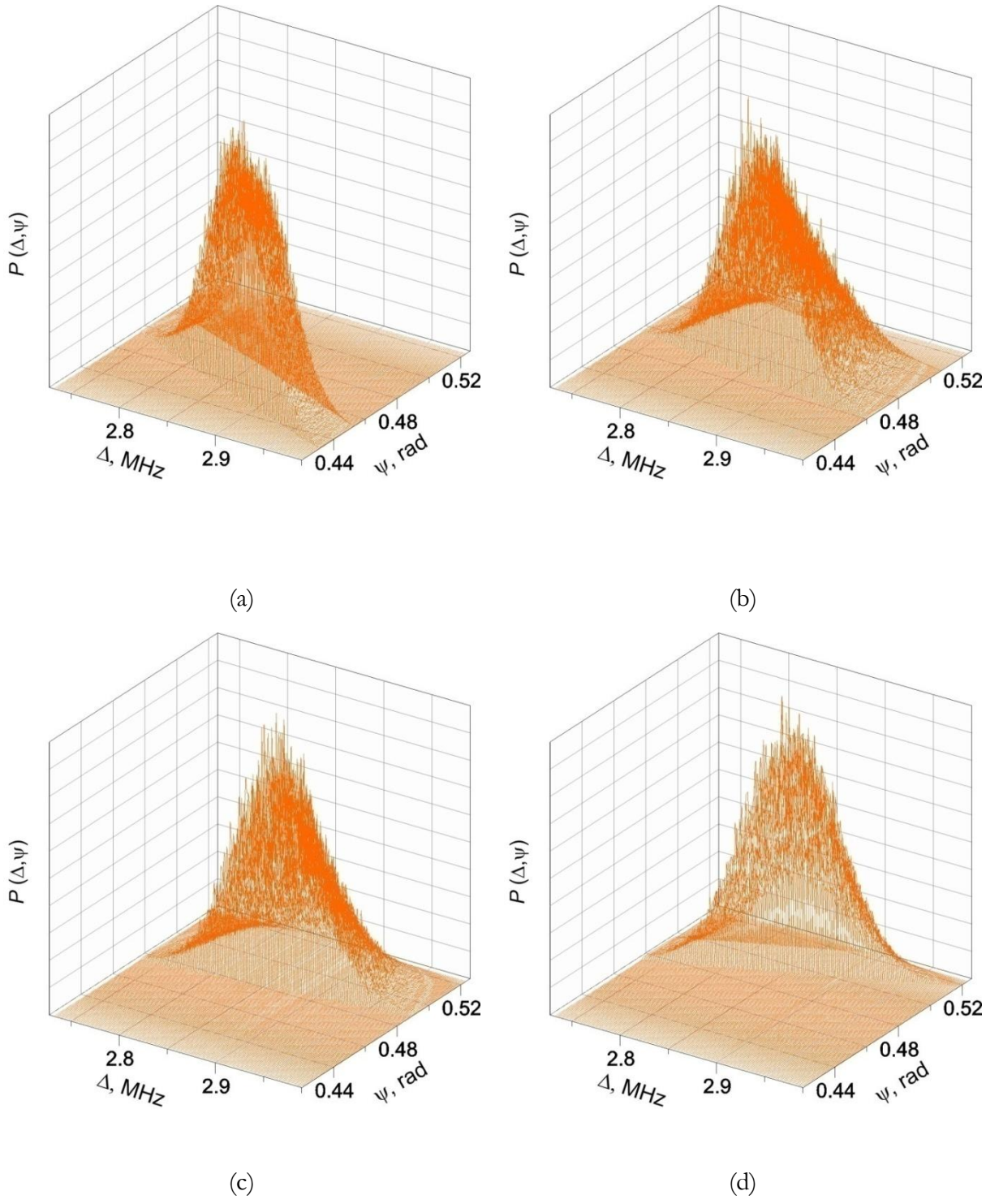

Figure 5.16 Normalized JDD for the Maurer's model computed with simulation parameters: $\delta_{iso} = 24.5\,\text{ppm}$, $\Delta_0 = 2.86\,\text{MHz}$, $\sigma_\Delta = 0.04\,\text{MHz}$, $\psi_0 = \frac{\pi}{6}$, $\sigma_\psi = 0.015$ and $\rho = -0.9$, -0.3, 0.3 and 0.9 for (a), (b), (c) and (d), respectively.

5.4 Experimental details

The ^{11}B MAS NMR spectra of $Fe_xGa_{1-x}BO_3$ ground to powders were measured at 128.384 MHz frequency in 9.4 T magnetic field using a Bruker Avance-400 NMR spectrometer. A 4 mm in diameter zirconia (ZrO_2) rotor cell equipped with boron nitride, BN stator filled with powdered sample was spinning under magic angle with 10 kHz frequency.

In the actual case, the FID signal from the BN stator was much more intense than the signal produced by the sample [5.23]. Therefore, a "$90^\circ - \tau - 180^\circ - \tau - Acquisition$" Hahn two pulse echo sequence with echo delay τ, as shown in Figure 5.3, has been used to record NMR signals from ^{11}B nuclei [5.4, 5.6, 5.7]. This sequence for τ = 1 ms significantly reduced the signal from the stator and allowed clear detection of the sample signals.

For ^{11}B with $I = 3/2$ nuclear spin, the optimal pulse duration for selective excitation of the central transition equals to the duration of a non-selective 90° pulse divided by $I + 1/2 = 2$ [5.4, 5.24]. In our experiments, the duration of this pulse was $t_i = 1.75$ μs. The recycle delay between acquisitions was 0.5 s, and a total of 1024 acquisitions was sufficient to resolve characteristic spectral features of ^{11}B.

Because of a large second-order quadrupole coupling, the ^{71}Ga ($I = 3/2$) NMR lines were very broad, so that special acquisition conditions were required in order to obtain comprehensible spectra. The ^{71}Ga MAS NMR spectra were measured at 122.0564 MHz with 4 mm rotors at the spinning rate of 14 kHz. These spectra were recorded by classical direct acquisitions under single pulse FID excitations with an acquisition of 1000 pulse signals repeated with 2.4 μs RF pulse length. The NMR spectra were obtained by Fourier transformation of the FID signals.

The spin-lattice relaxation time T_1 for ^{71}Ga nuclei in $Fe_xGa_{1-x}BO_3$ was measured by saturation-recovery method. For samples with x = 0.01 and 0.02, T_1 was 23 and 2 ms, respectively. One can see that T_1 drastically decreased with an increase in iron concentration. Because of a spurious ^{11}B NMR signal from the BN stator, similar measurements for ^{11}B could not be carried out.

5.5 Experimental results and discussion

5.5.1 MAS NMR spectra of ^{11}B

Figure 5.17 shows ^{11}B MAS NMR spectra for $Fe_xGa_{1-x}BO_3$ powders with x = 0, 0.01 and 0.02 together with the best-fit computer simulations. The spectra display a characteristic two-peak MAS quadrupole powder pattern for a single boron site [5.8, 5.24]. Clearly, an increase of iron concentration results in broadening of the spectra.

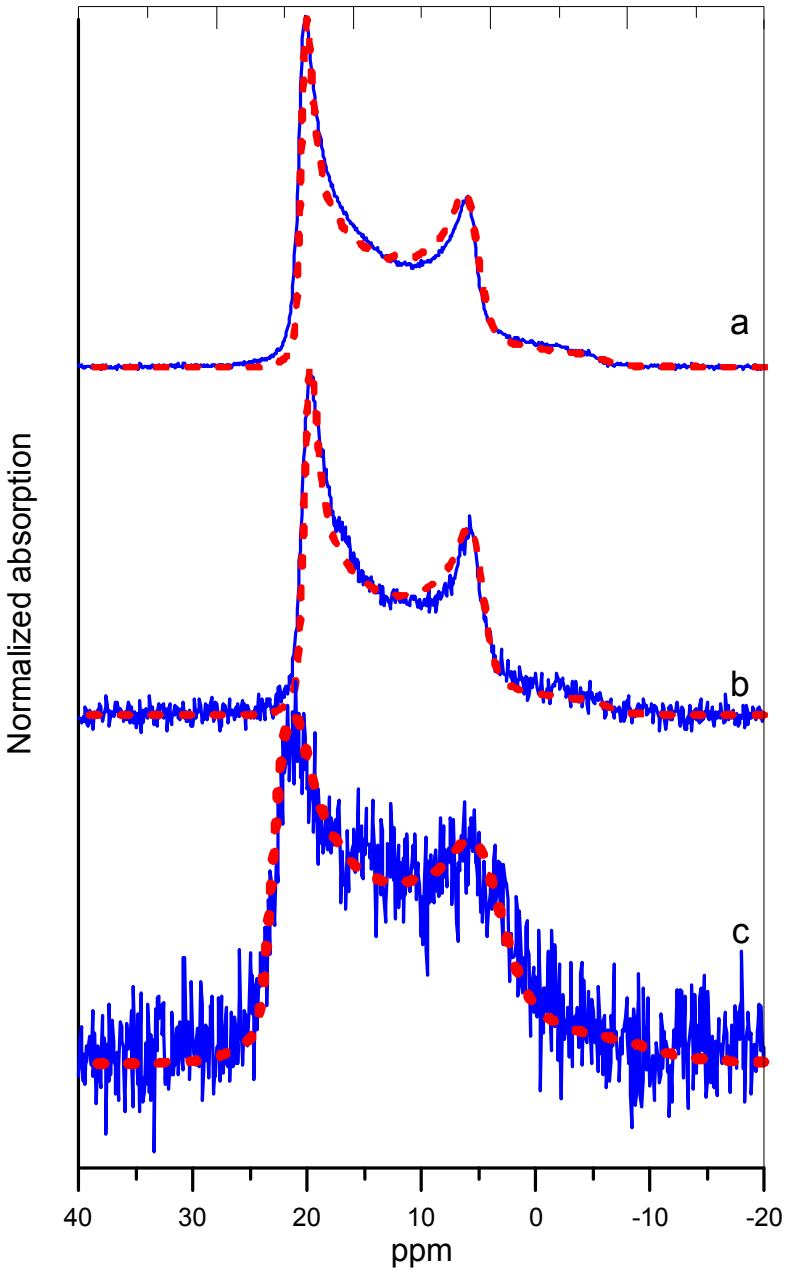

Figure 5.17 Experimental (continuous, blue) and computer-generated (dashed, red) MAS NMR spectra of ^{11}B in $Fe_xGa_{1-x}BO_3$ with x = 0.00 (a), 0.01 (b) and 0.02 (c).

The best-fit simulation parameters and corresponding "conventional" parameters C_Q, η, their distribution widths σ_{C_Q} and σ_η and the correlation coefficient $\rho_{C_Q\eta}$ are given in Table 5.1 C_Q and η are related to Δ and ψ as: $C_Q = \Delta\cos\left(\frac{\pi}{6}-\psi\right) = V_z$ and $\eta = \sqrt{3}\tan\left(\frac{\pi}{6}-\psi\right)$.

The values of C_Q and δ_{iso} extracted from the simulations allow to determine the coordination of boron [5.7, 5.24]. Indeed, the fourfold-coordinated boron possesses C_Q values lower than 1 MHz, whereas the threefold-coordinated boron has much larger C_Q, 2.4 to 2.9 MHz [5.7, 5.24]. Besides, δ_{iso} for the three-coordinated boron is in the range from ca. 10 to

27 ppm [5.7, 5.24, 5.25] while for the fourfold-coordinated boron $\delta_{iso} \approx 4$ ppm [5.23]. Our simulation results clearly indicate that boron is threefold coordinated.

Table 5.1 Best-fit NMR Parameters for ^{11}B isotope in $Fe_xGa_{1-x}BO_3$.

x	0.00	0.01	0.02
δ_{iso}, ppm	24.7±0.1	24.5±0.1	27.6±0.1
Δ_0, MHz	2.84±0.0	2.86±0.02	3.16±0.02
σ_Δ, MHz	0.04±0.0	0.04±0.01	0.08±0.01
ψ_0		0.510 to 0.523	
σ_ψ	0.011±0.	0.015±0.0	0.027±0.005
ρ	0.1±0.1	0.2±0.1	−0.3±0.1
C_Q, MHz	2.84±0.0	2.86±0.02	3.16±0.02
σ_{C_Q}, MHz	0.04±0.0	0.04±0.01	0.08±0.01
η		0.0 to 0.023	
σ_η	0.019±0.	0.026±0.	0.047±0.009
$\rho_{C_Q\eta}$	−0.1±0.1	−0.2±0.1	0.3±0.1

5.5.2 MAS NMR spectra of ^{71}Ga

Figure 5.18 shows the MAS NMR spectrum of the central transition of ^{71}Ga nuclei for $Fe_xGa_{1-x}BO_3$ powders with different iron contents. The behaviour of the spectra is qualitatively similar to that described above for ^{11}B isotope. In particular, the two-peak quadrupole powder pattern characteristic of axially symmetric EFG tensor is clearly seen.

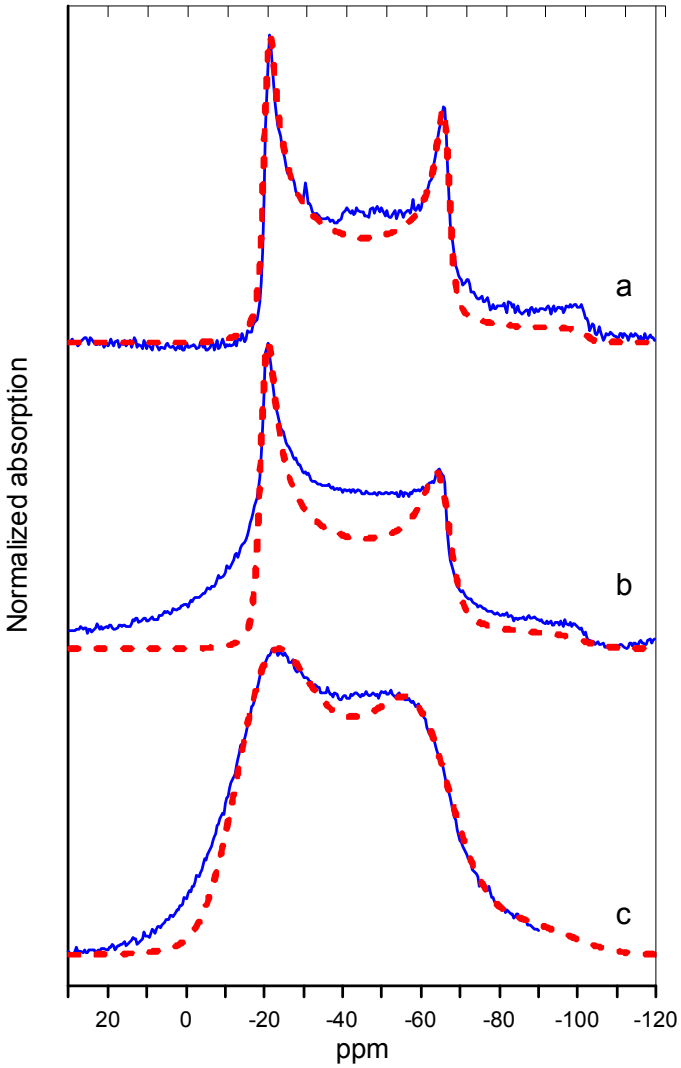

Figure 5.18 Experimental (continuous blue line) and computer-generated (dashed red line) MAS NMR spectra of ^{71}Ga in $Fe_xGa_{1-x}BO_3$ with x = 0.00 (a), 0.01 (b) and 0.02(c).

The simulation procedure for ^{71}Ga NMR spectra has been similar to that for ^{11}B; meanwhile, in order to obtain closer fittings, we had to take into account a Gaussian distribution of δ_{iso} with a standard deviation σ_δ. Nevertheless, the best-fit computer-generated spectra displayed in Figure 5.18 show a certain discrepancy with the experimental ones. This discrepancy can be ascribed to an underlying signal arising from ^{71}Ga in heavily disordered environment or to a superposed contribution from the non-central NMR transitions.

The best-fit simulation parameters for ^{71}Ga NMR spectra given in Table 5.2 are consistent with sixfold-coordinated gallium [5.8].

Table 5.2 NMR Parameters for ^{71}Ga isotope in $Fe_xGa_{1-x}BO_3$.

x	0.00	0.01	0.02
δ_{iso}, ppm	−6.90±0.1	−6.10±0.1	−2.80±0.1
σ_δ	0.0 to 0.4	0.0 to 0.8	6.5±1.0
Δ_0, MHz	4.77±0.02	4.78±0.02	4.82±0.02
σ_Δ, MHz	0.02±0.005	0.06±0.005	0.06±0.005
ψ_0		0.510 to 0.523	
σ_ψ	0.013±0.005	0.018±0.005	0.050±0.005
ρ	0±0.1	0.1±0.1	−0.2±0.1
C_Q, MHz	4.77±0.02	4.78±0.02	4.82±0.02
σ_{C_Q}, MHz	0.02±0.005	0.06±0.005	0.06±0.005
η		0.0 to 0.023	
σ_η	0.022±0.005	0.031±0.005	0.087±0.005
$\rho_{C_Q\eta}$	0±0.1	−0.1±0.1	0.2±0.1

5.6 Conclusions

The MAS NMR spectroscopy of the ^{11}B and ^{71}Ga allows to determine the local symmetry and to identify surrounding structural units for these atoms in $Fe_xGa_{1-x}BO_3$ crystals. The best-fit parameters obtained for ^{11}B and ^{71}Ga confirm the threefold coordination and C_3 intrinsic symmetry for the former and the sixfold coordination with lower-than-cubic symmetry for the latter. For both nuclei, broadening of the MAS NMR spectra with the increase in iron contents has been related to variations of quadrupole parameters and chemical shift (in the case of ^{71}Ga) caused by disorder in the local environment. This assumption is corroborated with accurate computer simulations of Fe^{3+} EPR spectra, showing the existence of local disorder in iron-doped gallium borate crystals.

A comparative analysis of the characteristics of the Czjzek's and Maurer's JDD has been carried out in order to elucidate the suitability of using them in the case of low or moderate local disorder. Moreover, for the Maurer's model we have considered in detail both the numerical and the analytical JDD. For the former case we have put forward a simulation code in order to obtain dependences of the mean values $\langle \Delta \rangle, \langle \psi \rangle$, standard deviations $\sigma_\Delta, \sigma_\psi$ of Δ and ψ, respectively, and a correlation coefficient ρ on the input value of σ for different Δ_0 and ψ_0. The obtained relationships have allowed to determine the limits of applicability of the Maurer's analytical JDD.

The Czjzek's JDD is well adapted to the case of heavily disordered solids; meanwhile it does not provide for local ordering in crystals, partially preserved in the presence of a certain degree of disorder. Indeed, it does not include mean values of the quadrupole parameters; besides, it contains only one parameter describing the distribution widths. As a result, the marginal distribution of the parameter ψ related to the asymmetry parameter η becomes too broad to be incompatible with the existence of short range ordering. In contrast, the Maurer's JDD has no these drawbacks, therefore it is expected to provide satisfactory fits to experimental NMR spectra in crystals with low degree of local disorder.

The above considerations are fully corroborated by applying the Czjzek's and Maurer's models to computer simulations of NMR spectra of ^{11}B isotope in gallium borate. With the former distribution no adequate description can be obtained while the latter one provides quite satisfactory fits. The present study shows that the Czjzek's model should not be used in computer-assisted analysis of NMR spectra of materials with low or even moderate local disorder. On the other hand, the Maurer's model is conceptually well adapted to this situation; therefore it is not surprising that it provides quite adequate fits to the experimental NMR spectra.

5.7 References

5.1 Pascal P. Man, *Quadrupole couplings in nuclear magnetic resonance, general,* in: *Encyclopedia of analytical chemistry*, R.A. Meyers ed., Wiley, Chichester (2000) pp. 12224–12265

5.2 E.R. Andrew, A. Bradbury, R.G. Eades, *Nuclear magnetic resonance spectra from a crystal rotated at high speed*, Nature **182(4650)** (1958) 1659

5.3 I.J. Lowe, *Free induction decays of rotating solids*, Phys. Rev. Lett **2(7)** (1959) 285-287

5.4 E.L. Hahn, *Spin echoes*, Phys. Rev. **80** (1950) 580-594

5.5 H.Y. Carr and E M. Purcell, *Effects of diffusion on free precession in nuclear magnetic resonance experiments*, Phys. Rev. **94** (1954) 630–638

5.6 A. Abragam, *The principles of nuclear magnetism*, Clarendon, Oxford, (1961) 599 pp.

5.7 D.Freude, *Quadrupolar nuclei in solid-state nuclear magnetic resonance*, in: *Encyclopedia of Analytical Chemistry*, R.A. Meyers ed., Wiley, Chichester (2000) pp. 12188-12224

5.8 D. Massiot, T. Vosegaard, N. Magneron, D. Trumeau, V. Montouillout, P. Berthet, T. Loiseau and B. Bujoliet, ^{71}Ga *NMR of reference* Ga_{IV}, Ga_{V}, and Ga_{VI} *compounds by MAS and QPASS*, *extension of gallium/aluminum NMR parameter correlation*, Solid State NMR **15** (1999) 159-169

5.9 D. Müller, *Determination of chemical shifts of NMR-frequencies of quadrupolar nuclei fron the MAS-NMR spectra*, Annalen der Phys. **39** (1982) 451-460

5.10 D. Freude and J. Haase, *Quadrupole effects in solid-state NMR, basic principles and experimental techniques for nuclei with half-integer spins,* in: *NMR Basic Principles and Progress*, Springer, Berlin, Heidelberg, v. **29** (1993) pp. 3-90 (updated version: August 2014 : http://www.quad-nmr.de)

5.11 G. Czjzek, J. Fink, F. Gotz, H. Schmidt, J.M.D. Coey, J.P. Rebouillat and A. Lienard, *Atomic coordination and the distribution of electric field gradients in amorphous solids*, Phys. Rev. B: Condens. Matter **23** (1981) 2513-2530

5.12 G. Czjzek, *Distribution of nuclear quadrupole splittings in amorphous materials and the topology of the* (V_{zz}, η)*-parameter space*, Hyperfine Interactions **14** (1983) 189-194

5.13 G. Le Caër and R.A. Brand, *General models for the distributions of electric field gradients in disordered solids*, J. Phys.: Condens. Matter **10** (1998) 10715-10774

5.14 J. Kliava, R. Berger, Y. Servant, J. Emery, J.-M. Greneche and J. Trokšs, *Electron paramagnetic resonance and Mössbauer effect studies in iron-doped* ^{57}Fe *isotope enriched phosphate glasses*, J. Non-Cryst. Solids **202** (1996) 205-214

5.15 C. Legein, J.-Y.Buzaré, G. Silly and C. Jacoboni, *The local field distribution of* Gd^{3+} *in transition metal fluoride glasses investigated by electron paramagnetic resonance*, J. Phys.: Condens. Matter **8** (1996) 4339-4350

5.16 C. Legein, J.-Y.Buzaré, J. Emery and C. Jacoboni, *Electron paramagnetic resonance determination of the local field distribution acting on* Cr^{3+} *and* Fe^{3+} *in transition metal fluoride glasses (TMFG),* J. Phys.: Condens. Matter **7** (1995) 3853-3862

5.17 J.-B. d'Espinose de Lacaillerie, C. Fretigny and D. Massiot, *MAS NMR spectra of quadrupolar nuclei in disordered solids: The Czjzek model*, J. Magn. Reson. (2008) **192** 244-251

5.18 M. Maurer, *Electric field gradients of randomly disordered compounds*, Phys. Rev. B **34** (1986) 8996-8999

5.19 J. Kliava and R. Berger, *Size and shape distribution of magnetic nanoparticles in disordered systems: computer simulations of superparamagnetic resonance spectra*, J. Magn. Magn. Mater. **205** (1999) 328-342

5.20 G. Le Caër, B. Bureau and D. Massiot, *An extension of the Czjzek model for the distributions of electric field gradients in disordered solids and an application to NMR spectra of* ^{71}Ga *in chalcogenide glasses*, J. Phys.: Condens. Matter **22** (2010) 065402, 1-17

5.21 J. Kliava, *EPR spectroscopy of disordered solids*, Zinātne, Riga (1988) 320 pp.

5.22 J. Kliava, *EPR of impurity ions in disordered solids*, Phys. Stat. Sol. B **134** (1986) 411-455

5.23 B.V. Padlyak, N.A. Sergeev, M. Olszewski, V.T. Adamiv and Ya.V. Burak, ^{11}B *and* ^{7}Li *MAS NMR spectroscopy of glassy and crystalline borate compounds*, Phys. Chem. Glasses: Eur. J. Glass Sci. Technol. B **55(1)** (2014) 25-33

5.24 M.E. Smith and E.R.H. Van Eck, *Recent advances in experimental solid state NMR methodology for half-integer spin quadrupolar nuclei,* Progress in NMR Spectroscopy **34** (1999)

5.25 S. Kroeker and J.F. Stebbins, *Three-coordinated boron-11 chemical shifts in borates*, Inorg. Chem. **40** (2001) 6239-6246

6. Magnetocrystalline anisotropy of iron borate and iron-gallium borates

6.1 Introduction

The anisotropic part of the density of the magnetic energy for $FeBO_3$, can be expressed as follows, *cf.* eq. (1.19) in Chapter 1, "Crystal and magnetic structure of iron borate":

$$\mathcal{E}_A = \frac{1}{6} a_{\text{eff}} \left(3\cos^2\vartheta - 1\right) + d_{FeBO_3} \sin^3\vartheta \cos\vartheta \sin 3\varphi + e_{FeBO_3} \sin^6\vartheta \cos 6\varphi \qquad (6.1)$$

where a_{eff} is the *effective* uniaxial anisotropy constant,

$$a_{\text{eff}} = a_{FeBO_3} + \frac{D^2_{FeBO_3}}{E_{FeBO_3}}, \qquad (6.2)$$

a_{FeBO_3} is the uniaxial anisotropy constant, D_{FeBO_3} and E_{FeBO_3} being the Dzyaloshinskii-Moriya and exchange constants, and d_{FeBO_3} and e_{FeBO_3} are the basal anisotropy constants for $FeBO_3$.

As far as for Fe^{3+} ($3d^5$ electronic configuration) the orbital moment equals zero, the exchange energy in a good approximation is isotropic [6.1], (*cf.* Chapter 1, "Crystal and magnetic structure of iron borate") so that for $FeBO_3$ the constants a_{FeBO_3}, d_{FeBO_3} and e_{FeBO_3} include only crystal field (cf) and dipole-dipole (dip) contributions:

$$\begin{aligned} a_{FeBO_3} &= a_{\text{cf}} + a_{\text{dip}} \\ d_{FeBO_3} &= d_{\text{cf}} + d_{\text{dip}} \\ e_{FeBO_3} &= e_{\text{cf}} + e_{\text{dip}} \end{aligned} \qquad (6.3)$$

The crystal field contributions to these constants have been reported by Seleznev [6.2]; here, for clarity, we give a more comprehensive analysis. These contributions can be calculated in perturbation theory using the spin Hamiltonian for isolated Fe^{3+} ions in a diamagnetic crystal isomorphous to iron borate, *e.g.* gallium borate [6.3]. Thus, $a_{\text{cf}}, d_{\text{cf}}$ and e_{cf} can be expressed through the spin Hamiltonian parameters.

The dipole-dipole contributions to these constants are usually calculated using the lattice-sum method. The value of $a_{\text{dip}} = 3.82 \cdot 10^5\ \text{Jm}^{-3}$ at 0 K for $FeBO_3$ has been obtained

previously [6.4]. a_{FeBO_3} has been determined by means of AFMR in a wide temperature range, see [6.2, 6.5]; its value, extrapolated to 0 K, is $a_{FeBO_3}^{exp} = 3.29 \cdot 10^5$ Jm^{-3}.

Earlier, the occurrence of the dipole-dipole contribution to hexagonal basal anisotropy in iron borate had been ruled out on the grounds of symmetry. Indeed, the dipole-dipole interaction energy is usually considered for "point dipoles" having a negligible size, in which case only uniaxial anisotropy is accounted for. Meanwhile, taking into account higher-order terms in the expansion of the dipole-dipole interaction energy in the Taylor series in the small parameter dipole size/interdipole distance would provide the possibility of describing more sophisticated symmetries, in particular, the hexagonal magnetocrystalline anisotropy. Clearly, such terms can be significant only in the case of "extended dipoles" having non-negligible dipole size. Thus, taking into consideration extended dipoles opens the possibility to reasonably account for the dipole-dipole contribution to the basal anisotropy constants and, subsequently, to estimate effective dipole dimensions in iron borate.

With this aim in mind, we have developed a theoretical description of the following models of an extended magnetic dipole: (i) a uniformly magnetized sphere, (ii) an Ampérian current, *i.e.* a circular current loop of a radius R delimiting an area $S = \pi R^2$ and (iii) an assembly of two fictitious "magnetic charges" $\pm q$ a distance d apart.

In the present chapter, in the framework of these models we describe the evaluation of the dipole sizes in $FeBO_3$ as well as of dipole-dipole contributions to the magnetocrystalline anisotropy constants of $Fe_xGa_{1-x}BO_3$.

6.2 Crystal field contribution to magnetocrystalline anisotropy

In order to calculate the crystal field contribution to the magnetic energy, we consider a Fe^{3+} ion in a diamagnetic $GaBO_3$ crystal. The conventional spin Hamiltonian in this case is [6.6, 6.7], *cf.* eq. (4.27) in Chapter 4, "EPR of iron-gallium borate single crystals with low x":

$$\mathcal{H} = g\beta \boldsymbol{B} \cdot \boldsymbol{S} + \tfrac{1}{3} D O_2^0 - \tfrac{1}{180}(a - F) O_4^0 + \tfrac{\sqrt{2}}{9} a \left(\mp O_4^3 \sin 3\alpha + O_4^{-3} \cos 3\alpha \right) \qquad (6.4)$$

where g is close to the free electron g-factor $g_e \approx 2$, β is the Bohr magneton, $\boldsymbol{B}$ is the magnetizing field, S is the electron spin of Fe^{3+}, $S = \frac{5}{2}$, D is the second-order axial fine-structure constant, a and F are, respectively, the fourth-order cubic and axial fine-structure constants and O_2^0, O_4^0, O_4^3 and O_4^{-3} are extended Stevens operators defined, *e.g.*, in the textbook by Al'tshuler and B. M. Kozyrev [6.8]. The $\mp$ signs refer to two non-equivalent iron sites with local magnetic axes rotated through the angle $\mp\alpha$ about the C_3 axis, see Figure 1.3 in Chapter 1, "Crystal and magnetic structure of iron borate".

As far as Fe^{3+} ions in $FeBO_3$ are in a strong exchange field, in order to obtain the spin Hamiltonian for a j^{th} Fe^{3+} ion in $FeBO_3$, $j=1,2$ numbering two non-equivalent iron sites, we substitute an effective exchange field $\boldsymbol{B}_{\mathrm{E}j}$ for the magnetizing field $\boldsymbol{B}$. We get:

$$\mathcal{H}=g\beta\boldsymbol{B}_{\mathrm{E}j}\cdot\boldsymbol{S}_j+\tfrac{1}{3}DO_{2j}^0-\tfrac{1}{180}(a-F)O_{4j}^0+\tfrac{\sqrt{2}}{9}a\left(\mp O_{4j}^3\sin 3\alpha+O_{4j}^{-3}\cos 3\alpha\right). \tag{6.5}$$

As far as in this equation the "Zeeman" term, $\mathcal{H}_0=g\beta\boldsymbol{B}_{\mathrm{E}j}\cdot\boldsymbol{S}_j$, is much larger than the remaining terms $\mathcal{H}'=\tfrac{1}{3}DO_{2j}^0-\tfrac{1}{180}(a-F)O_{4j}^0+\tfrac{\sqrt{2}}{9}a\left(\mp O_{4j}^3\sin 3\alpha+O_{4j}^{-3}\cos 3\alpha\right)$, we have calculated the energies of the spin levels using the perturbation theory. With this aim in view, we have followed the approach of "correct" zero-order wave functions, described by Landau and Lifshitz [6.9]. The zero-order energies and wave functions have been calculated by solving the secular equation

$$\left|\boldsymbol{H}_0-\mathcal{E}^{(0)}\boldsymbol{1}\right|=0 \tag{6.6}$$

where $\boldsymbol{H}_0$ is the matrix of $\mathcal{H}_0$ and $\boldsymbol{1}$ is a unit 6×6 matrix. The eigenvalues of eq. (6.6) are:

$$\mathcal{E}^{(0)}{}_{\pm\frac{5}{2}}=\pm\tfrac{5}{2}\,g\beta B\quad;\quad\mathcal{E}^{(0)}{}_{\pm\frac{3}{2}}=\pm\tfrac{3}{2}\,g\beta B\quad;\quad\mathcal{E}^{(0)}{}_{\pm\frac{1}{2}}=\pm\tfrac{1}{2}\,g\beta B. \tag{6.7}$$

The "correct" zero-order wave functions of the spin levels, $\Psi_M^{(0)}$, are expressed as linear combinations of the electron spin eigenfunctions Ψ_M where $M=-\tfrac{5}{2},-\tfrac{3}{2},\cdots,\tfrac{5}{2}$. The latter relationships can be written in the form of scalar products

$$\Psi_M^{(0)}=\boldsymbol{C}_M^{(0)}\cdot\boldsymbol{\Psi}_M \tag{6.8}$$

where $\boldsymbol{C}_M^{(0)}=\left(C_{-\frac{5}{2}}^{(0)}\;\;C_{-\frac{3}{2}}^{(0)}\;\;C_{-\frac{1}{2}}^{(0)}\;\;C_{\frac{1}{2}}^{(0)}\;\;C_{\frac{3}{2}}^{(0)}\;\;C_{\frac{5}{2}}^{(0)}\right)$ and $\boldsymbol{\Psi}_M=\left(\Psi_{-\frac{5}{2}}\;\;\Psi_{-\frac{3}{2}}\;\;\Psi_{-\frac{1}{2}}\;\;\Psi_{\frac{1}{2}}\;\;\Psi_{\frac{3}{2}}\;\;\Psi_{\frac{5}{2}}\right)$. The vectors $\boldsymbol{C}_M^{(0)}$ can be found from the equation:

$$\boldsymbol{C}_M^{(0)}\cdot\left(\boldsymbol{H}_0-\mathcal{E}_M^{(0)}\boldsymbol{1}\right)=\boldsymbol{0} \tag{6.9}$$

where **0** is a column 6-vector. Solving the latter equation, we get $\boldsymbol{C}_M^{(0)}$ for each spin level:

$$\boldsymbol{C}_{\pm\frac{5}{2}}^{(0)}=\begin{pmatrix}\pm\frac{\sqrt{2}}{8}\mathrm{e}^{-5i\varphi}\sin^5\vartheta\left(1\mp\cos\vartheta\right)^{-5/2}\\ \frac{\sqrt{10}}{8}\mathrm{e}^{-4i\varphi}\sin^4\vartheta\left(1\mp\cos\vartheta\right)^{-3/2}\\ \pm\frac{\sqrt{5}}{4}\mathrm{e}^{-3i\varphi}\sin^3\vartheta\left(1\mp\cos\vartheta\right)^{-1/2}\\ \frac{\sqrt{5}}{4}\mathrm{e}^{-2i\varphi}\sin^2\vartheta\left(1\mp\cos\vartheta\right)^{1/2}\\ \pm\frac{\sqrt{10}}{8}\mathrm{e}^{-i\varphi}\sin\vartheta\left(1\mp\cos\vartheta\right)^{3/2}\\ \frac{\sqrt{2}}{8}\left(1\mp\cos\vartheta\right)^{5/2}\end{pmatrix},$$

$$\boldsymbol{C}^{(0)}_{\pm\frac{3}{2}}=\begin{pmatrix}\frac{\sqrt{10}}{8}\mathrm{e}^{-5i\varphi}\sin^4\vartheta\left(1\mp\cos\vartheta\right)^{-3/2}\\ -\frac{\sqrt{2}}{8}\mathrm{e}^{-4i\varphi}\sin^3\vartheta\left(5\cos\vartheta\mp3\right)\left(1\mp\cos\vartheta\right)^{-3/2}\\ \mp\frac{1}{4}\mathrm{e}^{-3i\varphi}\sin^2\vartheta\left(5\cos\vartheta\mp1\right)\left(1\mp\cos\vartheta\right)^{-1/2}\\ -\frac{1}{4}\mathrm{e}^{-2i\varphi}\sin\vartheta\left(5\cos\vartheta\pm1\right)\left(1\mp\cos\vartheta\right)^{1/2}\\ \mp\frac{\sqrt{2}}{8}\mathrm{e}^{-i\varphi}\left(5\cos\vartheta\pm3\right)\left(1\mp\cos\vartheta\right)^{3/2}\\ \mp\frac{\sqrt{10}}{8}\sin\vartheta\left(1\mp\cos\vartheta\right)^{3/2}\end{pmatrix},$$

$$\boldsymbol{C}^{(0)}_{\pm\frac{1}{2}}=\begin{pmatrix}-\frac{\sqrt{5}}{4}\mathrm{e}^{-5i\varphi}\sin^3\vartheta\left(1\mp\cos\vartheta\right)^{-1/2}\\ \frac{1}{4}\mathrm{e}^{-4i\varphi}\sin^2\vartheta\left(5\cos\vartheta\mp1\right)\left(1\mp\cos\vartheta\right)^{-1/2}\\ -\frac{\sqrt{2}}{4}\mathrm{e}^{-3i\varphi}\sin\vartheta\left(5\cos^2\vartheta\mp2\cos\vartheta-1\right)\left(1\mp\cos\vartheta\right)^{-1/2}\\ \mp\frac{\sqrt{2}}{4}\mathrm{e}^{-2i\varphi}\left(5\cos^2\vartheta\pm2\cos\vartheta-1\right)\left(1\mp\cos\vartheta\right)^{1/2}\\ \mp\frac{1}{4}\mathrm{e}^{-i\varphi}\sin\vartheta\left(5\cos\vartheta\pm1\right)\left(1\mp\cos\vartheta\right)^{1/2}\\ \mp\frac{\sqrt{5}}{4}\sin^2\vartheta\left(1\mp\cos\vartheta\right)^{1/2}\end{pmatrix}. \tag{6.10}$$

The first- and second-order corrections to the energies of the spin levels are, respectively [6.9]:

$$\mathcal{E}_p^{(1)}=\mathcal{H}'_{pp}=\left\langle\Psi_p^{(0)}\middle|\mathcal{H}'\middle|\Psi_p^{(0)}\right\rangle\quad\text{and}\quad\mathcal{E}_p^{(2)}=\sum_{q\neq p}\frac{\left|\left\langle\Psi_p^{(0)}\middle|\mathcal{H}'\middle|\Psi_q^{(0)}\right\rangle\right|^2}{\mathcal{E}_p^{(0)}-\mathcal{E}_q^{(0)}} \tag{6.11}$$

where in our case p and q take the values $M=-\frac{5}{2},-\frac{3}{2},\cdots,\frac{5}{2}$. Substituting in these equations $\Psi_p^{(0)}=\Psi_M^{(0)}$ with $\boldsymbol{C}_M^{(0)}$ given in eqs. (6.10), we get the energies of the spin levels up to the second order in D and up to the first order in a and F:

$$\begin{aligned}\mathcal{E}_{Mj}&=g\beta M\boldsymbol{B}_{\mathrm{E}j}+\left[3M^2-S\left(S+1\right)\right]b_{2j}^1\\&+\frac{M}{g\beta B}\left[34M^2-18S\left(S+1\right)+5\right]b_{2j}^{21}+\frac{M}{g\beta B}\left[2S\left(S+1\right)-2M^2-1\right]b_{2j}^{22}\\&+\left[35M^4-30M^2S\left(S+1\right)+25M^2-6S\left(S+1\right)+3S^2\left(S+1\right)^2\right]b_{4j}^1\end{aligned} \tag{6.12}$$

where

$$\begin{aligned}b_{2j}^1&=\tfrac{1}{6}D\left(3\cos^2\vartheta_j-1\right)\\b_{2j}^{21}&=\tfrac{1}{8}D^2\sin^2\vartheta_j\cos^2\vartheta_j\\b_{2j}^{22}&=\tfrac{1}{8}D^2\sin^2\vartheta_j\\b_{4j}^1&=\tfrac{1}{72}\left[\sqrt{2}a\sin^3\vartheta_j\cos\vartheta_j\sin3\left(\varphi_j\mp\alpha\right)-\tfrac{1}{20}(a-F)\left(35\cos^4\vartheta_j-30\cos^2\vartheta_j+3\right)\right].\end{aligned} \tag{6.13}$$

In the strong exchange case, the spins of the two non-equivalent iron ions are antiparallel: $\vartheta_1 = \vartheta$, $\varphi_1 = \varphi$, $\vartheta_2 = \pi - \vartheta$, and $\varphi_2 = \varphi + \pi$.

In our case, the third and fourth terms on the right-hand side of eq. (6.12), *i.e.* the second-order corrections in D can be neglected; indeed, for $B_{\mathrm{E}\,j} \sim 300$ T [6.10], $D^2 / g\beta B_j \sim 10^{-5}$ while $|a|$ and $|F|$ have the order of 10^{-2} cm^{-1}.

At $T = 0\,\mathrm{K}$, the only occupied spin level is that with $M = -\frac{5}{2}$. Comparing matching symmetry terms in eqs. (6.12) for this level and in eq. (6.1) (the Dzyaloshinskii-Moriya term should not be considered in this comparison) we get the crystal field contributions a_{cf}, d_{cf} and e_{cf} to the corresponding magnetocrystalline anisotropy constants of $FeBO_3$ $a_{\mathrm{FeBO_3}}$, $d_{\mathrm{FeBO_3}}$ and $e_{\mathrm{FeBO_3}}$ at 0 K:

$$\begin{aligned} a_{\mathrm{cf}}(0\,\mathrm{K}) &= 2N\left[5D + \tfrac{5}{4}(a - F)\right] \\ d_{\mathrm{cf}}(0\,\mathrm{K}) &= \tfrac{5\sqrt{2}}{6} Na\cos 3\alpha \\ e_{\mathrm{cf}}(0\,\mathrm{K}) &= 0 \end{aligned} \tag{6.14}$$

where N is the number of Fe^{3+} ions per unit volume (for $FeBO_3$ $N = 2.236\,10^{28}$ m^{-3}).

In order to calculate these contributions at elevated temperatures, we express the partition function of a magnetic sublattice of $FeBO_3$ using eq. (6.12):

$$Z_j = \sum_M \mathrm{e}^{-\frac{E_{Mj}}{kT}} \tag{6.15}$$

where k is the Boltzmann constant and T is the absolute temperature, and calculate the crystal field contribution to the density of the magnetocrystalline anisotropy energy for $FeBO_3$ as follows [6.9]:

$$\mathcal{E}_{\mathrm{cf}} = -\tfrac{1}{2} NkT \sum_j \ln Z_j \tag{6.16}$$

Taking into account that the first term on the right-hand side of eq. (6.12) is much larger than the remaining ones, we expand $\mathcal{E}_{\mathrm{cf}}$ in a Taylor series to first order in the small parameters $b^1_{2\,j} / g\beta M \boldsymbol{B}_{\mathrm{E}\,j}$ and $b^1_{4\,j} / g\beta M \boldsymbol{B}_{\mathrm{E}\,j}$:

$$\mathcal{E}_{\mathrm{cf}} = -\tfrac{1}{2} NkT \sum_j \ln \sum_M \mathrm{e}^{-\frac{g\beta B_{\mathrm{E}\,j} M}{kT}} \left\{ \begin{aligned} &1 - \left[3M^2 - S(S+1)\right] b^1_{2\,j} \\ &- \left[\begin{aligned} &35M^4 - 30M^2 S(S+1) + 25M^2 \\ &-6S(S+1) + 3S^2(S+1)^2 \end{aligned} \right] b^1_{4\,j} \end{aligned} \right\}. \tag{6.17}$$

Summing over M we get

$$\mathcal{E}_{\text{cf}} = -\tfrac{1}{2} N k T \ln \begin{bmatrix} \dfrac{\operatorname{sh} 3\xi}{\operatorname{sh} \frac{1}{2}\xi} - 4\left(5 \operatorname{ch} \tfrac{5}{2}\xi - \operatorname{ch} \tfrac{3}{2}\xi - 4 \operatorname{ch} \tfrac{1}{2}\xi\right) h_{2j}^{1} \\ -120\left(\operatorname{ch} \tfrac{5}{2}\xi - 3 \operatorname{ch} \tfrac{3}{2}\xi + 2 \operatorname{ch} \tfrac{1}{2}\xi\right) h_{4j}^{1} \end{bmatrix} \tag{6.18}$$

where $\xi = \dfrac{g\beta B_{\text{E}}}{kT}$. Expanding the latter expression in a bivariate Taylor series in h_{2j}^{1} and h_{4j}^{1} and retaining only anisotropic terms results in

$$\mathcal{E}_{\text{cf}} = -\tfrac{1}{2} N \sum_{j} \left[-2 h_{2j}^{1} t(\xi) + 24 h_{4j}^{1} r(\xi) \right] \tag{6.19}$$

where

$$t(\xi) = -\frac{\left(8 \operatorname{ch} \tfrac{1}{2}\xi + 2 \operatorname{ch} \tfrac{3}{2}\xi - 10 \operatorname{ch} \tfrac{5}{2}\xi\right) \operatorname{sh} \tfrac{1}{2}\xi}{\operatorname{sh} 3\xi}$$

and (6.20)

$$r(\xi) = -5 \frac{\left(2 \operatorname{ch} \tfrac{1}{2}\xi - 3 \operatorname{ch} \tfrac{3}{2}\xi + \operatorname{ch} \tfrac{5}{2}\xi\right) \operatorname{sh} \tfrac{1}{2}\xi}{\operatorname{sh} 3\xi}.$$

Summing eq. (6.19) over two non-equivalent Fe^{3+} sites $(j = 1, 2)$, we get the anisotropic part of the crystal field contribution to the density of the magnetocrystalline anisotropy energy for $FeBO_3$:

$$\begin{aligned} \mathcal{E}_{\text{cf}} = {} & N\left[D\, t(\xi) - \tfrac{1}{2}(a - F) r(\xi)\right] \cos^2 \vartheta + \tfrac{7}{12} N (a - F) r(\xi) \cos^4 \vartheta \\ & - \tfrac{\sqrt{2}}{3} N a\, r(\xi) \cos 3\alpha \sin^3 \vartheta \cos \vartheta \sin 3\varphi \end{aligned} \tag{6.21}$$

Comparing matching symmetry terms in eqs. (6.21) and (6.1) (the Dzyaloshinskii-Moriya term should not be considered in this comparison), we obtain the crystal field contributions to the magnetocrystalline anisotropy constants of $FeBO_3$ as a function of ξ:

$$\begin{aligned} a_{\text{cf}} &= 2N\left[D\, t(\xi) - \tfrac{1}{2}(a - F) r(\xi)\right] \\ d_{\text{cf}} &= -\tfrac{\sqrt{2}}{3} N a\, r(\xi) \cos 3\alpha \\ e_{\text{cf}} &= 0 \end{aligned} \tag{6.22}$$

At $T = 0\,\text{K}$ this equation reduces to eq. (6.14). Thus, with the spin Hamiltonian parameters $D = 0.1032, a = -0.0158, F = -0.0368\,\text{cm}^{-1}$ and $\alpha = 36^{\circ}$, *cf.* Chapter 4, "EPR of iron-gallium borate single crystals with low *x*" [6.7], we obtain the following crystal field contributions to the magnetocrystalline anisotropy constants for $FeBO_3$ at 0 K:

$$\begin{aligned} a_{\text{cf}}(0\,\text{K}) &= 4.82 \cdot 10^{5}\ \text{Jm}^{-3} \\ d_{\text{cf}}(0\,\text{K}) &= 2.55 \cdot 10^{3}\ \text{Jm}^{-3} \\ e_{\text{cf}}(0\,\text{K}) &= 0. \end{aligned} \tag{6.23}$$

Figure 6.1 shows the temperature dependences of a_{cf} and d_{cf} for $FeBO_3$, and Figure 6.2 shows a_{cf} and d_{cf} at 0 K for $Fe_xGa_{1-x}BO_3$ crystals with different *x*.

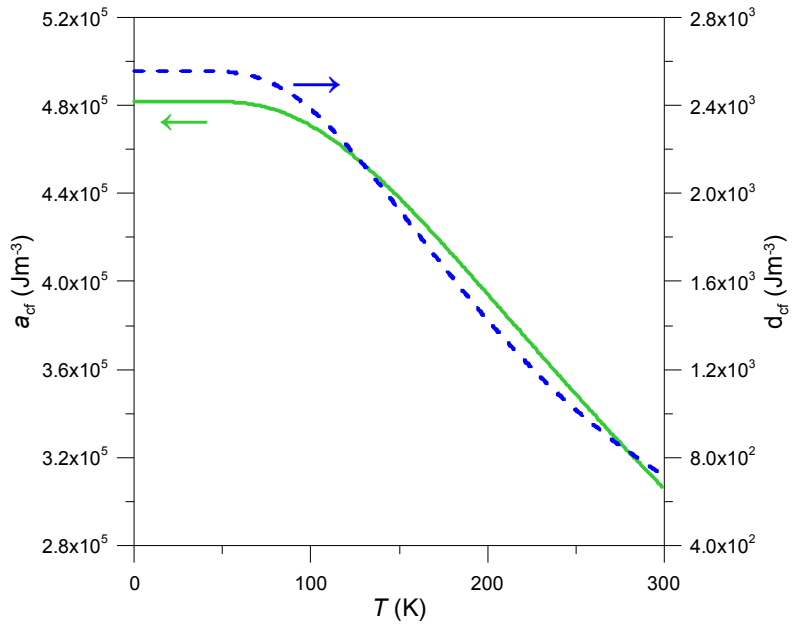

Figure 6.1 Temperature dependences of a_{cf} (continuous, green) and d_{cf} (dashed, blue) for $FeBO_3$.

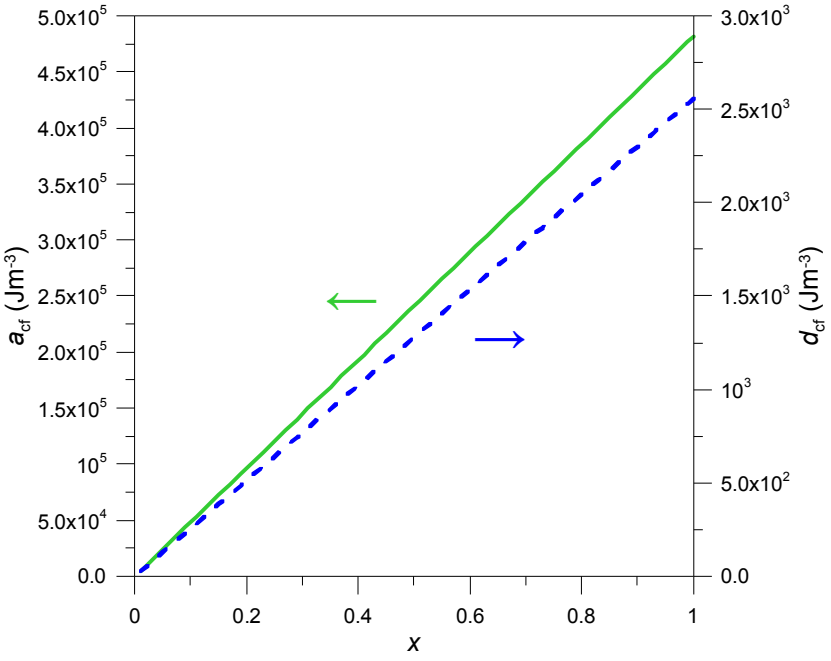

Figure 6.2 Concentration dependence of a_{cf} (continuous, green) and d_{cf} (dashed, blue) at 0 K.

6.3 Dipole-dipole contribution to magnetocrystalline anisotropy

6.3.1 Models of extended dipoles

In electrostatics, the primary source of the electric field is an electric charge. In contrast, in magnetostatics, insofar as "magnetic charges" – magnetic monopoles – have not been found in nature, the same fundamental role of primary source of the magnetic field is played by the magnetic dipole. Therefore, adequate modelling of the magnetic dipole is of paramount importance in scientific research.

As far as a *point* dipole is only an abstract idea, it is useful to consider dipole models – more realistic physical systems yielding the same magnetic field as the point dipole, at least, at distances much larger than their own size. Most often, as such a model in magnetostatics one considers a circular current loop or, by analogy with electrostatics, a pair of *fictitious* magnetic charges of opposite sign. Meanwhile, here we also consider the magnetic dipole as a *uniformly* magnetized three-dimensional body of a simple, *e.g.*, spherical shape. Usually, the uniformly magnetized sphere is considered in a different context, *viz.*, as an illustration of a boundary-value problem in magnetostatics [6.11, p. 198 ff], or an example of application of the vector potential [6.12, p. 236], thus overlooking the opportunity of using it as one more model of the magnetic dipole. Below we shall compare in detail all three models of the magnetic dipole:

a) a uniformly magnetized sphere,

b) a circular current loop,

c) a pair of fictitious magnetic charges.

Of course, the magnetic field produced by a dipole model, as well as the dipole-dipole interaction energy at intermediate and shorter distances will differ from that of the point dipole; moreover, the predictions of different models can be quite different. This issue is of importance, *e.g.*, in studying magnetic dipole-dipole interactions between paramagnetic ions in solid state, in which case a comparison with experimental observations allows choosing the most adequate description of a given magnetic source.

In one form or another, the models considered below have been described in a number of textbooks and/or research papers. Meanwhile, we have systematically considered them within the same formalism and have compared exact analytical expressions with Taylor expansions to higher-than-first order, providing simple expressions of potentials, fields and dipole-dipole interaction energy valid not only at large but also at intermediate distances. A computer code has been put forward, allowing to visualize magnetic field lines computed using both exact expressions and Taylor expansions.

6.3.1.1 Point dipole: an overview

According to the Biot-Savart law of magnetostatics, the magnetic field $\boldsymbol{B}(\boldsymbol{r})$ produced in a point of space $\boldsymbol{r}=(x,\ y,z)$ by an arbitrary distribution of steady currents in a volume V' is (*e.g.*, see ref. [6.11, pp. 175 ff; 6.12, pp. 215 ff]):

$$\boldsymbol{B}(\boldsymbol{r})=\frac{\mu_0}{4\pi}\int_{V'}\frac{\boldsymbol{j}(\boldsymbol{r}')\wedge(\boldsymbol{r}-\boldsymbol{r}')}{|\boldsymbol{r}-\boldsymbol{r}'|^3}\mathrm{d}V'. \tag{6.24}$$

The same expression is obtained with the help of the relation $\boldsymbol{B}(\boldsymbol{r})=\nabla\wedge\boldsymbol{A}(\boldsymbol{r})$, $\boldsymbol{A}(\boldsymbol{r})$ being the corresponding vector potential:

$$\boldsymbol{A}(\boldsymbol{r})=\frac{\mu_0}{4\pi}\int_{V'}\frac{\boldsymbol{j}(\boldsymbol{r}')}{|\boldsymbol{r}-\boldsymbol{r}'|}\mathrm{d}V'. \tag{6.25}$$

In eqs. (6.24) and (6.25) μ_0 is the permeability of vacuum, $\boldsymbol{j}(\boldsymbol{r}')$ is the current density in a point $\boldsymbol{r}'=(x',\ y',z')$ of the magnetic source, and the integration is performed over the whole distribution of currents. The corresponding analysis, outlined below, can be found, *e.g.*, in Jacksons' and Landau and Lifshitz's textbooks [6.11, pp. 184 ff, 6.13, pp. 103 ff].

Equation (6.25) can be expanded in powers of r^{-1} (the multipole expansion):

$$\boldsymbol{A}(\boldsymbol{r})=\frac{\mu_0}{4\pi}\frac{1}{r^{n+1}}\sum_{n=0}^{\infty}\int_{V'}r'^{n}\boldsymbol{j}(\boldsymbol{r}')P_n(\cos\alpha)\mathrm{d}V' \tag{6.26}$$

where P_n are the Legendre polynomials and α is the angle between $\boldsymbol{r}$ and $\boldsymbol{r}'$. The first term of this development ($n=0$),

$$\boldsymbol{A}_{\mathrm{m}}=\frac{\mu_0}{4\pi r}\int_{V'}\boldsymbol{j}(\boldsymbol{r}')\mathrm{d}V', \tag{6.27}$$

is the vector potential of the magnetic monopole, $\boldsymbol{A}_{\mathrm{m}}$, and it is shown to vanish. The second term in eq. (6.26), $n=1$, the magnetic dipole term,

$$\boldsymbol{A}_{\mathrm{d}}=\frac{\mu_0}{4\pi r^3}\int_{V'}(\boldsymbol{r}\cdot\boldsymbol{r}')\boldsymbol{j}(\boldsymbol{r}')\mathrm{d}V', \tag{6.28}$$

can be put in the following form:

$$\boldsymbol{A}_{\mathrm{d}}=-\frac{\mu_0}{4\pi}\boldsymbol{m}\wedge\nabla\frac{1}{r} \tag{6.29}$$

where $\boldsymbol{m}$ is the magnetic dipole moment:

$$\boldsymbol{m}=\tfrac{1}{2}\int_{V'}\boldsymbol{r}'\wedge\boldsymbol{j}(\boldsymbol{r}')\mathrm{d}V'. \tag{6.30}$$

Taking the curl of $\boldsymbol{A}_{\mathrm{d}}$, applying the product rule and keeping in mind that $\boldsymbol{m}$ is a fixed vector, for the magnetic field produced by a point dipole one gets:

$$\boldsymbol{B}_{\mathrm{d}} = \frac{\mu_0}{4\pi}\frac{3(\boldsymbol{m}\cdot\boldsymbol{r})\boldsymbol{r} - r^2\boldsymbol{m}}{r^5}. \tag{6.31}$$

According to the Curie symmetry principle [6.14], the effects generated by a cause can have only *higher* and not *lower* symmetry than the cause itself. We put the dipole at the origin O (in subsequent sections, O will be chosen in the centre of the dipole model). As far as the dipole field is invariant with respect to rotation about its axis denoted as Oz, the use of cylindrical coordinates ρ, φ, z and the corresponding unit vectors $\boldsymbol{e}_\rho$, $\boldsymbol{e}_\varphi$, $\boldsymbol{e}_z$ is the most appropriate, and all calculations can be restricted to a plane containing Oz. Meanwhile the results of calculations often are simpler in spherical coordinates $\boldsymbol{e}_r$, $\boldsymbol{e}_\vartheta$, $\boldsymbol{e}_\varphi$. Therefore, we use both coordinate systems; however, for the sake of uniformity, vector components in the cylindrical system are expressed in the spherical variables by substituting $\rho = r\sin\vartheta$ and $z = r\cos\vartheta$, the polar angle of the position vector $\boldsymbol{r}$ of the point of observation is denoted as ϑ.

Thus, eq. (6.29) in both cylindrical and spherical coordinates becomes:

$$\boldsymbol{A}_{\mathrm{d}} = \frac{\mu_0}{4\pi}\frac{m}{r^2}\sin\vartheta\,\boldsymbol{e}_\varphi. \tag{6.32}$$

The magnetic field becomes in cylindrical coordinates:

$$\boldsymbol{B}_{\mathrm{d}} = \frac{\mu_0}{4\pi}\frac{m}{r^3}\left[\tfrac{3}{2}\sin 2\vartheta\,\boldsymbol{e}_\rho + \left(3\cos^2\vartheta - 1\right)\boldsymbol{e}_z\right]. \tag{6.33}$$

and in spherical coordinates:

$$\boldsymbol{B}_{\mathrm{d}} = \frac{\mu_0}{4\pi}\frac{m}{r^3}\left(2\cos\vartheta\,\boldsymbol{e}_r + \sin\vartheta\,\boldsymbol{e}_\vartheta\right). \tag{6.34}$$

The dipole-dipole interaction energy can be obtained as the energy of a dipole n°2 placed in the magnetic field produced by a dipole n°1 (placed in the space origin):

$$\mathcal{E}_{1\leftrightarrow 2} = -\boldsymbol{m}_2\cdot\boldsymbol{B}_1 = -\frac{\mu_0}{4\pi}\frac{3(\boldsymbol{m}_1\cdot\boldsymbol{r})(\boldsymbol{m}_2\cdot\boldsymbol{r}) - \boldsymbol{m}_1\cdot\boldsymbol{m}_2 r^2}{r^5}. \tag{6.35}$$

In the case of interaction between identical *parallel* or *antiparallel* dipoles, this expression reduces to

$$\mathcal{E} = \mp\frac{\mu_0}{4\pi}\frac{3(\boldsymbol{m}\cdot\boldsymbol{r})^2 - m^2r^2}{r^5} = \mp\frac{\mu_0}{4\pi}\frac{m^2}{r^3}\left(3\cos^2\vartheta - 1\right) \tag{6.36}$$

where the – and + signs correspond to parallel and antiparallel dipoles, respectively, and ϑ is the angle between $\boldsymbol{r}$ and the common dipole axis.

6.3.1.2 Uniformly magnetized sphere

The magnetic field produced by a (uniformly) magnetized sphere, see Figure 6.3, has been considered in detail in the literature, *e.g.*, see [6.11, p. 198 ff]. A related model, that of a spinning spherical shell carrying a uniform surface charge, has been treated in the Griffith's textbook see [6.12, p. 236 ff].

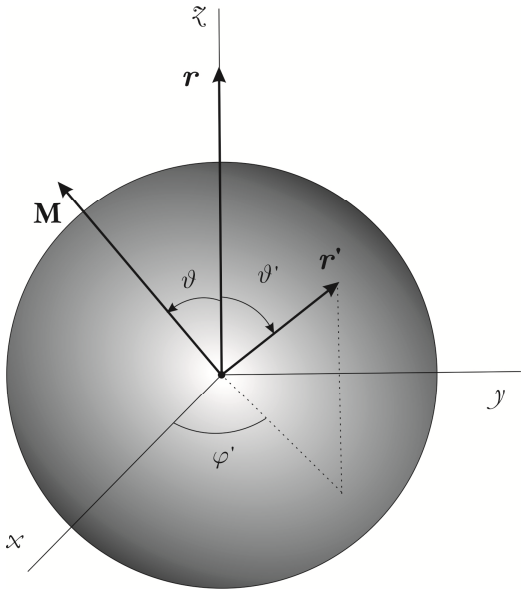

Figure 6.3 Magnetic dipole as a uniformly magnetized sphere.

The magnetic moment of a uniformly magnetized sphere of radius R and volume V can be calculated as

$$\boldsymbol{m} = V\boldsymbol{M} = \tfrac{4}{3}\pi R^3 \boldsymbol{M} \tag{6.37}$$

where $\boldsymbol{M}$ is the magnetization vector.

For a distribution of dipoles, $\boldsymbol{A}$ is obtained from eq. (6.25) as the *second* term of the multipole expansion in Legendre polynomials [6.12, p. 242 ff]. (The first term in this expansion vanishes.) One gets:

$$\boldsymbol{A}(\boldsymbol{r}) = \frac{\mu_0}{4\pi}\int_{V'} \frac{\boldsymbol{M}(\boldsymbol{r}')\wedge(\boldsymbol{r}-\boldsymbol{r}')}{|\boldsymbol{r}-\boldsymbol{r}'|^3}\mathrm{d}V' = \frac{\mu_0}{4\pi}\int_{V'} \boldsymbol{M}(\boldsymbol{r}')\wedge\nabla'\frac{1}{|\boldsymbol{r}-\boldsymbol{r}'|}\mathrm{d}V' \tag{6.38}$$

where ∇' operates over the coordinates of $\boldsymbol{r}'$. Applying the identity

$$\boldsymbol{M}(\boldsymbol{r}')\wedge\nabla'\frac{1}{|\boldsymbol{r}-\boldsymbol{r}'|} = -\nabla'\wedge\frac{\boldsymbol{M}(\boldsymbol{r}')}{|r-r'|} + \frac{1}{|\boldsymbol{r}-\boldsymbol{r}'|}\nabla'\wedge\boldsymbol{M}(\boldsymbol{r}') \tag{6.39}$$

and taking into account that $\nabla'\wedge\boldsymbol{M}(\boldsymbol{r}') = \boldsymbol{0}$ for a uniform $\boldsymbol{M}$, we rewrite eq. (6.38) as follows:

$$\boldsymbol{A}(\boldsymbol{r}) = -\frac{\mu_0}{4\pi}\int_{V'} \nabla' \wedge \frac{\boldsymbol{M}(\boldsymbol{r}')}{|\boldsymbol{r}-\boldsymbol{r}'|}\,\mathrm{d}V' . \tag{6.40}$$

According to a well-known theorem of vector analysis, the volume integral in this expression can be transformed to an integral over the closed surface S' delimiting the volume V':

$$\boldsymbol{A}(\boldsymbol{r}) = \frac{\mu_0}{4\pi}\oint_{S'} \frac{\boldsymbol{M}\wedge\boldsymbol{n}}{|\boldsymbol{r}-\boldsymbol{r}'|}\,\mathrm{d}S' \tag{6.41}$$

where $\boldsymbol{n} = \boldsymbol{r}'/r'$ is the unit vector normal to S, $\mathrm{d}S' = R^2 \sin\vartheta' \mathrm{d}\vartheta' \mathrm{d}\varphi'$ and the integration is performed over the whole surface of the sphere. A comparison between eqs. (6.41) and (6.25) shows that the latter expression represents the vector potential of a surface current of density

$$\boldsymbol{j}_S(\boldsymbol{r}') = \boldsymbol{M}\wedge\boldsymbol{n} . \tag{6.42}$$

We choose the space origin in the centre of the sphere and the z axis parallel to $\boldsymbol{r}$, $\boldsymbol{r} = r\boldsymbol{e}_z$ (such a choice allows simplifying the calculation, see ref. [6.12, p. 236 ff]. One can see from Figure 6.3 that $\boldsymbol{r}' = R\left(\sin\vartheta'\cos\varphi'\,\boldsymbol{e}_x + \sin\vartheta'\sin\varphi'\,\boldsymbol{e}_y + \cos\vartheta'\boldsymbol{e}_z\right)$ and $|\boldsymbol{r}-\boldsymbol{r}'| = \left(r^2 + R^2 - 2rR\cos\vartheta'\right)^{1/2}$. Because of the rotational symmetry about $\boldsymbol{M}$, without loss of generality $\boldsymbol{M}$ can be confined in the xz-plane, forming an angle ϑ with $\boldsymbol{r}$, $\boldsymbol{M} = M\left(\sin\vartheta\,\boldsymbol{e}_x + \cos\vartheta\,\boldsymbol{e}_z\right)$, so that

$$\boldsymbol{M}\wedge\boldsymbol{n} = M\left(-\sin\vartheta'\sin\varphi'\cos\vartheta,\ \sin\vartheta'\cos\varphi'\cos\vartheta - \cos\vartheta'\sin\vartheta,\ \sin\vartheta'\sin\varphi'\sin\vartheta\right). \tag{6.43}$$

Making all these substitutions in eq. (6.41), we notice that integrating over the range $0 \leqslant \varphi' < 2\pi$ will eliminate contributions of all φ'-dependent terms in eq. (6.43). The remaining integral over ϑ' is:

$$\boldsymbol{A} = -\tfrac{1}{2}\mu_0 M R^2 \sin\vartheta \int_{-1}^{1} \frac{\cos\vartheta'\,\mathrm{d}\cos\vartheta'}{\left(r^2 + R^2 - 2Rr\cos\vartheta'\right)^{1/2}}\boldsymbol{e}_\varphi = \begin{cases} \dfrac{\mu_0}{4\pi}\dfrac{\boldsymbol{m}\,r}{R^3}\sin\vartheta\,\boldsymbol{e}_\varphi, & r \leqslant R, \\ \dfrac{\mu_0}{4\pi}\dfrac{\boldsymbol{m}}{r^2}\sin\vartheta\,\boldsymbol{e}_\varphi, & r \geqslant R \end{cases} \tag{6.44}$$

where the Cartesian y-axis is identified as a radial cylindrical ρ-axis, and the magnetic dipole moment is introduced through eq. (6.37). Equation (6.44) is equivalent to eq. (5.111) in Jackson's textbook [6.11]. Taking the curl of $\boldsymbol{A}$ inside and outside the magnetized sphere, we get the corresponding magnetic fields $\boldsymbol{B}^{\mathrm{int}}$ and $\boldsymbol{B}^{\mathrm{ext}}$ in cylindrical coordinates:

$$\begin{aligned} \boldsymbol{B}^{\mathrm{int}} &= 2\frac{\mu_0}{4\pi}\frac{\boldsymbol{m}}{R^3}\boldsymbol{e}_z, \\ \boldsymbol{B}^{\mathrm{ext}} &= \frac{\mu_0}{4\pi}\frac{\boldsymbol{m}}{r^3}\left[\tfrac{3}{2}\sin 2\vartheta\,\boldsymbol{e}_\rho + \left(3\cos^2\vartheta - 1\right)\boldsymbol{e}_z\right] \end{aligned} \tag{6.45}$$

and in spherical coordinates:

$$\begin{aligned} \boldsymbol{B}^{\text{int}} &= 2\frac{\mu_0}{4\pi}\frac{\boldsymbol{m}}{R^3}\left(\cos\vartheta\,\boldsymbol{e}_r - \sin\vartheta\,\boldsymbol{e}_\vartheta\right), \\ \boldsymbol{B}^{\text{ext}} &= \frac{\mu_0}{4\pi}\frac{\boldsymbol{m}}{r^3}\left(2\cos\vartheta\,\boldsymbol{e}_r + \sin\vartheta\,\boldsymbol{e}_\vartheta\right). \end{aligned} \tag{6.46}$$

One can see that inside the uniformly magnetized sphere the magnetic field is uniform, as known from magnetostatics. Most interestingly, outside this sphere, the magnetic field at any distance coincides with that of the point dipole, *cf.* eqs. (6.45) and (6.46) with eqs. (6.33) and (6.34), respectively.

Obviously, in this model the interaction energy between two identical mutually non-penetrating dipoles is the same as that between two point dipoles, *cf.* eq. (6.36).

6.3.1.3 Circular current loop

Most often, in magnetostatics one takes a circular loop of electric current (Ampérian current) as a basic model of the magnetic dipole. Let us consider a loop of radius R and area $S=\pi R^2$, carrying a current I supposed to flow counterclockwise direction as seen from above the xy plane, see Figure 6.4. By definition, its magnetic moment is $m=IS=\pi R^2 I$. An element of current $I\,\mathrm{d}\boldsymbol{l}$, where $\mathrm{d}\boldsymbol{l}$ is an elementary vector tangent to the loop in a point M, produces an elementary vector potential in an arbitrary point in space P:

$$\mathrm{d}\boldsymbol{A} = \frac{\mu_0}{4\pi}\frac{I\,\mathrm{d}\boldsymbol{l}}{|MP|} = \frac{\mu_0}{4\pi}\frac{\boldsymbol{m}}{\pi R^2}\frac{\mathrm{d}\boldsymbol{l}}{|MP|}. \tag{6.47}$$

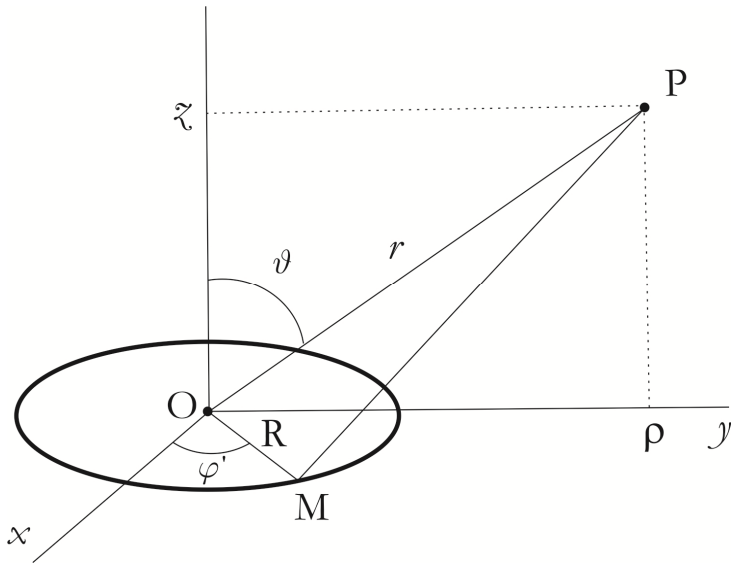

Figure 6.4 Magnetic dipole as an Ampérian current.

For definiteness, let the loop be placed in the *xy*-plane. Because of the rotational symmetry about the z-axis, without loss of generality P can be placed in the yz-plane. In spherical coordinates we get $\mathrm{d}\boldsymbol{l} = R\,\mathrm{d}\varphi'\boldsymbol{e}_{\varphi'}$. From Figure 6.4 one can see that $\overrightarrow{MP} = \overrightarrow{MO} + \overrightarrow{OP}$ and $|MP| = \sqrt{r^2 + R^2 - 2Rr\sin\vartheta\sin\varphi'}$.

In performing the integration of $\mathrm{d}\boldsymbol{A}$ given in eq. (6.47) over the current loop, $\mathrm{d}\boldsymbol{l}$ should be converted to Cartesian coordinates by substituting $\boldsymbol{e}_{\varphi'} = -\sin\varphi'\boldsymbol{e}_x + \cos\varphi'\boldsymbol{e}_y$. Thus,

$$\boldsymbol{A} = \frac{\mu_0}{4\pi}\frac{m}{\pi R}\int_0^{2\pi}\frac{-\sin\varphi'\boldsymbol{e}_x + \cos\varphi'\boldsymbol{e}_y}{\sqrt{r^2 + R^2 - 2Rr\sin\vartheta\sin\varphi'}}\mathrm{d}\varphi' = A_x\boldsymbol{e}_x + A_y\boldsymbol{e}_y. \tag{6.48}$$

It turns out that $A_y = 0$. Identifying A_x in both cylindrical and spherical coordinates as $-A_\varphi$ and denoting $r_\pm^{\,2} = r^2 + R^2 \pm 2Rr\sin\vartheta$ and $k = 2\sqrt{Rr\sin\vartheta}\big/r_+$, we get:

$$\boldsymbol{A} = 8\frac{\mu_0}{4\pi}\frac{m}{\pi R k^2 r_+}\Psi(k)\boldsymbol{e}_\varphi \tag{6.49}$$

where

$$\Psi(k) = \left(1 - \tfrac{1}{2}k^2\right)\mathrm{K}(k) - \mathrm{E}(k), \tag{6.50}$$

and $\mathrm{K}(k)$ and $\mathrm{E}(k)$ are, respectively, complete elliptic integrals of the first and the second kind. Equation (6.49) coincides with eq. (5.37) in Jackson's textbook [6.11]. From this equation we derive the magnetic field in cylindrical coordinates:

$$\begin{aligned} B_\rho &= 2\frac{\mu_0}{4\pi}\frac{m}{\pi R^2 r_+ r_-^{\,2}}\cot\vartheta\left[\left(r^2 + R^2\right)\mathrm{E}(k) - r_-^{\,2}\,\mathrm{K}(k)\right], \\ B_z &= 2\frac{\mu_0}{4\pi}\frac{m}{\pi R^2 r_+ r_-^{\,2}}\left[\left(R^2 - r^2\right)\mathrm{E}(k) + r_-^{\,2}\,\mathrm{K}(k)\right] \end{aligned} \tag{6.51}$$

and in spherical coordinates:

$$\begin{aligned} B_r &= 4\frac{\mu_0}{4\pi}\frac{m}{\pi r_+ r_-^{\,2}}\cos\vartheta\,\mathrm{E}(k), \\ B_\vartheta &= 2\frac{\mu_0}{4\pi}\frac{m}{\pi R^2 r_+ r_-^{\,2}\sin\vartheta}\left[\left(r^2 + R^2\cos 2\vartheta\right)\mathrm{E}(k) - r_-^{\,2}\,\mathrm{K}(k)\right]. \end{aligned} \tag{6.52}$$

Next, we calculate the interaction energy between two identical and parallel Ampérian currents of the same radii R, see Figure 6.5.

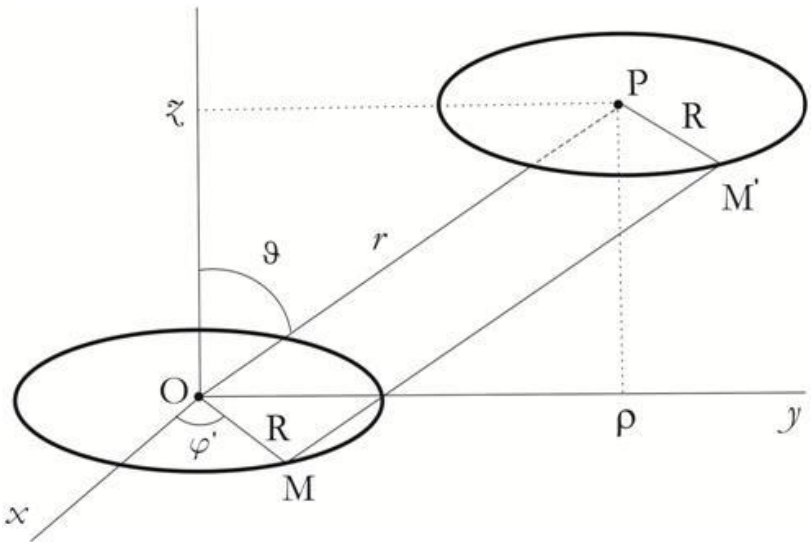

Figure 6.5 System of two interacting Ampérian currents.

In order to obtain the correct sign of the dipole-dipole interaction energy $\mathcal{E}$, we express its relation to the mutual inductance $\mathscr{M}$ of two equal currents flowing in the same direction in two parallel *coaxial* loops, as follows:

$$\mathcal{E} = -\mathscr{M} I^2 . \tag{6.53}$$

Indeed, the potential energy of attracting currents should be negative, and it is more convenient to define $\mathscr{M}$ as positive.

Using the expression of $\mathscr{M}$ given by Grover [6.15] and Akyel *et al.* [6.16], in the actual case we get:

$$\mathcal{E} = \mp 8 \frac{\mu_0}{4\pi} \frac{m^2}{\pi^2 R^3} \int_0^{\pi} \frac{1 - \frac{r}{R}\sin\vartheta\cos\varphi'}{v^{3/2}} \frac{\Psi(\kappa)}{\kappa} \mathrm{d}\varphi' \tag{6.54}$$

where the – and + signs correspond to parallel and antiparallel dipoles, respectively, Ψ has been defined in eq. (6.50) and

$$\kappa^2 = \frac{4v}{(1+v)^2 + \frac{r^2}{R^2}\cos^2\vartheta} \tag{6.55}$$

with

$$v = \left(\frac{r^2}{R^2}\sin^2\vartheta - 2\frac{r}{R}\sin\vartheta\cos\varphi' + 1 \right)^{1/2} . \tag{6.56}$$

In eqs. (6.54) to (6.56) φ' is the angle between the x axis and OM. $\mathrm{K}(\kappa)$ and $\mathrm{E}(\kappa)$ can be developed in infinite series, see ref. [6.17, p. 927 ff]:

$$\mathrm{K}(\kappa)=\tfrac{1}{2}\pi\left\{1+\left(\tfrac{1}{2}\right)^2\kappa^2+\left(\frac{1\cdot3}{2\cdot4}\right)^2\kappa^4+\cdots+\left[\frac{(2n-1)!!}{(2n)!!}\right]^2\kappa^{2n}+\cdots\right\} \tag{6.57}$$

and

$$\mathrm{E}(\kappa)=\tfrac{1}{2}\pi\left\{1-\left(\tfrac{1}{2}\right)^2\frac{\kappa^2}{1}-\left(\frac{1\cdot3}{2\cdot4}\right)^2\frac{\kappa^4}{3}-\cdots-\left[\frac{(2n-1)!!}{(2n)!!}\right]^2\frac{\kappa^{2n}}{2n-1}-\cdots\right\}. \tag{6.58}$$

According to these expressions,

$$\Psi(\kappa)=\pi\begin{pmatrix}\frac{1}{32}\kappa^4+\frac{3}{128}\kappa^6+\frac{75}{4096}\kappa^8+\frac{245}{16384}\kappa^{10}+\frac{6615}{524288}\kappa^{12}\\+\frac{22869}{2097152}\kappa^{14}+\frac{1288287}{134217728}\kappa^{16}+\frac{4601025}{536870912}\kappa^{18}+\cdots\end{pmatrix}. \tag{6.59}$$

In the model of a circular current loop, the vector potential, the dipole magnetic field and the dipole-dipole interaction energy can be analytically expressed only through the elliptical integrals, see eqs. (6.49), (6.51), (6.52) and (6.54). In order to obtain more simple expressions valid at intermediate distances, we have used expansions in Taylor series to the sixth order in the small parameter $\varepsilon = {\mathrm{R}}/{r}$. Expanding eq. (6.49), we get:

$$\boldsymbol{A}=\frac{\mu_0}{4\pi}\frac{\boldsymbol{m}}{r^2}\left(-P_1^1+\tfrac{1}{4}P_3^1\varepsilon^2-\tfrac{1}{8}P_5^1\varepsilon^4+\tfrac{5}{64}P_7^1\varepsilon^6\right)\boldsymbol{e}_\varphi\,. \tag{6.60}$$

The same development applied to eqs. (6.51) and (6.52) yields approximate expressions for the magnetic field, respectively, in cylindrical,

$$\begin{aligned}B_\rho&=\frac{\mu_0}{4\pi}\frac{\boldsymbol{m}}{r^3}\left(-P_2^1+\tfrac{3}{4}P_4^1\varepsilon^2-\tfrac{5}{8}P_6^1\varepsilon^4+\tfrac{35}{64}P_8^1\varepsilon^6\right),\\ B_z&=\frac{\mu_0}{4\pi}\frac{\boldsymbol{m}}{r^3}\left(2P_2-3P_4\varepsilon^2+\tfrac{15}{4}P_6\varepsilon^4-\tfrac{35}{8}P_8\varepsilon^6\right)\end{aligned} \tag{6.61}$$

and in spherical coordinates,

$$\begin{aligned}B_r&=\frac{\mu_0}{4\pi}\frac{\boldsymbol{m}}{r^3}\left(2P_1-3P_3\varepsilon^2+\tfrac{15}{4}P_5\varepsilon^4-\tfrac{35}{8}P_7\varepsilon^6\right),\\ B_\vartheta&=\frac{\mu_0}{4\pi}\frac{\boldsymbol{m}}{r^3}\left(-P_1^1+\tfrac{3}{4}P_3^1\varepsilon^2-\tfrac{5}{8}P_5^1\varepsilon^4+\tfrac{35}{64}P_7^1\varepsilon^6\right).\end{aligned} \tag{6.62}$$

Here for brevity we are using the Legendre polynomials $P_n(\cos\vartheta)$ and associated Legendre polynomials $P_n^m(\cos\vartheta)$ shortened to P_n and P_n^m, respectively [6.17, pp. 716 ff and 741 ff]. $P_n(\cos\vartheta)$ and $P_n^1(\cos\vartheta)$ used in this paper are:

$$
\begin{aligned}
P_1(\cos\vartheta) &= \cos\vartheta \\
P_2(\cos\vartheta) &= \tfrac{1}{2}(3\cos^2\vartheta - 1) \\
P_3(\cos\vartheta) &= \tfrac{1}{2}(5\cos^2\vartheta - 3)\cos\vartheta \\
P_4(\cos\vartheta) &= \tfrac{1}{8}(35\cos^4\vartheta - 30\cos^2\vartheta + 3) \\
P_5(\cos\vartheta) &= \tfrac{1}{8}(63\cos^4\vartheta - 70\cos^2\vartheta + 15)\cos\vartheta \\
P_6(\cos\vartheta) &= \tfrac{1}{16}(231\cos^6\vartheta - 315\cos^4\vartheta + 105\cos^2\vartheta - 5) \\
P_7(\cos\vartheta) &= \tfrac{1}{16}(429\cos\vartheta^6 - 693\cos^4\vartheta + 315\cos\vartheta^2 - 35)\cos\vartheta \\
P_8(\cos\vartheta) &= \tfrac{1}{128}\left(6435\cos^8\vartheta - 12012\cos\vartheta^6 + 6930\cos\vartheta^4 - 1260\cos^2\vartheta + 35\right)
\end{aligned}
\tag{6.63}
$$

$$
\begin{aligned}
P_1^1(\cos\vartheta) &= -\sin\vartheta \\
P_2^1(\cos\vartheta) &= -\tfrac{3}{2}\sin 2\vartheta \\
P_3^1(\cos\vartheta) &= -\tfrac{3}{2}(5\cos^2\vartheta - 1)\sin\vartheta \\
P_4^1(\cos\vartheta) &= -\tfrac{5}{4}(7\cos^2\vartheta - 3)\sin 2\vartheta \\
P_5^1(\cos\vartheta) &= -\tfrac{15}{8}(21\cos^4\vartheta - 14\cos^2\vartheta + 1)\sin\vartheta \\
P_6^1(\cos\vartheta) &= -\tfrac{21}{16}(33\cos^4\vartheta - 30\cos^2\vartheta + 5)\sin 2\vartheta \\
P_7^1(\cos\vartheta) &= -\tfrac{7}{16}(429\cos^6\vartheta - 495\cos^4\vartheta + 135\cos^2\vartheta - 5)\sin\vartheta \\
P_8^1(\cos\vartheta) &= -\tfrac{9}{32}(715\cos^6\vartheta - 1001\cos^4\vartheta + 385\cos\vartheta^2 - 35)\sin 2\vartheta
\end{aligned}
\tag{6.64}
$$

Alternatively, eqs. (6.61) and (6.62) can be obtained directly from the relation $\boldsymbol{B} = \nabla \wedge \boldsymbol{A}$ with $\boldsymbol{A}$ given by eq. (6.60). Finally, expanding eq. (6.54) in a Taylor series, we get the expression of the interaction energy:

$$
\mathcal{E} = \mp 2\frac{\mu_0}{4\pi}\frac{m^2}{r^3}\left[P_2 - 3P_4\varepsilon^2 + \tfrac{75}{8}P_6\varepsilon^4 - \tfrac{245}{8}P_8\varepsilon^6\right] \tag{6.65}
$$

where the – and + signs correspond to parallel and antiparallel dipoles, respectively.

6.3.1.4 Pair of fictitious magnetic charges

The third model represents the magnetic dipole as an assembly of two fictitious magnetic monopoles, or "magnetic charges" $\pm q$, a distance d apart, see Figure 6.6. By analogy with electrostatics, the magnetic dipole moment is defined as $\boldsymbol{m} = q\boldsymbol{d}$, so that in order to calculate the magnetic field produced by such a dipole, one is tempted to introduce a scalar magnetic potential, *e.g.*, see [6.11, p. 196 ff]. However, for the sake of consistency, we prefer using here a vector potential, and, in accordance with the superposition principle, it can be taken as a sum of the vector potentials of two magnetic monopoles of opposite signs.

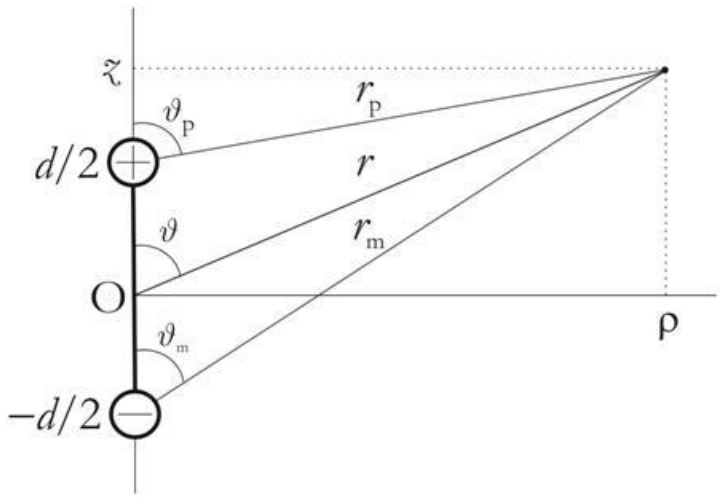

Figure 6.6 Magnetic dipole as an assembly of two "magnetic charges".

The vector potential of a magnetic monopole introduced by Dirac [6.18]:

$$\boldsymbol{A} = \frac{\mu_0}{4\pi}\frac{m}{dr}\frac{1-\cos\theta}{\sin\theta}\boldsymbol{e}_\varphi . \tag{6.66}$$

yields a correct expression of the magnetic field expected to be produced by a magnetic monopole. However, it is not quite satisfactory from both mathematical and physical standpoints, as far as it exhibits a singularity along the half-line $\vartheta = \pi$ (the so-called Dirac string); while for a magnetic monopole the direction of this half-line is completely arbitrary. Meanwhile, it can be readily shown that the vector potential of a pair of magnetic monopoles of opposite signs:

$$\boldsymbol{A} = \frac{\mu_0}{4\pi}\frac{m}{d}\left(\frac{1-\cos\vartheta_p}{r_p\sin\vartheta_p} - \frac{1-\cos\vartheta_m}{r_m\sin\vartheta_m}\right)\boldsymbol{e}_\varphi \tag{6.67}$$

has no more such singularities. The latter equation can be rewritten as:

$$\boldsymbol{A} = \frac{\mu_0}{4\pi r}\frac{m}{d\sin\vartheta}\left(\frac{r\cos\vartheta + \frac{1}{2}d}{r_m} - \frac{r\cos\vartheta - \frac{1}{2}d}{r_p}\right)\boldsymbol{e}_\varphi \tag{6.68}$$

where the connotation of different symbols is shown in Figure 6.6. Obviously, the following relations hold: $r_p = \sqrt{r^2 - dr\cos\vartheta + \frac{1}{4}d^2}$, $r_m = \sqrt{r^2 + dr\cos\vartheta + \frac{1}{4}d^2}$, $\cos\vartheta_p = \frac{r\cos\vartheta - \frac{1}{2}d}{r_p}$, $\cos\vartheta_m = \frac{r\cos\vartheta + \frac{1}{2}d}{r_m}$ and $r_p\sin\vartheta_p = r_m\sin\vartheta_m = \rho = r\sin\vartheta$.

For the magnetic field we get: in cylindrical coordinates,

$$B_\rho = \frac{\mu_0}{4\pi}\frac{m}{d} r\sin\vartheta\left(\frac{1}{r_\mathrm{p}^{\,3}} - \frac{1}{r_\mathrm{m}^{\,3}}\right),$$
$$B_z = \frac{\mu_0}{4\pi}\frac{m}{d}\left(\frac{r\cos\vartheta - \frac{1}{2}d}{r_\mathrm{p}^{\,3}} - \frac{r\cos\vartheta + \frac{1}{2}d}{r_\mathrm{m}^{\,3}}\right) \tag{6.69}$$

and in spherical coordinates,

$$B_r = \frac{\mu_0}{4\pi}\frac{m}{d}\left(\frac{r - \frac{1}{2}d\cos\vartheta}{r_\mathrm{p}^{\,3}} - \frac{r + \frac{1}{2}d\cos\vartheta}{r_\mathrm{m}^{\,3}}\right),$$
$$B_\vartheta = \frac{1}{2}\frac{\mu_0}{4\pi} m\sin\vartheta\left(\frac{1}{r_\mathrm{p}^{\,3}} + \frac{1}{r_\mathrm{m}^{\,3}}\right). \tag{6.70}$$

For the interaction energy between two parallel/antiparallel dipoles, we get:

$$\mathcal{E} = \pm\frac{\mu_0}{4\pi}\frac{m^2}{d^2}\left(\frac{2}{r} - \frac{1}{r_\mathrm{mp}} - \frac{1}{r_\mathrm{pm}}\right) \tag{6.71}$$

where $r_\mathrm{mp} = \sqrt{r^2 + d^2 + 2dr\cos\vartheta}$ and $r_\mathrm{pm} = \sqrt{r^2 + d^2 - 2dr\cos\vartheta}$, see Figure 6.7 for the notation. The choice of $\pm$ signs refers to parallel and antiparallel dipoles, respectively.

Note that eqs. (6.69) to (6.71) can be immediately obtained from the corresponding expressions for electric dipoles by substituting the electric dipole moment and the permittivity of vacuum ε_0 by the magnetic dipole moment and $1/\mu_0$, respectively.

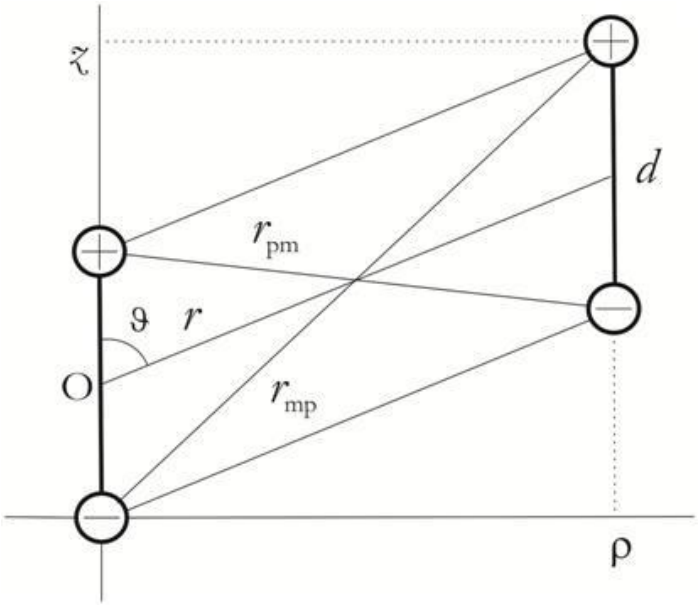

Figure 6.7 System of two interacting magnetic-charge dipoles.

The expressions for the field and the energy in the model of a pair of magnetic charges are simpler in comparison with those obtained with the model of a circular current loop. Nevertheless, we still have provided the corresponding expansions in the Taylor series, useful for a direct comparison between these two models. In the same approximation as in the previous section, redefining the small parameter as $\varepsilon = d/r$, eqs. (6.67) to (6.70) become:

$$\boldsymbol{A} = -\frac{\mu_0}{4\pi}\frac{\boldsymbol{m}}{r^2}\left(P_1^1 + \tfrac{1}{12}P_3^1\varepsilon^2 + \tfrac{1}{80}P_5^1\varepsilon^4 + \tfrac{1}{448}P_7^1\varepsilon^6\right)\boldsymbol{e}_\varphi, \tag{6.72}$$

$$\begin{aligned} B_\rho &= -\frac{\mu_0}{4\pi}\frac{\boldsymbol{m}}{r^3}\left(P_2^1 + \tfrac{1}{4}P_4^1\varepsilon^2 + \tfrac{1}{16}P_6^1\varepsilon^4 + \tfrac{1}{64}P_8^1\varepsilon^6\right), \\ B_\zeta &= \frac{\mu_0}{4\pi}\frac{\boldsymbol{m}}{r^3}\left(2P_2 + P_4\varepsilon^2 + \tfrac{3}{8}P_6\varepsilon^4 + \tfrac{1}{8}P_8\varepsilon^6\right) \end{aligned} \tag{6.73}$$

and

$$\begin{aligned} B_r &= \frac{\mu_0}{4\pi}\frac{\boldsymbol{m}}{r^3}\left(2P_1 + P_3\varepsilon^2 + \tfrac{3}{8}P_5\varepsilon^4 + \tfrac{1}{8}P_7\varepsilon^6\right), \\ B_\vartheta &= -\frac{\mu_0}{4\pi}\frac{\boldsymbol{m}}{r^3}\left(P_1^1 + \tfrac{1}{4}P_3^1\varepsilon^2 + \tfrac{1}{16}P_5^1\varepsilon^4 + \tfrac{1}{64}P_7^1\varepsilon^6\right). \end{aligned} \tag{6.74}$$

An analogous expansion for $\mathcal{E}$ yields:

$$\mathcal{E} = \mp 2\frac{\mu_0}{4\pi}\frac{\boldsymbol{m}^2}{r^3}\left[P_2 + P_4\varepsilon^2 + P_6\varepsilon^4 + P_8\varepsilon^6\right] \tag{6.75}$$

where the – and + signs correspond to parallel and antiparallel dipoles, respectively.

6.3.1.5 Comparison between the dipole models

Figure 6.8 compares radial dependences of B_ζ in the equatorial plane $\vartheta = \pi/2$ for different dipole models. The calculations have been made using the exact expressions for B_ζ. The model sizes and the distances are scaled in relative distance units (rdu). As one can see, for the uniformly magnetized sphere of radius R, B_ζ remains uniform at $\rho < R$, has a discontinuity at $\rho = R$ and follows the corresponding dependence for the point dipole at $\rho > R$. The analogous dependence for the current loop of radius R has a singularity at $\rho = R$, and for the pair of magnetic charges B_ζ it has a minimum at $\rho = 0$. Thus, at small and intermediate distances in comparison with the model size, the behaviour of all three models is very different. At large distances, see inset in Figure 6.8, the magnetic fields produced by different magnetic dipole models match that of the point dipole, as expected.

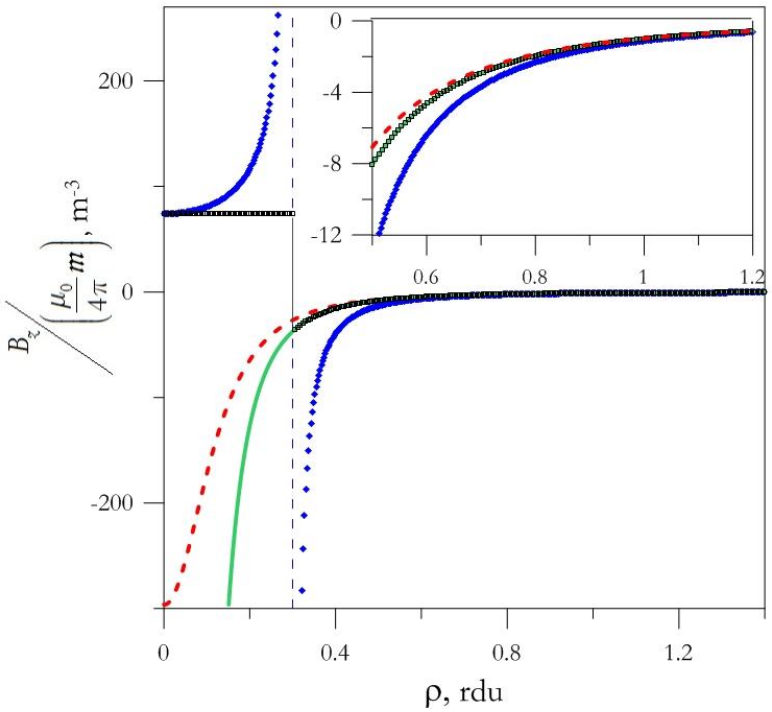

Figure 6.8 $B_z(\rho, \vartheta = \pi/2)$ dependences for a uniformly magnetized sphere of radius $R = 0.3$ rdu (circles, grey), a circular current loop of radius $R = 0.3$ rdu, (diamonds, blue) and a pair of fictitious magnetic charges, $d = 0.3$ rdu apart, (dashed, red) compared do that of the point dipole (continuous, green). The inset: shows a zoom in the behaviour of B_z at larger distances.

A still better insight in the behaviour of different models at small and intermediate distances can be achieved by visualizing magnetic field lines. By definition, the elementary vector of the tangent to the field line, $\mathrm{d}\boldsymbol{L}$, in each point of this line is parallel to the field vector. The vector product for parallel vectors vanishes, so, for the magnetic field lines we get $\mathrm{d}\boldsymbol{L} \wedge \boldsymbol{B} = \boldsymbol{0}$. In cylindrical coordinates this reduces to $\mathrm{d}z \Big/ \mathrm{d}\rho = B_z \Big/ B_\rho$, and we get the following equation for the magnetic field lines:

$$z(\rho) = \int_{y=\rho_{\mathrm{inf}}}^{\rho \le \rho_{\mathrm{sup}}} \frac{B_z(y, z)}{B_\rho(y, z)} \mathrm{d}y \tag{6.76}$$

where ρ_{inf} and ρ_{sup} are, respectively, the smallest and the largest value of ρ for a given field line, and $z \in [\rho_{\mathrm{inf}}, \rho_{\mathrm{sup}}]$ is a dummy variable.

We have put forward a FORTRAN 77 computer code for calculating the magnetic field lines for different dipole models according to both the exact expressions and their Taylor expansions, see [6.19]. Visualization of the field lines calculated using the Taylor expansions allows to estimate contributions of various expansion terms and the general convergence of the Taylor series for different models.

In the model of a circular current loop the exact expressions of the magnetic field components, eqs. (6.51), are very complicated, so, we have chosen to compute them by numerical integration over the angle φ' of the elementary field components expressed through the Biot-Savart law, see eq. (6.24) and Figure 6.4:

$$\begin{aligned} B_\rho &= \frac{\mu_0}{4\pi}\frac{m}{\pi R}\int_0^{2\pi}\frac{z\sin\varphi'}{\left(R^2+\rho^2-2R\rho\sin\varphi'+z^2\right)^{3/2}}\,\mathrm{d}\varphi', \\ B_z &= \frac{\mu_0}{4\pi}\frac{m}{\pi R}\int_0^{2\pi}\frac{R-\rho\sin\varphi'}{\left(R^2+\rho^2-2R\rho\sin\varphi'+z^2\right)^{3/2}}\,\mathrm{d}\varphi'. \end{aligned} \tag{6.77}$$

The corresponding exact expressions for the model of a pair of magnetic charges have been given in the previous section, see eqs. (6.69).

The Taylor expansions of the field line equation in the computer code have been obtained by expanding in the Taylor series the ratio B_z over B_ρ. For the model of a current loop this results in

$$\frac{B_z}{B_\rho} = \frac{2}{3}\frac{1}{\sin 2\vartheta}\left[\begin{aligned} &3\cos^2\vartheta - 1 + \tfrac{1}{4}\left(5\cos^2\vartheta+3\right)\varepsilon^2 - \tfrac{5}{32}\left(7\cos^4\vartheta-6\cos^2\vartheta-1\right)\varepsilon^4 \\ &+\tfrac{5}{512}\left(203\cos^6\vartheta-273\cos^4\vartheta+65\cos^2\vartheta+5\right)\varepsilon^6 \end{aligned}\right], \tag{6.78}$$

and for that of a pair of magnetic charges we get:

$$\frac{B_z}{B_\rho} = \frac{2}{3}\frac{1}{\sin 2\vartheta}\left[\begin{aligned} &3\cos^2\vartheta - 1 - \tfrac{1}{12}\left(5\cos^2\vartheta+3\right)\varepsilon^2 - \tfrac{1}{144}\left(7\cos^4\vartheta-15\cos^2\vartheta\right)\varepsilon^4 \\ &-\tfrac{1}{1728}\left(26\cos^6\vartheta-63\cos^4\vartheta+45\cos^2\vartheta\right)\varepsilon^6 \end{aligned}\right]. \tag{6.79}$$

We remind the reader that in eqs. (6.78) and (6.79) ε has different meaning. In all cases, the numerical integration over ρ in eq. (6.76) has been performed using the Runge–Kutta method [6.20, pp. 420 ff].

With the aid of this program we have visualized the field lines for all models, see Figure 6.9. The calculations have been made using the exact expressions, *vide supra*, and the modelling parameters have been chosen in such a way that all the field lines ostensibly merge at the maximal distance $r_{\max}$ from the source. As one can see, at distances comparable with the model size, the appearance of the field lines predicted by each model is totally different. The lines produced by a uniformly magnetized sphere are parallel to the dipole axis inside the sphere and coincide with those of the point dipole outside the sphere. The lines due to a current loop close on themselves inside the loop while those of a pair of magnetic charges diverge from the positive charge and converge towards the negative one. In all cases, at small distances the behaviour of the field lines has nothing in common with that expected for the point dipole, in which case the field lines close on themselves in the space origin.

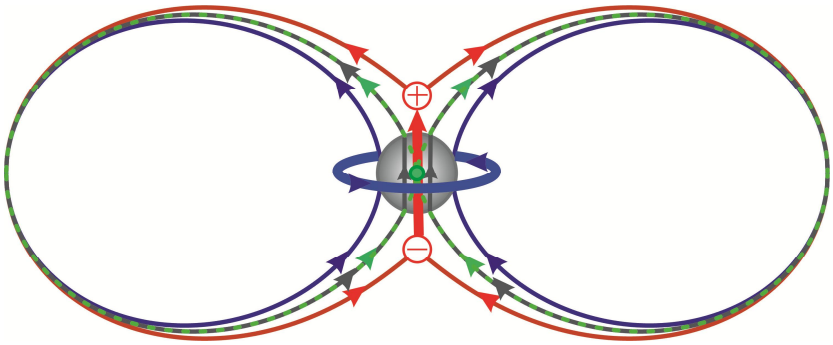

Figure 6.9 Magnetic field lines for different dipole models scaled in rdu. The external line (red) corresponds to a pair of magnetic charges $d = 0.75$ apart. The intermediate dashed (green) and continuous (grey) lines refer to a point dipole and uniformly magnetized sphere of radius $R = 0.20$, respectively. The internal line (blue) is due to a current loop of radius $R = 0.40$. All the lines merge at the maximal distance $r_{\max} = 2.0$.

In certain applications, *e.g.* in calculating the interaction energy between magnetic moments embedded in a condensed matrix, one needs a good approximation for the magnetic field produced at intermediate distances from the magnetic source. Figure 6.10 compares the magnetic field lines calculated using the exact expressions and Taylor expansions to different orders in the corresponding small parameter for the models of a circular current loop and a pair of fictitious magnetic charges. One can see that in the model of a current loop the expansion up to the 6th order in $\varepsilon = R/r$ provides a good approximation for $R/r_{\max} \leqslant 3/4$, and in the model of a pair of magnetic charges the same expansion in $\varepsilon = d/r$ already for $d/r_{\max} = 3/4$ yields a result practically indistinguishable from that of the exact calculation.

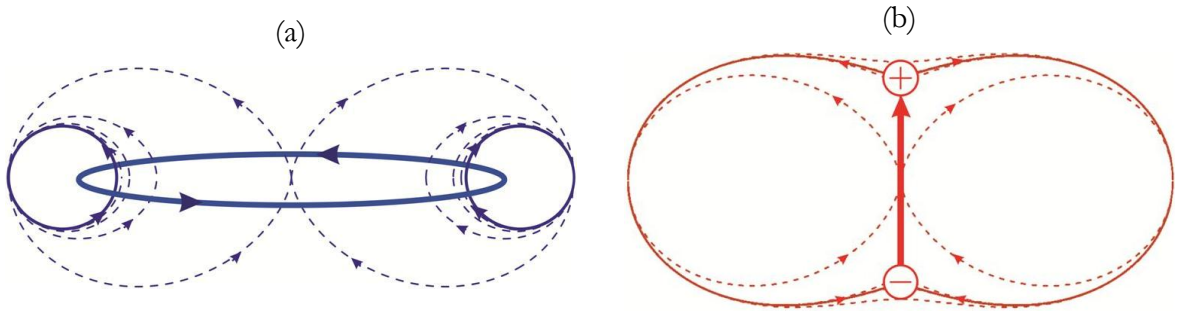

Figure 6.10 Magnetic field lines in the models of a current loop (a) and of a pair of magnetic charges (b) calculated using the exact expressions of the magnetic fields (continuous lines) and the Taylor expansions to the 0th, 2nd, 4th and 6th order in the corresponding small parameters. All the lines merge at the maximal distance $r_{\max} = 2.0$ rdu. With increasing the expansion order, in (a) each subsequent field line remains confined inside the previous one, while in (b) it passes alternately from inside to outside of the exact field line profile.

6.3.2 Applying the models of extended dipoles to calculate dipole-dipole contribution to magnetocrystalline anisotropy

In the model of uniformly magnetized sphere, *vide supra*, the dipole-dipole interaction energy is the same as for the point dipoles; therefore it is entirely described by the $P_2(\cos\vartheta)$ Legendre polynomial, see eq. (6.36). Hence, this model can describe only uniaxial magnetocrystalline anisotropy and not the hexagonal basal magnetocrystalline anisotropy in iron borate. Thus, in what follows we consider only the two remaining models. We have seen that, starting from the second term in the Taylor series, the expressions of the dipole-dipole interaction energy in these models totally diverge. Interestingly, this divergence goes in opposite directions, so that the characteristics of the magnetic dipole at small and intermediate distances become quite sensible to the choice between these two models.

In order to calculate the dipole-dipole contribution to the magnetocrystalline anisotropy constants of $FeBO_3$ we shall consider a more general case where the dipole axis does not necessarily coincide with C_3-axis, *cf.* Chapter 1, "Crystal and magnetic structure of iron borate".

6.3.2.1 Two circular current loops

Here we consider the interaction energy $\mathcal{E}$ between two identical and parallel circular current loops (Ampérian currents) of the same radii R and areæ $S=\pi R^2$, carrying a current I, see Figure 6.11. By definition, the magnetic moment of a loop is $\boldsymbol{m}=SI\boldsymbol{e}_m=\pi R^2 I\boldsymbol{e}_m$, $\boldsymbol{e}_m=\left(\sin\vartheta\cos\varphi \quad \sin\vartheta\sin\varphi \quad \cos\vartheta\right)$ being the unit vector in the direction of $\boldsymbol{m}$. For definiteness, we choose the loops centred at the space origin O_p and at an arbitrary point O_s as the primary and secondary loops, respectively.

The dipole-dipole interaction energy in this model is straight related to the mutual inductance $\mathscr{M}$ as in eq. (6.53). By definition,

$$\mathscr{M}=\frac{\Phi}{I} \tag{6.80}$$

where Φ, the magnetic flux induced by the current in the primary loop and passing through the secondary loop, can be calculated as follows:

$$\Phi=\oint_{l_s}\oint_{l_p}\mathrm{d}\boldsymbol{A}\cdot\mathrm{d}\boldsymbol{l}_s\,. \tag{6.81}$$

Here l_p and l_s are perimeters of the primary and secondary loops, $\mathrm{d}\boldsymbol{A}$ is a differential element of the vector potential at a point M_s on the secondary loop, produced by the primary loop:

$$\mathrm{d}\boldsymbol{A} = \frac{\mu_0}{4\pi}\frac{I}{M_\mathrm{p}M_\mathrm{s}}\mathrm{d}\boldsymbol{l}_\mathrm{p}, \tag{6.82}$$

$M_\mathrm{p}M_\mathrm{s}$ is the distance between two points on the primary and secondary loops, and $\mathrm{d}\boldsymbol{l}_\mathrm{p}$ and $\mathrm{d}\boldsymbol{l}_\mathrm{s}$ are differential elements of the corresponding loops.

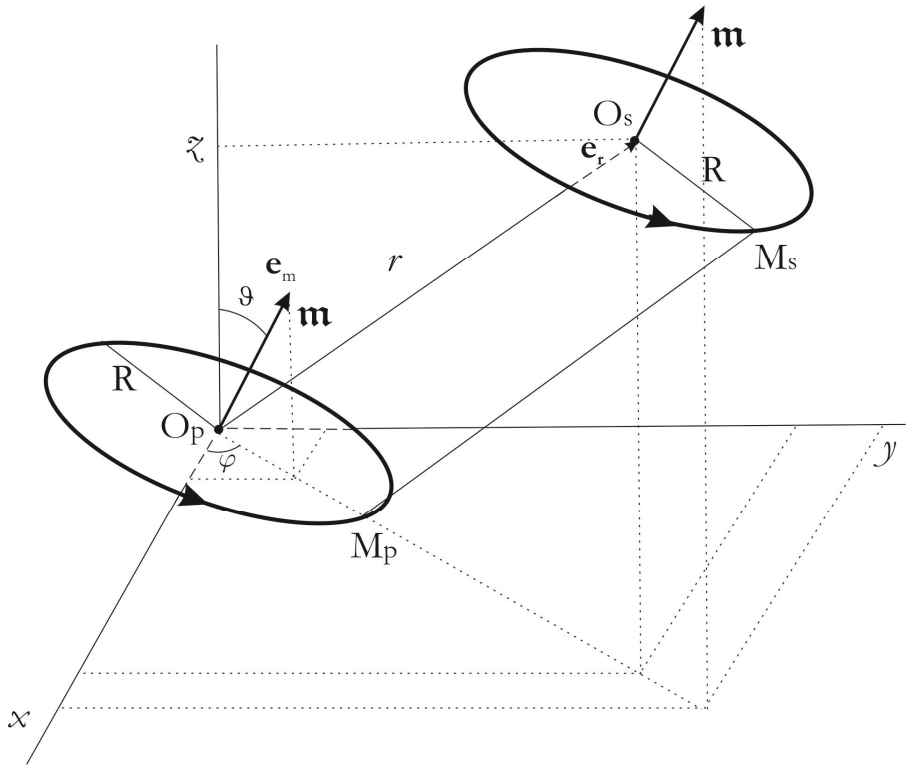

Figure 6.11 System of two interacting Ampérian currents.

In order to evaluate the closed curve integrals in eq. (6.81) we express $M_\mathrm{p}M_\mathrm{s}$, $\mathrm{d}\boldsymbol{l}_\mathrm{p}$ and $\mathrm{d}\boldsymbol{l}_\mathrm{s}$ as follows:

$$\begin{aligned}\left|M_\mathrm{p}M_\mathrm{s}\right|^2 = {} & r^2 + 2R^2\left[1-\sin(\phi-\tau)\right] \\ & +2Rr_x\left[\sin\varphi(\cos\phi+\sin\tau)+\cos\varphi\cos\vartheta(\sin\phi-\cos\tau)\right], \\ & +2Rr_y\left[\sin\varphi\cos\vartheta(\sin\phi-\cos\tau)-\cos\varphi(\cos\phi+\sin\tau)\right] \\ & -2Rr_z\sin\vartheta(\sin\phi-\cos\tau)\end{aligned} \tag{6.83}$$

$$\mathrm{d}\boldsymbol{l}_\mathrm{p} = \begin{pmatrix} -R(\cos\varphi\cos\vartheta\sin\tau+\sin\varphi\cos\tau)\mathrm{d}\tau \\ R(-\sin\varphi\cos\vartheta\sin\tau+\cos\varphi\cos\tau)\mathrm{d}\tau \\ \mathrm{R}\sin\vartheta\sin\tau\,\mathrm{d}\tau \end{pmatrix} \tag{6.84}$$

and

$$\mathrm{d}\boldsymbol{l}_\mathrm{s} = \begin{pmatrix} -R\left(\sin\varphi\sin\phi - \cos\vartheta\cos\varphi\cos\phi\right)\mathrm{d}\phi \\ R\left(\sin\varphi\cos\vartheta\cos\phi + \cos\varphi\sin\phi\right)\mathrm{d}\phi \\ -R\sin\vartheta\cos\phi\,\mathrm{d}\phi \end{pmatrix}. \tag{6.85}$$

In eqs. (6.83) to (6.85) τ and ϕ are *polar* angles of arbitrary points of the primary and secondary loops, respectively. Putting these expressions in eq. (6.81), for the interaction energy, *cf.* eq. (6.53), we get:

$$\mathcal{E} = -\frac{\mu_0}{4\pi} I^2 \int_0^{2\pi}\int_0^{2\pi} \frac{\mathrm{d}\boldsymbol{l}_\mathrm{p}\cdot\mathrm{d}\boldsymbol{l}_\mathrm{s}}{M_\mathrm{p}M_\mathrm{s}} \tag{6.86}$$

where the integrations are over τ and ϕ.

Since we need only an approximate expression of $\mathcal{E}$ for $\varepsilon \ll 1$, we can first expand the integrand in eq. (6.86) in a Taylor series up to the fourth order in the small parameter $\varepsilon = R/r$ and then integrate the result. We get:

$$\mathcal{E} = \mp 2\frac{\mu_0}{4\pi}\frac{\boldsymbol{m}^2}{r^3}\left(P_2 - 3P_4\varepsilon^2 + \tfrac{75}{8}P_6\varepsilon^4\right) \tag{6.87}$$

where P_n are Legendre polynomials [6.21] of the scalar product $\boldsymbol{e}_r\cdot\boldsymbol{e}_m$, $\boldsymbol{e}_r$ being the unit vector in the direction of r, and the – and + signs correspond to parallel and antiparallel dipoles, respectively. Obviously, eq. (6.87) can be directly obtained by substituting the scalar product $\boldsymbol{e}_r\cdot\boldsymbol{e}_m$ for $\cos\vartheta$ in the Legendre polynomials given above in eq. (6.63).

6.3.2.2 Two pairs of fictitious magnetic charges

Figure 6.12 shows a system of two interacting dipoles implemented as a pair of "magnetic charges" $\pm q$ spaced a distance d apart. For the dipole-dipole interaction energy we get:

$$\mathcal{E} = \pm\frac{\mu_0}{4\pi}\frac{\boldsymbol{m}^2}{d^2}\left(\frac{2}{r} - \frac{1}{r_\mathrm{mp}} - \frac{1}{r_\mathrm{pm}}\right) \tag{6.88}$$

where μ_0 is the permeability of vacuum, $\boldsymbol{m} = q\boldsymbol{d} = qd\boldsymbol{e}_m$ is the magnetic moment, defined by analogy with electrostatics; $r = \left(r_x{}^2 + r_y{}^2 + r_z{}^2\right)^{1/2}$ is the distance between the centres of the dipoles, $r_\mathrm{mp} = \sqrt{r^2 + d^2 + 2rd\,\boldsymbol{e}_r\cdot\boldsymbol{e}_m}$ and $r_\mathrm{pm} = \sqrt{r^2 + d^2 - 2rd\,\boldsymbol{e}_r\cdot\boldsymbol{e}_m}$, see Figure 6.12 for the notation. The choice of the $\pm$ signs refers to parallel and antiparallel dipoles, respectively.

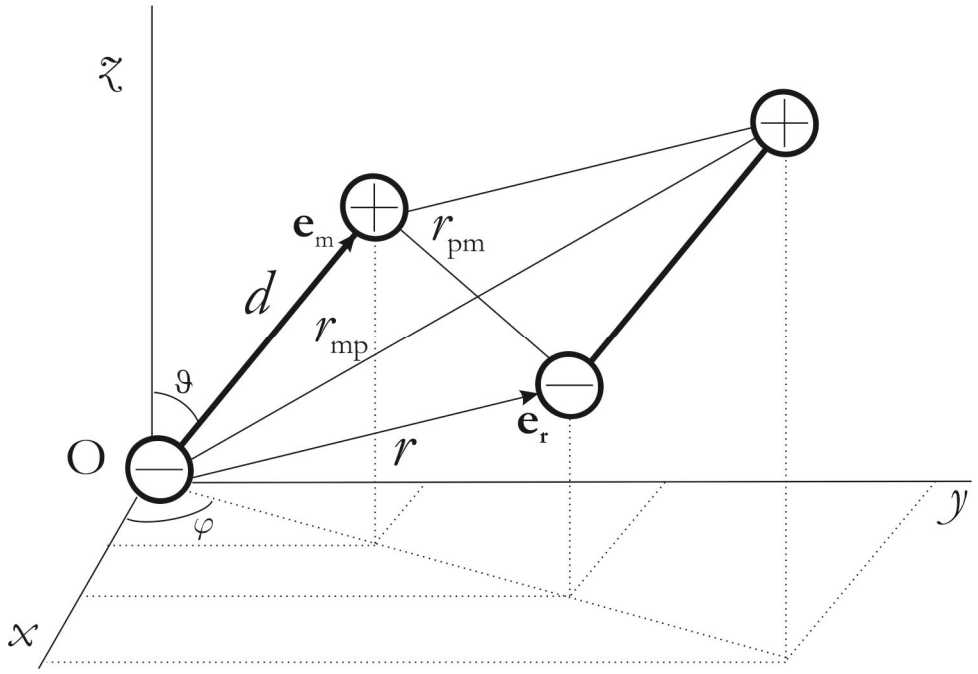

Figure 6.12 System of two interacting dipoles in the model of a pair of magnetic charges.

Introducing $\varepsilon = d/r$ in eq. (6.88) one gets:

$$\mathcal{E} = \pm\frac{\mu_0}{4\pi}\frac{m^2}{d^2}\left(\frac{2}{r} - \frac{1}{r\sqrt{1+\varepsilon^2+2\varepsilon\,\boldsymbol{e}_r\cdot\boldsymbol{e}_m}} - \frac{1}{r\sqrt{1+\varepsilon^2-2\varepsilon\,\boldsymbol{e}_r\cdot\boldsymbol{e}_m}}\right). \tag{6.89}$$

As in the previous case, the approximate expression of $\mathcal{E}$ can be expressed in terms of the Legendre polynomials of the scalar product $\boldsymbol{e}_r\cdot\boldsymbol{e}_m$ up to the fourth order:

$$\mathcal{E} = \mp 2\frac{\mu_0}{4\pi}\frac{m^2}{r^3}\left(P_2 + P_4\varepsilon^2 + P_6\varepsilon^4\right) \tag{6.90}$$

where the – and + signs correspond to parallel and antiparallel dipoles, respectively.

6.3.2.3 Dipole-dipole contribution to magnetocrystalline anisotropy constants of iron borate

In order to calculate the dipole-dipole contribution to the magnetocrystalline anisotropy constants for $FeBO_3$, we have put forward a computer code implementing the lattice-sum method. We have chosen to do the summation in the volume of a rhombohedron congruent to the primitive rhombohedron shown in Figure 6.13.

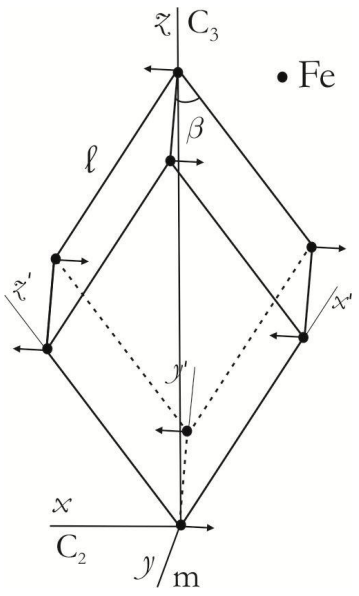

Figure 6.13 A primitive rhombohedron with the edge length $\ell = 3.6\,\text{Å}$ and the apex angle $\beta = 79.9^\circ$ used to calculate the dipole-dipole interaction energy.

The axes of the rhombohedral coordinate system x', y', z' coincide with the edges of the rhombohedron, see Figure 6.13. In transforming the radius vector from the Cartesian to the rhombohedral system, we express the coordinates of iron sites through the edge length ℓ of the rhombohedron: $x' = m\ell$, $y' = n\ell$ and $z' = k\ell$, where m, n, k are integers numbering the sites along the corresponding axes. The radius vector in a new coordinate system is

$$\boldsymbol{r} = \ell \begin{pmatrix} (z' - x')\cos\widehat{k'i} \\ (x' - 2y' + z')\cos\widehat{i'j} \\ (x' + y' + z')\cos\widehat{k'k} \end{pmatrix} \tag{6.91}$$

where $\cos\widehat{k'i} = \sqrt{\dfrac{1-\cos\beta}{2}}$, $\cos\widehat{i'j} = \sqrt{\dfrac{1-\cos\beta}{6}}$ and $\cos\widehat{k'k} = \sqrt{\dfrac{1+2\cos\beta}{3}}$ are the cosines of angles between corresponding axes of two coordinate systems. Substituting eq. (6.91) in the expressions for the dipole-dipole interaction energy, eqs. (6.87) and (6.90) for the models of a circular current loop and a pair of magnetic charges, respectively, we express this energy in terms of integers numbering the iron sites along the edges of the rhombohedron.

The calculation of the density of dipole-dipole interaction energy now is reduced to computing the following sum:

$$\mathcal{E}_{\text{dip}} = \tfrac{1}{2} N \sum_{m,n,k} (-1)^{m+n+k} \mathcal{E}(m,n,k) \tag{6.92}$$

where the factor $(-1)^{m+n+k}$ takes into account antiferromagnetic ordering and $\mathcal{E}(m,n,k)$ is the dipole-dipole interaction energy between ions at the origin (numbered $0,0,0$) and at a site numbered m,n,k.

Henceforth, the magnetic dipole moment at $T=0\text{K}$ will be expressed as

$$m = g\beta S \tag{6.93}$$

where g,β and S have the same meanings as in eq. (6.4).

The dipole-dipole contributions at 0 K, together with those of the crystal field, *vide supra*, are listed in Table 6.1. One can see that the models of a circular current loop and a pair of magnetic charges result in substantially different expressions for the dipole-dipole interaction energies.

Table 6.1 Crystal field and dipole-dipole contributions to the magnetocrystalline anisotropy constants of iron borate at 0 K.

Constants, Jm^{-3}	Crystal field contribution	Dipole-dipole contribution	
		Circular current loop	Pair of fictitious magnetic charges
a_{FeBO_3}	$4.82\cdot10^5$	$3.82\cdot10^5$	
d_{FeBO_3}	$2.55\cdot10^3$	$-2.11\cdot10^6\,\frac{R^2}{\ell^2}$	$7.02\cdot10^5\,\frac{d^2}{\ell^2}$
e_{FeBO_3}	0	$-9.19\cdot10^5\,\frac{R^4}{\ell^4}$	$-9.80\cdot10^4\,\frac{d^4}{\ell^4}$

In order to get the dipole-dipole contributions to the magnetocrystalline anisotropy at different temperatures, these contribution at 0 K should be multiplied by $\left(\mathscr{M}_T/\mathscr{M}_0\right)^2$, where $\mathscr{M}_T$ is the sublattice magnetization at a temperature T, *cf.* Chapter 1, "Crystal and magnetic structure of iron borate". $\mathscr{M}_T/\mathscr{M}_0$ for $FeBO_3$ have been tabulated [6.2]. The temperature dependences of the crystal field contributions are given in eqs. (6.22) and in Figure 6.1.

6.3.2.4 Estimation of the dipole size for $FeBO_3$

The *effective* hexagonal anisotropy constant for $FeBO_3$ is *cf.* eq. (1.28) in Chapter 1, "Crystal and magnetic structure of iron borate":

$$e_{\text{eff}} = e_{\text{FeBO}_3} + \frac{1}{4}\frac{d_{\text{FeBO}_3}^2}{a_{\text{eff}}} \tag{6.94}$$

The experimental value $e_{\text{eff}}^{\text{exp}} = 0.936\ \text{Jm}^{-3}$ has been determined from the AFMR experiments at 77 K *cf.* Chapter 3, "Electron magnetic resonance of iron-gallium borate single crystals with $0.2 \le x \le 1$". In the following, we assume that $e_{\text{eff}} = e_{\text{eff}}^{\text{exp}}$. Substituting $e_{\text{eff}}^{\text{exp}}$ in (6.94) and taking into account eqs. (6.2) and (6.3), we get:

$$e_{\text{eff}}^{\text{exp}} = e_{\text{cf}} + e_{\text{dip}} + \frac{1}{4}\frac{\left(d_{\text{cf}} + d_{\text{dip}}\right)^2}{a_{\text{FeBO}_3} + \dfrac{D_{\text{FeBO}_3}{}^2}{E_{\text{FeBO}_3}}}. \tag{6.95}$$

For a_{FeBO_3} we have also used the experimental value $a_{\text{FeBO}_3}^{\text{exp}} = 3.2 \cdot 10^5\ \text{Jm}^{-3}$ determined by AFMR at 77 K [6.2, 6.5]. D_{FeBO_3} and E_{FeBO_3} at 77 K have been calculated from experimental values of corresponding effective fields and sublattice magnetization, see Table 3.1 in Chapter 3, "Electron magnetic resonance of iron-gallium borate single crystals with $0.2 \le x \le 1$". Substituting to eq. (6.95) these values as well as those given in Table 6.1, for the model of a circular current loop we get:

$$7.47 \cdot 10^3 R^4 - 405.4 R^2 + 3.2 = 0.936, \tag{6.96}$$

yielding two positive solutions: $R_1 = 0.2189$ and $R_2 = 0.0797$ Å.

For a pair of fictitious magnetic charges we get:

$$853 d^4 + 135 d^2 + 3.2 = 0.936. \tag{6.97}$$

Obviously, the latter equation can have only complex solutions; therefore, this model is not applicable in the actual case.

In order to assess the plausibility of R_1 and R_2 values, they should be compared with the ionic radius R_i of Fe^{3+}; indeed, we can reasonably infer that the effective dipole size should be of the same order of magnitude as the size of the physical object producing the corresponding dipole moment. For high-spin Fe^{3+} in sixfold coordination $R_i = 0.645$ Å [6.22]; therefore the R_1 value seems to be a more realistic estimate than R_2, the latter value being an order of magnitude smaller than R_i. Nevertheless, we have chosen to calculate the dipole-dipole contributions to the magnetocrystalline anisotropy constants of $FeBO_3$ at 77 K with both values.

With the R_1 value we get:

$$e_{\text{dip}} = -12.2\,\text{Jm}^{-3} \quad ; \quad d_{\text{dip}} = -7.57 \cdot 10^3\,\text{Jm}^{-3}, \tag{6.98}$$

and with R_2 value we get:

$$e_{\text{dip}} = -0.215\,\text{Jm}^{-3} \quad ; \quad d_{\text{dip}} = -1 \cdot 10^3\,\text{Jm}^{-3}. \tag{6.99}$$

6.3.2.5 Dipole-dipole contribution to magnetocrystalline anisotropy constants of iron-gallium borates

In order to calculate the dipole-dipole contribution to the magnetocrystalline anisotropy constants e_{dip} and d_{dip} for mixed borates $Fe_xGa_{1-x}BO_3$, we have put forward a computer code implementing the lattice-sum method as for $FeBO_3$. With this aim in mind, we have modelled a diamagnetically diluted crystal lattice using the Monte Carlo technique [6.23].

Figure 6.14 shows the spatial distribution of dia- and paramagnetic ions in mixed borates in a layer parallel to the basal plane. The probabilities of iron or gallium occupying a given site, are x or 1-x, respectively. One can see that nanoscopic iron domains — nanoclusters — occur at intermediate x. Such nanoclusters are expected to possess magnetic properties similar to those of magnetic nanoparticles [6.24].

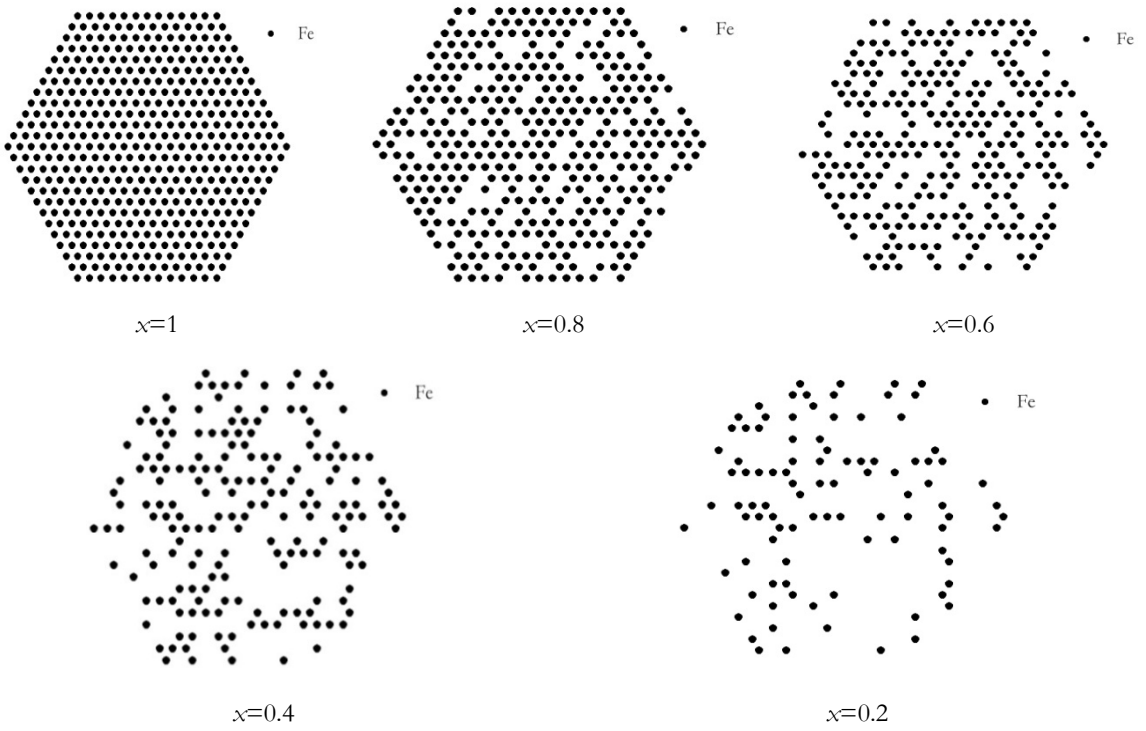

Figure 6.14 Spatial distribution of dia- and paramagnetic ions in $Fe_xGa_{1-x}BO_3$ in a layer parallel to the basal plane

The calculation of the dipole-dipole interaction energy has been done using a model of a circular current loop in the same way as for $FeBO_3$, *i.e.* computing the sum in eq. (6.92) taking into account only the sites occupied by iron.

The dependence of a_{dip} on x is shown in Figure 6.15. Using the effective dipole sizes determined for $FeBO_3$, *vide supra*, we get the dependences of d_{dip} and e_{dip} on the iron concentration at 0 K, see Figures 6.16 and 6.17, respectively.

The experiments for the determination of e_{eff}^{exp} for diamagnetically diluted $Fe_xGa_{1-x}BO_3$ crystals are in progress and could provide the possibility of making an unambiguous choice between two possible dipole sizes.

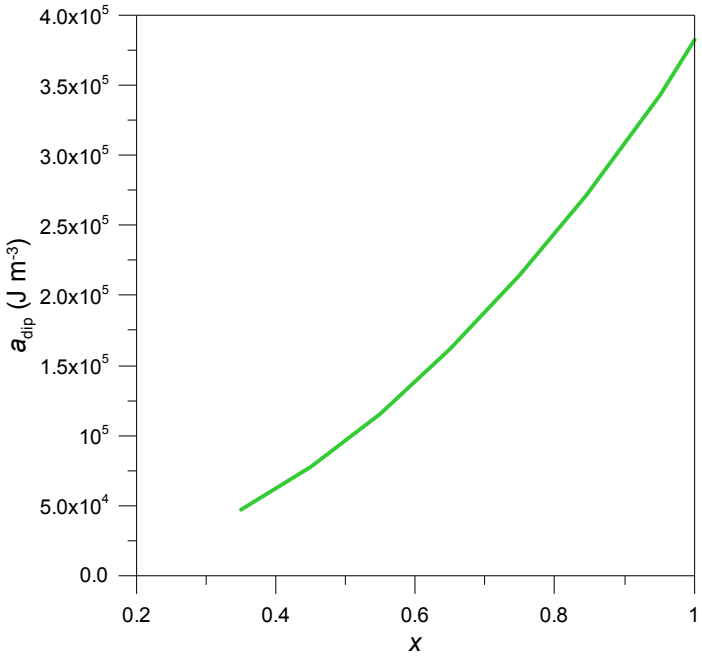

Figure 6.15 Concentration dependence of a_{dip} at 0 K.

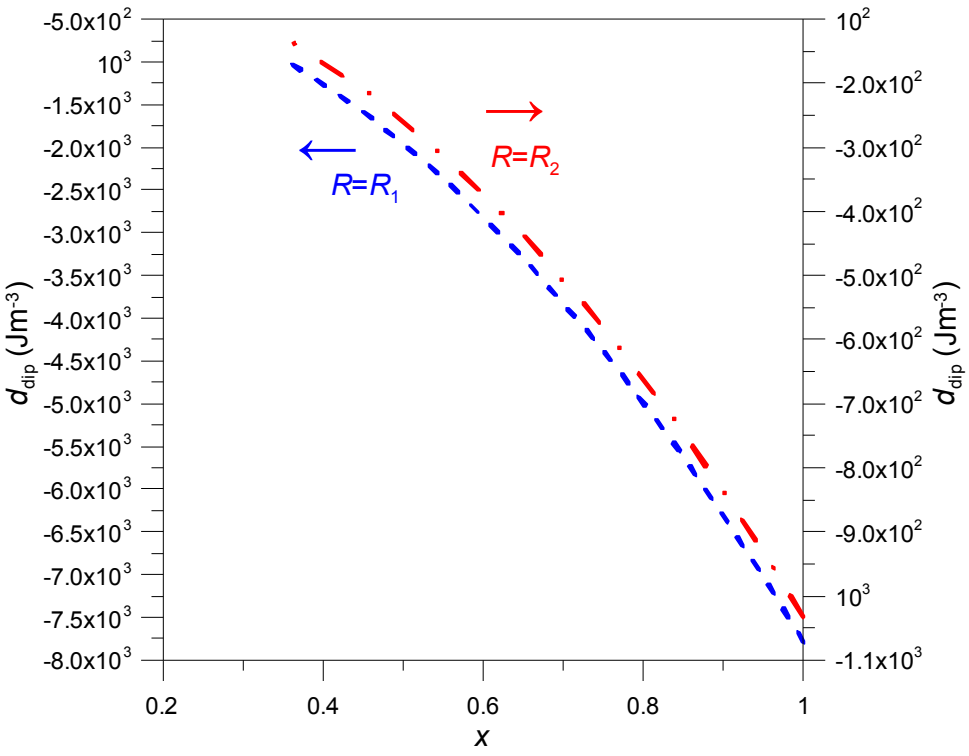

Figure 6.16 Concentration dependence of d_{dip} calculated with R_1 (dashed, blue) and R_2 values (dashed-dotted, red) at 0 K.

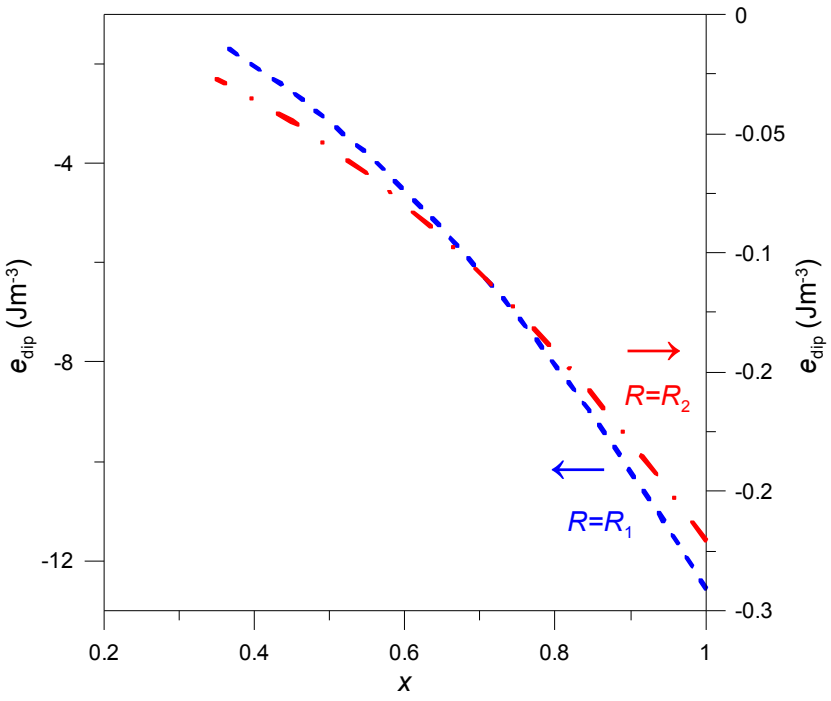

Figure 6.17 Concentration dependence of e_{dip} calculated with R_1 (dashed, blue) and R_2 values (dashed-dotted, red) at 0 K.

6.4 Conclusions

Possible contributions to the magnetocrystalline anisotropy of mixed iron-gallium borates $Fe_xGa_{1-x}BO_3$, namely, crystal field and dipole-dipole, have been considered in detail. The former contribution has been calculated in perturbation theory using the spin Hamiltonian parameters for isolated Fe^{3+} ions in (diamagnetic) gallium borate. The latter contribution has been evaluated under the assumption that the ratio dipole size/ interdipole distance is non-negligible, *i.e.* that we are dealing with the extended dipoles.

We have developed a theoretical description of three models of an extended magnetic dipole: (i) a uniformly magnetized sphere, (ii) an Ampérian current and (iii) an assembly of two fictitious "magnetic charges". We have shown that all three models yield identical results at large distances with respect to the dipole size. Indeed, the *first* terms of Taylor expansions of the magnetic fields produced by the models of a circular current loop and of a pair of magnetic charges coincide with the *exact* expression of the magnetic field outside the uniformly magnetized sphere, the latter being the same as for the point dipole. Therefore, the uniformly magnetized sphere can describe only the uniaxial magnetocrystalline anisotropy and not the hexagonal basal magnetocrystalline anisotropy in iron borate.

The dipole-dipole interaction energy has been calculated for two extended dipole models, *viz.*, a pair of magnetic charges and a circular current loop. The dipole-dipole contribution to the magnetocrystalline anisotropy constants for $FeBO_3$ has been calculated by the lattice-sum method. A comparison between the experimental and calculated values of the effective basal anisotropy constant has shown that the model of a pair of magnetic charges fails to explain the experimental results. In contrast, the model of a circular current loop provides consistent evidence in support of the dipole-dipole contribution to the basal magnetocrystalline anisotropy of iron borate and, incidentally, yields two more or less realistic estimates of the dipole sizes associated with Fe^{3+} ion. In spite of the fact that the approach based on the models of extended dipoles, put forward in this work, provides new insight in the nature of the basal magnetocrystalline anisotropy of iron borate, it is certainly oversimplified. More sophisticated (*ab initio*) calculations are necessary in order to obtain a more detailed picture of spatial distribution of the magnetic field produced by paramagnetic ions at short and intermediate distances.

The dipole-dipole interaction energy for mixed borates $Fe_xGa_{1-x}BO_3$ has been calculated by the same technique as for $FeBO_3$. In order to simulate a diamagnetically diluted crystal lattice we have used the Monte Carlo technique. The dipole-dipole contributions to the magnetocrystalline anisotropy constants for crystals with different x have been obtained; e_{dip} and d_{dip} have been calculated for the dipole sizes determined for $FeBO_3$.

6.5 References

6.1 J. Kanamori, *Anisotropy and magnetostriction of ferromagnetic and antiferromagnetic materials,* in: *Magnetism, A Treatise on Modern Theory and Material*, G.T. Rado, H. Suhl, ed., Acad. Press, v. **1** (1963) 127-203

6.2 В.Н. Селезнев, *Магнитоупорядоченные бораты железа (физическиесвойства, применение, синтез)*, Диссертация, Симферопольский гос. университет (1988) 371 с.

6.3 S. Yagupov, M. Strugatsky, K. Seleznyova, E. Maksimova, I. Nauhatsky, V. Yagupov, E. Milyukova and J. Kliava. $Fe_xGa_{1-x}BO_3$ *single crystals: synthesis and characterization*, Appl. Phys. A **121** (2015) 179-185

6.4 V.V. Rudenko, V.N. Seleznev and A.S. Hlystov, in: Abstracts Sov. Symp. on Physics of Magnetic Phenomena, Donetsk (1977) 80

6.5 L.V. Velikov, A.S. Prokhorov, E.G. Rudashevskii and V.N. Seleznev, *Antiferromagnetic resonance in* $FeBO_3$, Soviet Physics JETP **39** (1974) 909-915

6.6 С.Н. Лукин, В.В. Руденко, В.Н. Селезнев и Г.А. Цинцадзе, *ЭПР ионов в гомологическом ряду боратов со структурой кальцита*, Физика Твердого Тела (1980) **22** 51-56

6.7 K. Seleznyova, M. Strugatsky, S. Yagupov, N. Postivey, A. Artemenko and J. Kliava, *Electron paramagnetic resonance of* Fe^{3+} *in gallium borate: Superposition model analysis*, Phys. Stat. Sol. B **251** (2014) 1393-1400

6.8 S.A. Al'tshuler and B.M. Kozyrev, *EPR in compounds of transition elements*, 2nd ed., Wiley, New York, Toronto, Jerusalem, London (1974) 512 pp.

6.9 L.D. Landau and E.M. Lifshitz, *Quantum mechanics: non-relativistic theory.*, 3rd ed., Pergamon, Oxford (1977) 677 pp.

6.10 В.Д. Дорошев, Клочан В.А., Ковтун Н.М. и др., *Экспериментальное и теоретическое изучение температурной зависимости подрешеточной намагниченности слабого ферромагнетика* $FeBO_3$, Препринт Дон. ФТИАН УССР **7**(102), Донецк (1985) 60 с.

6.11 J.D. Jackson, *Classical electrodynamics,* 3rd ed., Wiley, Hoboken, NJ (1998) 808 pp.

6.12 D.J. Griffiths, *Introduction to electrodynamics,* 3rd ed., Prentice Hall, NJ (1999) 576 pp.

6.13 L.D. Landau and E.M. Lifshitz, *The classical theory of fields*, 3rd ed., Pergamon, Oxford (1971) 374 pp.

6.14 P. Curie, *Sur la symétrie dans les phénomènes physiques, symétrie d'un champ électrique et d'un champ magnétique*, J. Phys. **3** (1894) 393-415

6.15 F.W. Grover, *The calculation of the mutual inductance of circular filaments in any desired positions*, Proc. I.R.E. (October 1944) 620-629

6.16 C. Akyel, S.I. Babic and M.-M. Mahmudi, *Mutual Inductance Calculation for Noncoaxial Circular Air Coils with Parallel Axes*, Progr. Electromagn. Res. **91** (2009) 287-301

6.17 G.B. Arfken, H.J. Weber and F.E. Harris, *Mathematical methods for physicists*, 7th ed., Academic Press, Waltham (2012) 1205 pp.

6.18 P.A.M. Dirac, *Quantised Singularities in the Electromagnetic Field*, Proc. R. Soc. London A **133** (1931) 60-72

6.19 K. Seleznyova, M. Strugatsky and J. Kliava, *Modelling the magnetic dipole*, Eur. J. Phys. **37**, (2016) 025203, 1-14

6.20 K.E. Atkinson, *An introduction to numerical analysis*, 2nd ed., John Wiley & Sons, Inc., NY, (1989), 693 pp.

6.21 G. Korn and T. Korn, *Mathematical handbook for scientists and engineers,* Dover Publications, Mineola, New York (2000) 1130 pp.

6.22 R.D. Shannon, *Revised Effective Ionic Radii and Systematic Studies of Interatomie Distances in Halides and Chaleogenides*, Acta Cryst. A **32** (1976) 751-767

6.23 L. Devroye, *Non-Uniform Random Variate Generation*, Springer, New York, Berlin, Heidelberg, Tokyo (1986) 843 pp.

6.24 J. Kliava, *Electron Magnetic Resonance of Nanoparticles: Superparamagnetic Resonance,* in : *Magnetic Nanoparticles*, S.P. Gubin ed., Wiley-VCH (2009) pp. 255-302

7. Surface magnetocrystalline anisotropy of iron borate single crystals

7.1 Theoretical background

The surface magnetism – a specific magnetic state of a thin near-surface layer of magnets – is caused by lowering of symmetry in the environment of near-surface magnetic ions in comparison with those in the volume. Néel was the first to specify the existence of surface magnetocrystalline anisotropy energy, due to this effect [7.1]. However, the manifestation of this anisotropy in conventional ferromagnets is usually obscured by the demagnetizing field and large volume magnetocrystalline anisotropy. In contrast, in iron borate the surface magnetocrystalline anisotropy can be observed due to the fact that the demagnetizing field, proportional to the (weak) magnetization of the antiferromagnetic crystal with weak ferromagnetism, is small and the basal anisotropy is weak [7.2]. Therefore, magnetic characteristics of a thin (0.01-0.1 μm) near-surface layer of iron borate drastically differ from those of the volume.

The gas-phase deposition technique allows growing bulk single crystals of iron borate with large *non-basal* faces of optical quality [7.3]. Such crystals have made possible finding out the surface magnetism in iron borate by the magneto-optical Kerr effect [7.4].

The surface magnetocrystalline anisotropy energy can be calculated as the difference of the magnetic energies of ions in the near-surface layer and in the crystal volume. This difference is due to two causes: (i) the occurrence of the crystal surface *per se* (without modification of the oxygen environment of near-surface iron ions) and (ii) structural distortions in the near-surface layer.

As we have already indicated, *cf.* Chapters 1 and 6, "Crystal and magnetic structure of iron borate" and "Magnetocrystalline anisotropy of iron borate and iron-gallium borates", respectively, in iron borate the exchange energy in a good approximation is isotropic; therefore, the *density* of the surface magnetocrystalline anisotropy energy, σ is expected to include only dipole-dipole, σ_{dip} and crystal field, σ_{cf} contributions. Obviously, the cause (i) intervenes only in the calculation of the dipole-dipole contribution whereas the cause (ii) is expected to modify both the dipole-dipole contribution – as a result of alteration of mutual disposition of iron ions in the near-surface layer – and the crystal field contribution – in as much as the oxygen environment of iron ions in the near-surface layer undergoes additional distortions in comparison with the volume.

In the paper by Zubov *et al.* [7.4] and later in the Strugatsky's thesis [7.5] a theoretical description of σ has been put forward taking into account only the cause (i), *i.e.* neglecting structural distortions in the near-surface layer. In this approximation, σ will include only dipole-dipole contribution, σ_{dip} *vide supra*, and the maximal value is obtained for the $(10\bar{1}4)$ face:

$$\sigma_{\text{dip}} = \sigma_{\text{dip}_1} \sin^2\vartheta\cos^2\varphi + \sigma_{\text{dip}_2} \sin^2\vartheta\sin^2\varphi + \sigma_{\text{dip}_3} \cos^2\vartheta + \sigma_{\text{dip}_4} \sin\vartheta\cos\vartheta\sin\varphi \qquad (7.1)$$

where $\sigma_{\text{dip}_1} = -2.2\cdot10^{-5}$, $\sigma_{\text{dip}_2} = 0.8\cdot10^{-5}$, $\sigma_{\text{dip}_3} = -1.6\cdot10^{-5}$ and $\sigma_{\text{dip}_4} = 3.9\cdot10^{-5}$ in Jm^{-2} (at 0 K), ϑ and φ are, respectively, the polar angle with respect to C_3 and the azimuthal angle with respect to C_2 of the antiferromagnetic vector $\boldsymbol{l}$, see Chapter 1, "Crystal and magnetic structure of iron borate", in the near-surface layer.

Minimizing σ_{dip} with respect to ϑ and φ, the equilibrium orientation of $\boldsymbol{l}$ in the near-surface layer is [7.5]:

$$\vartheta_0 = 2.64 \text{ and } \varphi_0 = \frac{\pi}{2}\,(\text{in rad}). \qquad (7.2)$$

As one can see, $\boldsymbol{l}$ in the near-surface layer has an orientation different from its equilibrium orientation in the volume, see Chapter 1, "Crystal and magnetic structure of iron borate". As a consequence, a transition layer between the volume and the near-surface layer will form, similar to a domain wall, where $\boldsymbol{l}$ will gradually turn from the equilibrium orientation in the volume to that in the near-surface layer. The density of the magnetocrystalline anisotropy energy in this layer can be expressed as [7.4, 7.5]:

$$\gamma_\vartheta = \sqrt{a_{\text{eff}} A}\,(1-\sin\vartheta) \qquad (7.3)$$

where a_{eff} is the effective uniaxial anisotropy constant, *cf.* Chapter 1, "Crystal and magnetic structure of iron borate", A is a constant in the expression describing exchange interaction in the non-uniform transition layer [7.5]. For $FeBO_3$ at 0 K $A \approx 0.7\cdot10^{-11}\,\text{Jm}$ and $a_{\text{eff}} \approx 4.85\cdot10^5\,\text{Jm}^{-3}$ [7.5]. Thus, $\sqrt{a_{\text{eff}} A} \approx 1.8\cdot10^{-3}\,\text{Jm}^{-2}$. Minimizing the sum of σ_{dip} and γ_ϑ with respect to ϑ and φ, we get the equilibrium orientation of $\boldsymbol{l}$ in the near-surface layer [7.4, 7.5]:

$$\vartheta_0 = \frac{\pi}{2} \text{ and } \varphi_0 = 0,\ \pi\,. \qquad (7.4)$$

Indeed, a considerable deviation of $\boldsymbol{l}$ from the basal plane would result in a significant increase of γ_ϑ, of the order of magnitude of $\sqrt{a_{\text{eff}} A}$, *cf.* eq. (7.3). This situation is energetically unfavorable. Thus, $\boldsymbol{l}$ in the near-surface layer will lie in the basal plane or make a small angle with it. Its azimuthal angle will be determined by surface magnetocrystalline anisotropy. Putting $\vartheta = \frac{\pi}{2}$ in eq. (7.1), we get [7.4, 7.5]:

$$\sigma_{\text{dip}} = a_{S\,\text{dip}} \sin^2\varphi \qquad (7.5)$$

where $a_{S\,\mathrm{dip}}$ is the dipole-dipole contribution to the surface magnetocrystalline anisotropy constant. At room temperature $a_{S\,\mathrm{dip}} = 1.4 \cdot 10^{-5}\ \mathrm{J\,m^{-2}}$ [7.5]. In equilibrium $\boldsymbol{l}$ is parallel to one of C_2 axes, see eq. (7.4); therefore, the reduced ferromagnetic vector $\boldsymbol{m} \perp \boldsymbol{l}$, see Chapter 1, "Crystal and magnetic structure of iron borate", is perpendicular to this axis, so that C_2 is the hard magnetization axis in the basal plane. This result has been confirmed by experimental observations for $\left(10\bar{1}4\right)$ face of the crystal [7.4].

The saturation field along the hard magnetization axis in the near-surface layer, called the critical field H_{c}, is considered as the measure of the surface anisotropy. In fact, an application of such a field would totally erase the transition layer. Applying a magnetizing field $\boldsymbol{H}$ in the basal plane, the direction of $\boldsymbol{l}$ in the transition layer will gradually change from that in the volume, determined by $\boldsymbol{H}$, to that in the near-surface layer, determined by both $\boldsymbol{H}$ and the surface magnetocrystalline anisotropy. The density of the magnetocrystalline anisotropy energy in this layer will be [7.4-7.6]

$$\gamma_{\varphi} = 4\sqrt{AMH}\left[1 - \cos\left(\tfrac{\pi}{4} + \tfrac{\beta}{2} - \tfrac{\varphi}{2}\right)\right] \tag{7.6}$$

where $M = 2\mathscr{M}_T \dfrac{D}{E}$ is the saturation magnetization of the crystal, $\mathscr{M}_T$ being the sublattice magnetization at a temterature T, D and E being the Dzyaloshinskii-Moriya and exchange constants, *cf.* Table 1.4 and eq. (1.14) in Chapter 1, "Crystal and magnetic structure of iron borate"; and β is the angle between $\boldsymbol{H}$ and C_2. Taking into account that $\mathscr{M}_0 / \mathscr{M}_{300} \approx 1.47$ [7.7] and the values of D and E quoted in Table 1.5, we get $M \approx 12\,\mathrm{G}$ at room temperature. The equilibrium orientation of $\boldsymbol{l}$ in the near-surface layer will be determined by the minimum of the sum $\gamma_{\varphi} + \sigma_{\mathrm{dip}}$, and as far as this quantity is independent of ϑ, see eqs. (7.5) and (7.6), we just have to solve the equation:

$$\frac{\partial}{\partial \varphi}\left(\gamma_{\varphi} + \sigma_{\mathrm{dip}}\right) = -2\sqrt{AMH}\sin\left(\tfrac{\pi}{4} + \tfrac{\beta}{2} - \tfrac{\varphi}{2}\right) + a_{S\,\mathrm{dip}}\sin 2\varphi = 0\,. \tag{7.7}$$

Applying $\boldsymbol{H}$ along the hard axis C_2 $\left(\beta = 0\right)$, in the limit of $H \to H_{\mathrm{c}}$, $\boldsymbol{m}$ will align on C_2, and $\boldsymbol{l} \perp \boldsymbol{m}$ will make with C_2 an angle $\varphi \to \frac{\pi}{2}$, so that eq. (7.7) will give:

$$H_{\mathrm{c}} = \frac{4 a_{S\,\mathrm{dip}}{}^2}{AM}\,. \tag{7.8}$$

Zubov *et al.* have found that on the $\left(10\bar{1}4\right)$ face of iron borate $H_{\mathrm{c}} \approx 1\,\mathrm{kOe}$ [7.4]; meanwhile, the H_{c} value calculated with eq. (7.8) is much lower, $H_{\mathrm{c}} = 0.2\,\mathrm{kOe}$ [7.5]. From the preceding analysis we can suppose that this discrepancy could be removed if we allow for structural distortions in the near-surface layer, ("surface reconstruction"). Earlier, an attempt in this direction has been made; however, only changes in the positions of iron ions have been

considered, but concomitant distortions in their oxygen environment has been neglected [7.6]. (In such an approximation, only the dipole-dipole contribution to the surface anisotropy is accounted for.) In this case, the experimental H_c value could be obtained only for relative extensions as large as $7-12\,\%$ [7.6].

Meanwhile, it is evident that in the near-surface layer, the oxygen environment of iron ions undergoes additional distortions in comparison with the crystal volume, giving rise to the crystal field contribution to the surface magnetocrystalline anisotropy energy. In the present chapter, we provide a model of these distortions and give a complete description of the surface anisotropy of iron borate, including both the dipole-dipole and crystal field contributions.

7.2 Surface reconstruction

Previously, in order to calculate the dipole-dipole contribution to the magnetocrystalline anisotropy constants for $FeBO_3$, we have used a rhombohedron congruent to the primitive rhombohedron, with faces of $(01\bar{1}2)$ type, *cf.* Figure 6.13 in Chapter 6, "Magnetocrystalline anisotropy of iron borate and iron-gallium borates". Here we are interested in the smallest rhombohedron with faces of $(10\bar{1}4)$ type.

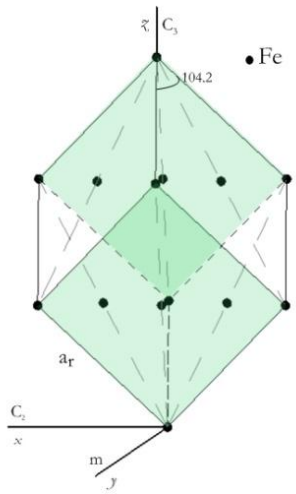

Figure 7.1 A rhombohedron with edge length $a_r = 5.862\,\text{Å}$ and apex angle 104.2° used to calculate the density of surface anisotropy energy. The Cartesian coordinate axes are directed as follows: $x \parallel C_2$, y lies in the symmetry plane m and $z \parallel C_3$ [7.2].

This rhombohedron is face-centred, *i.e.* it contains iron ions in all vertices and face centres, see Figure 7.1; the faces parallel to the crystal surface (and perpendicular to yz planes) are coloured. On the basis of symmetry, we can assume that the distortions of interatomic distances in the near-surface layer occur in yz planes.

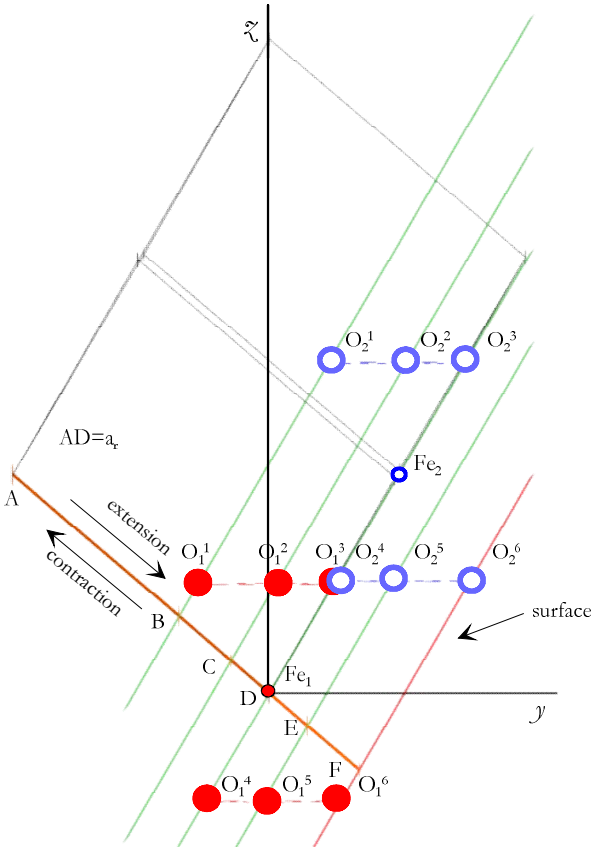

Figure 7.2 Two non-equivalent Fe^{3+} sites and their oxygen environments in the absence of distortions (full red and empty blue circles for Fe_1 and Fe_2, respectively). The Cartesian coordinate axes are directed as in Figure 7.1. The x-axis is perpendicular to the plane of the figure and points towards the reader. The nearest-neighbouring "top" and "bottom" oxygen triangles for both iron sites have the same z-coordinate and different x-coordinates.

In the crystal volume each iron is surrounded by six oxygens forming a nearly perfect octahedron, see Figure 1.3 in Chapter 1, "Crystal and magnetic structure of iron borate". In the near-surface layer the oxygen octahedra are distorted. Consider the positions of two non-equivalent iron sites and their oxygen ligands with respect to the crystal surface. Figure 7.2 shows a projection of the rhombohedron of Figure 7.1 on yOz plane, the crystal surface and the basal planes being orthogonal to this plane. For simplicity, we show only two non-equivalent sites, Fe_1 and Fe_2 and their oxygen environments in the absence of distortions.

We assume that the distortions occur only in the near-surface layer of the oxygen octahedra. The crystal surface (denoted by F in Figure 7.2) passes through O_1^6 and O_2^6 oxygens. We can divide the near-surface layer into four parallel sub-layers separated by planes passing through oxygen and iron ions, see Figure 7.2. The B plane is supposed to remain immobile, the distortions occur along the AD edge of the rhombohedron, and the displacements of ions lying at different distances from B are supposed to vary in proportion to these distances.

7.3 Crystal field contribution to the surface anisotropy energy

Previously, we have carried out EPR studies of Fe^{3+} in $GaBO_3$ single crystals and determined the spin Hamiltonian parameters using crystallographic data and the Newman's superposition model. In order to calculate the crystal field contribution to the surface magnetocrystalline anisotropy energy, we have followed the procedure described in detail in Chapter 4, "EPR of iron-gallium borate single crystals with low x".

For near-surface iron ions, the superposition model parameters are expected to remain the same as for those in the volume, at least as far as distortions in their environment remain weak. We have used the following values of $\overline{b}_l$ and t_l, *cf.* Chapter 4, "EPR of iron-gallium borate single crystals with low x":

$$\begin{gathered} \overline{b}_2 = 0.408\,\mathrm{cm}^{-1},\ t_2 = 8 \\ \text{and} \\ \overline{b}_4 = 3.1\cdot 10^{-5}\,\mathrm{cm}^{-1},\ t_4 = 5. \end{gathered} \tag{7.9}$$

The $\overline{b}_3$ and $\overline{b}_5$ parameters are very small, see Chapter 4, "EPR of iron-gallium borate single crystals with low x", so, here they are neglected. On the other hand, the spin Hamiltonian for iron ions in the near-surface layer should include terms describing the concomitant lowering of symmetry. Besides, as far as Fe^{3+} ions in $FeBO_3$ are subject to a strong exchange field, we can use the mean field approximation and substitute an effective exchange field $\boldsymbol{H}_k$ for the magnetizing field $\boldsymbol{H}$ ($k = 1,2$ numbering the non-equivalent iron sites). For the type of distortions described above, the spin Hamiltonian takes the form

$$\mathcal{H} = g\beta \boldsymbol{H}_k \cdot \boldsymbol{S}_k \pm B_2^{-2}O_2^{-2}{}_k + B_2^{-1}O_2^{-1}{}_k + B_2^0 O_{2k}^0 \pm B_2^1 O_{2k}^1 + B_2^2 O_{2k}^2 + B_4^0 O_{4k}^0 \pm B_4^3 O_{4k}^3 + B_4^{-3}O_4^{-3}{}_k \tag{7.10}$$

where g is close to the free electron g-factor, $g_e = 2.0023$, β is the Bohr magneton, $\boldsymbol{S}_k$ is the electron spin for the k^{th} Fe^{3+} ion ($S_k = 5/2$); $O_{2k}^0, O_2^{\pm 1}{}_k, O_2^{\pm 2}{}_k, O_{4k}^0$ and $O_4^{\pm 3}{}_k$ are the extended Stevens operators [7.8]; B_{2k}^0, $B_2^{\pm 1}{}_k$, $B_2^{\pm 2}{}_k$ and $B_{4k}^0, B_4^{\pm 3}{}_k$ are, respectively, the second and fourth-order fine structure parameters. In eq. (7.10) as well as in the subsequent equations the $\pm$ signs before certain terms correspond to $k = 1,2$, respectively.

Assuming the "Zeeman" term $\mathcal{H}_0 = g\beta \boldsymbol{H}_k \cdot \boldsymbol{S}_k$ in eq. (7.10) to be much larger than the remaining terms, we have calculated the energies of the spin levels $\mathcal{E}_{mk}$ using the perturbation theory in the same way as in Chapter 6, "Magnetocrystalline anisotropy of iron borate and iron-gallium borates". In the first order of perturbations, we get:

$$\begin{aligned} \mathcal{E}_{mk} = {} & g\beta m H_k + \left[3m^2 - S(S+1)\right] h_{2k}^1 \\ & + \left[35m^4 - 30m^2 S(S+1) + 25m^2 - 6S(S+1) + 3S^2(S+1)^2\right] h_{4k}^1 \end{aligned} \tag{7.11}$$

where $S = S_k = \frac{5}{2}$, $m = -\frac{5}{2}, -\frac{3}{2}, \cdots, \frac{5}{2}$ and

$$\begin{aligned} b_{2k}^1 &= \pm\tfrac{1}{2} B_2^{-2} \sin^2\vartheta_k \sin 2\varphi_k + \tfrac{1}{4} B_2^{-1} \sin 2\vartheta_k \sin\varphi_k + \tfrac{1}{2} B_2^0 \left(3\cos^2\vartheta_k - 1\right) \\ &\quad \pm\tfrac{1}{4} B_2^1 \sin 2\vartheta_k \cos\varphi_k + \tfrac{1}{2} B_2^2 \sin^2\vartheta_k \cos 2\varphi_k; \\ b_{4k}^1 &= \tfrac{1}{8} B_4^{-3} \cos\vartheta_k \sin^3\vartheta_k \sin 3\varphi_k + \tfrac{1}{8} B_4^0 \left(35\cos^4\vartheta_k - 30\cos^2\vartheta_k + 3\right) \\ &\quad \pm\tfrac{1}{8} B_4^3 \cos\vartheta_k \sin^3\vartheta_k \cos 3\varphi_k. \end{aligned} \tag{7.12}$$

In the strong exchange case, the spins of two non-equivalent iron ions are antiparallel: $\vartheta_1 = \vartheta$, $\varphi_1 = \varphi$, $\vartheta_2 = \pi - \vartheta$, and $\varphi_2 = \varphi + \pi$.

At $T = 0\,\mathrm{K}$, the only occupied spin level is the lowest one (with $m = -\frac{5}{2}$), so that the anisotropic part of the right-hand side of eq. (6.12) for this level provides the crystal-field contribution to the density of the magnetocrystalline anisotropy energy of the near-surface layer:

$$\sigma_{\mathrm{cf}\,S} = \tfrac{1}{2} N \begin{bmatrix} 10 B_{2\,S}^{-1} \sin\vartheta\cos\vartheta\sin\varphi + \left(30 B_{2\,S}^0 - 450 B_{4\,S}^0 + 10 B_{2\,S}^2\right)\cos^2\vartheta + 525 B_{4\,S}^0 \cos^4\vartheta \\ +20 B_{2\,S}^2 \sin^2\vartheta\cos^2\varphi + 15 B_{4\,S}^{-3} \cos\vartheta\sin^3\vartheta\sin 3\varphi \end{bmatrix} \tag{7.13}$$

where N is the number of Fe^{3+} ions per unit surface ($N = 6.0036 \cdot 10^{18}\ \mathrm{m}^{-2}$ for $\left(10\bar{1}4\right)$ face) and the S subscript refers to the parameters for the near surface layer in the presence of distortions. The parameters in eq. (7.13) depend on relative distortions, $\varepsilon = \Delta a_r / a_r$ where a_r is the edge length of the rhombohedron shown in Figures 7.1 and 7.2 and Δa_r is an absolute distortion of a_r. The positive and negative ε values correspond to contractions and extensions, respectively.

In the absence of structural distortions, *i.e.* at $\varepsilon = 0$, the crystal-field contribution to the density of the magnetocrystalline anisotropy energy of the near-surface layer would be the same as for an analogous layer in the crystal volume:

$$\sigma_{\mathrm{cf}\,V} = \tfrac{1}{2} N \begin{bmatrix} \left(30 B_{2V}^0 - 450 B_{4V}^0\right)\cos^2\vartheta \\ +525 B_{4\,V}^0 \cos^4\vartheta + 15 B_{4\,V}^{-3} \cos\vartheta\sin^3\vartheta\sin 3\varphi \end{bmatrix} \tag{7.14}$$

where the V subscript refers to the parameter in the volume, and N is the same as in eq. (7.13).

Thus, σ_{cf}, defined as $\sigma_{\mathrm{cf}\,S} - \sigma_{\mathrm{cf}\,V}$, can be expressed as:

$$\begin{aligned} \sigma_{\mathrm{cf}} &= \sigma_{\mathrm{cf}_1} \sin\vartheta\cos\vartheta\sin\varphi + \sigma_{\mathrm{cf}_2} \cos^2\vartheta \\ &\quad + \sigma_{\mathrm{cf}_3} \cos^4\vartheta + \sigma_{\mathrm{cf}_4} \sin^2\vartheta\cos^2\varphi + \sigma_{\mathrm{cf}_5} \cos\vartheta\sin^3\vartheta\sin 3\varphi \end{aligned} \tag{7.15}$$

where $\sigma_{\mathrm{cf}_1}, \sigma_{\mathrm{cf}_2}, \sigma_{\mathrm{cf}_3}, \sigma_{\mathrm{cf}_4}$ and σ_{cf_5} are defined as the difference between the parameters of matching symmetry terms in eqs. (7.13) and (7.14).

7.4 Comparison with experimental data

The parameters featuring in eq. (7.15), calculated for $|\varepsilon| \leqslant 3\%$, are given in Table 7.1. Obviously, the σ_{cf_3} and σ_{cf_5} parameters are much smaller than $\sigma_{cf_1}, \sigma_{cf_2}$ and σ_{cf_4}, thus they can be neglected.

Table 7.1 Crystal field contribution to the surface anisotropy constants, in Jm^{-3}.

ε, %	σ_{cf_1}	σ_{cf_2}	σ_{cf_3}	σ_{cf_4}	σ_{cf_5}
-3	$2.26\cdot10^{-4}$	$3.4\cdot10^{-5}$	$3.3\cdot10^{-7}$	$7.95\cdot10^{-5}$	$-9.5\cdot10^{-8}$
-2	$1.7\cdot10^{-4}$	$2.4\cdot10^{-5}$	$2.3\cdot10^{-7}$	$5.95\cdot10^{-5}$	$-6.1\cdot10^{-8}$
-1	$9.37\cdot10^{-5}$	$1.3\cdot10^{-5}$	$1.2\cdot10^{-7}$	$3.33\cdot10^{-5}$	$-2.8\cdot10^{-8}$
0	0	0	0	0	0
1	$-1.2\cdot10^{-4}$	$-1.45\cdot10^{-5}$	$-1.46\cdot10^{-7}$	$-4.17\cdot10^{-5}$	$2.4\cdot10^{-8}$
2	$-2.73\cdot10^{-4}$	$-3\cdot10^{-5}$	$-3.13\cdot10^{-7}$	$-9.307\cdot10^{-5}$	$3.9\cdot10^{-8}$
3	$-4.68\cdot10^{-4}$	$-4.5\cdot10^{-5}$	$-5.1\cdot10^{-7}$	$-1.55\cdot10^{-4}$	$4.2\cdot10^{-8}$

Now we can determine the equilibrium orientation of $\boldsymbol{l}$ in the near-surface layer in the absence of H taking into account the crystal field contribution. For this purpose, we minimize the sum $\sigma_{dip} + \sigma_{cf} + \gamma_\vartheta$ with respect to ϑ and φ, *cf.* eqs. (7.1), (7.3), (7.15) and Table 7.1. As far as for $|\varepsilon| \leqslant 3\%$ σ_{dip} only slightly changes with ε [7.6], for this quantity we can take its value in the absence of structural distortions, *cf.* eq. (7.1). These results are given in Table 7.2. As one can see, in the case of an extension, in the near-surface layer in equilibrium $\boldsymbol{l}$ becomes perpendicular to C_2, $\varphi_0 = \frac{1}{2}\pi, \frac{3}{2}\pi$, which contradicts the experimental data [7.4]; therefore, the eventuality of an extension can be ruled out. In contrast, in the case of a contraction, in equilibrium $\boldsymbol{l}$ remains parallel to C_2. Indeed, for ionic crystals, contractions rather than extensions are expected in the near-surface layer [7.9].

Table 7.2 Equilibrium orientation of $\boldsymbol{l}$ in the near-surface layer in the absence of H.

ε, %	ϑ_0	φ_0	ε, %	ϑ_0	φ_0
-3	$\vartheta_0 = \frac{\pi}{2} + 0.14$ $\vartheta_0 = \frac{\pi}{2} - 0.14$	$\varphi_0 = \frac{\pi}{2}$ $\varphi_0 = \frac{3}{2}\pi$	1		
-2	$\vartheta_0 = \frac{\pi}{2} + 0.11$ $\vartheta_0 = \frac{\pi}{2} - 0.11$	$\varphi_0 = \frac{\pi}{2}$ $\varphi_0 = \frac{3}{2}\pi$	2	$\vartheta_0 = \frac{\pi}{2}$	$\varphi_0 = 0$ $\varphi_0 = \pi$
-1	$\vartheta_0 = \frac{\pi}{2} + 0.07$ $\vartheta_0 = \frac{\pi}{2} - 0.07$	$\varphi_0 = \frac{\pi}{2}$ $\varphi_0 = \frac{3}{2}\pi$	3		

Taking into account the data in Table 7.2, eqs. (7.13) and (7.14), for σ_{cf}, defined as $\sigma_{\text{cf}S} - \sigma_{\text{cf}V}$, we get:

$$\sigma_{\text{cf}} = -10NB_{2S}^2 \sin^2\varphi . \tag{7.16}$$

Comparing eqs. (7.16) and (7.5), we get the crystal field contribution to the surface anisotropy constant:

$$a_{S\,\text{cf}} = -10NB_{2S}^2 , \tag{7.17}$$

and the total surface anisotropy constant can be expressed as

$$a_S = a_{S\,\text{dip}} + a_{S\,\text{cf}} . \tag{7.18}$$

The $a_{S\,\text{dip}}(\varepsilon)$ dependence for the layer containing Fe^{3+} ions (D in Figure 7.2) has been previously calculated at 300 K [7.6]. As the dipole-dipole interaction energy is proportional to the square of magnetization, *e.g.* see eq. (6.36) in Chapter 6, "Magnetocrystalline anisotropy of iron borate and iron-gallium borates", $a_{S\,\text{dip}}$ is expected to depend on the temperature as $\mathscr{M}_T^{\,2}$. Taking into account that $\mathscr{M}_0 / \mathscr{M}_{300} \approx 1.47$ [7.7], we have calculated $a_{S\,\text{dip}}(\varepsilon)$ at 0 K. Figure 7.3 shows the dependences on ε of $a_{S\,\text{dip}}$ [7.6], $a_{S\,\text{cf}}$ and a_S at 0 K. Obviously, the distortions much more affect $a_{S\,\text{cf}}$ than $a_{S\,\text{dip}}$.

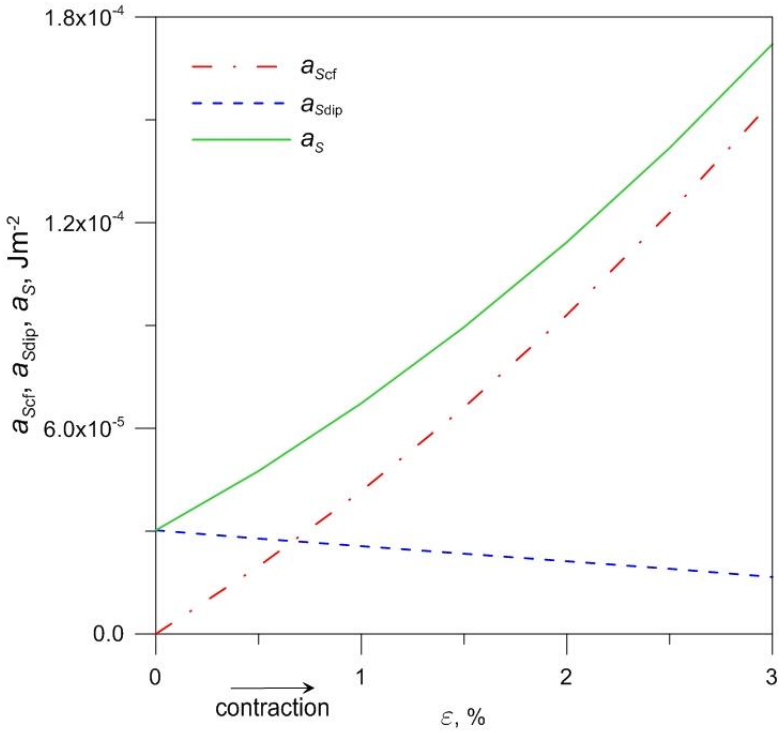

Figure 7.3 Values of $a_{S\,\mathrm{cf}}$, $a_{S\,\mathrm{dip}}$ [7.6] and a_S *vs.* ε at 0 K.

Next, using the $a_S(\varepsilon)$ dependence shown in Figure 7.3, we have calculated $H_\mathrm{c}(\varepsilon)$, *cf.* eq. (7.8). Figure 7.4 shows the latter dependence. The experimental value of H_c at 300 K, (1 kOe, *vide supra*) and the temperature dependence of H_c, see Figure 10 in the paper by Zubov *et al.* [7.4], suggest that at 0 K $H_\mathrm{c} \approx 1.47$ kOe. As one can see from Figure 7.4, such H_c value is attained at a contraction of ca. 1%.

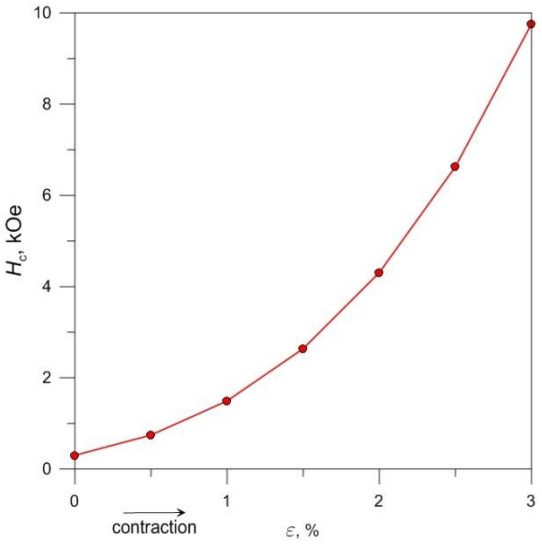

Figure 7.4 Calculated $H_\mathrm{c}(\varepsilon)$ dependence at 0 K.

Note that the crystal surface in itself constitutes a structure defect; nevertheless, other types of structure defects can occur in the near-surface layer, for instance, vacancies of magnetic ions or their substitutions by diamagnetic ions (diamagnetic dilution), and such defects are also expected to contribute to $a_{S\,\mathrm{cf}}$. In particular, in mixed iron-gallium borates $Fe_xGa_{1-x}BO_3$, $a_{S\,\mathrm{cf}}$ should depend on x. Studies on the surface magnetism in diamagnetically diluted crystals are in progress; here in Figure 7.5 we show the calculated $a_{S\,\mathrm{cf}}(x)$ dependence.

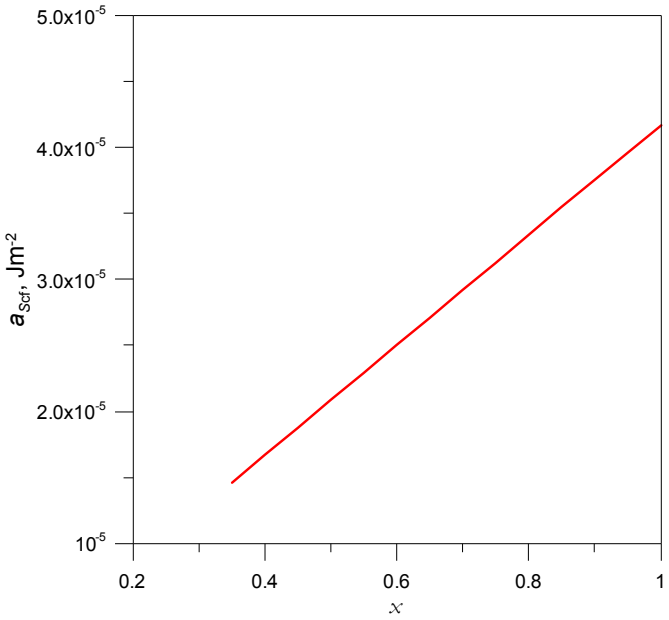

Figure 7.5 Calculated dependence of $a_{S\,\mathrm{cf}}$ on x for $\varepsilon = 1\%$ in $Fe_xGa_{1-x}BO_3$ crystals at 0 K.

7.5 Conclusions

The theory of the surface magnetism of iron borate has been extended to include, besides the dipole-dipole contribution, the crystal field contribution to the surface magnetocrystalline anisotropy energy.

A model of structural distortions in the near-surface layer for $(10\bar{1}4)$ face of iron borate has been developed, allowing all ions located in this layer to be displaced proportionally to their distance from a reference plane assumed to remain immobile. In order to account for the lowering of symmetry in the near-surface layer, the generalized spin Hamiltonian expressed through the tesseral spherical tensor operators has been applied, and the spin Hamiltonian parameters have been calculated within the superposition model. The crystal field contribution to the surface anisotropy energy at 0 K has been calculated in perturbation theory. Taking into account the distortions of the iron environment produces a significant crystal field contribution to the surface anisotropy constant; indeed, the experimental results can be satisfactorily described assuming relative contractions in the near-surface layer ca. 1%.

7.6 References

7.1 L. Néel, *L'anisotropie magnetique superficielle et substructures d'orientation*, J. Phys. Radium **15** (1954) 225-239

7.2 R. Diehl, W. Jantz, B.I. Nolang and W. Wettling, *Growth and properties of iron borate,* $FeBO_3$, in: *Current Topics in Materials Science*, E. Kaldis ed., Elsevier, New-York, v. **11** (1984) pp. 241-387

7.3 А.К. Панкратов, М.Б. Стругацкий и С.В. Ягупов, *Газотранспортный синтез и морфология изометричных монокристаллов бората железа*. Уч. записки Таврического национального университета им. В. И. Вернадского, Сер. Физ. **20(59)** (2007) 64-73

7.4 V.E. Zubov, G.S. Krinchik, V.N. Seleznyov and M.B. Strugatsky, *Near-surface magnetic structures in iron borate*, J. Magn. Magn. Mater. **86** (1990) 105-114

7.5 М.Б. Стругацкий, *Изометричные монокристаллы бората железа: магнитные и магнитоакустические эффекты*, Диссерация, Тавр. Нац. университет им. В.И. Вернадского, Симферополь (2008) 624 с.

7.6 E.M. Maksimova, I.A. Nauhatsky, M.B. Strugatsky and V.E. Zubov, *Surface magnetism of real iron borate monocrystals*, J. Magn. Magn. Mater. **322** (2010) 477-480

7.7 M. Kadomtseva, R.Z. Levitin, Yu.F. Popov, V.N. Seleznev and V.V. Uskov, *Magnetic and magnetoelastic properties of* $FeBO_3$ *single crystals*, Soviet Physics Solid State **14** (1972) 172-174

7.8 S.A. Al'tshuler and B.M. Kozyrev, *EPR in compounds of transition elements*, 2nd ed., Wiley, New York, Toronto, Jerusalem, London (1974) 512 pp.

7.9 J.E. Lennard-Jones and B.M. Dent, *The change in lattice spacing at a crystal boundary,* Proc. Royal Soc. London, Ser. A (1928) 247-259

Summary of results

The most significant results of this thesis are:

1. Working out a solution in the melt synthesis route for iron-gallium borates $Fe_xGa_{1-x}BO_3$, and preparing and characterizing high-quality single crystals in the whole range of compositions.

2. Electron magnetic resonance monitoring of iron-gallium borates in the transformation from magnetically ordered to paramagnetic state: antiferromagnetic resonance (AFMR) – coexistence of AFMR and cluster magnetic resonance (CMR) – CMR – electron paramagnetic resonance (EPR). Plausible observation of the Morin's transition in iron-gallium borates.

3. Determining temperature and concentration dependences of magnetic characteristics of iron-gallium borates, namely, the Néel temperature and Dzyaloshinskii-Moriya field.

4. Full parametrization of EPR spectra of Fe^{3+} ions in crystals with low iron contents by means of detailed computer simulations using laboratory-developed codes for the conventional, general and "tesseral" spin Hamiltonians, taking into account parameter distributions caused by local disorder.

5. Computer modelling of Magic Angle Spinning NMR spectra of ^{11}B and ^{71}Ga in $Fe_xGa_{1-x}BO_3$ with low iron contents, applying different distribution functions of quadrupole parameters and chemical shift in order to describe local disorder in the crystals.

6. Calculating magnetocrystalline anisotropy, uniaxial and basal, of iron-gallium borates as a sum of crystal field and dipole-dipole – in the model of extended dipoles – contributions; estimating the size of magnetic dipole related to Fe^{3+} ion.

7. Extending the theory of surface magnetism of iron borate by including, besides the dipole-dipole contribution, the crystal field contribution to surface magnetocrystalline anisotropy; modelling structural distortions in the near-surface layer of the crystals.

Author contribution

Articles in international journals and conference proceedings:

1. K. SELEZNYOVA, M. Strugatsky, S. Yagupov, N. Postivey, A. Artemenko and J. Kliava, *EPR of* Fe^{3+} *in* $GaBO_3$: *Superposition model analysis*, Phys. Stat. Sol. B **251** (2014) 1393-1400
2. K. SELEZNYOVA, M. Strugatsky, S. Yagupov, N. Postivey, A. Artemenko and J. Kliava, *Iron-doped gallium borate crystals: Synthesis and EPR study of local disorder*, in: *Proc. Int. Conf. on Oxide Materials for Electronic Engineering OMEE-2014* p. 205
3. S. Yagupov, E. Maksimova, I. Nayhatsky, V. Yagupov, E. Milyukova, K. SELEZNYOVA and M. Strugatsky, *Iron borate based monocrystals for research in magneto-ordered state physics*, in: *Proc. Int. Conf. on Oxide Materials for Electronic Engineering OMEE-2014* p. 207
4. K. SELEZNYOVA, N. Sergeev, M. Olszewski , P. Stepien, S. Yagupov, M. Strugatsky and J. Kliava, ^{11}B *MAS NMR study of* $Ga_{1-x}Fe_xBO_3$ *mixed crystals*, Solid State Nucl. Magn. Reson. **70** (2015) 38-42
5. S. Yagupov, M. Strugatsky, K. SELEZNYOVA, E. Maksimova, I. Nauhatsky, V. Yagupov, E. Milyukova and J. Kliava, $Fe_xGa_{1-x}BO_3$ *single crystals: synthesis and characterization*, Appl. Phys. A **121** (2015) 179-185
6. K. SELEZNYOVA, M. Strugatsky and J. Kliava, *Modelling the magnetic dipole*, Eur. J. Phys. **37** (2016) 025203, (1-14)
7. K. SELEZNYOVA, M. Strugatsky and J. Kliava, *Reply to Comment on 'Modelling the magnetic dipole'*, Eur. J. Phys. **37** (2016) 058002, (1-2)
8. M. Strugatsky, K. SELEZNYOVA, S. Yagupov, A. Drovosekov and J. Kliava, *Nature of magnetocrystalline anisotropy in the basal plane of iron borate*, J. Magn. Magn. Mater. (submitted, 2016)
9. M. Strugatsky, K. SELEZNYOVA, V. Zubov and J. Kliava, *On the nature of surface magnetic anisotropy in iron borate*, J. Magn. Magn. Mater. (submitted, 2016)
10. K. SELEZNYOVA, N. Sergeev, M. Olszewski , P. Stepien, S. Yagupov, M. Strugatsky and J. Kliava, *Fitting NMR spectra in crystals with local disorder: Czjzek's vs. Maurer's model for* ^{11}B *and* ^{71}Ga *in gallium borate*, Solid State Nucl. Magn. Reson. (submitted, 2016)

Articles in national journals:

11. M.B. Strugatsky, S.V. Yagupov, N.S. Postivey, K.A. SELEZNYOVA, E.T. Milyukova and V.S. Yagupov, *Monocrystal system* $Fe_xGa_{1-x}BO_3$ *for research in solid state physics*, Sci. Notes of Taurida National University, Ser. Phys. and Math. Sci. **24(63**) (2011) 169-174
12. M.B. Strugatsky, S.V. Yagupov, N.A. Postivey, K. SELEZNYOVA, A. Artemenko and J. Kliava, *On the choice of spin Hamiltonian for* Fe^{3+} *in* $Fe_xGa_{1-x}BO_3$ *single crystals*, Sci. Notes of Taurida National University, Ser. Phys. and Math. Sci. **26(65)** (2013) 132-137

Conference abstracts:

1. M.I. Nedokonceva, S.S. Krivoruchko, K.A. SELEZNYOVA and S.V. Yagupov, *Synthesis of rombohedric* $Fe_xGa_{1-x}BO_3$ *single crystals*, in: Abstracts of IVth National Scientific and Technical Conference (BFFH), Sebastopol (2008) p. 72
2. S.V. Yagupov, M.B. Strugatsky, N.S. Postivey, K.A. SELEZNYOVA., V.S. Yagupov and E.T. Milyukova, *Monocrystal system* $Fe_xGa_{1-x}BO_3$ *for research in solid state physics*, in: Abstracts of International conference "Functional Materials" (ICFM-2011), Partenit (2011) p. 184
3. K. SELEZNYOVA, M. Strugatsky, S. Yagupov, N. Postivey, A. Artemenko and J. Kliava, *Synthesis and EMR studies of* $Fe_xGa_{1-x}BO_3$ *single crystals*, in: Abstracts of 4th International Conference of Young Scientists "Low Temperature Physics" (ICYS-LTP-2013), Kharkiv (2013) p. 56
4. K. SELEZNYOVA, M. Strugatsky, S. Yagupov, N. Postivey, A. Artemenko and J. Kliava, *EPR of* Fe^{3+} *ions in* $GaBO_3$ *single crystals*, in: Abstracts of International Conference on Functional Materials (ICFM'2013), Gaspra (2013) p. 53
5. S.V. Yagupov, M.B. Strugatsky, N.S. Postivey, K.A. SELEZNYOVA, V.S. Yagupov and E.T. Milyukova, *Monocrystals based on Iron Borate for researches in solid state physics and magnetism*, in: Abstracts of International Conference on Physics and Technology of Thin Films and Nanosystems ICPTTFN-XIV (2013)
6. K. SELEZNYOVA, M. Strugatsky, S. Yagupov, N. Postivey and J. Kliava, *Electron magnetic resonance study of local disorder in iron doped gallium borate*, in: Abstracts of 4th International Conference on Superconductivity and Magnetism ICSM, Antalya (2014) p. 62
7. N. Sergeev, M. Olszewski, P. Stępień, K. SELEZNYOVA, M. Strugatsky, S. Yagupov and J. Kliava, *Magic angle spinning NMR of* ^{11}B *and* ^{71}Ga *in* $Ga_xFe_{1-x}BO_3$ *mixed crystals*, in: Abstracts of Conference Spin Physics, Spin Chemistry and Spin Technology, Saint Petersburg (2015) p. 153
8. J. Kliava, M. Strugatsky, P. Rosa, K. SELEZNYOVA and S. Yagupov, *Transparent magnetics based on iron borate*, in: Abstracts, Energy Materials Nanotechnology (EMN) Prague meeting (2016) pp. 97-98
9. S. Yagupov, M. Strugatsky, K. SELEZNYOVA, Yu. Mogilenec, A. Drovosekov, N. Kreines and J. Kliava, *Determination of the Dzyaloshinskii field for* $Fe_xGa_{1-x}BO_3$ *single crystals by AFMR technique*, in: Abstracts of the Euro-Asian Symposium "Trends in Magnetism" (EASTMAG), Krasnoyarsk (2016) p. 273.